Charles University in Prague
Faculty of Mathematics and Physics

DOCTORAL THESIS

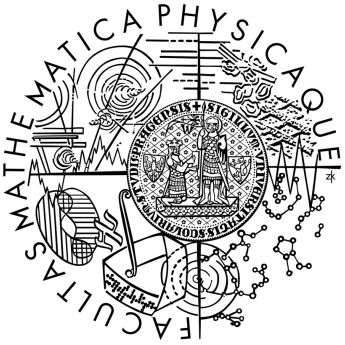

Josef Havlíček

Study of Equilibrium Magnetic Configuration in Tokamak Type Devices

Department of Surface and Plasma Science

Supervisor of the doctoral thesis: prof. RNDr. Milan Tichý, DrSc.

Study programme: Physics
Specialization: 4F2 Physics of plasmas and ionized media
Prague 2015

I would like to thank to my physics and mathematics teachers Lenka Nekolová, Martin Kapoun, Josef Málek, Jiří Podolský, Pavel Kudrna and Jan Stöckel for their great influence in teaching me to love the science, especially the physics.

I would like to thank to Radomír Pánek and Martin Hron for creating an opportunity to transfer the COMPASS tokamak to Prague.

I declare that I carried out this doctoral thesis independently, and only with the cited sources, literature and other professional sources.

I understand that my work relates to the rights and obligations under the Act No. 121/2000 Coll., the Copyright Act, as amended, in particular the fact that the Charles University in Prague has the right to conclude a license agreement on the use of this work as a school work pursuant to Section 60 paragraph 1 of the Copyright Act.

In…..... date..... signature

Název práce: Studium rovnovážné magnetické konfigurace v zařízeních typu tokamak
Autor: Josef Havlíček
Katedra / Ústav: Katedra fyziky povrchů a plazmatu
Vedoucí doktorské práce: prof. RNDr. Milan Tichý, DrSc.
Katedra fyziky povrchů a plazmatu

Abstrakt: Tato dizertační práce prezentuje magnetická pole tokamaku COMPASS a práci vykonanou během reinstalace COMPASSu v České republice. V technické části práce je popsána geometrie, vakuová magnetická pole a výkonové zdroje obvodů cívek poloidálního pole. Je představen návrh filtrů výkonových zdrojů a vylepšení algoritmu regulátorů výkonových zdrojů. Ve fyzikální části je popsána implementace modelu indukovaných proudů do kódu EFIT++, který se využívá pro rekonstrukci MHD rovnováhy. Kód EFIT++ byl přizpůsoben pro COMPASS. Je představeno využití kódu EFIT++ při provozu tokamaku COMPASS. Na příkladech je vysvětlena globální energetická bilance během nestacionárních fází výboje v tokamaku. Přiložené články popisují nové výkonové zdroje a zpětnovazební systém vyvinutý pro kontrolu plazmatu v tokamaku COMPASS.

Klíčová slova: tokamak, MHD rovnováha, napájecí zdroje, energetická rovnováha

Title: Study of Equilibrium Magnetic Configuration in Tokamak Type Devices
Author: Josef Havlíček
Department / Institute: Department of Surface and Plasma Science
Supervisor of the doctoral thesis: prof. RNDr. Milan Tichý, DrSc.
Department of Surface and Plasma Science

Abstract: This thesis presents the magnetic fields of the COMPASS tokamak and work done during the COMPASS reinstallation in the Czech Republic. The geometry, vacuum magnetic fields and Power Supplies for the poloidal field coils circuits are described in the technical part of the thesis. The design of Power Supplies filters and improvements in the controller algorithm are also introduced. The MHD equilibrium reconstruction code EFIT++ and implementation of the induced currents model are described in the physical part of the thesis. The EFIT++ code was adapted for COMPASS. The utilization of the EFIT++ code for the COMPASS operation is shown. The global power balance in the non-stationary phases of the tokamak discharge is explained and examples are shown. The attached articles describe Power Supplies and tokamak feedback system developed for the COMPASS plasma control.

Keywords: tokamak, MHD equilibrium, power supplies, global power balance

Contents

1 Introduction

This thesis summarizes part of the author's work during his doctoral studies at the Charles University in Prague. The work has been performed at the Tokamak Department, Institute of Plasma Physics of the Czech Academy of Sciences (IPP Prague). The reinstallation and commissioning of the COMPASS tokamak was in progress during the work on the doctoral thesis, strongly influencing the studies. There are two main topics in the thesis: 1) physical engineering description of the COMPASS magnetic field systems, and 2) utilization of the MHD equilibrium reconstruction for COMPASS physical programme.

The COMPASS tokamak is a small tokamak with clear H-mode and ITER-like geometry. Until 2001 it was operated by United Kingdom Atomic Energy Authority in Culham Science Centre in United Kingdom. The tokamak was offered to the IPP Prague in 2004. The opportunity to broaden the physical possibilities available to the Tokamak Department led the IPP management to accept such challenge. The project of reinstallation of the COMPASS tokamak officially started in July 2006, the same year as start of author's doctoral studies.

The reinstallation and commissioning of COMPASS required the Tokamak Department to acquire expertise in the fields where the know-how was available neither within the IPP Prague nor in the Czech Republic. It was necessary to learn about topics ranging from common, through technical, to physical. The common problems included for example the design of the tokamak hall to protect against radiation or cooling of the tokamak coils by demineralized water. The technical topics were ranging from requirements for newly built COMPASS Power Supplies systems to design of many new diagnostics. The physical knowledge, necessary to operate a tokamak with H-mode and diverted plasma, includes understanding the plasma control, first wall conditioning, physics of Neutral Beam Injection heating or plasma shape reconstruction from measured data.

The first main subject of this thesis is physical description of the poloidal magnetic field systems, particularly with respect to the feedback control of the tokamak plasma. The second main subject is focused on the numerical reconstruction of the MHD equilibrium, induced currents in the tokamak vacuum vessel and utilization of the reconstructed equilibria to determine plasma properties useful both for tokamak operators and for physicists studying the tokamak plasma.

1.1 Goals

The main goal of the work was to support the COMPASS reinstallation, commissioning and utilization in Prague. The particular topic was "everything connected with the magnetic field".

The individual goals were:

1) Characterize the vacuum magnetic field generated by COMPASS poloidal field coils
2) Commission the magnetic diagnostics of the COMPASS tokamak
3) Create a simple algorithm for real-time plasma position determination
4) Control the plasma current, position, shape and density
5) Understand and improve the Power Supplies used for plasma control
6) Understand, install and operate the MHD equilibrium reconstruction code EFIT
7) Utilize the reconstructed equilibria for COMPASS needs

The text of this thesis contains points 1) and 5) in Chapter 3 - Magnetic Field systems, and points 6) and 7) in Chapter 4 - Equilibrium reconstruction. The point 2) is briefly covered in the Chapter 2 - COMPASS tokamak. The articles attached at the end of the thesis cover the points 3) and 4).

The work was done in collaboration within the COMPASS team. Particularly the topic of control of the tokamak plasma was done in collaboration with Filip Janky. His doctoral thesis "*Design and implementation of the plasma control system for the COMPASS tokamak*" is focused more on the control tasks and should contain detailed description of points 3) and 4) which are covered only by attached articles here.

1.2 Thesis overview

The thesis is divided as follows:

- **Chapter 1** is this *Introduction*.
- **Chapter 2** - *COMPASS tokamak* - contains a brief introduction and overview of the COMPASS tokamak (Section 2.1), the available diagnostics (Section 2.2) and particularly the magnetic diagnostics (Section 2.3).
- **Chapter 3** - *Magnetic Field systems* - describes the magnetic field systems of the COMPASS tokamak. This chapter offers information about poloidal field (PF) coils, their magnetic field and used Power Supplies in a concise form suitable for physicists.
    - The technical part of the Section 3.1 is dedicated to description of the PF coils geometry (Section 3.1.1), the sign convention for currents in COMPASS (Section 3.1.2) and connection of PF coils windings into circuits (Section 3.1.3).
    - The physical part of the Section 3.1 covers theory for calculation of magnetic field of a toroidally wound coil (Section 3.1.4), characterization of vacuum magnetic fields of PF coils circuits

(Section 3.1.5) and tables with mutual and self- inductances of COMPASS PF coils circuits (Section 3.1.6).
    - Section 3.2 focuses on the COMPASS stray magnetic fields.
    - Section 3.3 describes filters designed for the PF coils Power Supplies. The principle (Section 3.3.1), simulations (Section 3.3.2), preliminary measurements (Section 3.3.3) and current status (Section 3.3.4) are discussed.
    - Section 3.4 contains description of the mutual influence between individual Power Supplies (Section 3.4.1), description of the Power supplies controller (Section 3.4.2 and Section 3.4.3) and improvements performed in the controller (Section 3.4.4).
- **Chapter 4** - *Equilibrium reconstruction* - focuses on numerical reconstruction of the MHD equilibrium.
    - The theory of the Grad-Shafranov equation (Section 4.1.1) and its use in numerical code EFIT (Section 4.1.2) is described in Section 4.1.
    - The theory (Section 4.2.1), implementation (Section 4.2.2) and benchmarking (Section 4.2.3) of the induced currents model for the EFIT code is in Section 4.2.
    - Section 4.3 describes use of one particular discharge (Section 4.3.1) for discussion about the induced currents in the vacuum vessel of the COMPASS tokamak (Section 4.3.2). Their influence on reconstructed equilibrium is assessed in Section 4.3.3.
    - The automatic inter-shot EFIT run (Section 4.4.1) and its use for tokamak operation (Section 4.4.2) is examined in Section 4.4.
    - Global power balance in non-stationary phases of the plasma discharge is described in Section 4.5. Theory (Section 4.5.1), numerical determination of externally induced voltage (Section 4.5.2), detailed analysis for L-mode discharge (Section 4.5.3) and interesting examples (Section 4.5.4) are discussed.
- **Chapter 5** - *General conclusions* - summarizes the results in the doctoral thesis.
- **Attached articles** provide information about the Fast Amplifiers and Vertical Kick Power Supply built for control of vertical plasma position (A1), real-time plasma position algorithm (A2) and about improvements in the real-time plasma control and in plasma position algorithm (A3).

2 COMPASS tokamak

The COMPASS tokamak is a small tokamak with a clear H-mode [1] and ITER-like geometry. The COMPASS tokamak was designed to study mainly MHD physics in Culham Science Centre in United Kingdom in 1980s, [2], [3], [4], [5], [6], [7], [8]. It is equipped with four quadrant set of saddle coils to create resonant magnetic perturbation (RMP) fields to influence the ELMs [9]. COMPASS had the first plasma in 1989 with circular a cross-section vacuum vessel. The vessel was upgraded to D-shaped vessel and tokamak was restarted in 1992. The COMPASS tokamak was successfully operated until 2001 when it was mothballed due to difficulties of operating the COMPASS tokamak simultaneously with spherical MAST tokamak.

The tokamak was offered to Institute of Plasma Physics on 29th October 2004. The project of reinstallation in Prague ([10]) officially started in July 2006 when the Preferential support of EURATOM was granted.

The timeline of the COMPASS tokamak in the Czech Republic is:

29 October 2004	Letter with official offer to transfer COMPASS to CR
2005	Preparation phase, governmental support provided
July 2006	Preferential support of EURATOM granted, **start of the COMPASS Project**
2007	Construction of the buildings, Power Supplies, transport of COMPASS parts to CR
20 October 2007	Arrival of the COMPASS tokamak to CR, temporary storage
12 December 2007	Moving the COMPASS to final place in tokamak hall
9 December 2008, 11:45	**First plasma** (#180) achieved during engineering test, up to 150 ms discharge duration achieved in next two days
19 February 2009	Official start of the tokamak test operation
November 2009	First design [11] of Fast Amplifiers (FA) for plasma position stabilization built, 23 November 2009: information from IST Lisbon that the design is faulty
June 2010	Commissioning of altered first design of FAs failed
November 2010	Fundamental error in the first design of FAs found, design of a completely new FAs started
July 2011	First tests of the FA for radial position stabilization with power supply from flywheel (#1847)
September 2011	Radial position feedback for **circular limiter plasma** is fully functional
November 2011	Feedback for plasma current functional
March 2012	Start of commissioning of vertical plasma position feedback
November 2012	Vertical position feedback fully operational, **plasma in divertor configuration**
29 November 2012, 13:07	**First H-mode** achieved (#4073), ELM free, NBI assisted

The timeline of the COMPASS reinstallation in the Czech Republic can be divided into several periods: preparation (2005-2006), transportation and reinstallation (2006-2008), commissioning (2009-2011) and scientific exploitation (2012 onwards).

The dismantled tokamak after the transport to the Czech Republic is depicted in the **Figure 2.1**. The tokamak is on its place in the tokamak hall.

The status of the tokamak before the first plasma in December 2008 is in the **Figure 2.2**. The radial preload system for toroidal field coils, gallery over the tokamak, the Upper Link Board for poloidal field coils, a vacuum pumping system and basic diagnostics are installed. The cables leading from tokamak to the computer on the right connect the fast visible camera [12].

The current status of the tokamak COMPASS is in the **Figure 2.3**.

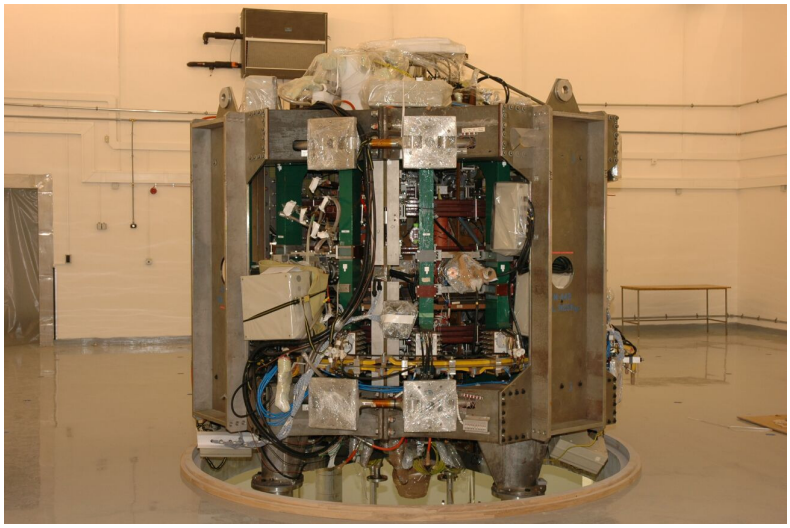

Figure 2.1: Dismantled COMPASS in the tokamak hall in Prague, 2008

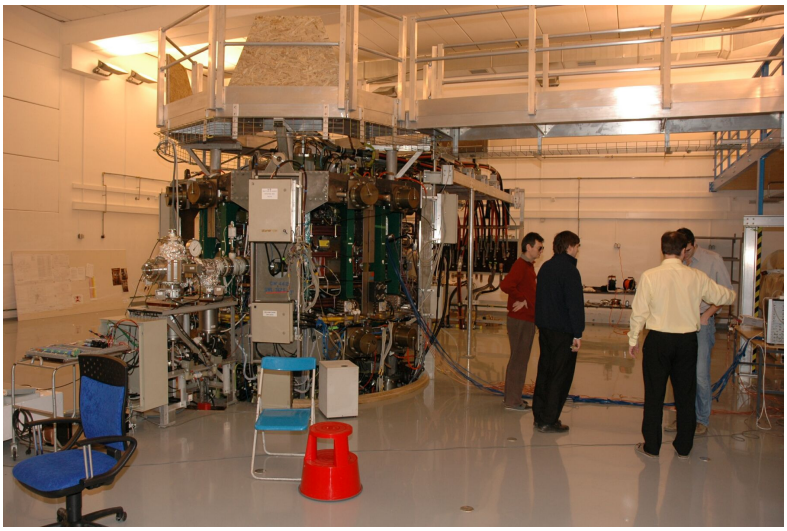

Figure 2.2: COMPASS before the first plasma, 9.12.2008. The Upper Link Board, gallery over the tokamak, vacuum systems and basic diagnostics including fast visible camera installed.

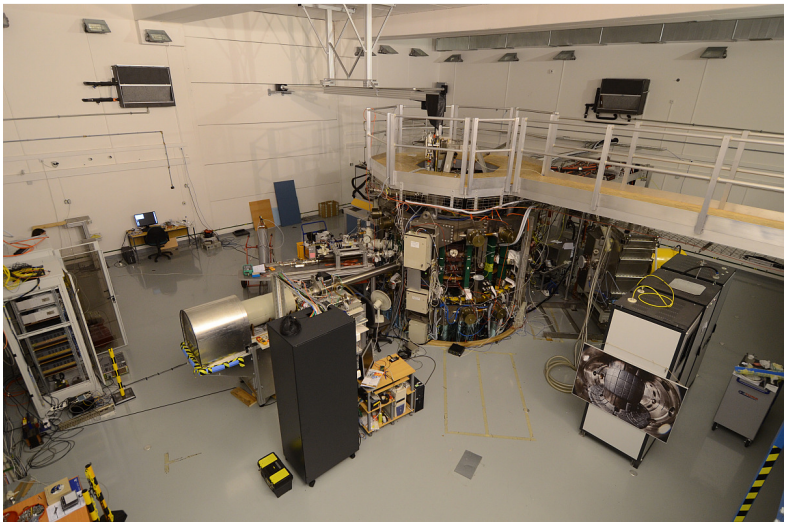

Figure 2.3: COMPASS, current status (as of 11.6.2015). Thomson scattering system, Li beam diagnostics and Neutral Beam Injection systems are visible.

The physical programme of the COMPASS tokamak is mainly concentrated on the edge plasma, particularly during H-mode:

- L-H transition, multi-parameter scaling
- Edge Localized Modes (ELMs)
- plasma-wall interaction, heat transfer during ELMs
- ELM control techniques (Magnetic Perturbation, vertical kicks)
- Scrape-Off Layer (SOL) physics
- pedestal physics
- long range correlations of turbulent structures and MHD modes
- runaway electrons studies
- disruption studies

2.1 Overview

This section provides quick overview of the basic parameters of the COMPASS tokamak.

The COMPASS tokamak [10] has major radius 0.56 m, minor radius 0.2 m and elongation 1.8. The ITER-like geometry is depicted in the **Figure 2.4**. It can be operated with various plasma shapes (circular, elliptic, diverted with smaller or larger triangularity) and sizes, allowing good flexibility of important parameters: elongation, triangularity or SOL width.

The parameters of the COMPASS tokamak are summarized in the **Table 2-1**.

The tokamak has maximal achievable toroidal magnetic field 2.1 T. This toroidal magnetic field requires 92 kA current in the toroidal field coils and vertical hydraulic preload system [13], [14] to compensate the forces acting on the coils. The tokamak is routinely operated with toroidal magnetic field 1.15 T, where the stress on the coils allows infinite amount of cycles.

The plasma current up to ~350 kA is achievable for B_T = 1.15 T. The pulse duration of ~0.5 s with plasma current flat-top up to 300 ms is regularly achieved. The maximal achieved pulse duration was 1 s.

The line integrated density is up to 1.2×10^{20} m^{-3} (for B_T = 1.15 T).

The ohmic heating is up to ~500 kW and additional heating is provided by two Neutral Beam Injection systems 2x400 kW, see [15], [16]. This power allows reaching ~4x higher power than the L-H threshold.

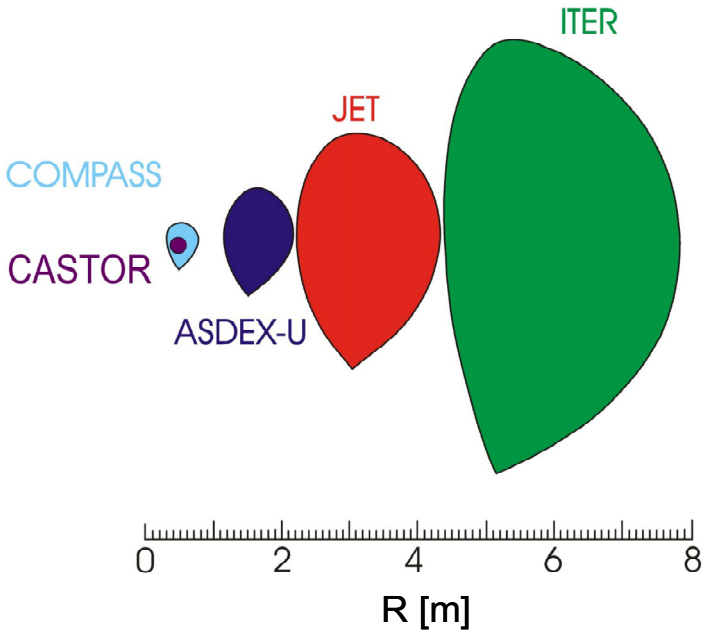

Figure 2.4: Comparison of the dimensions of tokamaks with ITER-like shape. The COMPASS tokamak is 10 times smaller than the ITER tokamak in the linear dimension.

Parameters	Values
Major radius R	0.56 m
Minor radius a	0.2 m
Plasma current I_{pl} (max)	350 kA
Magnetic field B_T	0.9 - 2.1 T
Ultimate pressure	1x10-6 Pa
Elongation	1.8
Triangularity	0.5
Palsma shape	circular, elliptical, SND, SNT
Pulse length	~0.5 s
Beam heating P_{NBI} 40 keV	2 x 0.4 MW

Table 2-1: The COMPASS parameters.

2.2 Diagnostics

This section contains brief summary of the diagnostic available on the COMPASS tokamak.

The article of Weinzettl, et al., *Overview of the COMPASS diagnostics* [17] provides references for the listed diagnostics:

- magnetic diagnostics, [18], [14]
- Thomson scattering diagnostic system, [19], [20]
- Fast cameras, [12]
- Multi-range tomographic system: fast bolometry and SXR tomography, [21], [22], [23]
- Charge Exchange Recombination Spectroscopy (in construction), [24]
- Interferometer, [25]
- Radiometer, [26], [27]
- Reflectometer
- Reciprocating probes, [28], [29]
- Divertor probes, [30]
- Beam emission spectroscopy, [31], [32]
- Atomic probe diagnostics, [33]
- Neutral particle analyzer, [34]

2.3 Magnetic diagnostics

This section briefly summarizes the status of the magnetic diagnostic of the COMPASS tokamak. The diagnostic coils used further in the thesis are described in more detail. This section is extended and updated form of two articles: Havlicek et al., 2009, *Magnetic Diagnostics for Start-up Phase of COMPASS* [18] and Havlicek et al., 2010, *Status of Magnetic Diagnostics on COMPASS* [14].

There are 392 magnetic diagnostics coils (see **Table 2-2**) positioned all over the vacuum vessel (see **Figure 2.5**) in the COMPASS tokamak. These coils were transported in a functional state from Culham. Replacement of the data cables and rack cabinets containing analogue integrators was performed because to the data acquisition system location outside of the tokamak hall.

All diagnostic coils were checked for short circuit with the vacuum vessel during COMPASS reinstallation. It was found out that several of them are functionless. Cables going from tokamak hall to CODAC room with data acquisition were laid and equipped with connectors.

Name	Location with respect to the vessel	Number of coils	Measures
Full toroidal loops	ext	8	loop voltage and poloidal flux (used for real time cotrol and EFIT)
Saddle loops	ext	22x4 and 2x8	the difference in poloidal flux
Remote loops	ext	5	loop voltage and poloidal flux, not used routinelly
Diamagnetic loops	int	2	perpendicular beta
Diamagnetic compensation loops	int	2	toroidal field
Mirnov coils	int	3x24x3	local poloidal, radial and toroidal fiels (hence 3 times), 24 at one cross section
High n Mirnov coils	int	4	n-number of MHD instabilities
Divertor Mirnov coils	int	2x8	coils at imbeded in divertor plates (usable for ELMs study)
Internal Partial Rogowski coils	int	16	local magnetic field parallel to a vacuum vessel (real time cotrol and EFIT)
External Partial Rogowski coils	ext	16	local magnetic field parallel to a vacuum vessel, eddy currents
Full Rogowski coils	1 ext and 1 int	2	plasma current
Diamagnetic Rogowski coil	ext	1	toroidal field current

Table 2-2: Available diagnostic coils.

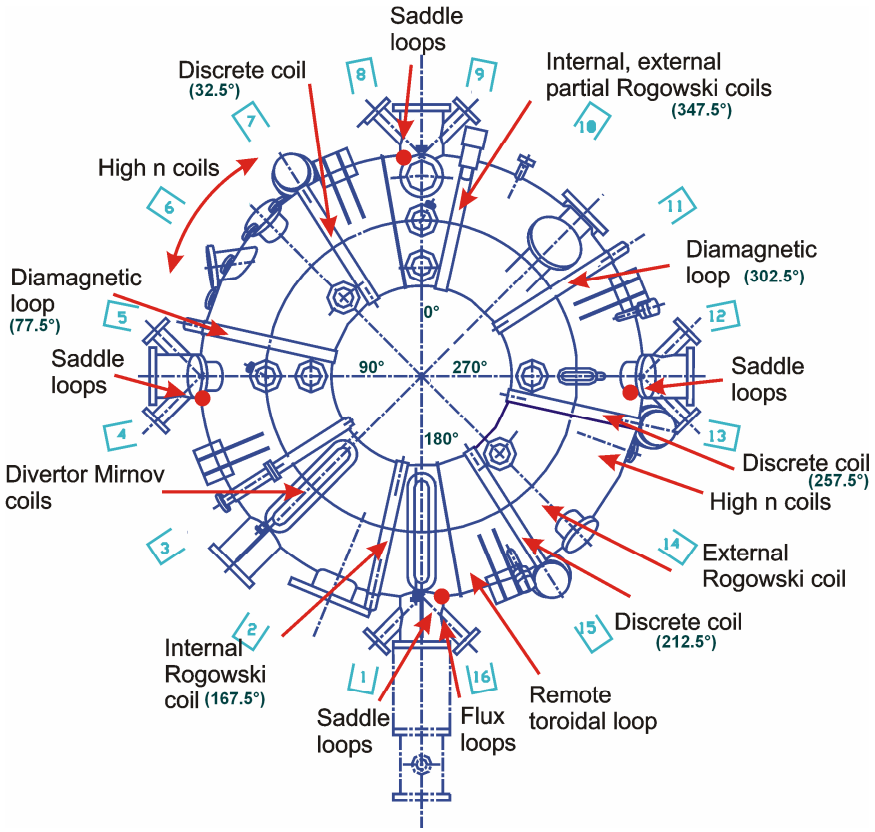

Figure 2.5: Top view of the COMPASS tokamak vacuum vessel with magnetic diagnostics coils. Discrete coils are Mirnov coils.

Magnetic coils measure time derivative of the magnetic field. An analogue integration is required to obtain a reliable value of the magnetic field. Numerical integration is often not suitable because it is hard to fulfil the requirements to AD converters – accurate measurement of ranges from tenths of μV to tens of volts with ~ MS/s sampling rate. Fifteen active analogue Quad Integrators with variable gain and drift compensation were transported from Culham to IPP Prague. Each of these integrators has four independent output channels. These integrators are used for basic set of diagnostic coils, particularly those used for real-time feedback control of the plasma column.

The majority of the diagnostic coils is connected to the data acquisition systems without integrators. The advantage against signals integrated with analogue integrator is better frequency bandwidth. These coils are mainly used for studies of magnetic field fluctuations. The numerical integration is used, but the integrated signal often looses continuity during plasma disruptions.

The current status of the magnetic diagnostics (as of 11.6.2015) is that ~290 diagnostic coils are measured routinely:

- Data acquisition system called "ATCA1", 2 MS/s, 16 bit resolution:
  - 24 discrete Mirnov coils in ring B - integrated - measurement of local B_θ on 24 positions around plasma on toroidal angle 215.5º.
  - 16 Internal Partial Rogowski coils - integrated - measurement of line averaged B_θ on 16 poloidal positions around plasma on toroidal angle 347.5º. Used for real-time plasma position reconstruction.
  - 4 flux loops without integration – measurement of loop voltage U_{FL}. Voltage divider is used to decrease the measured voltage to the operational range +/-10 V of data acquisition system.
  - 4 flux loops with integration – measurement of the poloidal flux function Ψ. Real-time plasma position reconstruction.
  - 8 commercial Rogowski coils MFC 150 (Algodue Elettronica) – measurement of currents in the poloidal and toroidal field coils circuits.
  - 1 Internal Rogowski Coil – winded inside the vacuum vessel. Measures plasma current I_{pl}.
  - 1 External Rogowski Coil – winded around the vacuum vessel. Measures sum of plasma current and vessel current.
  - 2 diamagnetic loops – measurement of plasma energy.
- Data acquisition system "Nimbus", 2 MS/s, 16 bit resolution, ~2x lower noise than ATCA1, higher bandwidth: 650 kHz:
  - 3x24 discrete Mirnov coils in ring A - not integrated - full ring of all three components of magnetic field, toroidal angle 32.5º.
  - 24 discrete Mirnov coils in ring C - not integrated - measurement of local B_θ on 24 positions around plasma on toroidal angle 257.5º

- 104 Saddle loops - not integrated - the vacuum vessel is covered with 22x4 coils in four toroidal quadrants, measuring normal magnetic field. There are 8x2 coils in eight octants on the LFS midplane.
- 16 External Partial Rogowski coils - not integrated - measurement of line averaged B_θ on 16 poloidal positions around plasma and vacuum vessel on toroidal angle 347.5º.
- 2x8 Divertor Mirnov coils - not integrated - eight tangential and normal measurements in the divertor plate.

▪ 4 commercial Hall sensors GH-601 (F.W.Bell) – direct measurement of toroidal field. The Hall sensors do not require analogue integration and are used in machine protection system to control the current in the TF coils.

Figure 2.6 shows positions and numbers of 16 Internal Partial Rogowski (IPR) coils and positions of 24 Mirnov coils.

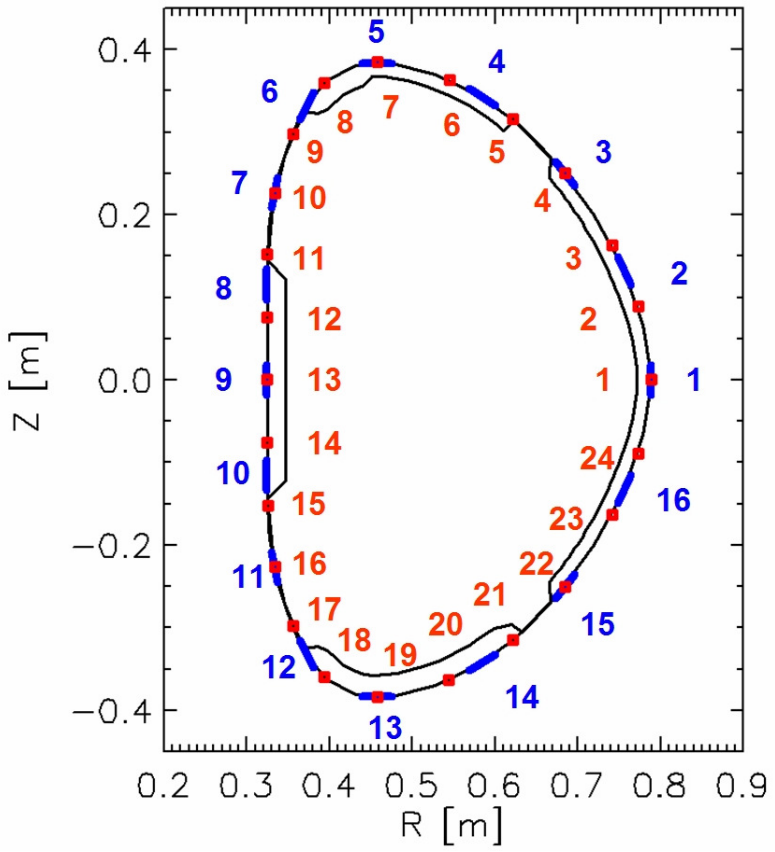

Figure 2.6: Poloidal cut of the COMPASS tokamak with Internal Partial Rogowski coils (blue) and Discrete Mirnov coils (red) numbers.

Diagnostic coils calibration

The flux loops do not require calibration because their spatial dimensions are big enough and error of its measurement negligible enough to just compute the calibration factor in Tesla per volt.

The Internal and External Rogowski coils used for determination of the plasma and vacuum vessel currents, as well as Rogowski coils used for measurement of

currents in the poloidal field coils circuits, were calibrated together with particular integrators assigned to each of the coils. A capacitor with capacitance 3.2 F and voltage 50 V was discharged into thick flexible wire coming through Rogowski coils producing current in the wire up to ~ 230 A. The effective current flowing in the cross-section of the Rogowski coils was increased by passing the thick wire several times through the cross-section (14x for commercial Rogowski coils, 3x for Internal and External Rogowski coils). The current in the thick wire was accurately measured on the invar resistor shunt with four-point method. Then, the sought after calibration constant in ampere per volt was then determined from the output voltage of the integrator.

No.	Name	R [m]	Z [m]	angle [deg]	calibration	unit
37	MIRNOV 07 BΘ	0.4575	0.3845	-1.1598	-0.1343	T/V
38	MIRNOV 08 BΘ	0.3934	0.3594	40.65079	-0.1135	T/V
39	MIRNOV 03 BΘ	0.7411	0.1632	-62.7661	XXX	T/V
40	MIRNOV 04 BΘ	0.6845	0.2500	-51.8462	-0.1206	T/V
41	MIRNOV 09 BΘ	0.3553	0.2981	67.9658	-0.1146	T/V
42	MIRNOV 10 BΘ	0.3336	0.2265	78.702	XXX	T/V
43	MIRNOV 05 BΘ	0.6213	0.3160	-41.6335	XXX	T/V
44	MIRNOV 06 BΘ	0.5447	0.3637	-22.6175	0.1153	T/V
45	MIRNOV 11 BΘ	0.3249	0.1522	88.27893	0.1188	T/V
46	MIRNOV 12 BΘ	0.3245	0.0762	90	-0.1166	T/V
47	MIRNOV 13 BΘ	0.3245	0.0000	90	0.1180	T/V
48	MIRNOV 14 BΘ	0.3244	-0.0762	90.57873	-0.1168	T/V
49	MIRNOV 19 BΘ	0.4575	-0.3845	181.1598	0.1229	T/V
50	MIRNOV 20 BΘ	0.5444	-0.3631	202.5083	-0.1161	T/V
51	MIRNOV 15 BΘ	0.3252	-0.1522	91.1598	0.1146	T/V
52	MIRNOV 16 BΘ	0.3335	-0.2265	101.8887	-0.1171	T/V
53	MIRNOV 21 BΘ	0.6210	-0.3150	222.1451	XXX	T/V
54	MIRNOV 22 BΘ	0.6846	-0.2500	232.2981	0.1186	T/V
55	MIRNOV 17 BΘ	0.3553	-0.2981	112.0342	-0.1149	T/V
56	MIRNOV 18 BΘ	0.3933	-0.3594	139.3492	0.1137	T/V
57	MIRNOV 23 BΘ	0.7411	-0.1633	243.065	-0.1181	T/V
58	MIRNOV 24 BΘ	0.7728	-0.0890	252.1645	0.1197	T/V
59	MIRNOV 01 BΘ	0.7892	0.0000	-90	-0.1151	T/V
60	MIRNOV 02 BΘ	0.7729	0.0890	-72.1438	0.1159	T/V

note: Mirnov coils MDMB are at 212.5 deg, zero is north cross
angle is measured from outward oriented vector, clockwise is negative

Table 2-3: Positions, angles and calibrations of discrete Mirnov coils in ring B.

The Internal Partial Rogowski coils and discrete Mirnov coils were calibrated with magnetic field originating from poloidal field coils circuits EFPS (Equilibrium Field Power Supply circuit) and SFPS-SND (Shaping Field Power Supply circuit, Single Null Divertor configuration). The purpose and magnetic field of these circuits is described in the Section 3.1.5. The magnetic field on position of diagnostic coils was determined by using numerical integration of Biot-Savart law from known geometrical description of PF coils circuit. The computed magnetic field was then projected into the direction of diagnostic coils. A series of dedicated vacuum

discharges with different currents in EFPS and SFPS-SND circuits measured by Rogowski coils was used for obtaining standard deviation of the calibration constant.

Currents induced in the vacuum vessel during PF coils circuit current ramp-up and ramp-down create a magnetic field which influence the signal in the diagnostic coils. Only data sampled during stationary phase were included to the computation of calibration constants.

The results from the calibration are summed in the **Table 2-3** and in the **Table 2-4**, together with positions and angles.

No.	Name	R	Z	angle	calibration	unit
		[m]	[m]	[deg]		
1	MFPS - Rogowski coil				-2856	A/V
2	EFPS - Rogowski coil				-2850	A/V
3	SFPS - Rogowski coil				-1420	A/V
4	BR - Rogowski coil				576	A/V
5	BV - Rogowski coil				-574	A/V
6	TF - Rogowski coil				14060	A/V
7	RMP 1 – Rogowski coil				579	
8	RMP 2 – Rogowski coil				560	
9	Iplasma				43125	A/V
10	vessel current+Iplasma				62706	A/V
11	diamagnet TF11 (NBI) 1					
12	diam. TF11 (NBI) 2 (comp.)					
	diam TF5 (Thoms) 1					
	diam TF5 (Thoms) 2 (comp.)					
13	Flux loop 4	0.325	-1.71E-06		6.256	V/V
14	Flux loop 5	0.325	1.00E-02		6.193	V/V
15	Flux loop 2	0.356288	0.300091		6.256	V/V
16	Flux loop 7	0.356291	-0.3001		6.256	V/V
17	Flux loop 1	0.772301	0.089481		0.055758	V.s/V
18	Flux loop 3	0.325188	0.15541		0.055758	V.s/V
19	Flux loop 6	0.325188	-0.15542		0.055758	V.s/V
20	Flux loop 8	0.772301	-8.95E-02		0.055758	V.s/V
21	Internal Partial Rogowski 1	0.7885	0	-90	0.0842	T/V
22	Internal Partial Rogowski 2	0.7563	0.1317	-66.35	0.0878	T/V
23	Internal Partial Rogowski 3	0.685	0.2495	-51.01	-0.0878	T/V
24	Internal Partial Rogowski 4	0.5849	0.3425	-31.99	-0.0849	T/V
25	Internal Partial Rogowski 5	0.4574	0.3829	0	-0.0879	T/V
26	Internal Partial Rogowski 6	0.3726	0.3313	61.99	-0.0864	T/V
27	Internal Partial Rogowski 7	0.3334	0.2266	78.33	-0.0884	T/V
28	Internal Partial Rogowski 8	0.324	0.1155	90	-0.0848	T/V
29	Internal Partial Rogowski 9	0.324	0	90	0.0876	T/V
30	Internal Partial Rogowski 10	0.324	-0.1155	90	0.0878	T/V
31	Internal Partial Rogowski 11	0.3334	-0.2266	101.7	0.0272	T/V
32	Internal Partial Rogowski 12	0.3726	-0.3313	118	0.0275	T/V
33	Internal Partial Rogowski 13	0.4574	-0.3829	180	0.0877	T/V
34	Internal Partial Rogowski 14	0.5849	-0.3425	-148	0.0866	T/V
35	Internal Partial Rogowski 15	0.685	-0.2495	-129	0.0860	T/V
36	Internal Partial Rogowski 16	0.7563	-0.1317	-113.7	0.0808	T/V

note: IPR coils are at toroidal angle 347.5 deg, zero is north cross
angle is measured from outward oriented vector, clockwise is negative

Table 2-4: Positions, angles and calibrations of magnetic diagnostic coils.

3 Magnetic Field systems

This chapter contains information about systems used for generation of magnetic fields in the COMPASS tokamak. The systems consist of Poloidal Field (PF) coils, Toroidal Field (TF) coils, Power Supplies (PS) used to energize the coils and of various control systems. The primary goal of the chapter is to describe the systems aspects, which are potentially interesting for physicists: geometry, connections, produced magnetic fields, possibilities and limitations of Power Supplies, interaction between Power supplies. These parameters are occasionally useful when an experiment is planned and performed. The secondary goal of the chapter is to provide documentation of part of the tokamak sub-systems commissioned during COMPASS reinstallation in Prague [10].

3.1 Poloidal Fields circuits

This section deals with the poloidal magnetic fields created by COMPASS PF coils. The geometry, coils connection, generated vacuum magnetic field and mutual inductances between individual circuits are presented.

First, used terminology should be clarified. Tokamak COMPASS is equipped with *poloidal field coils* (P1-P7, see **Figure 3.1**) which consist of several electrically separated *windings*. The windings have different numbers of *turns*. The windings are organized into *poloidal field coils circuits*. Each circuit is powered by its own *power supply* after which it is named.

For example: "MFPS (Magnetizing Field Power Supply) circuit" is an electrical circuit consisting of a) several windings connected together with direction of current selected on a link board, and b) connected power supply. The term "MF coils" (or "MFPS coils") refers to connected *windings* in the *coils*. The terms "MF circuit" or "MFPS" or "MF coils" are often used to describe either the connected windings or power supply or both together, depending on the context. This dependence on the context is avoided and proper terminology is used whenever practically possible in this thesis.

COMPASS tokamak uses five circuits [35], [36] consisting of different windings in different poloidal field (PF) coils. These are:

1. MFPS circuit – Magnetizing Field Power Supply (PS) circuit for plasma current drive and ohmic heating. It acts as the primary winding in the air transformer. COMPASS power supplies are discussed in *Zajac et al.* [37], [38] and *Pavelka et al.*, [39].
2. EFPS circuit – Equilibrium Field PS circuit for generating vertical magnetic field which prevents plasma column from expanding its main radius.
3. SFPS circuit – Shaping Field PS circuit for plasma shaping and creation of divertor plasma configuration. Several configurations are used for different plasma shapes. Commonly used are SND (Single Null Divertor) and SNT (Single Null divertor with higher Triangularity).

4. BR (or FABR) circuit – horizontal magnetic field circuit powered by Fast Amplifier (*Havlicek et al.*, [Attached publication A1]) for fast feedback control of vertical plasma position [40].
5. BV (or FABV) circuit – vertical magnetic field for horizontal plasma position feedback, powered by Fast Amplifier.

It should be noted that "COMPASS-D PF system was designed so that different parameters (R, z, Ip, shape) were controlled independently with single-function power supplies. This is different from MAST and other modern tokamaks where multi-variable control is used, but is very much simpler to implement, if less precise and flexible", A. W. Morris, *COMPASS-D Plasma Control Systems and Operating Limits*, in *PIC/SL/DPIC training*, 15-19 Sept 1997.

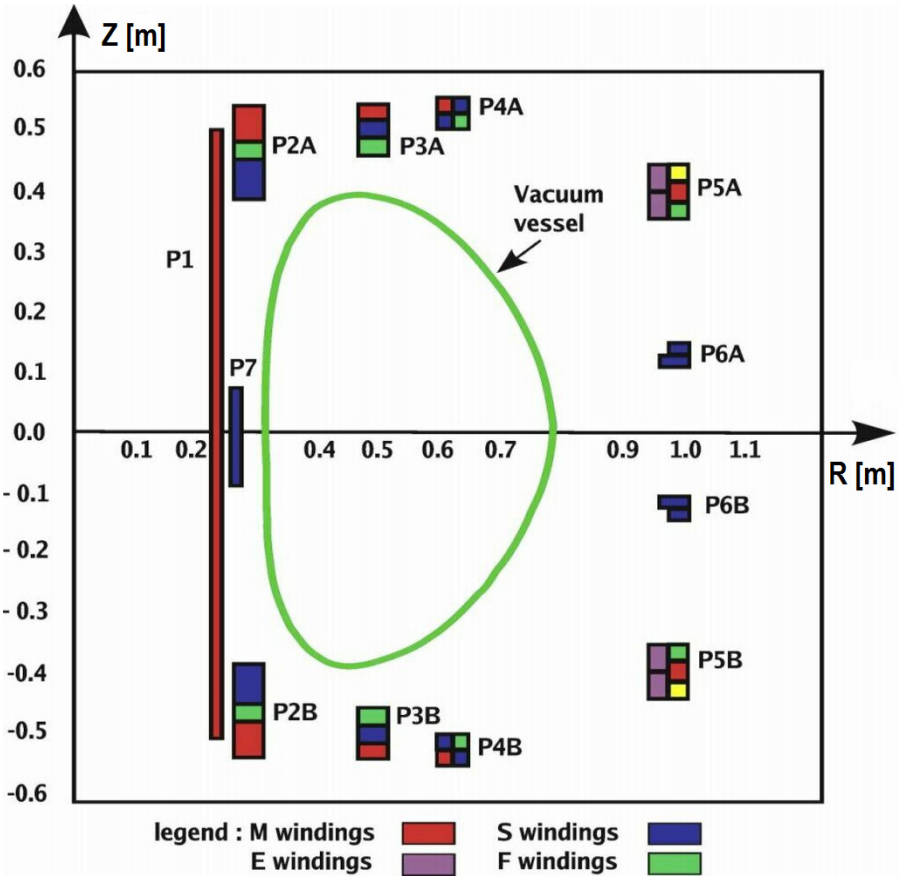

Figure 3.1: Poloidal plane cut of the COMPASS tokamak. Different windings in the PF coils (P1-P7) are distinguished by colors. M, E, S and F windings are historical markings – actually used circuits use various windings.

3.1.1 Poloidal field coils geometry

The geometry of the poloidal field coils and windings is known from documentation provided by UK Atomic Energy Authority (UKAEA, now renamed to Culham Centre for Fusion Energy - CCFE) when COMPASS was transported from Culham to Prague. The geometrical values used in this thesis are taken from the drawing E/CPS/840369 (see **Figure 3.4**), from COMPASS Machine Assembly &

Installation QA Records (item 52 in COMPASS archive, see **Figure 3.2** and **Figure 3.3**) and from EFIT (Equilibrium FITting code) input files.

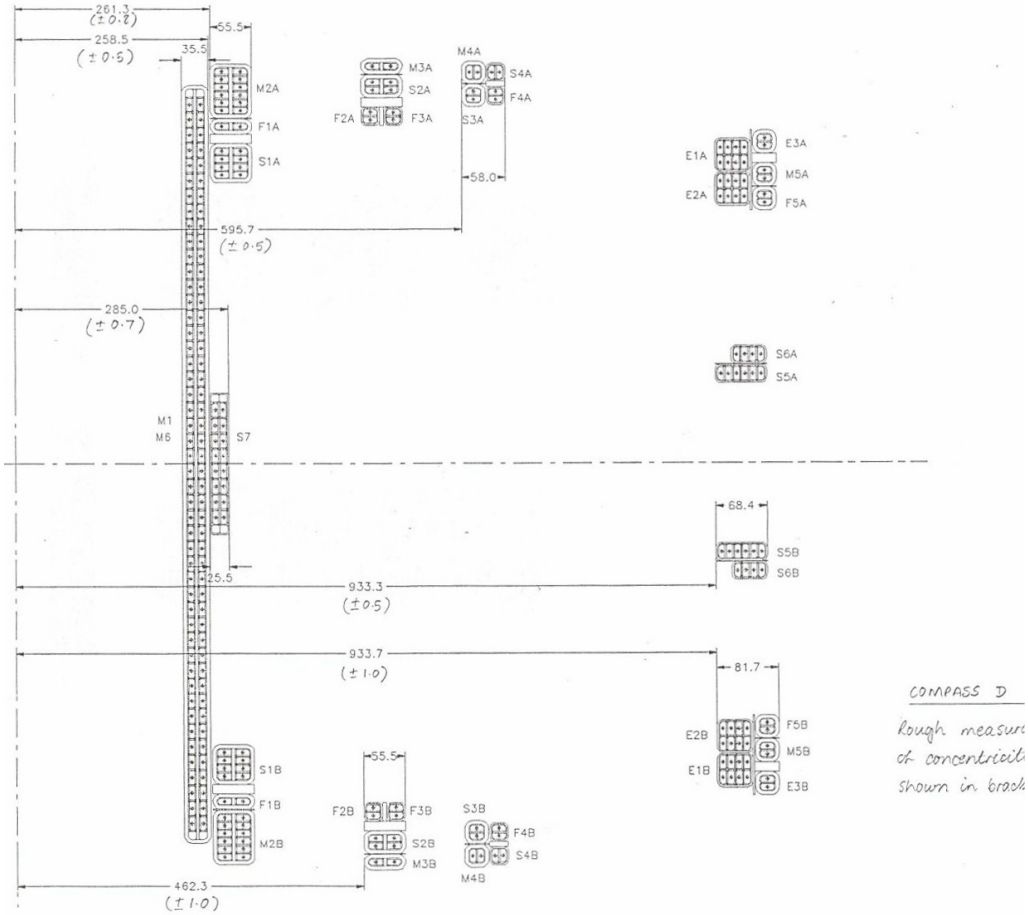

Figure 3.2: Radial positions of PF coils as measured in Culham, taken from COMPASS Machine Assembly & Installation QA Records (item 52 in archive). Courtesy of CCFE.

Figure 3.2 and **Figure 3.3** show geometry of the PF coils measured after their installation in Culham, together with names of individual windings in the coils. It can be seen that for example coil P2A (see **Figure 3.1**) consists of three windings M2A, F1A and S1A, each with 12, 2 and 8 turns respectively.

A special attention should be given to the coil P1 with windings M1 and M6. Each of the windings has 48 turns geometrically organized into chessboard pattern.

This can be achieved by winding two wires together from the top to the bottom 24 times in inner half of the coil P1, then transiting to the outer half of the P1 coil and winding them together 24 times from the bottom to the top. With this procedure the chessboard pattern of two windings is created. This makes the location of four winding ends suitable for connection to the link boards with cables organized into pairs + and -. This ensures that the stray magnetic field of the cables is minimized.

The windings M1 and M6 are therefore geometrically identical and can be swapped with each other without any consequences to the geometry of created magnetic field. This feature was used already in Culham. The coil M1 was connected

closer to the electrical ground than M6 in the MFPS circuit, while according the documentation M6 should had been closer to the electrical ground. The reason was better leakage resistance to the electrical ground of the winding M6.

It should be noted that the winding M1 is also called MB and that the group of windings M6+M2A+M2B+M3A+M3B+M4A+M4B+M5A+M5B is called MA. There is some Culham documentation, where M1 and M6 are swapped in this marking. The real situation is described in this thesis.

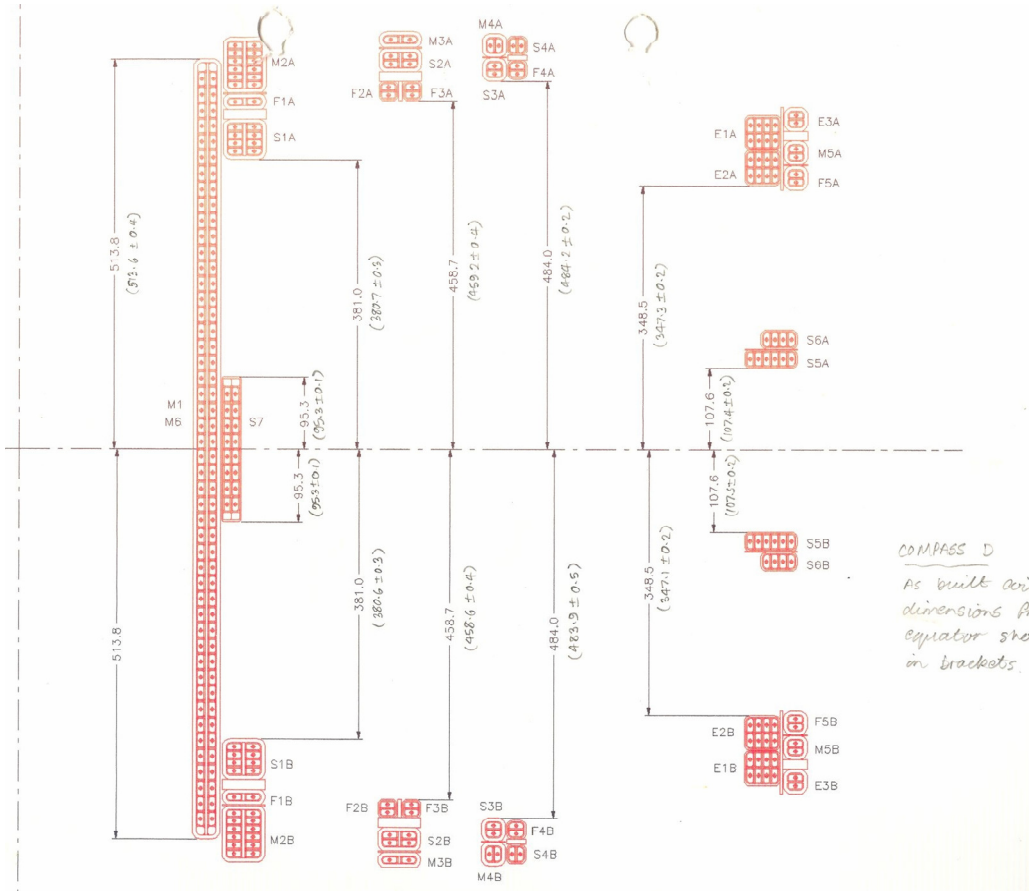

Figure 3.3: Vertical positions of the PF coils as measured in Culham, taken from COMPASS Machine Assembly & Installation QA Records (item 52 in archive). Courtesy of CCFE.

An attention should also be given to the coil P1, windings E1 and E2. These are connected together with M1 into the EFPS circuit (connection of coils will be described in more details in Section 3.1.3), each of the windings E1A, E1B, E2A and E2B have eight turns. The difference of E1 and E2 to the rest of the windings is that E1 and E2 are connected in parallel. E1A is in series with E2B and they are together in parallel to E2A and E1B, which are in series. Details can be found in bachelor thesis by O. Kudláček: *Elektromagnetická pole v zařízeních s magnetickým udržením horkého plazmatu* [41].

Figure 3.4 shows table with geometrical centres of individual windings, geometry of individual coils and windings, and geometry of one turn used in the

windings. It was created by removing redundant information from drawing E/CPS/840369.

Geometrical information about one turn of the windings was used to calculate values for I^2t protection of the coils. I^2t is commonly used as a measure of thermal energy deposited in the wire during a short pulse, i.e. without any cooling applied during duration of the pulse. Time duration of currents flowing in the COMPASS coils is usually shorter than one second, therefore this approximation is valid. The energy *E* deposited in the wire can be described by equation:

$$E = \int P(t) \cdot \mathrm{d}t = R \int I^2(t) \cdot \mathrm{d}t \,, \tag{3.1}$$

where *P* is power, *R* is the resistance of the wire and *I* is the current flowing in the wire. The value of the $\int I^2(t) \cdot dt$ should be kept lower than a threshold value given by:

$$E = c \cdot m \cdot \Delta T \,, \tag{3.2}$$

where c = 384.5 $\mathrm{J \cdot K^{-1} \cdot kg^{-1}}$ is the copper specific heat capacity, m is the mass of the copper wire and ΔT is the selected maximal allowed temperature change. The COMPASS inter-turn insulation is rated up to 80º and ΔT was selected to be 50 K.

In the Equation (3.1) the resistance is assumed to be constant. This assumption is only partially valid because the copper temperature coefficient α is 0.00386 $\mathrm{K^{-1}}$, giving the resistance change of 19.3 % for 50 K temperature change. For the long wire approximation the mass m is given by $m = \rho_{dens} \cdot S \cdot l$, where copper density ρ_{dens} is 8960 $\mathrm{kg/m^{-3}}$, l is the wire length and S is the wire area. The resistance of the long wire is $R = \rho \cdot l / S$, where ρ = 1.68×10^{-8} Ωm is copper resistivity. In the case of COMPASS windings the area of one turn is 18 x 8 - $\pi \cdot 2^2$ - (4-π)$\cdot 1.5^2$ $\mathrm{mm^2}$ (see **Figure 3.4**).

The final value of the I^2t is then given by:

$$\int I^2(t) \cdot \mathrm{d}t < c \cdot \frac{\rho_{dens}}{\rho} \cdot S^2 \cdot \Delta T \tag{3.3}$$

and the numerical value for the COMPASS poloidal field coils is:

$$\int I^2(t) \cdot \mathrm{d}t < 172\ \mathrm{kA^2 s}. \tag{3.4}$$

This critical value is checked by the COMPASS feedback system which requests current values to be zero if the I^2t reaches 80 % of 172 $\mathrm{kA^2 s}$. The implementation of the I^2t protection was reported in the article *Upgrade of the COMPASS tokamak real-time control system* [Attached publication A3].

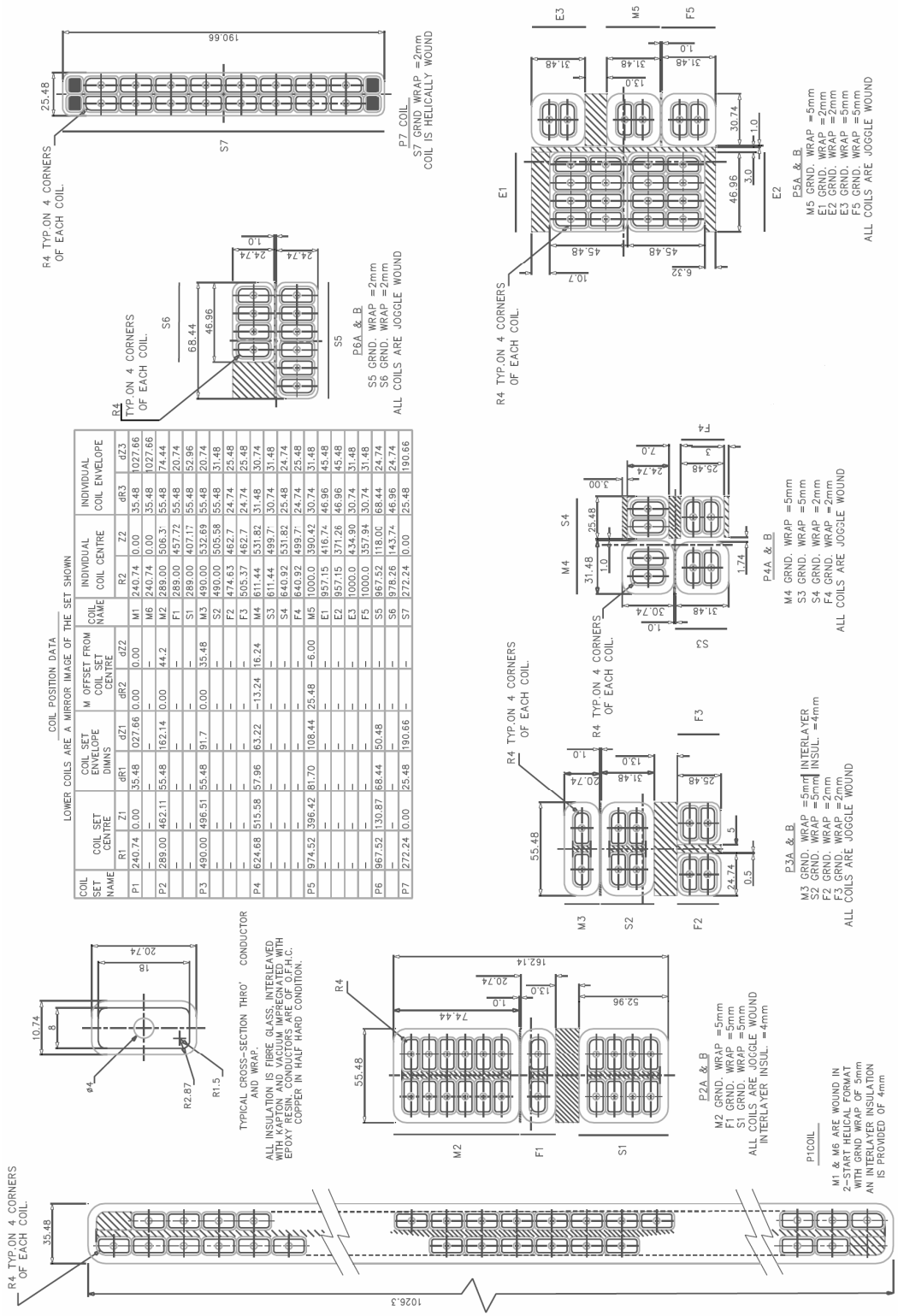

Figure 3.4: Excerpt from drawing E/CPS/840369. Number of turns in windings M1 and M6 in the coil P1 is 48 in each. Courtesy of CCFE.

3.1.2 CCC - COMPASS Currents Convention

This section establishes convention for the polarity of the Power Supplies and their connection to the PF coils circuits for the COMPASS tokamak.

Before and during the reinstallation of COMPASS in Prague we had to understand the connection of the tokamak coils to the Power Supplies in order to install them correctly. We used the documentation provided by CCFE, which was available at that time. The used documentation was:

1. Datasheets "COMPASS Magnetic Field Configuration" describing connection of the PS with tokamak windings for different campaigns (see **Figure 3.5**).
2. Technical drawing E/CPS/902091 of the link boards and their connection to the Power Supplies.
3. Signals from CCFE database - particularly signals for EFIT, e.g. MA_EFITMACURR - current in the winding MA = M6 + M2A + M2B + M3A + M3B + M4A + M4B + M5A + M5B, MA_MBCURR(S) - current in the windings MB = M1, ...

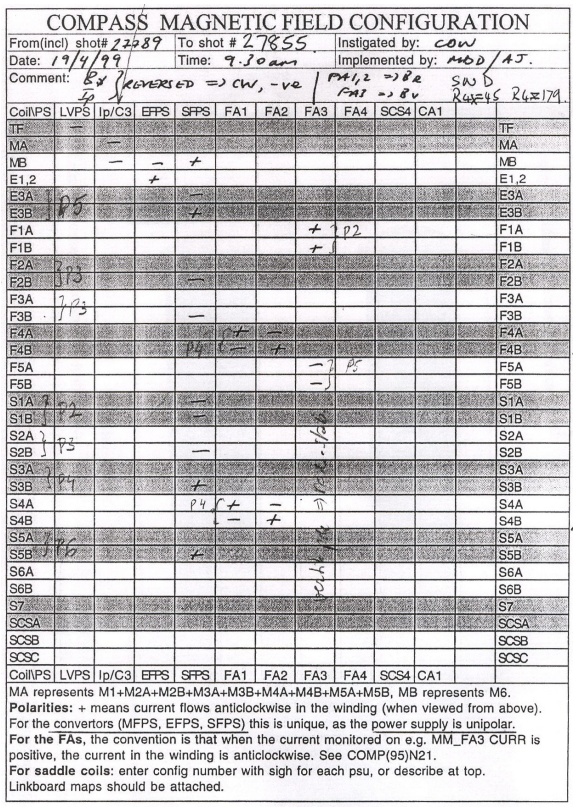

COMPASS MAGNETIC FIELD CONFIGURATION

From(incl) shot# 27789 | To shot # 27855 | Instigated by: COW

Date: 19/4/99 | Time: 9.30 am | Implemented by: MDD/AJ.

Comment: Bt reversed => CW, -ve | FA1,2 => 8v, FA3 => 8v | SN5 R45=45 R6=179.

Coil\PS	LVPS	Ip/C3	EFPS	SFPS	FA1	FA2	FA3	FA4	SCS4	CA1	
TF	−										TF
MA		−									MA
MB		−	−	+							MB
E1,2			+								E1,2
E3A	P5			−							E3A
E3B				+							E3B
F1A							+				F1A
F1B							+				F1B
F2A	P3										F2A
F2B	P3			−							F2B
F3A	P3										F3A
F3B				−							F3B
F4A				P4	+	−					F4A
F4B				P4	−	+					F4B
F5A							−				F5A
F5B							−				F5B
S1A	P2			−							S1A
S1B	P2			−							S1B
S2A	P3										S2A
S2B	P3			−							S2B
S3A	P4										S3A
S3B	P4			+							S3B
S4A				P4	+	−					S4A
S4B					−	+					S4B
S5A	P6										S5A
S5B	P6			+							S5B
S6A											S6A
S6B											S6B
S7											S7
SCSA											SCSA
SCSB											SCSB
SCSC											SCSC
Coil\PS	LVPS	Ip/C3	EFPS	SFPS	FA1	FA2	FA3	FA4	SCS4	CA1	

MA represents M1+M2A+M2B+M3A+M3B+M4A+M4B+M5A+M5B, MB represents M6.
Polarities: + means current flows anticlockwise in the winding (when viewed from above).
For the convertors (MFPS, EFPS, SFPS) this is unique, as the power supply is unipolar.
For the FAs, the convention is that when the current monitored on e.g. MM_FA3 CURR is positive, the current in the winding is anticlockwise. See COMP(95)N21.
For saddle coils: enter config number with sigh for each psu, or describe at top.
Linkboard maps should be attached.

Figure 3.5: COMPASS Magnetic Field Configuration sheet used in Culham. Note that M1 and M6 are swapped against reality during reinstallation. Superseded by CCC.

At that time we did not realize that the documentation is not self-consistent. This can be demonstrated on the polarity of the Magnetizing Field. Due to the Faraday's law of induction the *negative* plasma current (clockwise when viewed from above) is created and maintained by *positive* derivative of the current in the central solenoid - either the central solenoid current is *positive* and is *increasing* its amplitude or it is *negative* and is *decreasing* the amplitude. This can be in achieved either by: 1/ connecting central solenoid with *negative* direction to the Power Supply with *negative* current derivative (as in "COMPASS Magnetic Field Configuration" for shots #27789 to #27855 and signal MA_EFITMACURR) or by 2/ connecting central solenoid with positive direction to the Power Supply with positive current derivative (as in drawing E/CPS/902091 and signal MA_MBCURR(S)). In both cases the physical direction of the current in the

central solenoid is identical, only convention of marking of windings connection and polarity of the measured current signal is changed.

The problem with documentation and marking self-consistency was increased during COMPASS reinstallation when Power Supplies manufacturer selected polarity of the MF Power Supply which was in contradiction to the convention used by IPP physicists.

In order to solve the inconsistencies and establish a unified documentation, an official convention was approved by COMPASS management at the end of the year 2012. This convention is called COMPASS Currents Convention and is abbreviated CCC.

The COMPASS Currents Convention consists of these rules:

1. The **cylindrical coordinate system** is (R, φ, Z) and uses right hand rule for the orientation of the vectors. The major radius is *R*, vertical position is *Z* and the toroidal angle φ is positive for counterclockwise direction when viewed from above. Note that the coordinate system (R, Z, φ) has orientation of the toroidal angle opposite to the CCC.
2. The *standard* polarity of the **plasma current** in COMPASS is *negative*, which means that the orientation of the current is counterclockwise when viewed from above. The *reversed* polarity of the plasma current is *positive* (clockwise orientation).
3. The *standard* orientation of the **toroidal magnetic field** is *negative* (counterclockwise). The *reversed* orientation of the TF is *positive* (clockwise). Both orientations are achieved by changed connection of TF coils to PS, i.e. TFPS current is always *positive*.
4. The **MFPS current** should have *positive derivative* (e.g. swing from -14 kA to +14 kA) for *standard plasma current polarity*. The connection of the MFPS circuit windings should respect this convention.
5. The **EFPS and SFPS currents** should be *positive* for *standard plasma current polarity*. The connection of the windings into circuits should respect this convention.
6. The **FABR and FABV currents** should be positive for positive B_{rad} and B_{vert} respectively. Therefore the $\vec{j} \times \vec{B}$ force acting on the plasma with standard plasma current polarity should be *upwards* for positive I_{BR}, i.e. positive B_{rad}, and *inwards* (towards HFS) for positive I_{BV}, i.e. positive B_{vert}. The connection of the windings into circuits should respect this convention.

This convention is closely connected to the way how measured signals should be stored in the COMPASS database (CDB, reference article [42]). The CCC covers the polarity of the signals. Further rules are that time axis stored in CDB should be in milliseconds and all other quantities should be in SI units. The milliseconds were chosen for user's convenience because COMPASS discharges are shorter than one second.

The reversed plasma current polarity is possible for COMPASS tokamak and is used occasionally when there is physical justification (as in articles [43], [44], [45]),

but the procedure of changing mechanical connections of windings to the PS and reprogramming the feedback and diagnostic system is not straightforward. As a consequence the signals stored in the COMPASS database are not conforming to the CCC and in some cases are not consistent with each other, when the plasma current polarity is reversed. An example of the inconsistent data in CDB is measurement of the HFS tangential diagnostic magnetic coil IPR_09 (Internal Partial Rogowski coil): the measured magnetic field is in reality opposite against standard orientation, it is measured with correct polarity by fast measurement (2 MS/s, CDB signal name: " Internal_Partial_Rogowski_coil_09_RAW"), but feedback signal (20 kS/s, CDB signal name: " MARTE_NODE.ChannelDataCollection.Channel_019") stores the signal with incorrect polarity. The reason is that feedback system is, from the most part, reprogrammed to behave as if the polarity of the plasma current was not changed, thus ensuring correct control of the plasma. In the future the CCC should be broadened to properly cover reversed plasma current operation and signals in CDB should be treated retroactively.

3.1.3 Connections of poloidal field coils circuits

As was already stated in introduction to Section 3.1, tokamak COMPASS uses five poloidal field coils circuits to create and control plasma column. This section purely describes the connection of the windings into these circuits, without further discussion. The created magnetic field, circuit function and capabilities in regard to influencing COMPASS plasma are discussed later in Section 3.1.5 - Characterization of PF coils circuits magnetic fields. Mutual coupling between the PF coils circuits is generally discussed in Section 3.1.6 - Mutual inductances of poloidal field coils circuits and practically exploited in Section 3.4 - Simulation of the EFPS PID controller.

Connections of poloidal field coils circuits were already partially published by O. Kudláček in his bachelor thesis: *Elektromagnetická pole v zařízeních s magnetickým udržením horkého plazmatu* [41], but without conforming to the CCC, which was introduced later.

Tokamak COMPASS has all windings in the coils connected to two link boards. Upper Link Board is situated roughly 4-5 m north of the tokamak, Lower Link Board is situated two floors below the tokamak. With the exception of the windings F1, F5, E1 and E2, all other windings are connected to the link boards individually (see **Figure 3.6**) and circuits can be changed by reconnection of the terminals on the link boards. Copper bars with cross-section 50 mm x 12 mm or cables with cross-section ~ 250 mm^2 and bolts M16 (24 mm nut) are used to connect individual windings. Polarity of the winding in the circuit is determined by the polarity of the power supply output connected to the terminal marked with dot (see **Figure 3.6**).

Polarity of a winding connected in the circuit is marked by either + or -. The meaning is that winding connected in + direction (+ output of PS on the terminal marked with dot) has current flowing counterclockwise (positive in coordinate system R, φ, Z) when viewed from above, for positive current generated by the

Power Supply, and clockwise for negative current generated by the Power Supply. The winding connected in - direction to positive current from PS has current flowing clockwise.

Shaping Field circuit uses several possible configurations selectable on the link boards. These are: **SND (Single Null Divertor)**, **SNT (Single Null divertor with higher Triangularity)**, ellipse and Dee. All SFPS circuit configurations were adopted from CCFE and no changes were done in IPP Prague.

The most relevant for COMPASS operation is SFPS-SNT configuration, which creates plasma shape highly relevant to the ITER tokamak [10]. Therefore the **SFPS-SNT configuration is used exclusively from the shot #3087** (3.4.2012) up to now (as of 11.6.2015 the shot number is #10169). Before the shot #3087, SFPS-Dee without Central Solenoid (#2896 - #2898) was used without active vertical position stabilization to elongate plasma vertically and achieve higher line averaged electron density, and SFPS-SND (#2983 - #3086) was used briefly during vertical position feedback commissioning. No fully stabilized plasmas with SND configuration were achieved, but there are discharges with briefly achieved divertor configuration (e.g. #3002 and #3005). Commissioning of the vertical position stabilization for the diverted plasma was done is SNT configuration between shots #3087 and #3925 (30.10.2012), when the last major obstacle (diagnostic magnetic coils used in radial position feedback algorithm were reaching data acquisition voltage limit, solved by lowering integration constant) was removed. Soon after that the first H-mode (#4073) after COMPASS reinstallation in Prague was achieved in the SNT configuration of the plasma.

The windings and their polarities connected in individual Power Supply circuits (see introduction to Section 3.1 for explanation of circuit purpose) are:

- MFPS: +M6+M2A+M2B+M3A+M3B+M4A+M4B+M5A+M5B+M1
- EFPS: -M1 + (+E1A+E2B)||(+E2A+E1B) which is technically equal to -M1 + E1A||E2A + E1B||E2B
- SFPS-SND: +M1-E3A+E3B-F2B-F3B-S1A-S1B-S2B+S3B+S5B
- SFPS-SNT: +M1-E3A+E3B-F2B-F3B-S1A-S1B-S2B-S3A-S3B+S5B+S7
- SFPS-ellipse: +M1-S2A-S2B-S3A-S3B+S6A+S6B, note that the configuration is top-down symmetrical
- SFPS-Dee: +M1-S1A-S1B-S2A-S2B-S3A-S3B+S5A+S5B+S7, note that the configuration is top-down symmetrical
- BR: -F4A+F4B-S4A+S4B
- BV: -F1A-F1B+F5A+F5B

Expected current waveform in the MF Power Supply is first negative (e.g. -14 kA) and then rising, then the current flowing in the central solenoid (CS, windings M1 and M6) has clockwise (negative) direction for -14 kA and magnetic field created by MF circuit inside central solenoid is oriented downwards and it's derivative upwards, which creates negative (standard direction) plasma current, with downwards magnetic field in central solenoid.

Expected current in the EF Power Supply is positive, the magnetic field interacts with negative plasma current creating force with direction to HFS, counteracting plasma column natural expansion towards LFS.

Expected current in the SF Power Supply for negative plasma current is positive.

FABR and FABV currents can be either positive or negative, depending on the movement of the plasma and requests from the feedback system.

Connection of the windings into circuits and to the Power Supplies on Upper and Lower Link Boards is described in the following figures. In the figures the Lower Link Board consists of three terminal panels: Plasma Current Direction Link Board, Turns Ratio Link Board and Lower Shaping Link Board. The Upper Link Board is created only from Upper Shaping Link Board panel. Physical placement of the windings terminals corresponds to the position in the figures.

Figure 3.6 shows connections of the Magnetizing Field circuit (MFPS), Equilibrium Field circuit (EFPS), vertical position stabilization circuit FABR (Fast Amplifier, B_{rad}) and radial position stabilization circuit FABV (Fast Amplifier, B_{vert}). Note that the windings E1A, E1B, E2A and E2B are connected in parallel. **Figure 3.7**, **Figure 3.8**, **Figure 3.9** and **Figure 3.10** show different configurations of the Shaping Field Power Supply circuit.

The figures use IPP Prague notation for the names of the Power Supplies. Power Supplies FABR and FABV can be found under different names in the documentation from Culham. RFPS (Radial Field Power Supply) and VFPS (Vertical Field Power Supply) as well as FA1 (Fast Amplifier 1), FA2 and FA3 were used in different places. Polarities of the Power Supplies shown in the figures conform to the COMPASS Currents Convention, polarities of the connected windings is decided by polarity of the PS connected to the dot mark of the winding.

Shaping switch has "unknown position" marked in the **Figure 3.9** and **Figure 3.10** for ellipse and Dee configuration of the SFPS circuit. The shaping switch allows to bypass winding M1 in the circuit and to operate SFPS circuit without direct electrical connection through the winding M1 to the MF Power Supply and EF Power Supply. Then the mutual coupling is purely inductive. We assume that the winding M1 should be connected in the ellipse and Dee configuration of the SFPS circuit (as indicated by the previous text description). Nevertheless the circuit can be used with or without the central solenoid (CS, winding M1) depending on the required plasma shape. The decision to include the central solenoid in the SFPS circuit will be made when the ellipse or Dee configuration is used, based on the EFIT reconstruction of the plasma shape and the plasma shape required for the experiment.

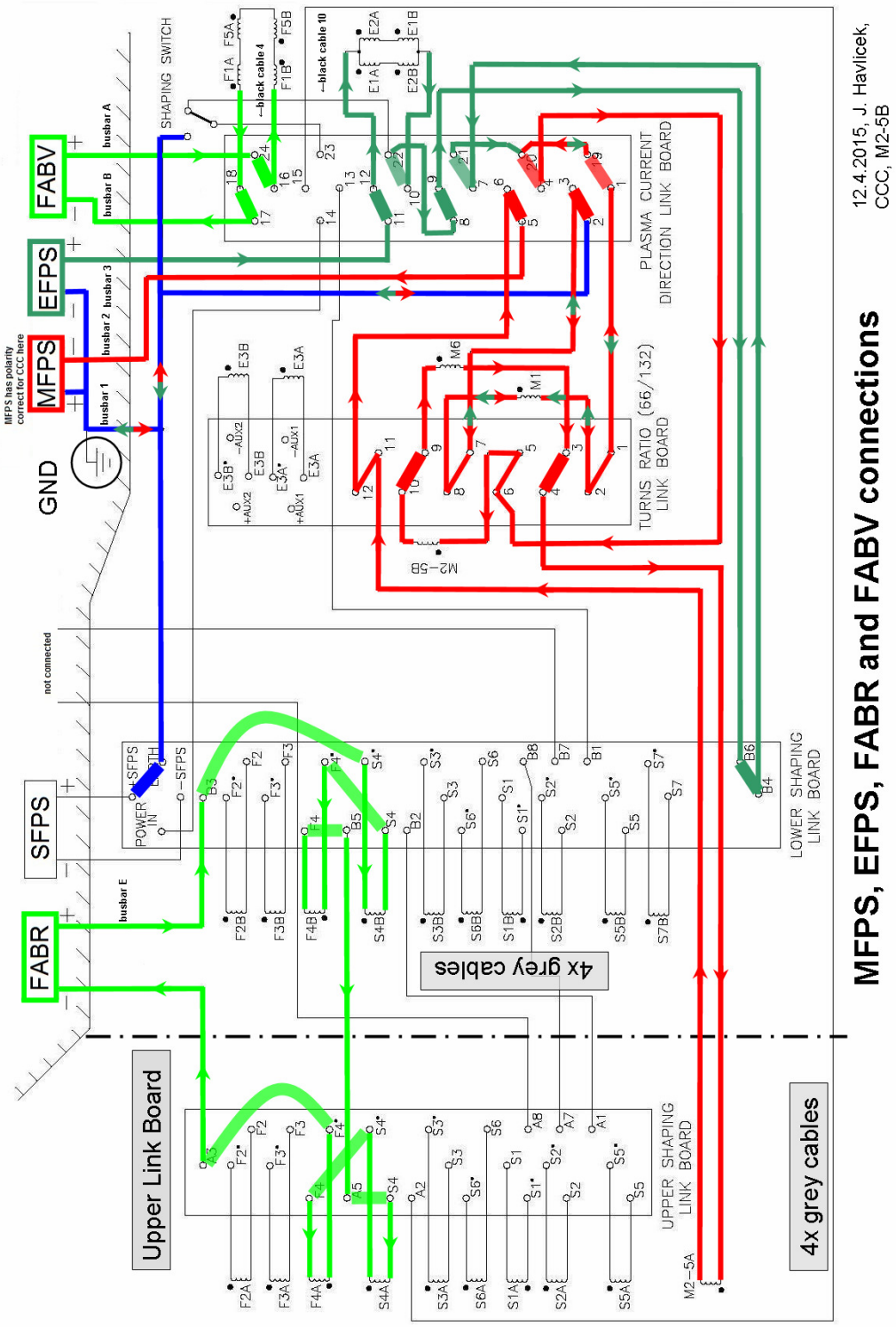

Figure 3.6: Connection of MFPS, EFPS, FABR and FABV circuits to Power Supplies on Upper and Lower Link Boards. Conforms to CCC.

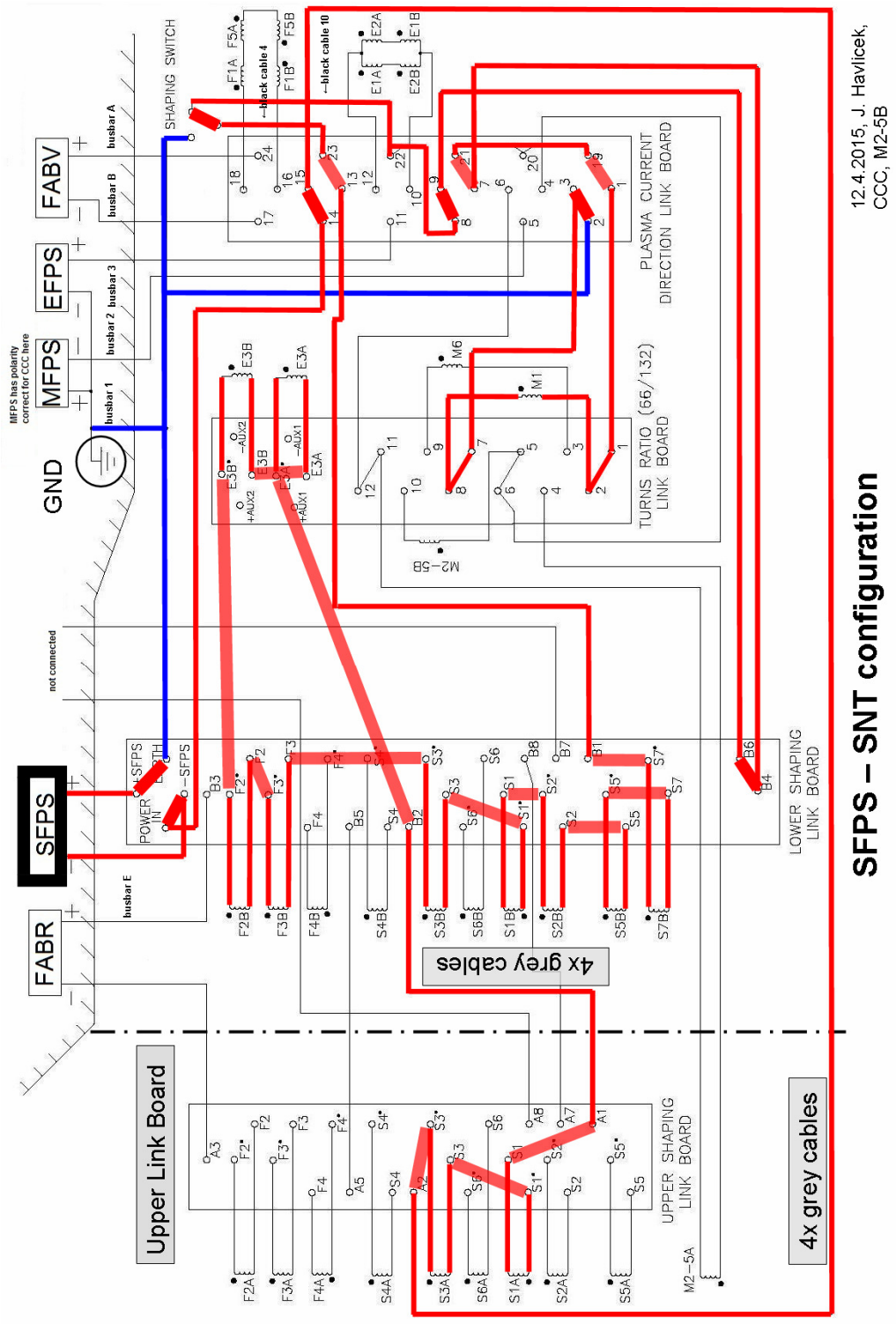

Figure 3.7: Connection of SF circuit on Upper and Lower Link Boards. Configuration SFPS-SNT (Single Null divertor, higher Triangularity), conforms to CCC.

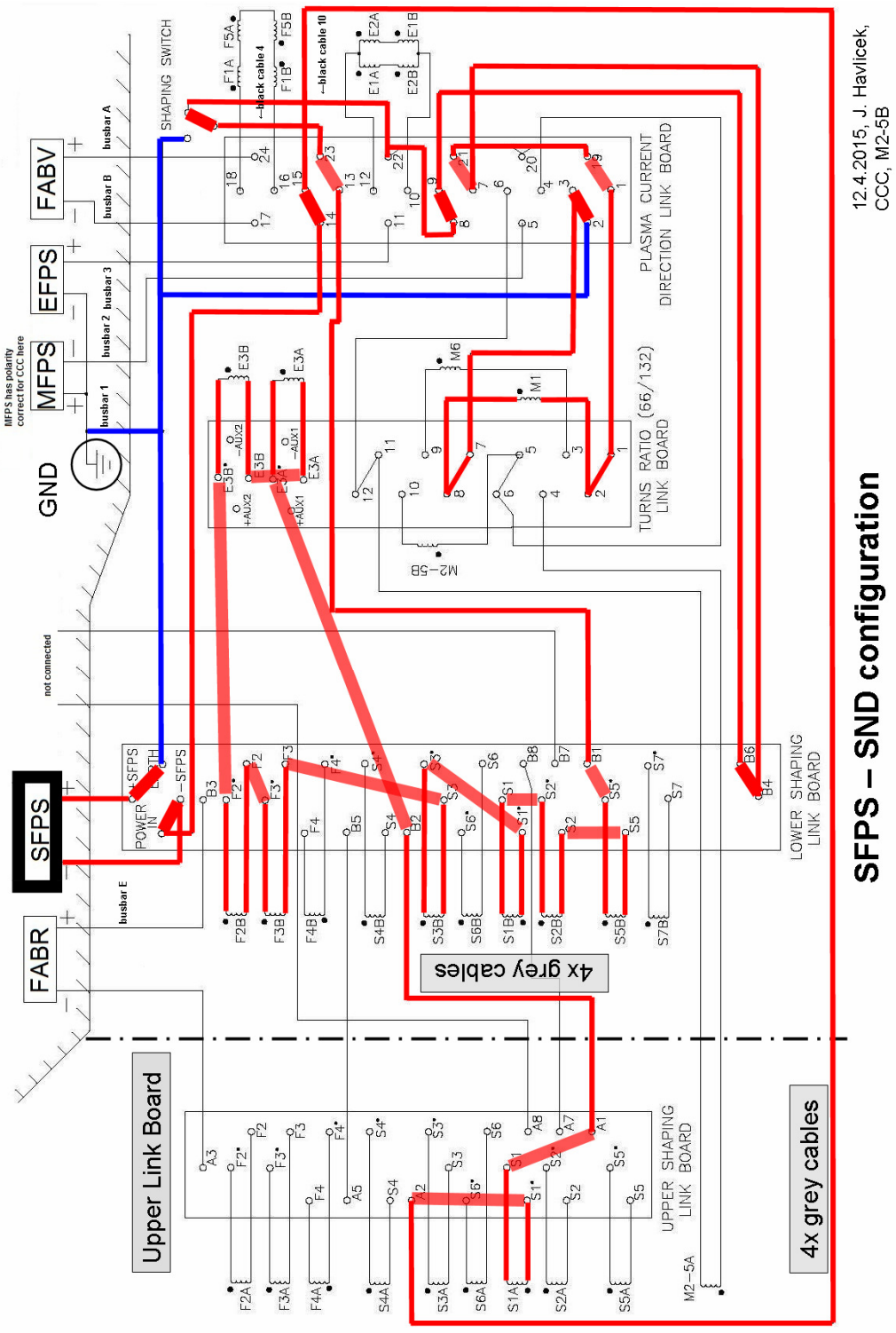

Figure 3.8: Connection of Shaping Field Power Supply circuit on Upper and Lower Link Boards. Configuration SFPS-SND (Single Null Divertor), conforms to CCC.

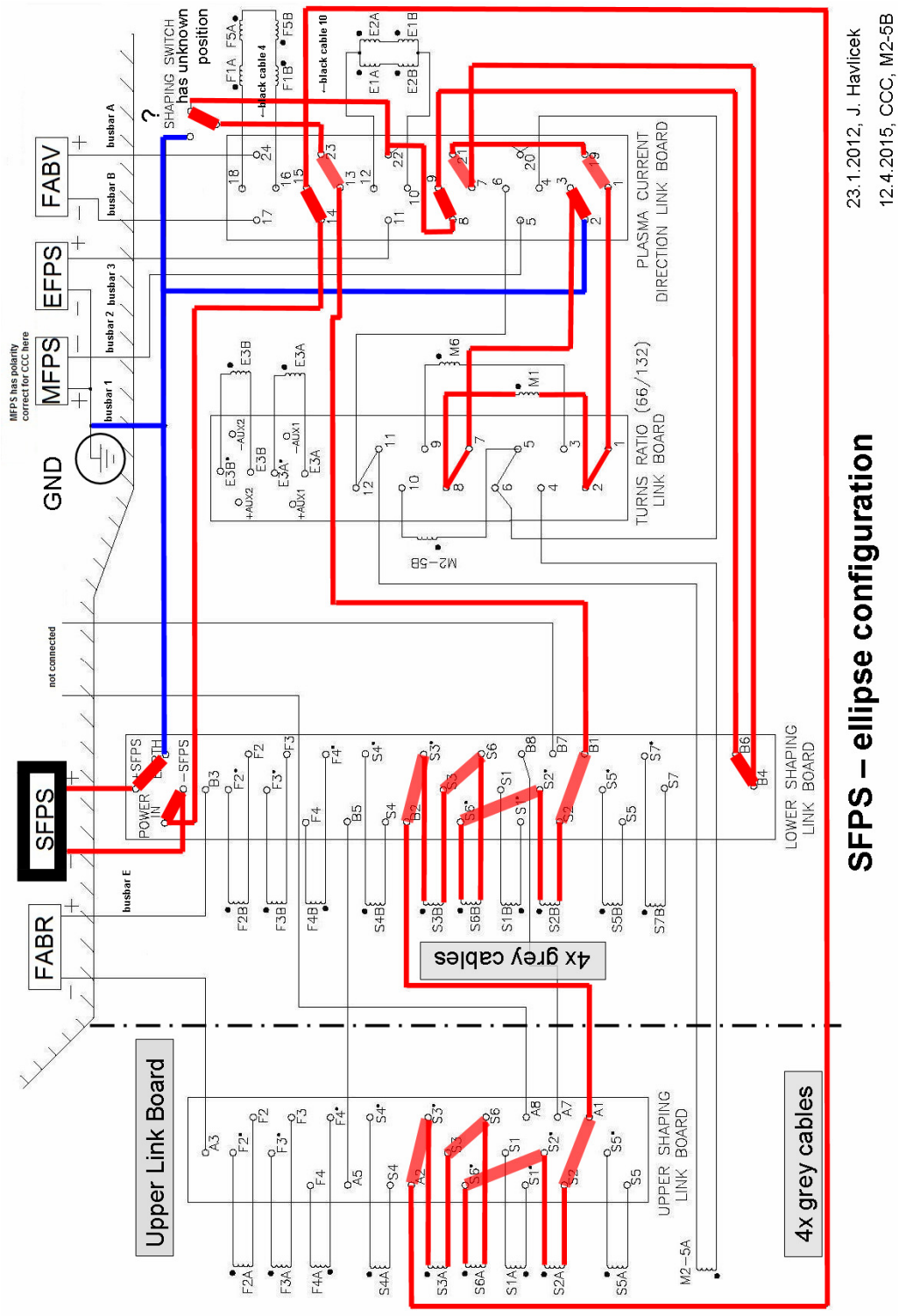

Figure 3.9: Connection of Shaping Field Power Supply circuit on Upper and Lower Link Boards. Configuration SFPS-ellipse, conforms to CCC.

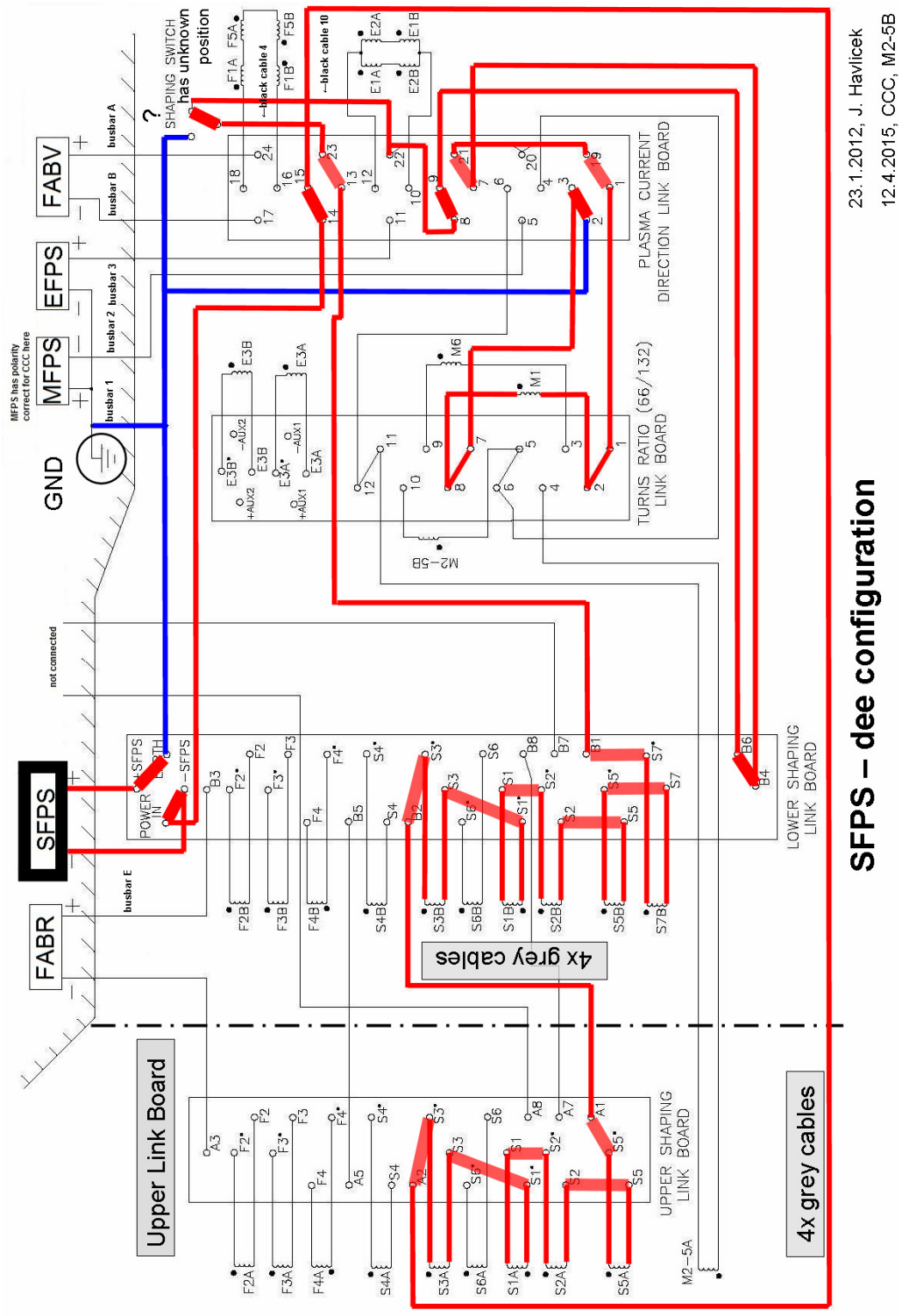

Figure 3.10: Connection of Shaping Field Power Supply circuit on Upper and Lower Link Boards. Configuration SFPS-Dee, conforms to CCC.

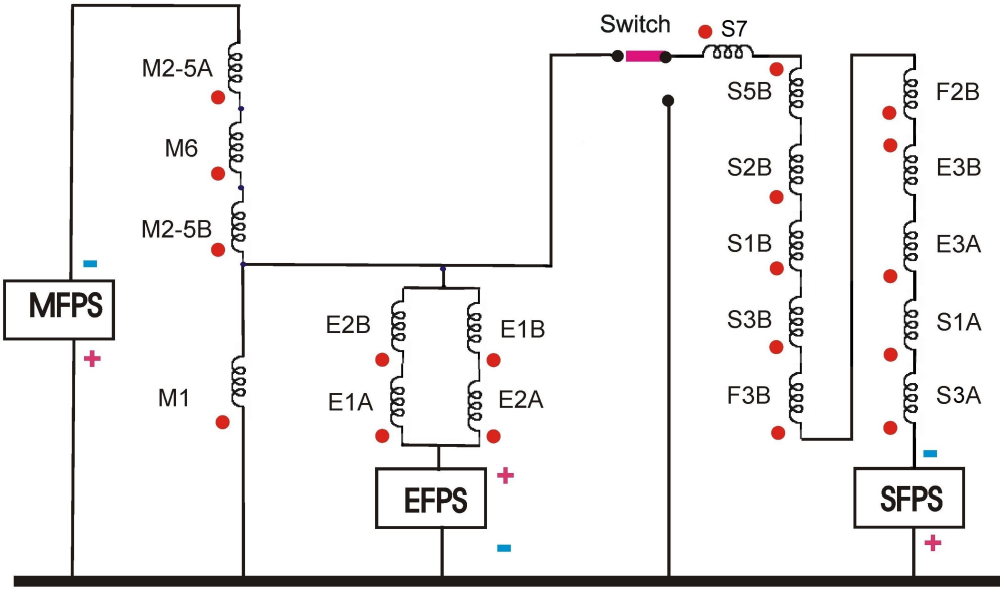

Figure 3.11: General connection of the MF, EF and SF Power Supplies for the *SFPS-SNT configuration*. The three individually controlled currents are flowing through the winding M1 in central solenoid. Decoupling transformers and PS choke coils are not depicted.

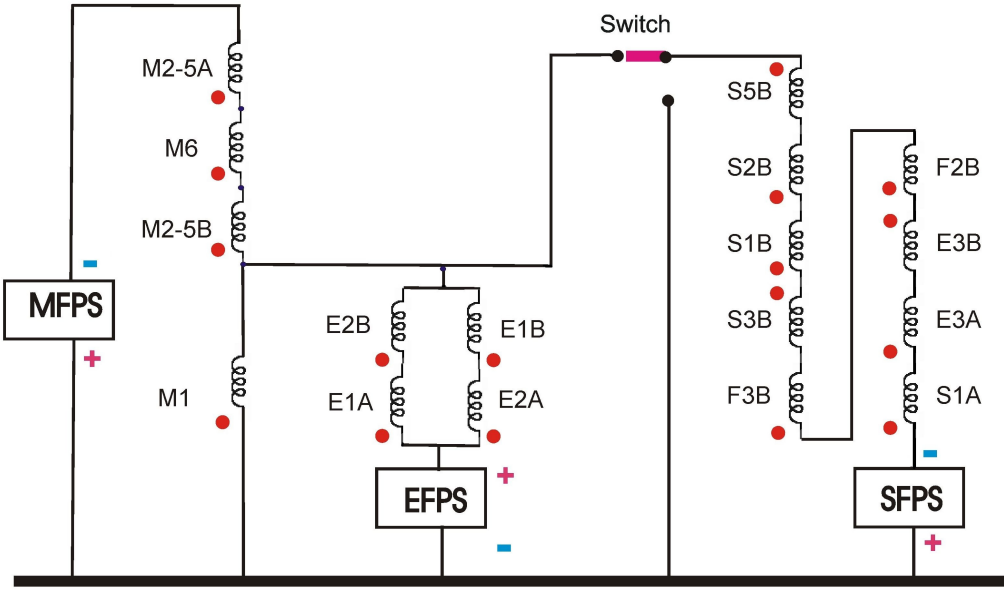

Figure 3.12: General connection of the MF, EF and SF Power Supplies for the *SFPS-SND configuration*. The three individually controlled currents are flowing through the winding M1 in central solenoid. Decoupling transformers and PS choke coils are not depicted.

Power Supplies of the tokamak are influencing each other through the mutual inductance (see Section 3.1.6 for quantitative description) and in the case of the MFPS, EFPS and SFPS also through direct electrical connection in the winding M1 in the central solenoid. Consequences of this coupling are discussed in the Section 3.4 - Simulation of the EFPS PID controller. The SFPS circuit can be electrically

disconnected from MFPS and EFPS circuit through the "Shaping Switch", but that influences its magnetic field (the SFPS current is no longer flowing through M1 winding) and therefore the shape of the plasma.

The electrical connection of the Power Supplies together is explained for the SFPS-SNT configuration in the **Figure 3.11** and for the SFPS-SND configuration in the **Figure 3.12**. The current of the MFPS circuit flows through windings M6 (half of the central solenoid) and M2-5 to the winding M1 and then connects through ground to the MF Power Supply. The current of the EFPS circuit flows through windings E1 and E1 to the winding M1. The current of the SFPS also flows through the winding M1. Therefore the winding M1 is used by all three circuits and the current inside is combination of them:

$$I_{MB} = I_{MFPS} + I_{SFPS} - I_{EFPS}, \tag{3.5}$$

which has consequences for the winding M1 I^2t protection, discussed already in the Section 3.1.1.

Figure 3.11 and **Figure 3.12** show only connection of the Power Supplies to the tokamak windings: the choke coils of the Power Supplies and decoupling transformers between power supplies are not shown. The three Power Supplies are 12-pulse thyristor converters, each consisting from two 6-pulse thyristor converters connected in parallel. The choke coil after each 6-pulse converter makes parallel connection possible by balancing current distribution between converters. Its influence on the global behaviour of the circuit is negligible from the point of view of added resistance or inductance. The mutual inductance of the Power Supplies can be negated by adding so called decoupling transformer between two Power Supplies. The advantage of the decoupling transformer is decreased mutual inductance at the expense of increased self-inductance (by self-inductance of primary and secondary winding of decoupling transformer) of the individual circuits. The decoupling transformer must not have iron core to allow different currents in primary and secondary winding. There is "Decoupling Transformer EF-BV" connected in EFPS and BV circuit, not depicted it the **Figure 3.11** and **Figure 3.12**. There is also "Decoupling Transformer SF-BV" connected in the SFPS circuit but not in BV circuit. The practical experience gained after COMPASS reinstallation in Prague has shown that the mutual inductance between SFPS and BV does not prevent robust operation of the circuits. However, faster reaction of the BV circuit was beneficial to the reliability of the tokamak operation (radial position stabilization) and it was decided to decrease self-inductance of the BV circuit by disconnecting it from Decoupling Transformer SF-BV. The decoupling transformer was left connected in the SFPS circuit to keep its self-inductance high. The reasoning was that the voltage of the SF Power Supply is high enough to provide sufficient dynamic response ($\mathrm{d}I_{EF}/\mathrm{d}t$) and higher SF self-inductance lowers the ripple (and therefore the generated noise) of the SFPS current. The additional inductance of the primary winding of the Decoupling Transformer SF-BV was therefore deemed beneficial.

Occasionally, it is more convenient to imagine the circuits as depicted in the **Figure 3.13**. Then the individual windings in the circuits are grouped together into

coils MA, MB, E, S, BR and BV, while respecting correct polarities according the CCC. The coils are then:

- MA: +M6+M2A+M2B+M3A+M3B+M4A+M4B+M5A+M5B
- MB: +M1
- E: (+E1A+E2B)||(+E2A+E1B)
- S(SND): -E3A+E3B-F2B-F3B-S1A-S1B-S2B+S3B+S5B
- S(SNT): -E3A+E3B-F2B-F3B-S1A-S1B-S2B-S3A-S3B+S5B+S7
- BR: -F4A+F4B-S4A+S4B
- BV: -F1A-F1B+F5A+F5B

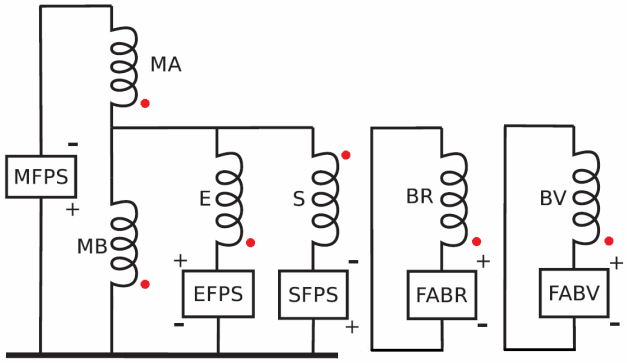

Figure 3.13: Simplified connection of the Power Supplies. When using this simplification, configuration of the SFPS should be specified. Decoupling transformers and PS choke coils are not depicted. Adjusted from attached article [A3].

With this notation the circuit MFPS = + MA + MB, EFPS = - MB + E and SFPS = + MB + S, which is determining the position of the dot mark in the **Figure 3.13**.

3.1.4 Theory for calculation of poloidal magnetic field

The poloidal magnetic field of toroidally wound loop can be computed using numerical integration of the Biot-Savart law in approximation for infinitely thin wire:

$$\vec{B} = \frac{\mu_0}{4\pi} I \int \frac{\mathrm{d}\vec{l} \times (\vec{r} - \vec{r}_l)}{|\vec{r} - \vec{r}_l|^3}, \tag{3.6}$$

where $\mu_0 = 4\pi \times 10^{-7}$ H/m is vacuum permeability, I is current in the infinitely thin wire, $\mathrm{d}\vec{l}$ is the element of the loop of thin wire, $\vec{r}$ is the point where magnetic field is computed and $\vec{r}_l$ is the position of the thin wire element.

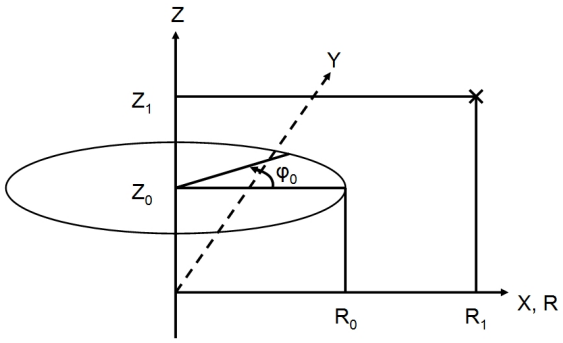

Figure 3.14: Geometrical situation for numerical integration of toroidally symmetrical coil at position R_0, Z_0 creating poloidal magnetic field at position R_1, Z_1.

Numerical integration of the single turn toroidal loop can be done by filling positions expressed in cylindrical coordinates into Cartesian coordinates (see **Figure 3.14**):

$$\vec{r} = \left(R_1,\ 0,\ Z_1\right) \tag{3.7}$$

$$\vec{r_l} = \left(R_0 \cos\varphi_0,\ R_0 \sin\varphi_0,\ Z_0\right) \tag{3.8}$$

$$d\vec{l} = dl\left(-\sin\varphi_0,\ \cos\varphi_0,\ 0\right) = \frac{2\pi R_0}{N}\left(-\sin\varphi_0,\ \cos\varphi_0,\ 0\right), \tag{3.9}$$

where N is number of the loop elements used in the integration.

Then the Equations (3.7), (3.8) and (3.9) are inserted into Biot-Savart law (Equation (3.6)) and numerical integration over toroidal angle is performed:

$$\varphi_{0,i} = \frac{2\pi i}{N} \tag{3.10}$$

$$D_{R,i}^3 = \left|\vec{r} - \vec{r_l}\right|^3 = \left(\left(R_1 - R_0\cos\varphi_{0,i}\right)^2 + \left(R_0 \sin\varphi_{0,i}\right)^2 + \left(Z_1 - Z_0\right)^2\right)^{3/2} \tag{3.11}$$

$$B_R = 10^{-7} \cdot I \cdot dl \cdot \left(Z_1 - Z_0\right) \cdot \sum_{i=0}^{N-1} \frac{\cos\varphi_{0,i}}{D_{R,i}^3} \tag{3.12}$$

$$B_Z = 10^{-7} \cdot I \cdot dl \cdot \sum_{i=0}^{N-1} \frac{R_0 \sin^2\varphi_{0,i} - \cos\varphi_{0,i} \cdot \left(R_1 - R_0\cos\varphi_{0,i}\right)}{D_{R,i}^3}. \tag{3.13}$$

A function performing computation of the components of the magnetic field B_R and B_Z was created in the Interactive Data Language (IDL) and successfully benchmarked against existing analytical solutions. The analytical solutions exist for the axis of the circular loop: $B_Z = \frac{\mu_0 I R_0}{2\left(Z_1^2 + R_0^2\right)^{3/2}}$, for the dipole approximation (position R_1, Z_1 far away from the position of the loop R_0, Z_0; $\left|\vec{r} - \vec{r_l}\right| >> R_0$) and for the infinitely long straight wire (Ampere's law, $\left|\vec{r} - \vec{r_l}\right| << R_0$). The IDL function has selectable number of the loops elements N, typically 1000 - 10000 is used.

Alternative method to speed up the calculation time of magnetic field from single turn toroidal loop is to use Legendre's complete elliptic integrals of the first and second kind K(k) and E(k) for parameter k to solve the Biot-Savart law, as

described in [46, pages 47-48], [47]. The numerical solution of the Biot-Savart law is then:

$$B_R = \frac{\mu_0 I}{4\pi} \frac{(Z_0 - Z_1) f_1(k)}{R_1 \sqrt{R_0 R_1}} \tag{3.14}$$

$$B_Z = \frac{\mu_0 I}{4\pi} \frac{R_1 f_1(k) + R_0 f_2(k)}{R_1 \sqrt{R_0 R_1}} \tag{3.15}$$

and quantities $f_1(k)$, $f_2(k)$ and k are:

$$k^2 = \frac{4 R_0 R_1}{(R_0 + R_1)^2 + (Z_1 - Z_0)^2} \tag{3.16}$$

$$f_1(k) = k \left[K(k) - \frac{2 - k^2}{2(1 - k^2)} E(k) \right] \tag{3.17}$$

$$f_2(k) = \frac{k^3}{2(1 - k^2)} E(k) . \tag{3.18}$$

The form used in Equations (3.14) - (3.18) is fully compatible with the CCC, coordinate system (R, φ, Z) and with Equations (3.12), (3.13).

Calculation of the Biot-Savart law has been transformed to calculation of the elliptic integrals, which is well researched mathematical problem with multiple possible solutions. One possibility is to use iterative method described in [48]. Another possibility are polynomial approximations from [49] for *complementary parameter* m_1:

$$m_1 = 1 - k^2 \tag{3.19}$$

$$K(k) = a_0 + m_1(a_1 + m_1(a_2 + m_1(a_3 + m_1 a_4))) + b_0 + m_1(b_1 + m_1(b_2 + m_1(b_3 + m_1 b_4)))\ln(1/m_1) \tag{3.20}$$

$a_0 = 1.38629436112$ $\quad b_0 = 0.5$

$a_1 = 0.09666344259$ $\quad b_1 = 0.12498593597$

$a_2 = 0.03590092383$ $\quad b_2 = 0.06880248576$

$a_3 = 0.03742563713$ $\quad b_3 = 0.03328355346$

$a_4 = 0.01451196212$ $\quad b_4 = 0.00441787012$

$$E(k) = 1 + m_1(a_1 + m_1(a_2 + m_1(a_3 + m_1 a_4))) + m_1(b_1 + m_1(b_2 + m_1(b_3 + m_1 b_4)))\ln(1/m_1) \tag{3.21}$$

$a_1 = 0.44325141463$ $\quad b_1 = 0.24998368310$

$a_2 = 0.06260601220$ $\quad b_2 = 0.09200180037$

$a_3 = 0.04757383546$ $\quad b_3 = 0.04069697526$

$a_4 = 0.01736506451$ $\quad b_4 = 0.00526449639$

When the magnetic field is calculated both by direct numerical integration and by elliptic integrals, the methods can be compared to each other with respect to the precision of calculation. The comparison shows agreement about 6-7 significant digits for the toroidal loop with radius $R_0 = 1$ m for $N = 10000$ and distance of the point of magnetic field calculation around 0.5 m, dropping to 4 significant digits when distance of the calculation point is 1 mm from the toroidal loop.

The mutual inductance of the two toroidally symmetrical loops can be computed with procedure very similar to described calculation of the magnetic field.

Faraday's law of inductance is:

$$U = -\frac{\mathrm{d}}{\mathrm{d}t}\Phi_B = -\frac{\mathrm{d}}{\mathrm{d}t}\int_S \vec{B}\cdot d\vec{S}\,, \tag{3.22}$$

where U is induced voltage, Φ_B is magnetic flux, $\vec{B}$ is magnetic field, $\mathrm{d}\vec{S}$ is area element with vector normal to the area, and S is area of the loop in which the voltage is induced.

The law describes a situation when changing magnetic field induces voltage in the closed loop encasing area S. There are two major possibilities for the thin wire approximation: either the loop itself has a flowing current I_1 and magnetic field generated by the current lowers external voltage applied to the loop by the induced voltage U_1, or there are two loops and current I_2 flowing in second one generates magnetic field, inducing voltage U_1 in the first loop. In both cases it is beneficial to introduce a new quantity called self-inductance L_{11} or mutual inductance L_{12}, respectively:

$$U_1 = -\frac{\mathrm{d}}{\mathrm{d}t}\left(L_{11}I_1\right) = -L_{11}\frac{\mathrm{d}I_1}{\mathrm{d}t} - I_1\frac{\mathrm{d}L_{11}}{\mathrm{d}t} \tag{3.23}$$

$$U_1 = -\frac{\mathrm{d}}{\mathrm{d}t}\left(L_{12}I_2\right) = -L_{12}\frac{\mathrm{d}I_2}{\mathrm{d}t} - I_2\frac{\mathrm{d}L_{12}}{\mathrm{d}t}\,. \tag{3.24}$$

It should be noted that the terms $I\dfrac{\mathrm{d}L}{\mathrm{d}t}$ in Equations (3.23) and (3.24) are often neglected and an assumption that inductance is constant is made. This assumption is valid for wires which are not changing position and therefore the (self or mutual) inductance. In the case of tokamaks this assumption is not valid for plasma column which is changing both position and current distribution during the discharge. The poloidal field coils can in principle change geometry as well because of flexing due to the acting forces during the discharge.

The mutual inductance is a quantity which is dependent purely only on geometry of the thin wires, as can be seen from its derivation:

$$\Phi_B = \int_{S_1}\vec{B}\cdot d\vec{S_1} = L_{12}I_2 = \int_{S_1}\left(\nabla\times\vec{A}\right)\cdot d\vec{S_1} = \oint_{l_1}\vec{A}\cdot d\vec{l_1} = \oint_{l_1}\left(\frac{\mu_0 I_2}{4\pi}\oint_{l_2}\frac{d\vec{l_2}}{\left|\vec{r_1}-\vec{r_2}\right|}\right)\cdot d\vec{l_1}\,. \tag{3.25}$$

Then the mutual inductance L_{ij} between the source loop marked with index j and target loop with the index i is (in the thin wire approximation):

$$L_{ij} = \frac{\mu_0}{4\pi}\oint_{l_i}\oint_{l_j}\frac{d\vec{l_i}\cdot d\vec{l_j}}{\left|\vec{r_i}-\vec{r_j}\right|}\,. \tag{3.26}$$

It can be seen that the mutual inductance between two loops is symmetrical, i.e. $L_{ij}=L_{ji}$.

The self-inductance cannot be calculated by the formula (3.26), because the denominator causes divergence of the integral for the thin wire approximation. A finite thickness of the wires must be taken into account and the volume integrals with current density $\vec{j}$ must be used.

Up to now the mutual inductance was derived for general shape of the loop. In the case of tokamak poloidal field coils with toroidal symmetry and one common major axis, the Equation (3.26) can be numerically solved with methods similar to the procedure used to solve Biot-Savart law Equation (3.6). Then the expression for numerical integration of the mutual inductance between two single turn toroidally symmetrical loops on positions (R_i, Z_i) and (R_j, Z_j) is:

$$L_{ij} = L_{ji} = 4\pi^2 \cdot 10^{-7} \cdot \frac{R_i R_j}{N} \cdot \sum_{k=0}^{N-1} \frac{\cos\varphi_{i,k}}{D_{R,k}}, \tag{3.27}$$

where N is number of the loop elements used in the integration and variables $\varphi_{i,k}$ and $D_{R,k}$ are defined by equations similar to the Equations (3.10) and (3.11):

$$\varphi_{i,k} = \frac{2\pi k}{N} \tag{3.28}$$

$$D_{R,k} = \left|\vec{r}_i - \vec{r}_j\right| = \sqrt{\left(R_j - R_i\cos\varphi_{i,k}\right)^2 + \left(R_i \sin\varphi_{i,k}\right)^2 + \left(Z_j - Z_i\right)^2}\ . \tag{3.29}$$

The numerical equation for the mutual inductance (3.27) can be calculated faster when elliptic integrals are used, similarly to Equations (3.14) and (3.15):

$$L_{ij} = L_{ji} = \frac{8\pi \cdot 10^{-7} \cdot R_i R_j}{\sqrt{\left(R_i + R_j\right)^2 + \left(Z_j - Z_i\right)^2}} \cdot \frac{(2-k^2)K(k) - 2E(k)}{k^2}, \tag{3.30}$$

$$k^2 = \frac{4R_i R_j}{\left(R_i + R_j\right)^2 + \left(Z_j - Z_i\right)^2}\ . \tag{3.31}$$

The comparison between the direct numerical integration (Equation (3.27)) and method with elliptic integrals (Equation (3.30)) shows agreement of 6-7 significant digits for N = 10000, R_i = 1 m and distance between i-th and j-th loop 0.5 meters. This agreement drops to 4 significant digits when distance between i-th and j-th loop is 0.1 mm and N = 100000.

Calculation of the self-inductance L_{ii} of the toroidally symmetrical loop is different from calculation of mutual inductance. A simple method is to use approximated equation [50]:

$$L_{ii} = \mu_0 r\left(\ln\left(\frac{8r}{a}\right) - 2 + \frac{Y}{2}\right), \tag{3.32}$$

where r is the loop major radius, a is minor radius (wire radius), constant Y = 1/2 (and therefore $Y/2$ = 0.25) for current uniformly distributed in the cross-section of the wire and Y = 0 for current uniformly distributed on the surface of the wire.

The Equation (3.32) for self-inductance calculation is insufficient for many cases in the tokamak. The plasma column does not fulfil requirement for uniform current distribution and for the circular shape of the wire. The vacuum vessel of tokamaks can be described as a set of elements with various geometrical shapes. Being limited to elements with shapes describable by one parameter a is often inconvenient.

A solution of the problem is to describe the geometry of the loop by a set of sub-elements on a square grid with fractions of the unitary current (1 A) assigned to each sub-element. With this solution both problematic cases can be solved: irregular shape

and non-uniform current distribution. Then the self-inductance of the loop described by M sub-elements on square grid takes the following form:

$$L = \sum_{k=0}^{M-1}\left(\sum_{l=0,l\neq k}^{M-1} L_{kl}\, \hat{I}_k\, \hat{I}_l \right) + \sum_{k=0}^{M-1} L_{kk}\, \hat{I}_k^{\,2}, \tag{3.33}$$

where L_{kl} is mutual inductance of two sub-elements described by Equation (3.26), L_{kk} is self-inductance described by Equation (3.32) with $Y = 1/2$, and $\hat{I}_k$ and $\hat{I}_l$ are dimensionless normalization factors describing fraction of the current in the sub-element $\sum_{k=0}^{M-1} \hat{I}_k = 1$. The importance of the approximated self-inductance is 1/M, e.g. for 10 sub-elements 10 self-inductances and 90 (2x45 as $L_{kl} = L_{lk}$) mutual inductances are calculated. An example for a loop described by two sub-elements with uniform current distribution ($\hat{I}_k = 0.5$) is:

$$L = \left(L_{12}0.5^2 + L_{21}0.5^2\right) + \left(L_{11}0.5^2 + L_{22}0.5^2\right). \tag{3.34}$$

Similar method can be used to calculate mutual inductance of two loops with either non-uniform current distributions or with irregular shape. In this case both loops are divided into sub-elements on a grid, but the requirement for square grid is not necessary because only mutual inductances are calculated. The square grid is necessary only for self-inductance calculation by Equation (3.32).

Note that this section dealt with numerical calculation of magnetic field and inductances of *single turn* toroidal loops, even though general equations valid for multi-turn coils were used. When numerical solutions for multi-turn toroidal windings are desired, appropriate multiplication by the count of turns must be used (N_T in Biot-Savart law, $N_{T1}N_{T2}$ in mutual inductance and N_T^2 in self-inductance).

3.1.5 Characterization of PF coils circuits magnetic fields

This section is extended form of two articles: Havlicek et al., *Characterization of Magnetic Fields in the COMPASS Tokamak* [35] and Havlicek et al., *Modelling of COMPASS tokamak PF coils magnetic fields* [36]. Additional figures were added to better describe the vacuum magnetic fields of the COMPASS PF coils circuits and more detailed text description was provided in comparison with the original articles. The figures were updated to the CCC.

The aim of this section is to describe vacuum magnetic fields of the COMPASS PF coils circuits and to explain their features and purpose.

As was already mentioned in the Section 3.1, COMPASS uses different approach to control plasma column than many modern tokamaks. COMPASS has windings organized into circuits which are dedicated to control different plasma parameters which are independent on each other whenever possible. There is MFPS circuit to control loop voltage applied to plasma, EFPS and BV circuit to control radial position *r*, BR circuit to control vertical position *z* and SFPS circuit to control shape of the plasma.

This approach has an advantage of simplicity and low number of required independent Power Supplies, but these advantages are offset by more rigid control of

plasma shape. The plasma shape is controlled by current in the SFPS circuit and by configuration selected before the discharge on the link boards (SND, SNT, ...). While plasma shape during the plasma current flat-top can be well prescribed by selection on the link boards, the process of changing shape from circular to diverted plasma cannot be well controlled without multiple circuits and Power Supplies.

This is connected with another disadvantage: less precise control of the distance between plasma Last Closed Flux Surface (LCFS) and the first wall elements. The shape of the COMPASS plasma is fully controlled by three parameters: 1) ratio between plasma current and SFPS current, 2) radial position r and 3) vertical position z. The positions, as currently implemented ([Attached publication A2], [Attached publication A3]) in the feedback system, are artificial signals which are - in the first order approximation - describing the plasma current centre, which should be close to the position of the magnetic axis. When the thermal energy stored in the plasma increases, the distance between plasma geometrical axis and magnetic axis is increasing. Therefore the actual shape of the plasma and distance to the first wall depend on the plasma thermal energy as well as on the settings in the feedback. It is, in principle, possible to change the feedback controlled variables to different ones, e.g. use distance from separatrix LFS midplane point to the first wall instead of magnetic axis radial position r, but without more independent plasma shape actuators the shape will still change with the plasma thermal energy. Furthermore the distance from separatrix to the first wall can be for shots with similar plasma thermal energy controlled by changing the plasma centre in the feedback settings on inter-shot basis.

The limitations in the control possibilities of the COMPASS plasma shape have to be taken into account when experiment is planned. In practice the limitations are not significantly constraining experimental possibilities and simplicity of the feedback system is beneficial to the small tokamak with relatively small team of available physicists, engineers and technicians.

In contrast to COMPASS, many modern tokamaks prefer to use multi-variable control systems with more required Power Supplies. Example references for the JET tokamak can be found in [51], [52], [53].

The theory described in the Section 3.1.4, particularly numerical equations (3.14) and (3.15), was used to calculate poloidal magnetic field of COMPASS poloidal field coils circuits. PF coils circuits were represented as a list of elements with positions R, Z, current orientations (sign of number of turns) and numbers of turns (usually 1 turn per element, but 1.333, 1.5 and 2 turns were also used). The figures in this section show magnetic fields inside the vessel generated by unit current flowing through the PF coils circuits.

The primary motivation for the computation of the magnetic field originating from the PF coils circuits is to calibrate the COMPASS tokamak magnetic detectors. The graphs are also very useful to get better idea of magnetic fields in the COMPASS tokamak.

MFPS circuit

MFPS circuit (Magnetizing Field PS) purpose is to generate loop voltage to drive the plasma current. The circuit acts as a primary winding of air transformer, where secondary winding is plasma column, vacuum vessel and other PF coils circuits.

It is created from both windings in the central solenoid (M1 and M6) and from additional windings in other PF coils which prevent MFPS magnetic field from disturbing plasma inside the tokamak vacuum vessel. This is achieved by moving magnetic field lines out of the area of vacuum vessel.

MFPS circuit magnetic field overview is depicted in the **Figure 3.15**, two cuts along the important vectors in the vacuum vessel are in the **Figure 3.16**. It can be seen that MFPS magnetic field inside the vacuum vessel is small – e.g. in the centre of vacuum vessel (R = 0.56 m, Z = 0.0 m) it is 0.008 mT/kA. The result is that magnetic field of the MFPS circuit does not influence plasma shape or position, even for extreme values of the MFPS current (-18 kA, +16 kA). The directions of the magnetic field are visible in the **Figure 3.15**, left panel show its multi-pole character.

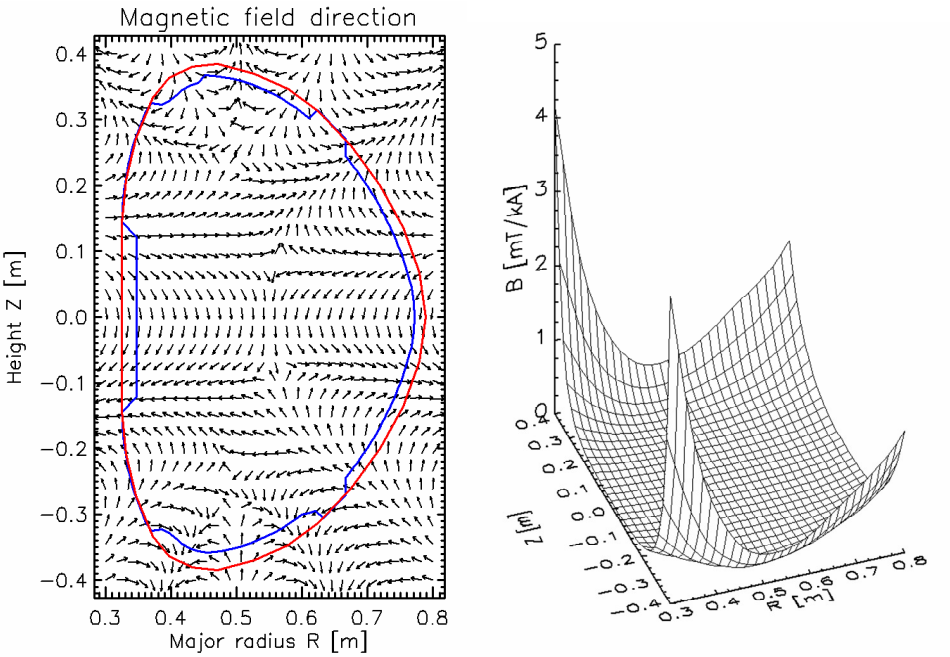

Figure 3.15: MFPS circuit. Left panel: direction of B (vectors have unit length), right panel: absolute value of the magnetic field for unit current in the MFPS.

Another result of the connection of the MFPS circuit is constant mutual inductance between MFPS and any point in the vacuum vessel - 22 μH (see **Table 3-3** in the Section 03.1.6 - Mutual inductances of poloidal field coils circuits).

The loop voltage acting on the plasma is generated by changing current in the MFPS current. The plasma breakdown (described in [54]) is achieved by applying high loop voltage. This is done by driving negative current in the MFPS and then forcing the current to flow through two resistors R1 and R2 by use of thyristor switches and a large capacitor bank. The L/R constant of the MFPS circuit is decreased for large R and fast change of the MFPS circuit current towards zero amps

provides loop voltage for plasma breakdown. Both the negative MFPS current (-18 kA to 0 A) and the loop voltage profile are pre-programmed before the discharge by setting minimal value of the MFPS current (-14 kA produces higher loop voltage than -12 kA) and by setting switch-on times of thyristors TV1 and TV2 in the Shaper. These thyristors remove resistors R1 and R2 from the circuit, effectively lowering loop voltage during the plasma current ramp-up. As a result, plasma current evolution is controlled only indirectly when MFPS current is negative.

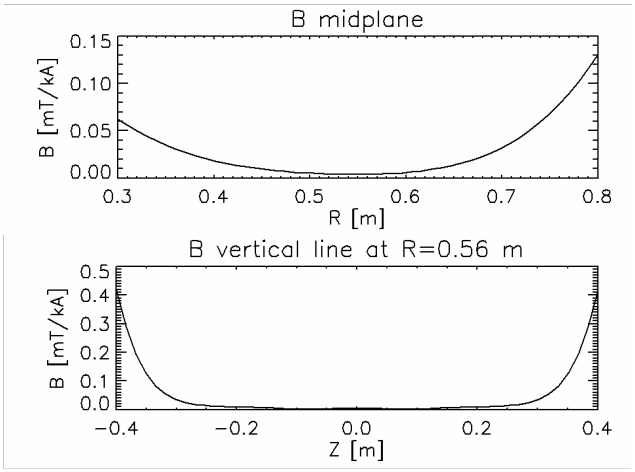

Figure 3.16: MFPS circuit. Top panel: absolute value of $\vec{B}$ on the midplane, bottom panel: absolute value of $\vec{B}$ on the vertical line crossing the vacuum vessel centre. The graphs are normalized to unit current in the MFPS.

The MF Power Supply is created from two thyristor converters in anti-parallel connection. Therefore the positive current is created by different converter than negative current. Before the positive current is applied to the circuit, a certain time must pass to ensure that converters do not damage each other. We call this "MFPS current passing zero" and the time is usually > 5 ms, depending on the current requests in MFPS and other circuits.

The positive MFPS current is controlled by COMPASS feedback software MARTe [Attached publication A2], [55], [56]. The principle is that operator requests time waveform of the plasma current and MARTe uses PI controller to calculate requested derivative of the MFPS current (control variable) based on the measured plasma current (process variable) and requested plasma current setpoint. The detailed description of the feedback algorithm of all PF coils circuits should be part of the doctoral thesis of Filip Janky: *Design and implementation of the plasma control system for the COMPASS tokamak*. Part of the description was published in [Attached publication A3].

EFPS circuit

The EFPS circuit (Equilibrium Field PS) purpose is, same as BV circuit, to create vertical magnetic field, which prevents plasma column radial expansion, and control plasma radial position. The EFPS circuit has thyristor converter as a Power Source, allowing higher current and voltage than BV circuit. The result is that EFPS

circuit creates strong, slowly reacting vertical magnetic field, while BV circuit provides fast vertical magnetic field for control of radial plasma position.

The EFPS circuit consists of parallel connected windings E1 and E2 on the LFS of the tokamak, and of one half (M1) of the windings in the central solenoid.

Figure 3.17 contains overview of the magnetic field of the EFPS circuit, **Figure 3.18** depicts three cuts along the important vectors in the vacuum vessel. The left panel in the **Figure 3.17** shows that the direction of the magnetic field is mainly vertical with relatively small curvature below and above the midplane. The produced $\vec{j} \times \vec{B}$ force acting on the plasma has direction towards HFS for the standard plasma current direction (negative = clockwise when viewed from above), preventing natural expansion of the plasma column caused by its magnetic field and plasma pressure. The curvature of the EFPS circuit magnetic field is such that it produces $\vec{j} \times \vec{B}$ with downwards direction for plasma above the midplane, providing passive vertical position stabilization (values are visible in the **Figure 3.18**, middle panel). This allows to operate plasma with circular cross-section without active vertical position stabilization. The force is not large enough to stabilize plasmas which are vertically elongated.

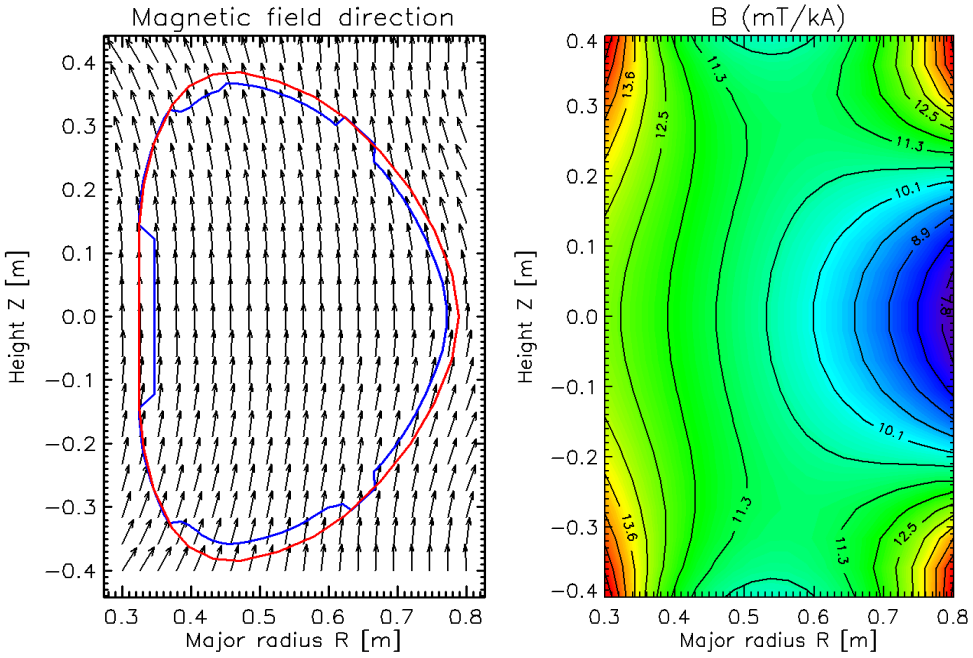

Figure 3.17: EFPS circuit. Left panel: direction of B, (vectors have unit length), right panel: absolute value of the magnetic field for unit current in the EFPS. Plasma current flows in the negative direction (clockwise when viewed from above).

Right panel in the **Figure 3.17** and **Figure 3.18** provide further information about values and homogeneity of the magnetic field. The vertical component of the magnetic field created by EFPS circuit is changing from 13 mT/kA on HFS to 7.5 mT/kA on LFS on the midplane, while on the vertical line crossing the vacuum vessel centre it is 10.4 - 11 mT/kA. The EFPS circuit magnetic field normalized to

unit current is ~ 5 times stronger than the magnetic field of the BV circuit. Furthermore the EF Power Supply can achieve up to 16 kA, while BV circuit Fast Amplifier is limited to +/- 5 kA.

The EFPS current is controlled by the COMPASS feedback. The current requested by MARTe software from the PS controller is sum of three parts: it is directly proportional to the plasma current, directly proportional to current in the BV circuit and there is PI controller on the calculated radial position signal.

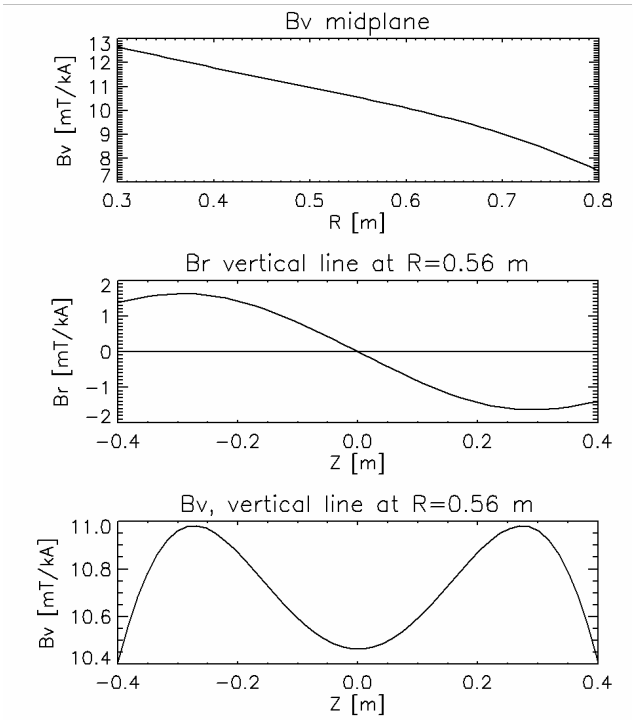

Figure 3.18: EFPS circuit. Top panel: vertical component of $\vec{B}$ on the midplane, middle panel: radial component of $\vec{B}$ on the vertical line crossing vacuum vessel centre, bottom panel: vertical component of $\vec{B}$. The graphs are normalized to unit current in the EFPS.

SFPS circuit

The purpose of the SFPS circuit (Shaping Field PS) is to provide shaping of the plasma column based on the configuration of the SFPS circuit selected on the link boards.

The SFPS circuit consists of wide variety of windings in different coils, see Section 3.1.3 for details.

Figure 3.19 and **Figure 3.20** describe magnetic field for the SFPS-SND configuration, while **Figure 3.21** and **Figure 3.22** show magnetic field of the SFPS-SNT configuration. In both cases the plasma is elongated vertically by the shaping field (see direction of $\vec{B}$ above and below midplane). This elongation is not top-down symmetrical and has a consequence that the plasma is no longer vertically stable. This can be easily seen from the fact that the $\vec{j} \times \vec{B}$ force acting on the top part of the plasma column has upwards direction and the force acting on the bottom

part of the plasma has downwards direction. Then any deviation of the vertical plasma position results into total force increasing the deviation. The vertical position instability must be controlled by active position feedback.

Furthermore the X-point and divertor plasma configuration is created if the ratio between current in the SFPS and plasma current is large enough. The X-point is located on the bottom of the vacuum vessel, see asymmetry in absolute value of the magnetic field in bottom part of the right panels in the **Figure 3.19** and **Figure 3.21**. The asymmetry is created by cluster of windings F2B, F3B and S2B in which the direction of the SFPS current is identical as in the plasma, creating the X-point.

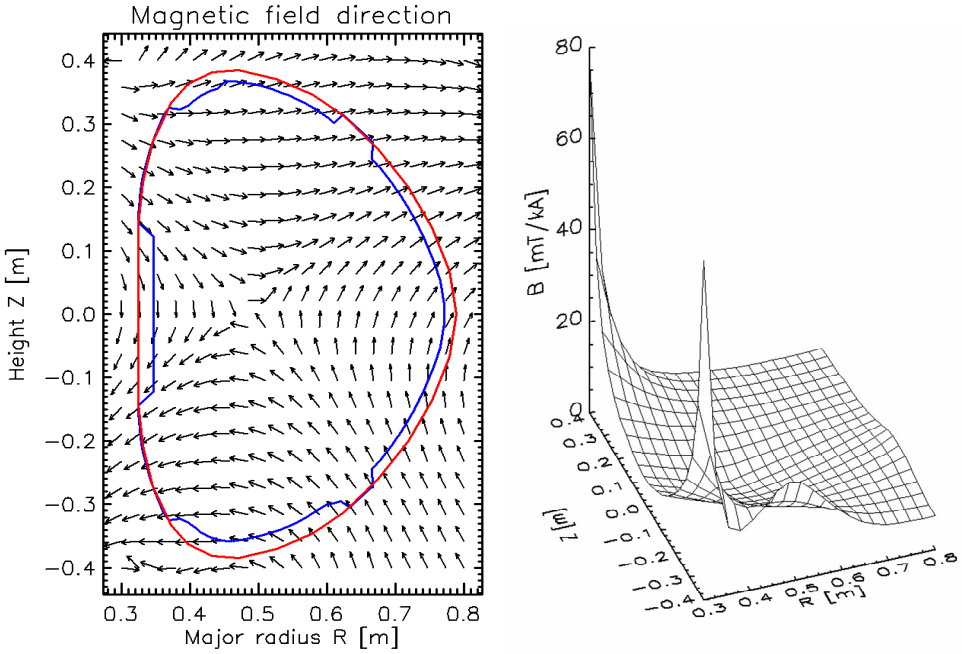

Figure 3.19: SFPS - SND circuit. Left panel: direction of B, (vectors have unit length), right panel: absolute value of the magnetic field for unit current in the SFPS.

Figure 3.20 and **Figure 3.22** show radial component of the SFPS magnetic field along the vertical line crossing vacuum vessel centre. It can be seen that absolute value of the radial component is larger in the bottom part of the vacuum vessel, resulting into two important effects.

Firstly, the total $\vec{j} \times \vec{B}$ force potential (from the SFPS circuit magnetic field for the plasma column) has maximum in the vacuum vessel, but not necessarily on the vertical position z required for the divertor plasma. The additional radial magnetic field, created by the BR circuit, is necessary to move the potential maximum to the desired vertical position. Furthermore the BR circuit then must be controlled by feedback loop to stabilize the plasma vertical position.

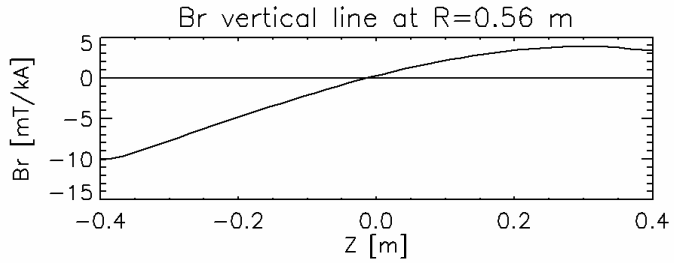

Figure 3.20: SFPS - SND circuit radial component of $\vec{B}$ on the vertical line crossing vacuum vessel centre, normalized to unit current in the SFPS.

Secondly, the SFPS magnetic field radial component is stronger in the part of the vessel closer to the X-point (bottom in showed cases). This has consequences for the plasma column movement speed in case of a disruption. All disruptions of divertor configuration plasmas are accompanied by failure to control vertical position. Disruptions which move in the upwards direction are slower than disruptions going downwards.

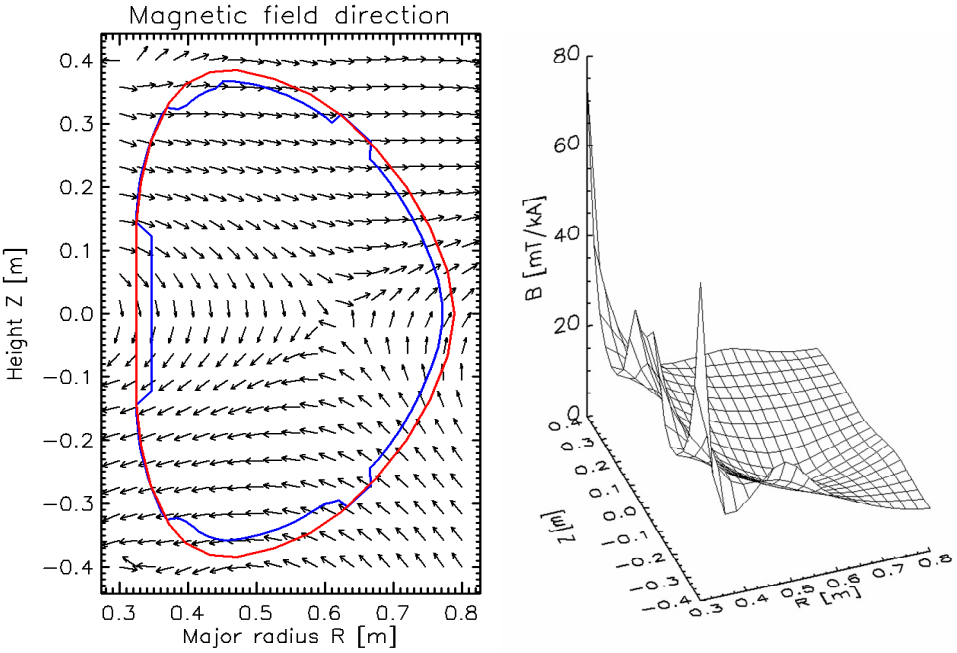

Figure 3.21: SFPS - SNT circuit. Left panel: direction of B, (vectors have unit length), right panel: absolute value of the magnetic field for unit current in SFPS. Plasma is more triangular than in SFPS – SND configuration. Higher triangularity is advantageous because of higher energy confinement time than in lower triangularity plasmas.

The current in the SFPS circuit is controlled by COMPASS feedback. It is directly proportional to the smoothed plasma current. The smoothing is necessary to prevent oscillation between plasma shape and plasma current, because the SFPS current changes generate non-negligible loop voltage, influencing plasma current (see Section 3.1.6 - Mutual inductances of poloidal field coils circuits). The tokamak operator can request predefined waveform or the feedback controlled current. The

shape of the plasma depends on radial plasma position, vertical plasma position and ratio between SFPS current and plasma current. It should be noted that ratio between SFPS current and plasma current changes primarily the area of the plasma column cross-section and only marginally changes plasma elongation.

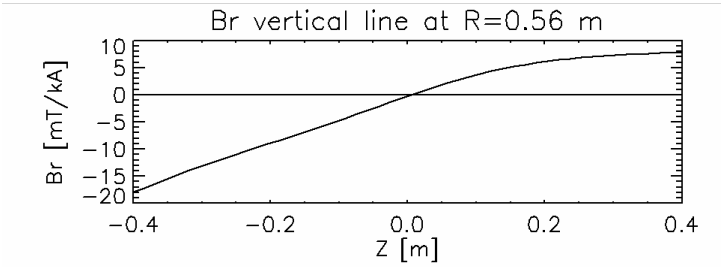

Figure 3.22: SFPS - SNT circuit radial component of $\vec{B}$ on the vertical line crossing vacuum vessel centre, normalized to unit current in the SFPS

BR circuit

The purpose of the BR circuit (radial magnetic field) is to provide control of the vertical position of the plasma column. The circuit is powered by Fast Amplifier FABR.

The BR circuit is created from four toroidal turns in windings F4A and S4A above midplane at position $R \cong 0.64\,m, Z \cong 0.52\,m$ with negative current direction (positive I_{BR} flows clockwise when viewed from above) and from four turns below midplane in windings F4B and S4B with positive current direction. This connection of the windings creates magnetic field described by **Figure 3.23** and **Figure 3.24**.

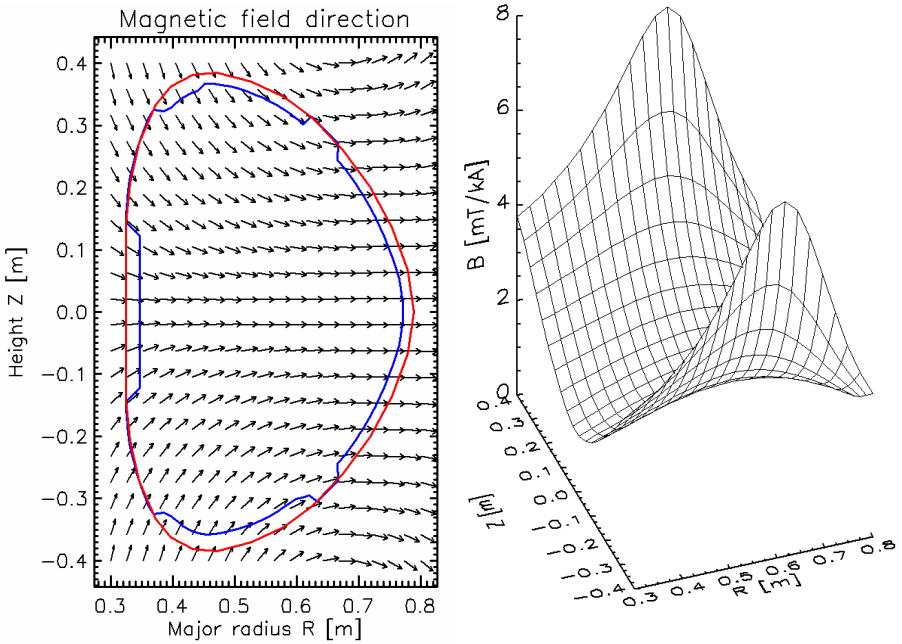

Figure 3.23: BR circuit. Left panel: direction of magnetic field B, (vectors have unit length), right panel: absolute value of the magnetic field for unit current in the FABR.

The figures show that created magnetic field is really radial only nearby of the midplane. Above and below the midplane the direction of the magnetic field has strong vertical component. **Figure 3.23**, right panel, also shows that the magnetic field normalized to 1 kA in the BR circuit is significantly stronger above and below midplane than on the midplane (the radial magnetic field is changing from 2 mT/kA to 4 mT/kA inside the vacuum vessel). Precise values can be found from the **Figure 3.24**.

The unfavourable direction of the BR magnetic field above and below midplane led us to propose alternative connection of the circuit in the article *Modelling of COMPASS tokamak PF coils magnetic fields* [36], but the alternative connection was never realized, primarily because the currently used connection has mostly satisfactory practical results in the controlling of the vertical plasma position.

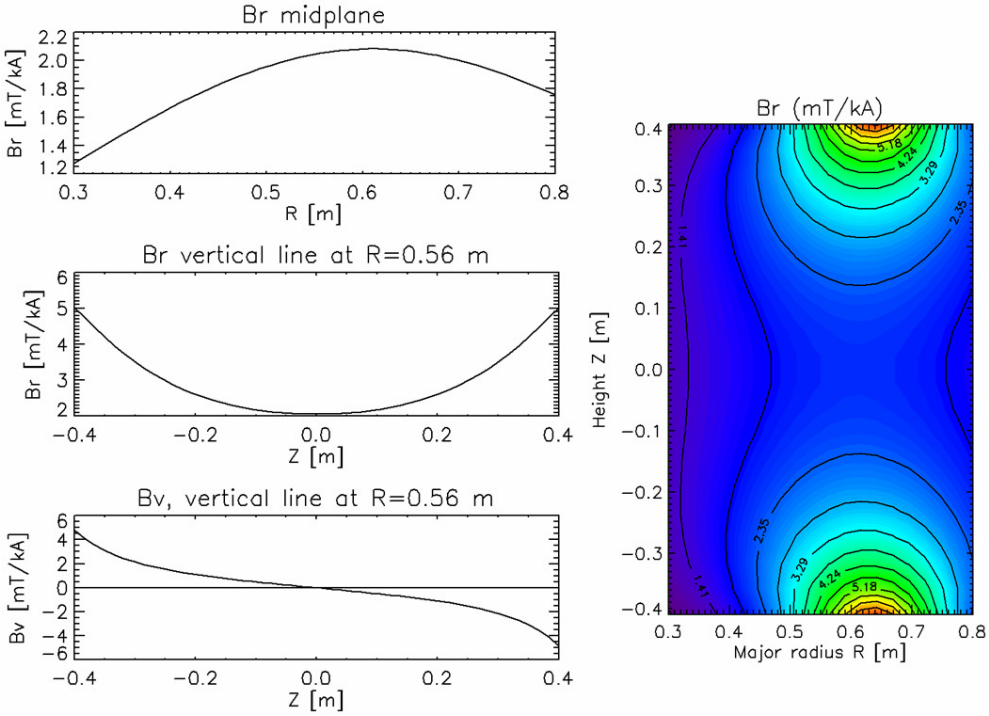

Figure 3.24: BR circuit. Top left panel: radial component of $\vec{B}$ on the midplane, middle left panel: radial component of $\vec{B}$ on the vertical line crossing vacuum vessel centre, bottom left panel: vertical component of $\vec{B}$. Right panel: contour graph of the radial component of $\vec{B}$. The graphs are normalized to unit current in the FABR.

A different connection of the BR circuit with only two toroidal turns above and below midplane (i.e. after removal of S4A and S4B winding) was practically examined with intention to speed-up reaction time of the vertical position stabilization. In this configuration the strength of the magnetic field created by 1 kA current is halved, but self-inductance of the circuit is decreased to one quarter, effectively yielding two times faster $\mathrm{d}B/\mathrm{d}t$ at the expense of maximal achievable magnetic field. While physically sound, technical problems with the Fast Amplifier prevented us from using this configuration. For the connection with lower self-

inductance the Fast Amplifier [Attached publication A1] did not have any reserves with respect to voltage spikes during transistor switching. The problem of the decreased maximal achievable magnetic field is also potentially troubling because the FABR often operates in range of 2-3 kA in order to maintain plasma position above the midplane, to create the divertor configuration. Therefore this alternative BR circuit connection would need to operate between 4-6 kA which is over the limit of the FA. Nevertheless, this alternative connection of the BR circuit is still considered possible in case that new Power Supply is manufactured for the BR circuit.

The current in the currently used BR circuit is controlled by the COMPASS feedback system in the 50 μs *fast thread*, see [Attached publication A2]. The current requested by MARTe from the FABR controller is created by applying PI controller to the vertical plasma position. The proportional constant is controlling fast plasma position oscillations and integral part is keeping average position nearby of the requested vertical position.

BV circuit

The purpose of the BV circuit (vertical magnetic field) is to provide fast control of the radial position of the plasma column. Slow control of the radial plasma position is provided by EFPS circuit. The BV circuit is powered by Fast Amplifier FABV.

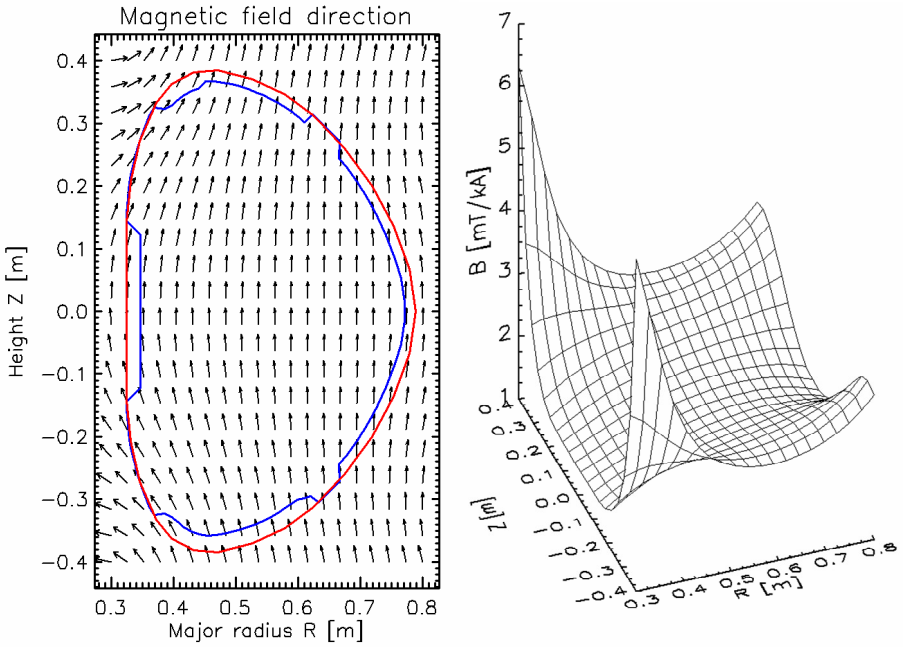

Figure 3.25: BV circuit. Left panel: direction of magnetic field B, (vectors have unit length), right panel: absolute value of the magnetic field for unit current in the FABV.

The circuit is created from windings F5A and F5B on the LFS and from windings F1A and F1B on the HFS. The direction of the BV circuit current in the F5 windings create vertical magnetic field, while a primary role of the F1 windings

(HFS) is to have opposite direction to F5 windings, effectively providing negligible mutual inductance to the MFPS circuit (see **Table 3-1** in the Section 3.1.6, without windings F1 the mutual inductance would be ~4 x 22 μH).

Figure 3.25 and **Figure 3.26** describe magnetic field of the BV circuit. It can be seen that the magnetic field is mostly vertical and has good homogeneity in the vacuum vessel. The strength of the vertical magnetic field is ~2 mT/kA, which is ~ 5 times less than the magnetic field of the EFPS circuit. Furthermore the EF Power Supply can achieve up to 16 kA, while FABV is limited to +/- 5 kA.

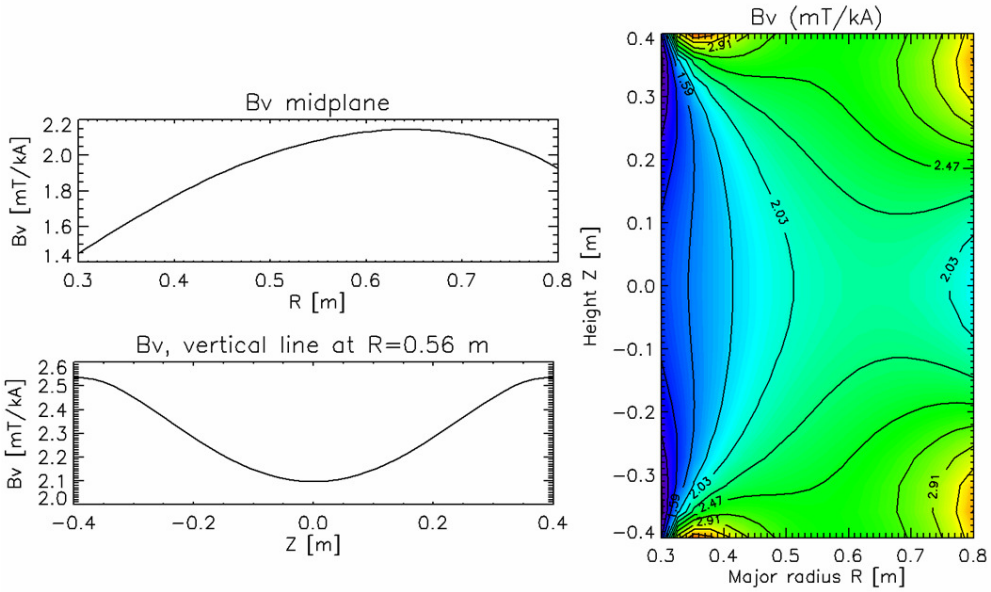

Figure 3.26: BV circuit. Top left panel: vertical component of $\vec{B}$ on the midplane, bottom left panel: vertical component of $\vec{B}$ on the vertical line crossing vacuum vessel centre. Right panel: contour graph of the vertical component of $\vec{B}$. The graphs are normalized to unit current in the FABV.

The BV current is controlled by the COMPASS feedback in the 50 μs *fast thread*. The current requested by MARTe from the FABV controller is created by applying PI controller to the radial plasma position. The EFPS circuit, which is also controlling radial plasma position, has part of its current request directly proportional to the current in the BV circuit. The reason is intention to transfer control of "average" plasma radial position to the EFPS circuit and allow BV circuit to control only fast changes of the radial position.

3.1.6 Mutual inductances of poloidal field coils circuits

Theory described in the Section 3.1.4, particularly the numerical equations for mutual inductance (3.30) and for self-inductance (3.32), was used to calculate inductances of COMPASS poloidal field coils circuits. PF coils circuits were represented by a list of elements with positions *R*, *Z*, current orientations (sign of number of turns) and numbers of turns (usually 1 turn per element, but 1.333, 1.5 and 2 turns were also used).

Mutual and self-inductances were calculated for both full PF coils circuits and for simplified circuits described in the **Figure 3.13**. Mutual inductances between circuits and important points of interest - either in-vessel points or positions of Flux Loops - were calculated as well. The purpose was to create a database of values necessary for simulations of the interaction of the PF coils systems with each other and with tokamak. Some values had been already known from the documentation from Culham but not in a form consistent with the COMPASS Currents Convention (CCC). Note that induced voltage is always $U = -L \cdot \mathrm{d}I/\mathrm{d}t$, e.g. voltage induced in the vessel centre by MFPS circuit current is:

$$U = -L_{\text{VESSEL CENTRE}-\text{MFPS}} \cdot \mathrm{d}I_{MFPS}/\mathrm{d}t = -22\,\mu H \cdot \mathrm{d}I_{MFPS}/\mathrm{d}t\,. \tag{3.35}$$

A part of the following values was already published in the bachelor thesis of Radek Beňo: *Modelování systému řízení polohy plazmatu v tokamaku COMPASS* [57] but without respecting the CCC, which was introduced later.

Table of COMPASS PF coils circuits inductances

Circuit	R [mΩ]	MFPS	EFPS	SND	SNT	BV	BR	BVproposal	BRproposal
MFPS	37	2934	-643	676	891	9.4	0	101.8	0
EFPS	16.5		924	-169	-323	137	0	119	0
SND	40.7			649		37	5.4	38.7	-0.2
SNT	47				1109	31.6	-12.2	33.2	-10.6
BV	9.2					61	0	---	---
BR	10						92	---	---
BVproposal								55.5	0
BRproposal									40.7

All inductance values are in μH.

Decoupling Transformer EF-BV: primary winding has resistance 10 mΩ, self-inductance ~500 μH; secondary winding has resistance 1.2 mΩ, self-inductance ~46 μH, mutual inductance ~ 130 μH. 21/24 primary winding turns used.

Decoupling Transformer SF-BV: primary winding "FI", resistance 4.5 mΩ, self-inductance ~130 μH, secondary winding "WZ", resistance 2 mΩ, self-inductance ~44 μH, mutual inductance ~50 μH**. Secondary winding not connected in BV circuit.**

Resistances and inductances in the table **do not include** values of the decoupling transformers. BR resistance consists of 8.36 mΩ of coils and 1.68 mΩ of cables, BV resistance include 7.5 mΩ of coils and 1.68 mΩ of cables.

Table 3-1: Resistances, mutual inductances and self-inductances of the COMPASS PF coils circuits.

Table 3-1 contains resistances, self-inductances and mutual inductances of five PF coils circuits described in Section 3.1.3 and of two additional circuits: BRproposal and BVproposal. These two are possible variants of the BR and BV circuits offering a faster reaction of the current change for the feedback system at the expense of lower maximal magnetic field available for maximal Fast Amplifier current (+/-5 kA). The alternative BR and BV connections were described in the article Havlicek et al., *Modelling of COMPASS tokamak PF coils magnetic fields* [36].

Furthermore, the **Table 3-1** contains notes with parameters of the decoupling transformers introduced in the Section 3.1.3 - Connections of poloidal field coils circuits.

The Decoupling Transformer EF-BV was designed and manufactured in the IPP Prague during the COMPASS reinstallation in Prague. The same IDL code as the one used for calculation of the inductances in this section was used to find geometry of the primary and secondary windings of the transformer. Then the transformer was manufactured, its inductances measured and it was installed into the EFPS and BV circuits. The transformer has a primary winding (in the EFPS circuit) made from 24 turns of the 185 mm^2 copper cable wound on a wooden barrel. The primary winding radius is 0.542 m and the vertical dimensions of 24 turns are from -0.4 m to 0.175 m (in an arbitrarily selected coordinate system). The primary winding has one tap on the 21st turn. The turns are counted from bottom. The secondary winding (in the BV circuit) has 6 turns consisting of two parallel wound 185 mm^2 cooper wires. The radius is 0.59 m and the vertical dimensions are from -0.36 m to 0.115 m. The electrical properties are summarized in the note of the **Table 3-1**.

It should be noted that the Decoupling Transformer EF-BV has too high resistance of the primary winding, limiting maximal achievable current in the EFPS circuit and therefore the maximal controllable plasma current. Theoretically, the current for the EFPS maximal effective line to line voltage U_{LL} = 280 V would be $(3/\pi \cdot \sqrt{2} \cdot 280\,\mathrm{V}) / 26.5\,\mathrm{m\Omega}$ = 14.3 kA, but the maximal voltage value is achieved only for no load. With increasing current the transformer provides lower voltage, typically by 10-20 %, depending on the u_k parameter of the transformer. In reality, up to 14 kA is achieved in the EFPS circuit, which is enough to control plasma current up to 350 kA. This is allowed by sharing a part of the circuit (winding MB = M1) with other Power Supplies, lowering current in the MB winding and therefore effectively lowering voltage necessary to achieve required current. It is envisaged that the transformer with similar geometrical disposition will be manufactured by a commercial enterprise, with significantly higher cross-section of the primary winding.

The Decoupling Transformer SF-BV, also known as TX (P79), has been transported together with COMPASS from Culham. It has multiple taps on both primary and secondary windings, see **Table 3-2**. Notes in the **Table 3-1** describe its parameters for the configuration of actually connected taps FI (10 turns) on the primary winding in the SFPS circuit, while the *secondary winding is not used* in the BV circuit, as has been explained in Section 3.1.3.

Table 3-2 contains measured values of the mutual inductances between primary and secondary windings of the Decoupling Transformer SF-BV. The measurement has been performed by feeding the primary winding from regular power grid via transformer with 50 Hz current with amplitude ~30 Amps. Then the voltage on the secondary winding was measured with oscilloscope. The relation between the current

measured on the shunt resistor and measured voltage is $U = -L \cdot \frac{\mathrm{d}I}{\mathrm{d}t} = -L \cdot I \cdot \omega \cdot \cos(\omega \cdot t)$, which allows to calculate the mutual inductance.

Primary windings taps names and number of turns

A	B	C	D	E	F	G	H	I	J	K	L
0	4	8.5	11.5	14.5	18	20	25	28	31	34	37

Secondary winding taps names and number of turns

W	X	Y	Z
0	2	6	8

Table of measured mutual inductances of Decoupling transformer SF-BV between primary (columns) and secondary (rows) windings

	FI	FL	BF	BL
WX	4	5	16	23
WY	31	42	52	99
WZ	38	71	55	128
XY	26	37	37	77
XZ	37	60	40	110
YZ	11	27	5	35

All inductance values are in μH.

Table 3-2: Taps and numbers of turns of Decoupling Transformer SF-BV (alternative name: TX (P79)). Measured mutual inductances between primary and secondary windings.

Table 3-2 shows measured mutual inductance 38 μH for connection FI-WZ, while the note in the **Table 3-1** has ~50 μH written, which is a theoretical value based on the numerical calculation for known geometry. A difference between these two numbers can be used as a basis for estimating error of the theoretical calculation. Some of the theoretical values in the **Table 3-1** and **Table 3-5** were, for comparison, measured with the same method used to create **Table 3-2**. These values are: *L(SFPS-SND, BV)* = 31 μH, *L(EFPS, BV)* = 128 μH, *L(BR, BR)* = 92.5 μH, *L(BV, BV)* = 50.7 μH and *L(MB, MB)* = 397 μH. The agreement between measured and calculated values is good - the difference is lower than 20 % in all cases. This is a reasonable upper estimation for the error of the inductance calculation for all tables in this section. It should be noted that all numbers in the Tables in this section are written with higher number of significant digits than the error estimation warrants. This is intentional, to keep the precision of the calculated data even though real values can have lower precision.

Table of mutual inductances between PF coils circuits and important in-vessel points

	plasma	Important in-vessel points		
	center	HFS	LFS	HFS-top
R [m] =>	0.56	0.347	0.7715	0.347
Z [m] =>	0	0	0	0.25
MFPS	22	22	22	22
EFPS	0.79	-6	9.02	-5.38
SND	7.84	8.2	11.4	6.1
SNT	10.25	15.8	11.63	8.28
BV	1.628	0.468	3.496	0.198
BR	0	0	0	-0.826
BVproposal	2.139	0.806	4.032	0.781
BRproposal	0	0	0	-0.87

All inductance values are in μH.

Table 3-3: Mutual inductances between COMPASS PF coils circuits and important in-vessel points.

Table 3-3 shows mutual inductances between the PF coils circuits and important space points in the vacuum vessel. These points are:

1. centre of the vacuum vessel (R = 0.56 m, Z = 0 m)
2. midplane, High Field Side, limiter position (R = 0.347 m, Z = 0 m)
3. midplane, Low Field Side, limiter position (R = 0.7715 m, Z = 0 m)
4. HFS, above midplane (R = 0.347 m, Z = 0.25 m)

These points cover some possible positions of the plasma column during tokamak operation or during plasma disruption. It is possible to simulate an influence of the plasma on the current in the Power Supplies by placing a thin wire with desired current waveform. The waveform can simulate either plasma current ramp-up phase ($\mathrm{d}I/\mathrm{d}t$ = 20-100 kA / 10 ms typically for COMPASS) or plasma disruption ($\mathrm{d}I/\mathrm{d}t$ = 150-675 kA/ms typically).

Table 3-3 shows that mutual inductance from the MFPS circuit to any point inside the vessel is 22 μH. This is an intention of the design of the MFPS circuit, where the central solenoid is augmented by windings in other coils to have exactly this effect. As a result, the voltage generated in any possible position or shape of plasma is always same: $U = -L \cdot \mathrm{d}I_{MFPS}/\mathrm{d}t = -22\mu H \cdot \mathrm{d}I_{MFPS}/\mathrm{d}t$. Note that the standard plasma current direction is negative (counter-clockwise when viewed from above) and plasma current is generated by negative voltage.

Another interesting values are mutual inductances from the EFPS circuit. It can be seen that the EFPS circuit generates negative loop voltage on the LFS of the plasma column and positive voltage on the HFS during the plasma current ramp-up (<=> EFPS current ramp-up). The effective voltage applied to the plasma from the EFPS circuit must be evaluated with respect to the plasma shape and current profile.

The last important values in the **Table 3-3** are mutual inductances from the SFPS circuit. Their value is non-negligible against 22 μH value of the MFPS circuit.

Therefore the SFPS circuit generates non-negligible part of the voltage applied to the plasma column during ramp-up of the SFPS current in the process of creating diverted plasma shape.

Voltages applied by different Power Supplies to the plasma column during different discharges are discussed in the Chapter 4, Section 4.5 - Global power balance and in article Havlicek et al., *Global Power Balance in Non-Stationary Discharge Phases in the COMPASS Tokamak* [58].

Table of mutual inductances between PF coils circuits and COMPASS Flux Loops

	FL4, 5	FL2	FL7	FL1	FL8	FL3	FL6
R [m] =>	0.325	0.356	0.356	0.7723	0.7723	0.32519	0.32519
Z [m] =>	0	0.3	-0.3	0.08948	-0.8948	0.1554	-0.1554
MFPS	22	22	22	22	22	22	22
EFPS	-6.62	-4.78	-4.78	9.38	9.38	-6.39	-6.39
SND	8.4	4.82	3.33	9.7	12.43	7.77	7.31
SNT	17.01	6.28	4.22	10.03	12.34	11.99	11.29
BV	0.395	0.078	0.078	3.55	3.55	0.306	0.306
BR	0	-1.05	1.05	-0.807	0.807	-0.443	0.443
BVproposal	0.706	0.81	0.81	4.09	4.09	0.698	0.698
BRproposal	0	-1.15	1.15	-0.51	0.51	-0.449	0.449

All inductance values are in μH.

Table 3-4: Mutual inductances between PF coils circuits and magnetic diagnostics Flux Loops.

Table 3-4 shows mutual inductances between the PF coils circuits and eight available Flux Loops. Flux Loops FL1 to FL8 are single turn toroidally wound wires measuring a local value of the loop voltage. **Table 3-4** can be used for separation of voltage induced by the PF coils circuits and voltage induced by plasma and vacuum vessel.

Table of simplified PF coils circuits inductances

Simplified circuits	R [mΩ]	MA	MB	SF = +S(SNT)+MB	EF = +E-MB	S(SNT)	E
MA	27	1301	602.9	454.5	-286.1	-148.4	316.8
MB	10		428	436.5	-357.7	8.5	70.3
SF=+S(SNT)+MB	47			1109	-323.0		
EF=+E-MB	16.5				924		
S(SNT)	37					664.6	43.3
E	6.5						636.9

All inductance values are in μH.

Table 3-5: Resistances, mutual inductances and self-inductances of the simplified PF coils circuits. See **Figure 3.13** for description of the simplified circuits.

Table 3-5 and **Table 3-6** show similar data as **Table 3-1** and **Table 3-3**: resistances, self-inductances and mutual inductances but for simplified coils described in Section 3.1.3 in the **Figure 3.13**. Both mutual and self-inductances of

the simplified coils as well as mutual inductances to important in-vessel points are shown.

Table of mutual inductances between simplified PF coils circuits and important in-vessel points

	plasma	Important in-vessel points		
	center	HFS	LFS	HFS-top
R [m] =>	0.56	0.347	0.7715	0.347
Z [m] =>	0	0	0	0.25
MA	14.5	12.8	15.89	13.51
MB	7.5	9.22	6.09	8.5
SF=+S(SNT)+MB	10.25	15.8	11.63	8.28
EF=+E-MB	0.79	-6	9.02	-5.38
S(SNT)	2.76	6.57	5.54	-0.22
E	8.29	3.17	15.12	3.12

All inductance values are in μH.

Table 3-6: Mutual inductances between simplified PF coils circuits and important in-vessel points. See **Figure 3.13** for description of the simplified circuits.

3.2 COMPASS stray magnetic field

This section is an extended form of part of the article Havlicek et al., *Characterization of Magnetic Fields in the COMPASS Tokamak* [35]. In comparison with the original article, more information is provided and updated figures are used.

Tokamaks create magnetic field not only in the plasma area inside the vacuum vessel but also in the vicinity of the tokamak. This stray magnetic field does no useful work and often causes problems for systems and structures around the tokamak. The stray magnetic field has to be taken into account even when the tokamak building is constructed. The floor in the circle around the COMPASS tokamak is made from steel reinforced concrete, but the steel bars are not welded together - they are insulated and tied together with plastic cable ties. This solution prevents existence of closed metallic circuits in the concrete floor and induced currents which could affect tokamak plasma.

The computation of the COMPASS stray magnetic field was motivated by the fact that some auxiliary systems require stray magnetic field lower than certain threshold. The first request on information about maximal possible stray magnetic field came from a manufacturer of the Neutral Beam Injection system (*Urban et al.*, [15]), which requires B less than 20 mT in the vicinity of the ion source (R = 3 m). Calculated stray magnetic field had to be known when position and shielding of the ion source were designed.

It was requested to compute the worst case scenario, i.e. the maximal possible value of the stray magnetic field in each spatial point. The computation of the stray magnetic field was performed only for the SFPS-SND configuration. Maximal currents flowing through the PF coils circuits in this simulation were selected: 16 kA for the MFPS, 16 kA for the EFPS, 12 kA for the SFPS-SND circuits, 3 kA for the

BR, 5 kA for the BV and 400 kA for the plasma current (which is marginally more than maximal achieved I_{pl} = 350 kA). Directions of the currents in individual circuits and in plasma were selected to maximize the magnitude of computed magnetic field vector in each spatial point individually. Therefore the calculated values of the stray magnetic field should be understood as the maximal envelope of realistically achievable magnetic field, because the selected combination of directions of currents is not necessarily possible from the plasma physics point of view.

The stray magnetic field was computed only from the PF coils and from the plasma column represented by a single wire in the vacuum vessel centre (R = 0.56 m, Z = 0 m). Toroidal component of the magnetic field created by the Toroidal Field coils was not included into the computation. Exact positions of different windings in the PF coils belonging to different circuits were neglected and positions of PF coils centres were used instead, i.e. the calculation used less precise positions than in Section 3.1.5.

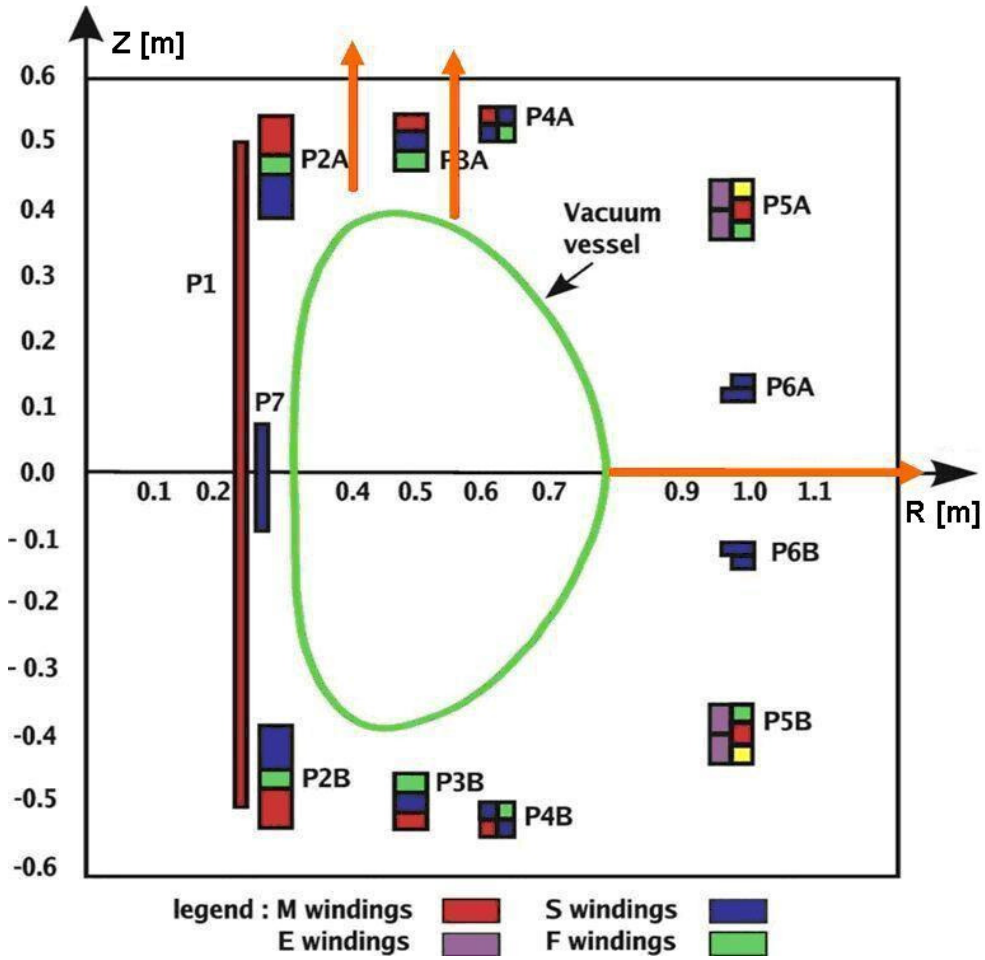

Figure 3.27: Poloidal plane cut of the tokamak. Different windings in the PF coils (P1-P7) are distinguished by colors. M, E, S and F windings are historical markings – actually used circuits use various windings, see Section 3.1.3. The orange vectors show where stray magnetic field was computed.

The calculation of the stray magnetic field was performed for spatial vectors starting at the location of three COMPASS vacuum vessel ports (see **Figure 3.27**):

1. horizontal (radial) direction at the midplane (Z = 0.0 m). The vessel ends at R = 0.792 m. The spatial vector starts inside the port H (Horizontal). The results are in the **Figure 3.28**.
2. vertical (upward) direction at R = 0.4 m. The ports VUI (Vertical Upper Inner) located at R = 0.4 m, Z = 0.44 m. The results are in the **Figure 3.29**.
3. vertical (upward) direction at R = 0.56 m. The ports VUC (Vertical Upper Centre) located at R = 0.56 m, Z = 0.4 m. The results are in the **Figure 3.30**.

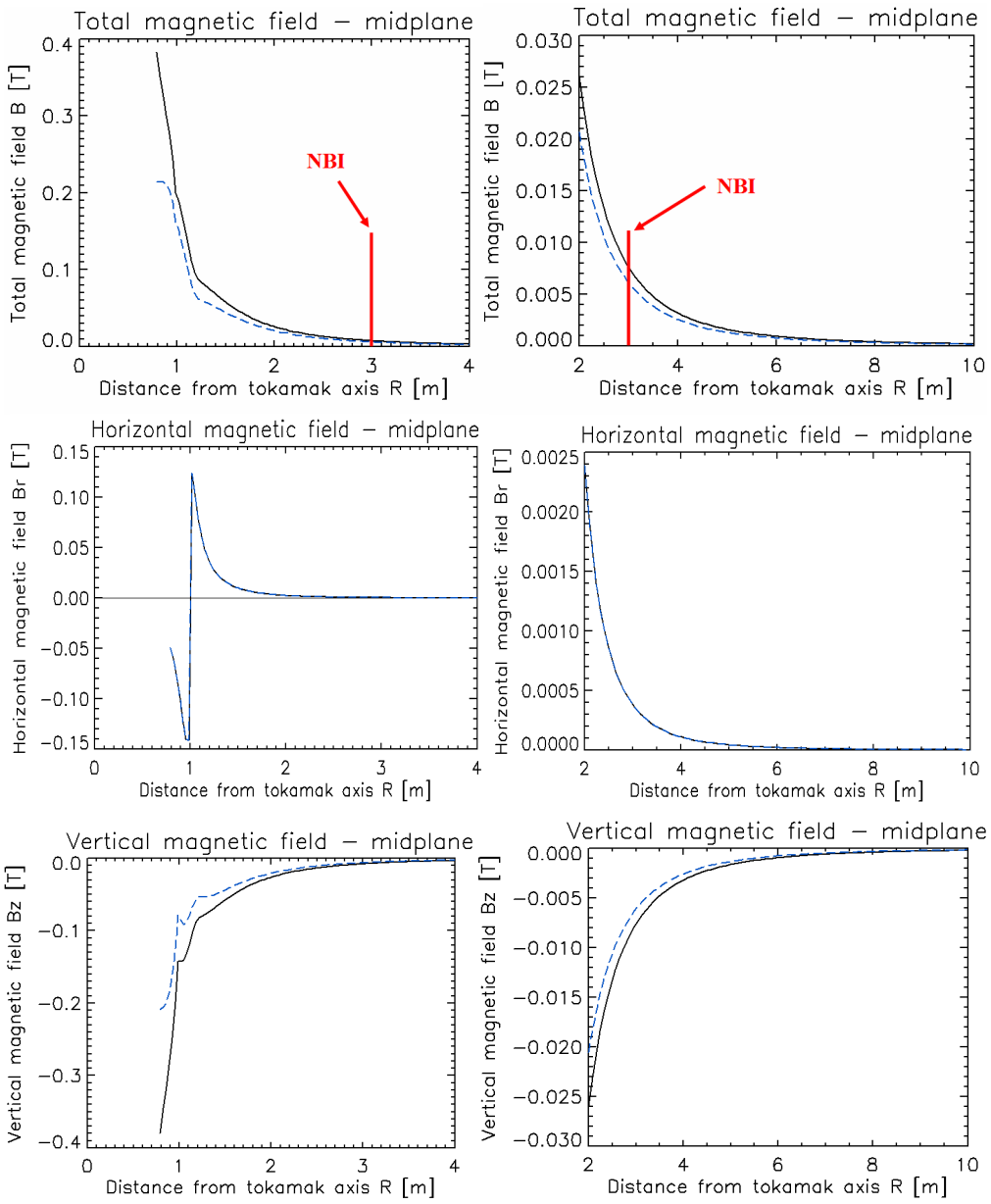

Figure 3.28: Stray magnetic field – horizontal spatial vector at Z = 0.0 m, midplane. Top row: total magnitude B, middle row: horizontal component of $\vec{B}$, bottom row: vertical component of $\vec{B}$. Left column: from centre to 4 m, right column: from 2 m to 10 m. The vessel ends at R = 0.792 m. Neutral Beam Injection (NBI) is located at R = 3 m. Black full line – with plasma current, blue dashed line – without plasma current.

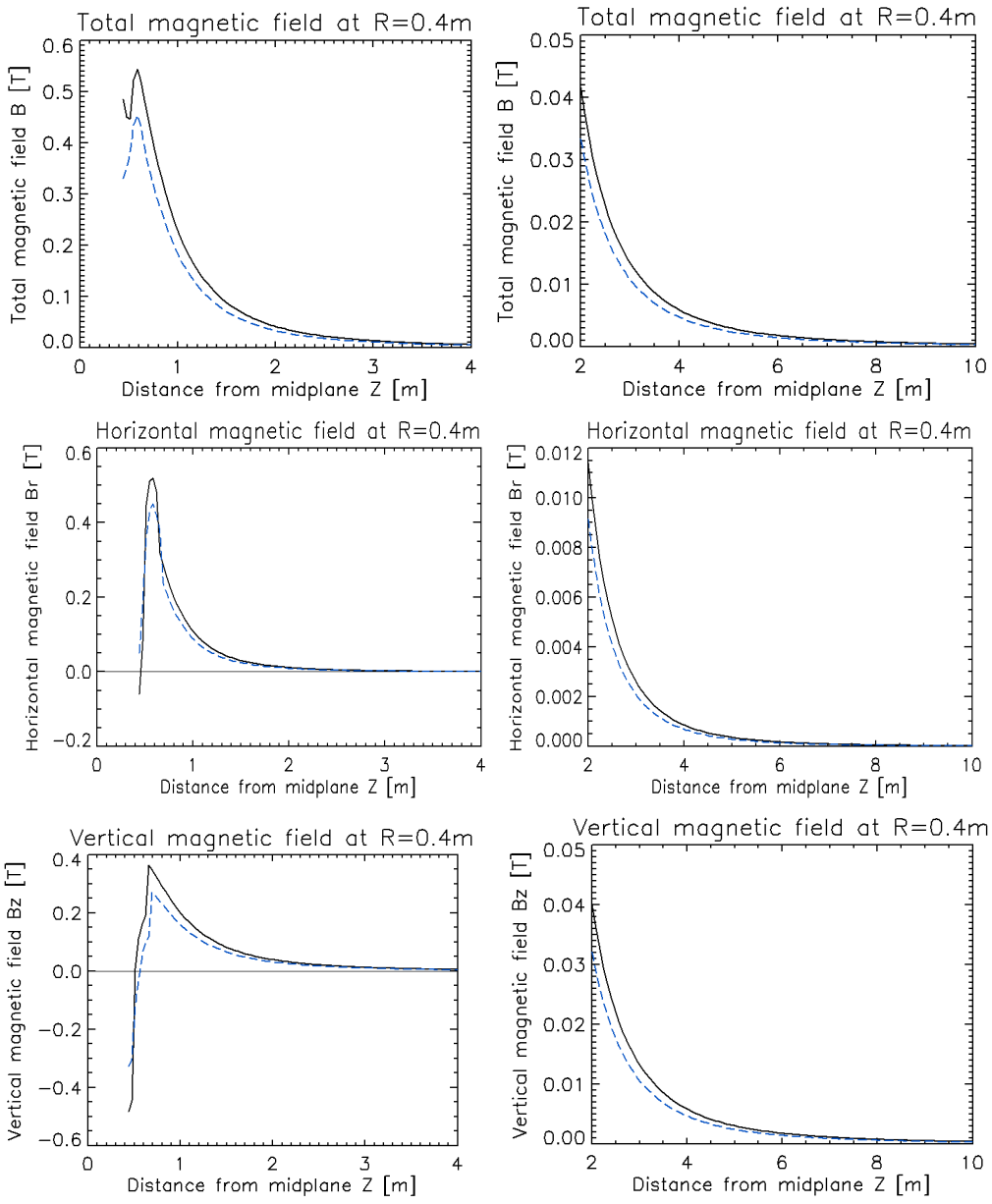

Figure 3.29: Stray magnetic field – vertical (upward) spatial vector at R = 0.4 m. Top row: total magnitude B, middle row: horizontal component of $\vec{B}$, bottom row: vertical component of $\vec{B}$. Left column: from midplane to 4 m, right column: from 2 m to 10 m. Ports VUI located at R = 0.4 m, Z = 0.44 m. Black full line – with plasma current, blue dashed line – without plasma current.

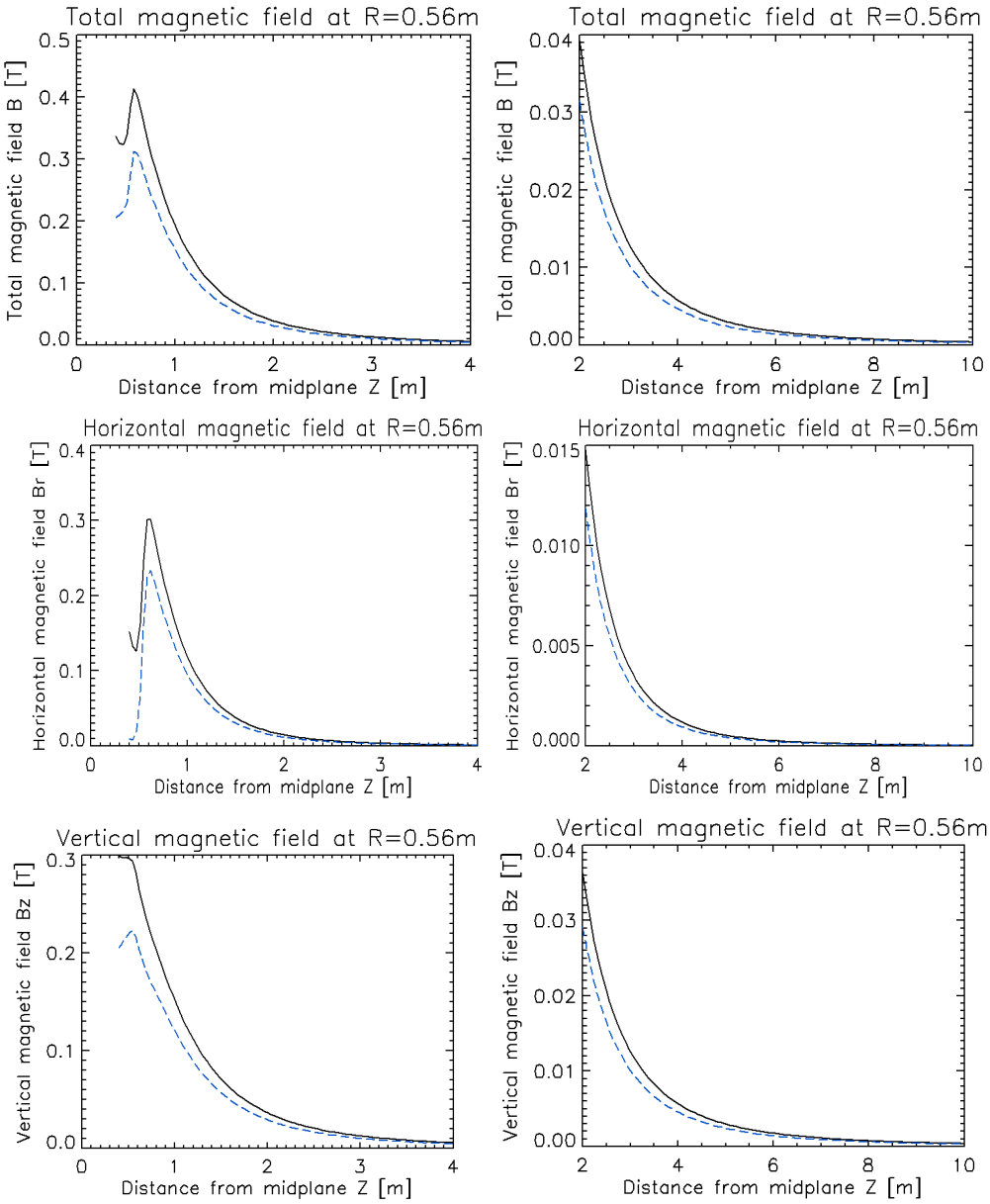

Figure 3.30: Stray magnetic field – vertical (upward) spatial vector at R = 0.56 m. Top row: total magnitude B, middle row: horizontal component of $\vec{B}$, bottom row: vertical component of $\vec{B}$. Left column: from midplane to 4 m, right column: from 2 m to 10 m. Ports VUC located at R = 0.56 m, Z = 0.4 m. Black full line – with plasma current, blue dashed line – without plasma current.

The results of the calculation show that stray magnetic field on the midplane (**Figure 3.28**) is significant even outside of the TF coils (R > 1.25 m) - vertical component of $\vec{B}$ is 75 mT and horizontal component is up to 20 mT. Farther from the tokamak the horizontal component becomes less important and vertical component is dominant. That is to be expected because the majority of the COMPASS tokamak magnetic fields are top-down symmetrical and from afar vertical: MFPS circuit field, EFPS circuit field and BV circuit field are fully vertical,

magnetic field from plasma is vertical in this simulation and nearly vertical in reality (diverted plasma is often moved above the midplane). **Figure 3.28** had also shown that the maximal possible stray magnetic field at the position of the NBI ion source is less than 8 mT, therefore the design of the NBI system did not require any changes.

Figure 3.29 and **Figure 3.30** show stray magnetic field above the tokamak on the radial location of two diagnostic ports. The ratio of the horizontal and vertical components of $\vec{B}$ is higher than on the tokamak midplane and the horizontal component is significant even farther from the tokamak. The calculated stray magnetic field in this area influenced for example placement of the turbomolecular vacuum pump of the vertical reciprocating probe drive. The particular type of the turbomolecular pump required smaller magnetic field and the pump had to be placed behind ~ 1 meter long vacuum pipe to avoid the area with the highest stray field.

The simulated stray magnetic fields were also used in design of the shielding system of the Lithium Beam diagnostics [33].

3.3 Power Supplies filtering

This section is extended form of the article Havlicek et al., *Design and Preliminary Results of the COMPASS Power Supplies Filters* [59]. In comparison with the original article, a description of new Power Supplies and more detailed filter description and discussion were added.

The COMPASS tokamak currently uses eight circuits (five PF coils circuits, one TF coils circuit, two Resonant Magnetic Perturbation - RMP - coils circuits) of the magnetic field coils to control and influence the plasma. There are five types of Power Supplies ([37], [38], [39], [Attached publication A1]) used to supply the circuits from energy stored in two flywheel generators [38]:

1) 24-pulse thyristor converter: (1440 - 2040 Hz)
   - TFPS (0 ÷ 92 kA) – Toroidal Field Power Supply for creation of up to 2.1 T magnetic field.
2) 12-pulse thyristor converters: (720 - 1020 Hz)
   - MFPS (-18 ÷ 16 kA) – Magnetizing Field Power Supply for plasma current drive and ohmic heating. At the moment the current is limited by software in the PS controller to -16 ÷ 14 kA.
   - EFPS (0 ÷ 16 kA) – Equilibrium Field PS for generating vertical magnetic field which prevents plasma column from expanding its main radius.
   - SFPS (0 ÷ 12 kA) – Shaping Field PS for shaping and creating divertor plasma configuration. At the moment (as of 11.6.2015), the current is limited by software in the PS controller to 10 kA.
3) Fast Amplifiers (FA) based on MOSFET transistor H-bridge: (40 kHz)
   - BR (+/- 5 kA) – horizontal magnetic field for fast feedback control [Attached publication A2] of the vertical plasma position.
   - BV (+/- 5 kA) – vertical magnetic field for horizontal plasma position feedback.
4) Vertical Kicks Power Supply (VKPS): (intermittent frequency up to 4 kHz)

- In series with FABR in the BR circuit, +/- 5 kA. It is powered from the capacitor bank and intended for ELM (Edge Localized Mode) pacing by "kicking" with plasma vertical position. Increase of allowed frequency to 6 kHz is foreseen for future.

5) RMP Power Supplies based on MOSFET transistor H-bridge: (40 kHz)
   - Two electrically independent (!) circuits [60] of Resonant Magnetic Perturbation coils for creation of ergodic layer at the edge of the plasma with intention of influencing ELMs. The design is similar to Fast Amplifiers, but used VMM 300-03F transistors have higher allowed voltage (either 140 V or 190 V operation voltages are available, depending on transformer taps connections).

All of these Power Supplies are in principle switched-mode power supplies with sharp changes in the voltage applied to the tokamak coils (see **Figure 3.31** for simplified explanation). The tokamak coils are mostly inductive loads with self-inductances in the range of 50 - 3000 μH and resistances in the range of 2 - 50 mΩ (see **Table 3-1** in Section 03.1.6 or **Table 3-7**). Due to the magnitude of the self-inductance the current ripple generated by repetitive voltage changes of the switched-mode power supplies is generally low (less than 1 % for thyristor converters for typical current values). Nevertheless this current ripple still poses a problem because it generates a significant noise in multiple diagnostics [17].

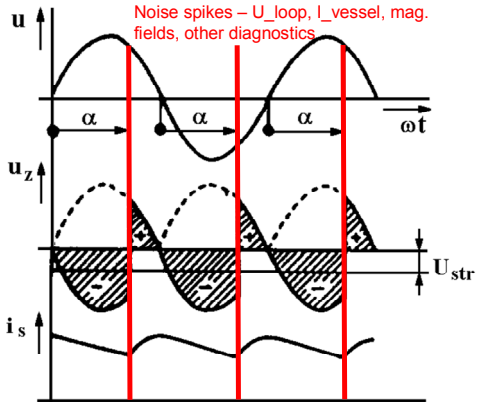

Figure 3.31: One phase of thyristor converter (regulation angle > 90˚ for negative effective voltage at the output). 12 - pulse converter uses six phases. Current ripple causes noise peaks in tokamak signals.

There are two major reasons for the noise in diagnostic measurements. The first one is the grounding of many diagnostics - specifically the diagnostics grounded to the tokamak vacuum vessel where an induced current is flowing. This current is generated inductively by the tokamak coils and reaches up to 40 kA during plasma current breakdown and then ~ 3 kA ripple with frequency of the 12-pulse converters during the plasma flat-top phase. The second source of the noise is direct inductive coupling between tokamak coils and various diagnostics - this can be coupling to the electronic circuits, coupling to the data cables (usually twisted shielded pairs or coaxial cables) or coupling to diagnostic coils in case of magnetic diagnostics.

The COMPASS tokamak uses two flywheel generators to provide energy for the Power Supplies [38]. The maximal rotation speed of the flywheels is 1700 rpm and the flywheels can slow down to 1200 rpm. Corresponding frequency of the 24-pulse thyristor converter is changing during the discharge from 2040 Hz (24 x 3 x 1700 rpm / 60 s) to 1440 Hz (or 1020 Hz to 720 Hz for 12-pulse converters feeding PF coils). It should be noted that the flywheels can start the discharge from lower than maximal rotation speed and 1400 rpm is commonly used.

Two Fast Amplifiers [Attached publication A1] are H-bridges based on MOSFET transistors with Controller Unit which uses fixed frequency (40.138 kHz) to apply positive or negative voltage (100 V) to the load, based on the requested and internally measured current.

The Vertical Kicks Power Supply [Attached publication A1] is supplied from the capacitor bank charged by a small auxiliary charging system before the plasma discharge. The VKPS is designed to operate at 1200 V and uses modern high current IGBT transistors FZ3600R17HP4. This Power Supply should not be filtered because any filter would interfere with intended "kicks" to the plasma column vertical position.

Recently designed and manufactured RMP Power Supplies were not described in any published work and brief description of the design is provided here. The two RMP PSs are constructed as H-bridge, each is composed from 30 MOSFET modules IXYS VMM 300-03F. Each half-bridge module is rated up to 300V. Each transistor has two snubber capacitors PMC-30uF/330V-VP 10 %, the main power is provided through the capacitor bank made from 60 EPCOS capacitors B43750A4538M003 with 5,3mF/350V each. The rectifier supplying the main capacitor bank is manufactured from 6 diodes DZ1070N. The drivers for the MOSFET modules were designed by IPP contractor (same as the overall design of the RMP PS), manufactured by IPP Prague and are controlled by in-house developed FPGA based controller which is fully electrically disconnected from the PS by HFBR optical elements. An important feature, added after gaining experience with the FAs, is over-current protection implemented in individual power transistor drivers. In the case that one power transistor fails and controller switches on a group of 15 opposite transistor modules, the entire group of 15 modules would be destroyed without this protection.

This section describes design and preliminary measurements of filters for all four thyristor converter Power Supplies. Filters for two Fast Amplifiers are not yet designed. Filters of two RMP PSs were designed and are used, but are not described in this thesis.

3.3.1 Filter principle

The principle of the filters will be explained on the EFPS circuit using measurements of the temporary testing filter unit manufactured for validation of the concept. The basic idea is to use a standard LC filter, however capacitor of such filter creates an oscillating LC circuit together with tokamak coils. These oscillations must be suppressed by a damping resistor which is in parallel with the capacitor.

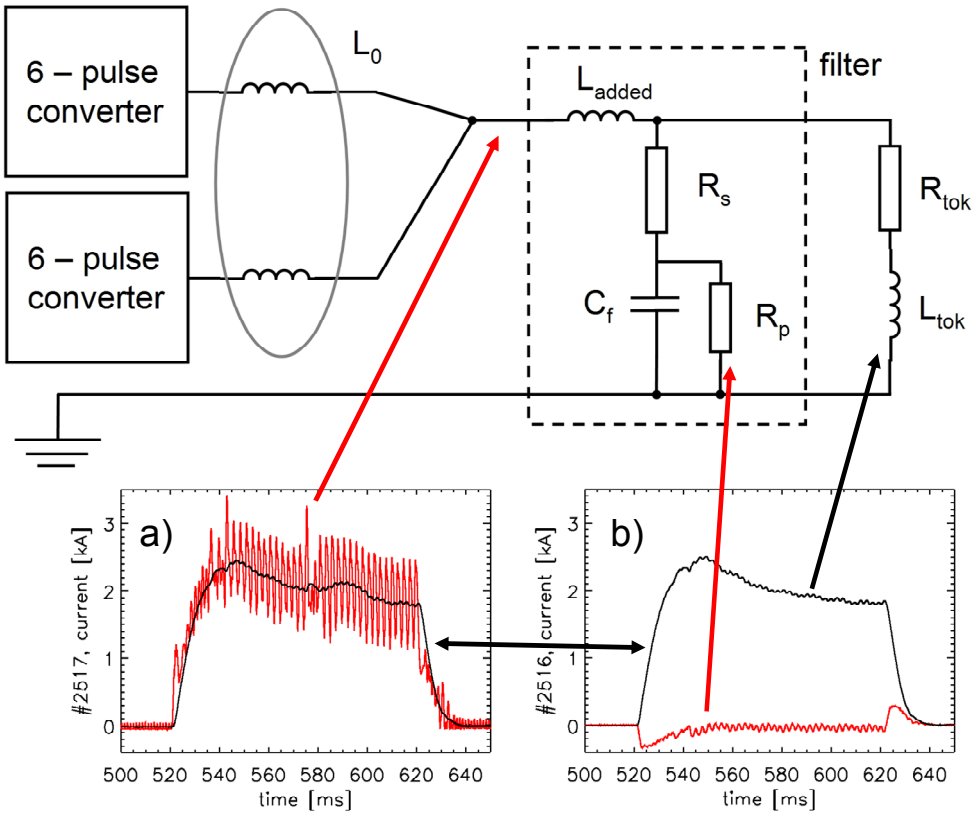

Figure 3.32: Filter principle for 12-pulse converter, a) shot #2517, 720-1020 Hz current ripple (red line) passes through choke coils L_0 and L_{added} to capacitor C_f which filters the current to tokamak coil (black line), b) shot #2516, current in the damping resistor R_p (red line), current in the tokamak coil (black line). Both cases for L_{added} = 0 µH, C_f = 4.2 mF, R_S = 75 mΩ and R_p = 1 Ω used in the temporary testing filter.

Two 6-pulse thyristor converters are supplied from three phase transformer (not depicted in the **Figure 3.32**) with two secondary windings - one in triangle, one in star configuration - providing six phase shifted voltage sine waves. The two 6-pulse thyristor converters are connected in parallel through two choke coils (each 45 µH, effectively L_0 = 22.5 µH) to tokamak EFPS circuit and the Decoupling Transformer EF-BV (temporary variant with high primary winding resistance 10 mΩ, described in Section 3.1.6) which forms together a circuit with R_{tok} = 26.5 mΩ and L_{tok} = 1450 µH (exact calculated values in the **Table 3-1** are slightly lower).

The filter consists of the capacitor C_f, series resistor R_S and parallel damping resistor R_p. The higher frequencies of the voltage generated by the converter create a current which can pass through the choke coils L_0 and L_{added} and capacitor C_f (**Figure 3.32a**, red line) while lower frequencies current is applied to the tokamak coils. Part of the converter current also goes into through L_0+L_{added} and the damping resistor R_p (**Figure 3.32b**, red line) effectively lowering the current available for the tokamak coils. The effective voltage applied to the tokamak coils U_{tok} consists of converter

voltage U_{conv} (switched, sharp changes) and voltage generated in the choke coils L_0 and L_{added} by the passing current:

$$U_{choke} = (L_0 + L_{added})\frac{\mathrm{d}(I_{filter} + I_{tok})}{\mathrm{d}t}. \tag{3.36}$$

Considering the fact that the high frequency part of the current passes through the filter, the resulting U_{tok} is smoothed in comparison to U_{conv}. In principle this is a standard LC filter, which is discussed in all basic electronics textbooks, but an oscillation problem of inductive load must be solved by adding the damping resistor R_p to satisfy stability criterion for LC filter.

The black lines (filtered current) in the **Figure 3.32a, b** and black lines (filtered current) and red lines (unfiltered current) in the **Figure 3.33** show various realizations for requested tokamak current (2kA, 100 ms long rectangular pulse) during tests of the temporary filter unit.

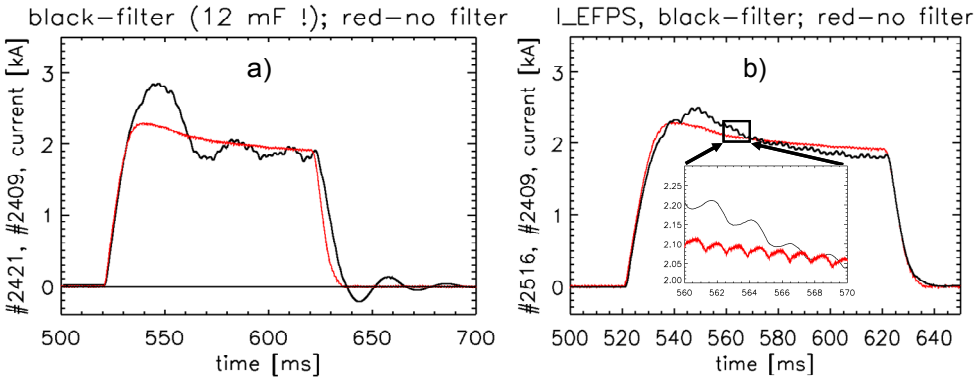

Figure 3.33: a) I_{tok} with higher capacity (12 mF) and no damping resistor leads to ~26 ms oscillations (filter: shot #2421, no filter: #2409), b) test without L_{added}, C_f = 4.2 mF, R_p = 1 Ω, R_S = 75 mΩ (shot #2516) leads to smoother current in tokamak coil when compared with unfiltered (shot #2409).

Figure 3.33a shows an experiment with higher capacity and disconnected damping resistor R_p. The black line shows oscillations of the tokamak current in comparison with unfiltered tokamak current (red). The oscillations have a period of $T = 2\pi\sqrt{L_{tok}C_f} = 26\,\mathrm{ms}$. This experiment clearly demonstrates the necessity of the damping resistor R_p even though the resistor lowers the power available for tokamak coils.

Figure 3.33b shows direct comparison between unfiltered tokamak current (red line) and current filtered by the testing filter unit (black line). It should be noted that smooth oscillations on the filtered current are exaggerated by the incorrect regulation. During these tests the control of the current was incorrect because the EFPS converter controller discretely measured current in the converter and did not take into account current flowing into the filter. In the final realization the filter current is measured by Hall sensor LT 4000-S/SP34 and provided to the controller to have correct regulation of the current flowing into tokamak coils.

3.3.2 Performed filter simulations

The actual filters for the TFPS, MFPS, EFPS, and SFPS circuits Power Supplies were designed after extensive simulations to achieve optimal performance with given constraints. The desired parameters of the filters were: 1) minimal achievable distortion of the circuit current response to the rectangular requested current pulse and 2) maximal suppression of the current ripple (1 kHz or 2 kHz). The constraints were:

- use of the available capacitors MKK B25650 with capacity 4.2 mF, U_{max} = 2.5 kV, $I_{steady,max}$ = 410 A
- financial limit to the overall cost - mostly limits possibility to add choke coils L_{added}
- spatial limit in the assembly area
- manageable power load of the damping resistor R_p, which limits its lowest value for given Power Supply maximal voltage

The simulations will be described on the EFPS filter example. The 5Spice Analysis Software [61] was used for initial filter design and then the results were confirmed by the Power Supplies manufacturer in the more realistic Matlab Simulink model with full description of the converter including control loop [62].

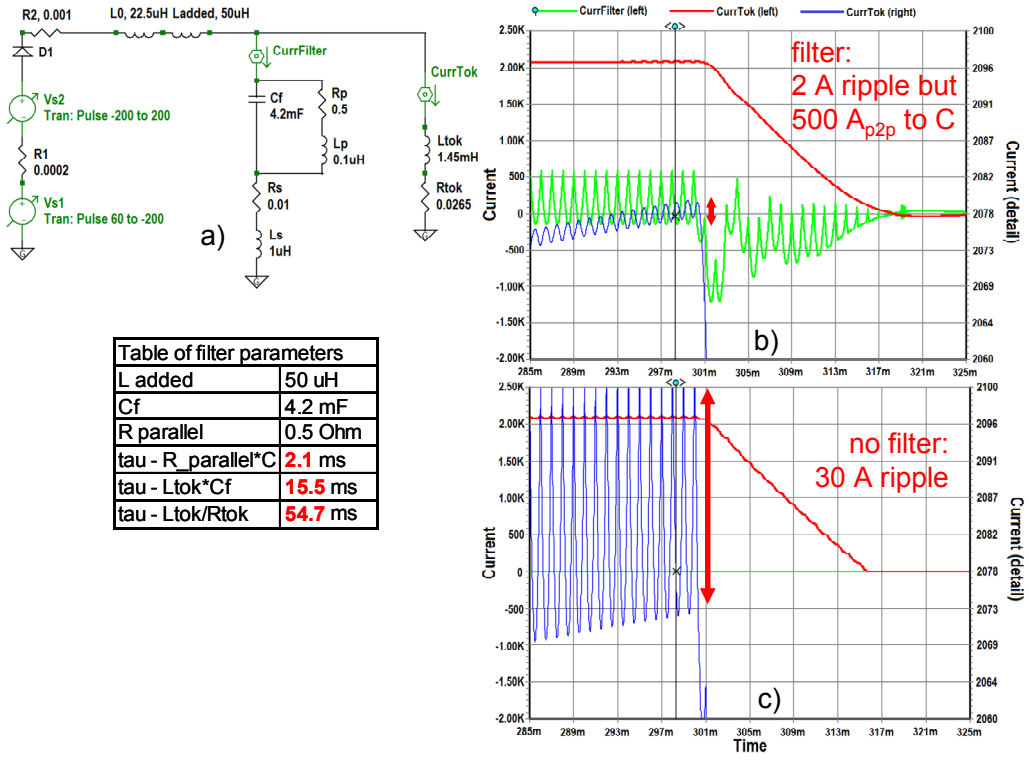

Table of filter parameters	
L added	50 uH
Cf	4.2 mF
R parallel	0.5 Ohm
tau - R_parallel*C	2.1 ms
tau - Ltok*Cf	15.5 ms
tau - Ltok/Rtok	54.7 ms

Figure 3.34: 5Spice Analysis Software was used to simulate all circuits, the EFPS circuit is shown. a) Schematics, b) EFPS circuit current with filter, c) without filter.

Figure 3.34 shows schematics (a) of the EFPS circuit with the filter. The schematics contains simplistic approximation of the converter in the form of DC voltage with superimposed 1 kHz triangular voltage, coils L_0 and L_{added}, filter with

added parasitic inductances L_p and L_s to test the sensitivity to such parameters, and tokamak coils L_{tok} with R_{tok}.

Table of filter parameters in the **Figure 3.34** summarizes the values of the selected electrical parts in the filter and time constants of the different parts of the entire circuit. The reaction speed of the EFPS circuit is determined by the tokamak coils inductance and resistance (RL circuit, time constant 54.7 ms) and by available voltage of the converter (line to line effective voltage 280 V in the transformer of the EFPS, converter controller software limits [63] and transformer u_k decreases the available voltage). The reaction speed is not significantly influenced by the filter design because tokamak coils have inductance much larger than L_0 and L_{added}. The filter capacitor creates oscillating LC circuit with tokamak coils with time constant 15.5 ms. These oscillations would negatively influence plasma control and must be dampened. This is achieved by using the damping resistor R_p which creates RC circuit with the capacitor C_f. The time constant of the RC circuit R_p x C_f (selected 2.1 ms) must be much smaller than the time constant of the LC circuit. This is one constraint in the filter design.

Another constraint in the filter design is power dissipated in the R_p resistor. The EFPS filter uses 0.5 Ω, which can be loaded with effective 255 kW when EFPS converter provides its maximal effective voltage of 356 V ($= 280\,V \cdot \sqrt{2} \cdot 0.9 \cong 280V \cdot 3/\pi \cdot \sqrt{2} \cdot 0.9$).

Choke coil L_{added} increases inductance of the already used choke coils (two 45 μH parallel coils = 22.5 μH). The higher value of L_{added} results in better filtration and the value is limited mostly by financial consideration. The reaction speed of the entire circuit (54.7 ms) is not significantly lowered as long as the tokamak coils have much larger self-inductance than the choke coils.

Figure 3.34b and **Figure 3.34c** show circuit response to the current request jump from 2 kA to 0A (red line, left axis and its detail: blue, right axis) together with current to the filter (green line, left axis). It is visible that the current ripple without the filter is ~ 30 A_{p2p}, while the decrease of the current from 2 kA to 0 A is 15 ms long. The filter decreases the current ripple significantly and the response to the current jump is reasonably undisturbed.

The final design of the EFPS filter uses C_f = 4.2 mF consisting of 2x2 capacitors MKK B25650 (each 60 kg, 4.2 mF, 2.5 kV, 410 A), resistance R_p = 0.5 Ω (rated for 300 kW/1sec then 10 minutes pause, 31 kg) and L_{added} = 50 μH (choke coil TLV 56/29, 20 kA/1sec then 10 minutes pause, 155 kg, 1000 V).

3.3.3 Preliminary measurements

Preliminary measurements of the filters influence on diagnostics signals are presented in this section. Loop voltage measured by the flux loop (toroidally wound wire) is the best to show the filter influence as it is directly proportional to the derivative of any toroidal current - PF coils current, induced toroidal current in the vacuum vessel or the toroidal component of the induced poloidal current flowing in

the vessel around the vacuum vessel ports. The poloidal current can be generated by changes of TF coils current.

Figure 3.35 shows a loop voltage measured by Flux Loop #4 located on the High Field Side (R = 0.325 m, Z = 0 m). There are three cases depicted:

1. "only TF filtered" - MF, EF and SF circuits are running and are not filtered while TF coils are filtered. Voltage structures with 840 Hz frequency (1400 rpm, 12-pulse) are visible while 1680 Hz voltage peaks from TF switching are suppressed.
2. "no filter" - all circuits are running without filter, both types of voltage structures and peaks are present.
3. "TF remains" - TF coils are unfiltered while all PF circuits with exception of EFPS are disconnected. EFPS is filtered by the temporary testing filter unit. 1680 Hz voltage peaks are visible while 840 Hz voltage structures are suppressed.

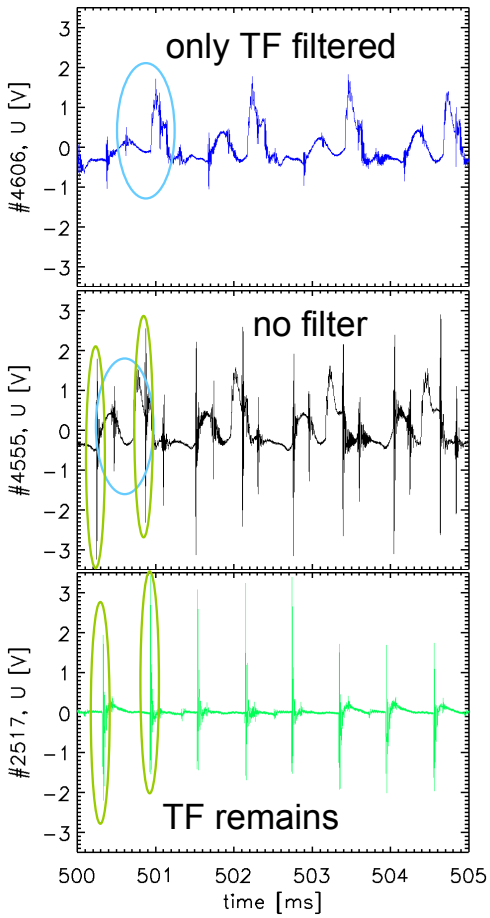

Figure 3.35: Loop voltage measured by the Flux Loop #4 on the HFS, all circuits currents are zero during the measurement (the worst case scenario for thyristor converter – the highest noise). The 840 Hz and 1680 Hz structures are marked by ellipses.

These preliminary measurements show good improvement in the noise observed by the loop voltage. It should be stated that magnetic signals are not the only signals influenced by the Power Supplies current ripple. The probe measurements are particularly sensitive to this type of noise (but mostly from Fast Amplifiers and RMP Power Supplies) and some of the bolometry channels are also affected.

3.3.4 Status of the filters realization

The thyristor Power Supplies filters were designed, manufactured and installed. The **Table 3-7** summarizes parameters of the Power Supplies and PF coils circuits (converter transformer line to line voltage U_{LL}, effective self-inductance of the parallel choke coils L_0, self-inductance L_{tok} and resistance R_{tok} of the circuit), parameters of the designed filters (added inductance L_{added}, capacity of the filter C_f,

series-parallel configuration of capacitors, resistance of the damping resistor R_p, peak dissipation power of the damping resistor $P_{parallel}$ and series resistor R_S) and optimized time constants of parts of the circuits.

Note that the damping resistors have very high dissipation power. The resistors are made from meander shaped cast metal and have mass sufficient to contain the dissipated energy during the tokamak pulse and release it between the pulses.

Power Supply	TF	EFPS	SFPS	MFPS
U_{LL} [V]	370	280	540	700
L_0 [μH]	5.5	22.5	35	50
L_{tok} [μH]	2500	1450	760	3000
R_{tok} [mΩ]	2.7	26.5	40.7	37
L_{added} [μH]	10.5	50	100	50
C_f [mF]	6.3	4.2	2.8	2.8
configuration of C_f	2x3	2x2	3x2	3x2
R_p [Ω]	1	0.5	0.8	1
R_s [mΩ]	10	10	10	10
$P_{parallel}$ [kW]	250	286	664	893
tau R_p*C_f [ms]	6.3	2.1	2.24	2.8
tau L_{tok}*C_f [ms]	24.9	15.5	9.2	18.2
tau L_{tok}/R_{tok}[ms]	925.9	54.7	18.7	81.1

Table 3-7: Parameters of the filters of the thyristor Power Supplies. EFPS and SFPS self-inductances with the decoupling transformers accounted. The SFPS is in SND configuration (worse noise and more difficult filtering than SNT). U_{LL} is line to line effective voltage of the converter transformer. Note that L_0 does not include effective inductance of the converter calculated from u_k transformer parameter, which adds ~ 20 % to L_0.

All individual filters were tested together with their respective Power Supply with exception of the MFPS filter (due to the time constraints in COMPASS operation and availability of experts from Power Supplies manufacturer).

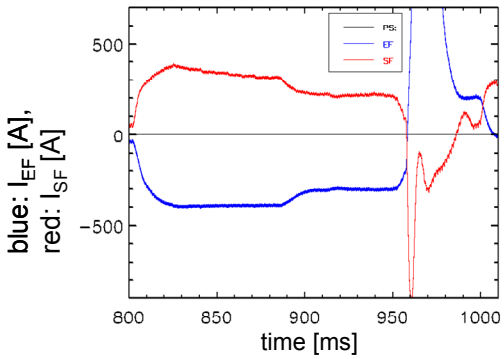

Figure 3.36: Cross-talk caused by MFPS current in the EFPS and SFPS circuits. Shot #4605, MFPS had requested current -14 kA between 800 ms and 950 ms.

A cross-talk problem between individual PF circuits was discovered - e.g. current in the MFPS circuit generates current going through the EF coils and the EFPS filter (see **Figure 3.36**). The cross-talk was not anticipated because all circuits were modelled individually. The reason for the cross-talk is electrical and inductive connection between the individual Power Supplies (**Figure 3.13**) in the MB winding. The individual controllers are not capable of compensating voltage generated from other Power Supplies to the same degree as without the filters, particularly $R_{parallel}$.

A possible solution to this problem is to provide the controllers of individual Power Supplies with information about current generated by other supplies. Then the controllers can adjust their voltage immediately without any delay caused by the PID controller reacting to the regulation error of the current.

Another possibility is to partially disconnect the individual circuits by diodes.

The least preferred solution is to lower the capacity and increase the $R_{parallel}$ of the designed filters, which would reduce the problematic cross-talk and allow controllers easier reaction.

The solution of the cross-talk problem delayed putting the filters into service. Only the TFPS filter is used now (see **Figure 3.37**), even the though filters were installed in the year 2013.

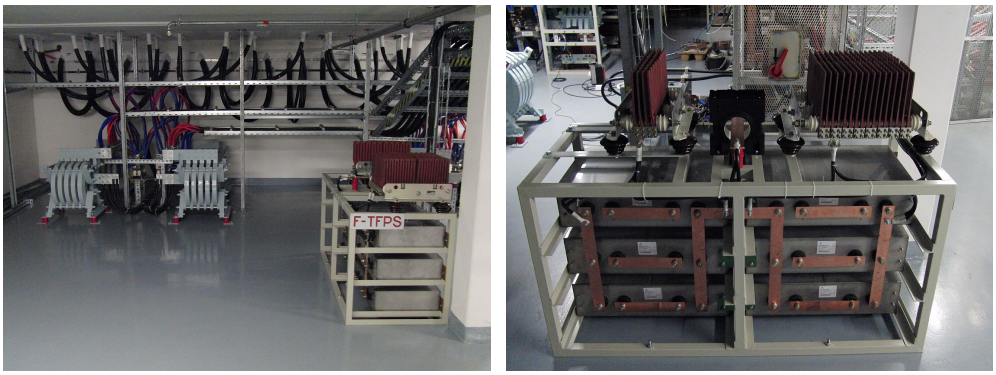

Figure 3.37: TFPS filter. Left panel: two from four parallel additional choke coils are visible in the back, filter in front, right. Right panel: TFPS filter: six capacitors in the metal frame, meander resistors R_p and R_s on the top, Hall sensor LT 4000-S/SP34 in the middle.

3.4 Simulation of the EFPS PID controller

This section is an extended form of the article Havlicek et al., *A Simulation of the COMPASS Equilibrium Field Power Supply PID Controller* [63]. In comparison with the original article, redundant information covered in previous sections of this thesis was removed and a wrong value of the EFPS maximal voltage was corrected. The description of the basis angle *akK* was also altered. Note that this simulation was performed before the PS filters, described in the previous section, were designed and the filters are not incorporated in the simulation. Nevertheless the description of the controller as well as description of the mutual influence of the unfiltered Power Supplies circuits is still valuable.

The COMPASS tokamak thyristor Power Supplies (TFPS, MFPS, EFPS and SFPS circuits) have individual control units which ensure safe operation and use a PI regulation with protective ramps to achieve currents requested by the higher level tokamak control system MARTe [Attached publication A2], [55], [56].

The individual control units do not have the information about currents flowing in the other circuits and that prevents them from adjusting for the voltage generated by mutual influence of the circuits. This influence is caused by mutual inductance of the circuits as well as electrical connection between some of the circuits.

The coupling between Magnetizing Field and Equilibrium Field Power Supplies is of particular concern because the influence is very significant. The voltage induced in the Equilibrium Field circuit during plasma breakdown phase is comparable to the voltage used by its Power Supply. As a result, the radial position of the plasma column is difficult to control for short time after the breakdown, because the main vertical magnetic field (created by EFPS circuit) has limited dynamic response to requests from the tokamak control system MARTe. This section describes the mutual influence between the MFPS and EFPS circuits, its use for modelling the EFPS circuit and improvements implemented in the controller algorithm.

3.4.1 Description of Power Supplies mutual influence

The Magnetizing Field, Equilibrium Field and Shaping Field circuits are coupled together by mutual inductance and by shared winding M1 (=MB) in the tokamak central solenoid (see **Figure 3.38**, which is for convenience reprinted **Figure 3.13**).

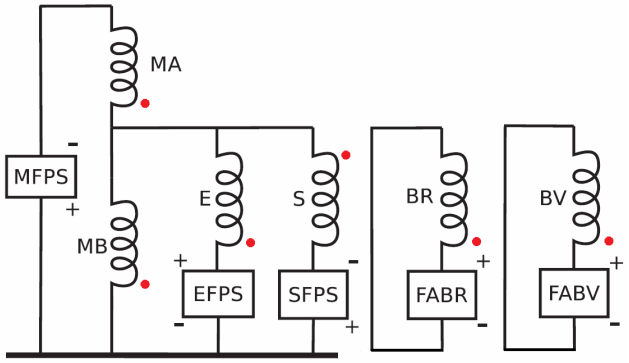

Figure 3.38: Reprinted **Figure 3.13**: Simplified connection of the Power Supplies. When using this simplification, configuration of the SFPS should be specified. Decoupling transformers and PS choke coils are not depicted. Adjusted from attached article [A3].

In this section we are limiting ourselves to describe the interconnection between MFPS and EFPS. The influence of the SFPS is not taken into account and all shown measurements were done with mechanically disconnected SFPS circuit. The EFPS circuit current is described by equation:

$$U_{EF} + U_{distortion} - L_{EF-EF} \cdot \mathrm{d}I_{EF}/\mathrm{d}t = R_{EF} \cdot I_{EF}\,, \tag{3.37}$$

where U_{EF} is voltage applied by the EF Power Supply, $U_{distortion}$ is distortion voltage generated by any other sources, $L_{EF\text{-}EF}$ is EFPS circuit self-inductance with decoupling transformer included (1540 μH used, see **Table 3-1**), R_{EF} is resistance of

the EFPS circuit with decoupling transformer (26.5 mΩ, **Table 3-1**) and I_{EF} is current in the EF circuit.

$U_{distortion}$ is in our case generated in the EFPS circuit by MFPS:

$$U_{distortion} = -L_{MF-EF} \cdot \mathrm{d}I_{MF} / \mathrm{d}t + R_{M1} \cdot I_{MF}, \tag{3.38}$$

where $L_{MF\text{-}EF}$ is mutual inductance between MFPS and EFPS circuit (-650 μH used, **Table 3-1**, resulting to positive $U_{distortion}$ for positive $\mathrm{d}I_{MF}/\mathrm{d}t$), R_{M1} is resistance of the shared coil M1 (=MB) (10 mΩ, **Table 3-5**) and I_{MF} is current in the MFPS circuit. The coils M1 and M6 together create the central solenoid of the tokamak (see Section 3.1.1 - Poloidal field coils geometry). Each of them has 48 turns.

3.4.2 PID controller basic principles

The proportional-integral-derivative (PID) controller is one of the simplest and the most commonly used active feedback control method [64], [65]. In this section a very brief explanation is given to provide basic understanding of its principles.

The PID controller uses "regulation error" e(t) – difference between measured process variable and requested setpoint - to calculate the "process control input". The regulation error is minimized by applying the process control input to the controlled system.

In our case the regulation error is difference between the realized and requested current $e(t) = (I_{realized} - I_{requested})$ and the process control input is the regulation angle of the thyristor converter. Then the equation describing the PID controller is:

$$reg.angle = K_P \cdot e(t) + K_I \cdot \int_0^t e(t)\mathrm{d}t + K_D \cdot \frac{\mathrm{d}}{\mathrm{d}t} e(t), \tag{3.39}$$

where K_P, K_I and K_D are parameters of the PID controller:

- Proportional term K_P: direct amplification of the regulation error. It can be viewed as a steepness of the Stabilizing potential hole created by the PID controller (see **Figure 3.39**).
- Integral term K_I: accelerates the reaction, but it can cause overshot. In the example from **Figure 3.39** it slowly moves the centre of total potential towards the desired setpoint.
- Derivative term K_D: slows down the reaction, reduces overshot, but amplifies the noise. It can be viewed as viscous fluid in the Total potential hole. It can have opposite sign to increase speed of the reaction at the expense of stability.

These parameters should be optimized to obtain the best performance of the controller for individual tokamak PS circuits. Due to the large self-inductances of the tokamak PS circuits the derivative term is not necessary to slow down the reaction.

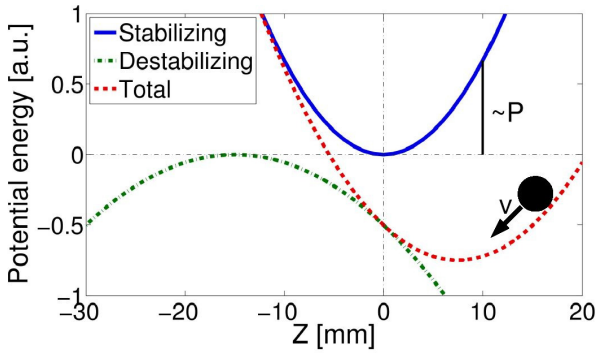

Figure 3.39: Illustration of the PID controller as "ball on the hill". The Destabilizing potential ("hill") is countered by Stabilizing potential created by proportional term of the PID controller. The Total potential has minimum at the point away from the desired setpoint (Z=0), which is solved by the integral term K_I. The oscillations of the "ball" are slowed down by K_D.

3.4.3 Description of the controller model for the simulation

The EFPS controller is a PI controller with several protective ramps used to protect the 12-pulse thyristor converter Power Supply from potential damage. The 12-pulse thyristor converter consists of two 6-pulse converters in parallel with shifted voltage phases. The regulation angle controls when the thyristor is switched on and conducts a current. Each of the three voltage phases of the 6-pulse thyristor converter module is controlled by two thyristors and each thyristor conducts current when the voltage sine wave is between regulation angle and regulation angle + 180˚ (see **Figure 3.31** in the Section 3.3). The resulting effective voltage of the thyristor converter is described by Equation (3.40).

One of the 6-pulse converters can be destroyed if the regulation angle is quickly increased, resulting into the current from the circuit moving into the converter and overloading it while the second converter is switched off by the steep change in the regulation angle. The regulation angle protective ramp can prevent this scenario.

The EFPS thyristor converter applies to the circuit the voltage:

$$U_{EF} = U_{EF\_\max} \cos(reg.angle), \tag{3.40}$$

where U_{EF_max} is 340 V. U_{EF_max} is 90 % from $3/\pi \cdot \sqrt{2} \cdot U_{LL}$, where U_{LL} is line to line effective voltage taken from **Table 3-1**.

The discrete differential form of the PI controller used by the PS manufacturer is:

$$\Delta reg.angle = K_P \cdot \left(e[k] - e[k-1] + \frac{e[k] + e[k-1]}{2T_i} \right), \tag{3.41}$$

where K_p/T_i is used instead of the K_I from the generic PID equation (3.39) and k is time index. This variant of the PID controller algorithm notation has the feature that both proportional and integral part from the Equation (3.39) are changed by changing K_p, while T_i allows change of the integral part relative to the proportional part. Equation (3.41) describing change of the regulation angle $\Delta reg.angle$ is differentiated $reg.angle = K_P \cdot \left(e[k] + 1/T_i \sum \left(e[k] + e[k-1] \right)/2 \right)$. The EFPS control

unit software, manufactured by the Power Supply contractor, uses $e[k] = (I_{measured}[k] - I_{requested}[k]) / 25000 \cdot 100$ measured in % from 25 kA and 100 % e[k] creates regulation angle 160° for $K_p = 1$ (i.e. the Equation (3.42) should have factor 1.6, when *e[k]* in % is used, to obtain reg. angle in degrees, see Equation (3.43)). The same values were used in the modelling.

A basis angle $akK = \langle 112.4^\circ; 82.4^\circ \rangle$ is used to avoid interrupted currents regime of the thyristor converter. The basis angle *akK* prevents a situation when the current is interrupted during converter voltage pulses if the load has low self-inductance. The EFPS circuit self-inductance (940 μH + 600 μH from decoupling transformer) is high enough to prevent this scenario, but the basis angle is nevertheless applied in the Power Source control unit as a safety measure. The exact value of the basis angle is tabulated and depends on actual frequency of the flywheels feeding the tokamak Power Supplies. As an approximation a value given by the following equation was used in the simulation:

$$akK = 112.4^\circ - 30^\circ \cdot \sqrt[3]{\sin\left(\frac{I_{requested}}{0.09 \cdot 25000}\right)}. \tag{3.42}$$

where $I_{requested}$ is in amps and sine is calculated from radians. Equation (3.42) is valid for $I_{requested}[A] < 0.09 \cdot 25000 \cdot \pi/2$, otherwise $akK = 82.4^\circ$.

The protective limitations of the EFPS model controller were:

- Maximal allowed regulation angle (= minimal negative voltage):135° at $I_{measured}$ < 5 % (current in % from 25 kA), 105° at $I_{measured}$ > 20 %, linear maximal allowed regulation angle between.
- Minimal regulation angle (= maximal positive voltage): 5°
- Protective ramps of the requested current (up/down): 2°/417 μs (417 μs is the control unit time step)
- Requested current protective ramps: 0.28 % / 417 μs (= 70 A / 417 μs)

The resulting regulation angle applied to the thyristor converter is sum of the basis angle $_{akK}$ and the regulation angle computed by Equation (3.41) after applying the protective limitations:

$$reg.angle[k] = reg.angle[k-1] + \Delta reg.angle[k] \cdot 1.6 + (akK[k] - akK[k-1]). \tag{3.43}$$

The model of the EFPS circuit uses equations (3.41) and (3.42) to compute the requested regulation angle, then applies the protective limitations to obtain the regulation angle with ramps. Equation (3.40) is used to compute the voltage applied by the thyristor converter to the coils and circuit current is computed by the Equation (3.37). Distortion voltage is taken from measured current I_{MF} and is computed by equation (3.38).

Using the measured current I_{MF} to compute the distortion voltage applied to the EFPS circuit is reasonable approximation only as long as the computed current of the EFPS is similar to the measured I_{EF} during the discharge when the I_{MF} was measured. The reason is that the EFPS current also influences MFPS current while the model takes into account only the MFPS circuit influencing the EFPS circuit. Nevertheless the EFPS controller algorithm can be optimized for one given $U_{distortion}$.

3.4.4 Results of comparison between simulation and measurement

The comparison of the created model with the EFPS current measured in the actual tokamak discharge is shown in the **Figure 3.40**. The requested EFPS current was linear ramp from 0 A at 951 ms to 1850 A at 957.5 ms (triangular request). The MFPS current was set to -14 kA with a quick drop to 0 A at 960 ms followed by linear ramp to 6.81 kA at 1100 ms. The EFPS current request was limited by the protective ramps. The EFPS current does not follow the request, which is caused by the strong $U_{distortion}$ induced from the quickly changing MFPS current.

The selected current scenario is favourable to be studied because the MFPS requested current is standard for the plasma breakdown phase and because the selected EFPS current request allows study of the worst case situation when the higher level tokamak control system requires to quickly slow down EFPS current rise during plasma current ramp up.

The regulation angle decreases (increasing U_{EF}) at the beginning of the discharge when the requested current is higher than the realized (or simulated) current. When the MFPS forces EFPS current to overshoot the requested current the regulation angle increases while the speed of the increase is limited by protective limits. The undesired behaviour starts when the regulation angle reaches its maximum value. It starts to decrease (the U_{EF} voltage, which is negative at the moment, increases) even though the regulation error is relatively high and still increases after t = 965ms. This is caused by the differential form of the PI controller, Equation (3.41), and the regulation angle clipping to the maximum allowed value. For the non-differential form this would not happen.

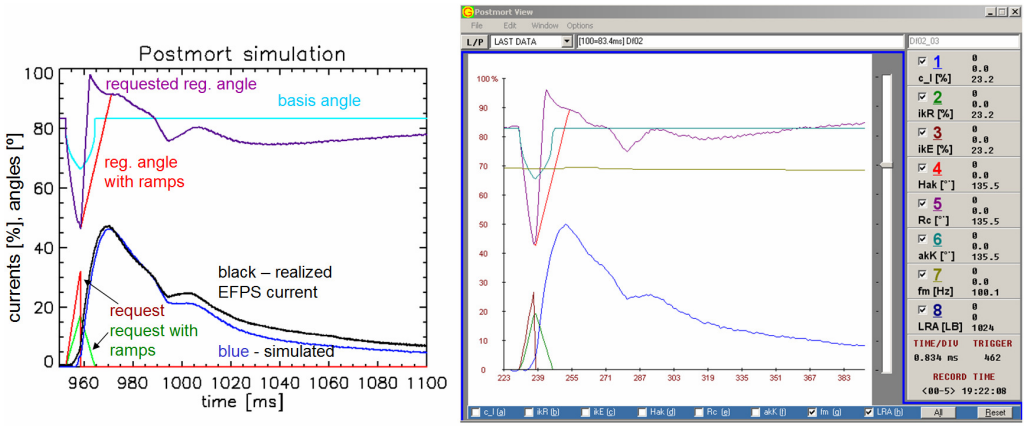

Figure 3.40: Shot #1301, K_P = 5, T_i = 60 ms. Comparison of simulated (left panel) and measured (right panel) EFPS for triangular request (*ikE*) and strong influence from starting MFPS. The right panel shows Print Screen from Postmort View – diagnostic program of the thyristor control units. Shown values are: *ikR* – realized request with ramps, *c_I* – realized current, *Rc* – requested regulation angle, *Hak* – reg. angle with ramps, *akK* – basis angle. The time axis of the right panel is in samples. Currents are shown in % from 25 kA, multiplied by factor 4.3. Angles are in ° multiplied by 100/135.

It can be seen in the **Figure 3.40** that the simulated and measured EFPS currents are almost identical. The model was able to predict correct behaviour of the PID controller and the EFPS circuit from measured I_{MF} and requested EFPS current.

The created model was used to optimize the behaviour of the EFPS controller. Relaxed protective limitations as well as adjustments to the realization of the PID controller were examined. **Figure 3.41** shows the most notable results.

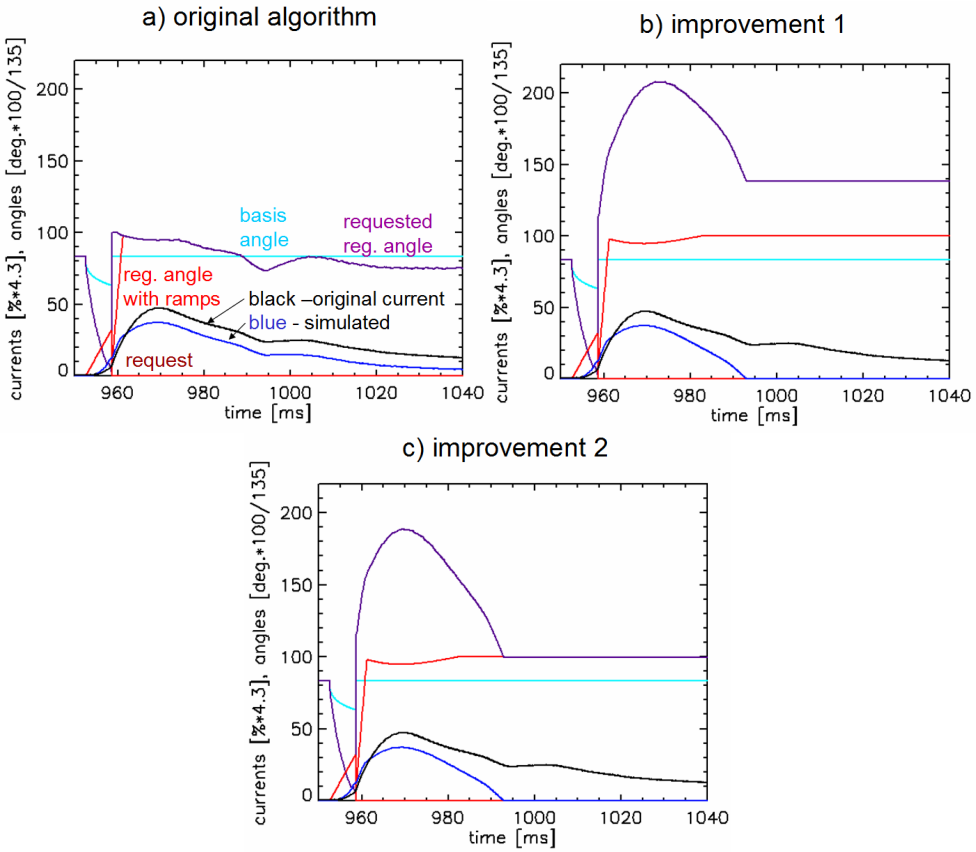

Figure 3.41: $K_P = 10$, $T_i = 40$ ms. Request current protective ramp fully removed. Regulation angle protective ramp relaxed to 20˚/417 µs. a) original algorithm, b) maximal allowed regulation angle applied to realized regulation angle and not to requested regulation angle, c) same as variant b) but integration part of the PI controller uses limited regulation error *e[k]* – 2% from 25 kA.

Figure 3.41a shows the original algorithm as described with different values of the proportional and integral terms and relaxed regulation angle protective ramp. It is compared to the **Figure 3.41b**, which has different application of the maximal allowed regulation angle limitation.

The protective limitation is applied to the realized regulation angle instead to the requested regulation angle. The result is that requested regulation angle can go much higher than is allowed to the reg. angle with ramps and the simulated EFPS current is brought to 0 A as quickly as possible. The curvature seen on the reg. angle with the ramps between 960 ms and 980 ms is caused by the dependence of the maximal

allowed regulation angle on the EFPS current. This improvement of the PID controller has a drawback as the requested regulation angle does not return to its initial value when the simulated current reaches 0 A. To mitigate this problem a further improvement can be made.

Figure 3.41c shows the identical algorithm as the **Figure 3.41b** with added limitation of the regulation error *e[k]* in the integral part of Equation (3.41). The regulation error is used in the proportional part without any changes, but in the integral part it is limited by selected maximal allowed value (2 % form 25 kA). This further improvement has the same behaviour of the simulated EFPS current as the variant from the **Figure 3.41b**, but the drawback – requested regulation angle not returning to initial value – is significantly improved.

The simulations of the EFPS controller together with further discussion with Power Supplies manufacturer (ČKD Elektrotechnika) resulted into realization of the following changes in the EF Power Supply controller unit:

- The PI controller parameters were set to $K_P = 5$ and $T_i = 30$ ms. The higher K_P was tested, but resulted into unbalanced currents between two parallel 6-pulse thyristor converters.
- Maximal allowed regulation angle was relaxed to 155˚ at 0 %, 125˚ at 100 % current, linear interpolation between.
- Regulation angle protective ramp was relaxed to 155˚/417 μs when EFPS current is between 0 % and 30 % of 25 kA, 2˚/417 μs when EFPS current is higher than 50 % from 25 kA, linear ramp between.
- Requested current protective ramps were completely removed.
- The regulation error *e[k]* was limited at upper regulation angle border. This yields almost identical results as the variant in the **Figure 3.41c**.

The result of the performed changes (incorporated into EFPS controller 8.9.2010) is better agreement between requested and realized currents in the EFPS circuit. The improvement is noticeable not only during the plasma current breakdown phase, when the MFPS circuit fast current change strongly influences the EFPS circuit but also during the plasma current flat-top phase. After the improvements were implemented, the control exerted on the plasma radial position by the EFPS circuit was improved to the level when plasma radial position can be sometimes controlled even when Fast Amplifier of the BV circuit is not operational. This situation is caused by failed communication between the FA controller and the higher level tokamak control system MARTe. Such failure occurs rarely (< 0.5 %) and is normally solved by a restart of both controller and MARTe. When FA is not operational, the radial position after the breakdown is controlled poorly and often leads to an untimely end of the plasma, but if this phase is overcome, the plasma is then controlled sufficiently by the EFPS circuit only. Such control was not possible before the improvements in the EFPS controller.

It is proposed to include information about all PS currents into each individual Power Supply control unit in future and to compensate for mutual influence of the circuits in the controller algorithms. That would be more effective than optimizing

individual controller settings. The understanding of the PS controller algorithms, described in this section, is important for design of the connection between the controllers.

4 Equilibrium reconstruction

This chapter contains theory of the MHD equilibrium reconstruction in toroidally symmetrical devices, introduction of the equilibrium fitting code EFIT algorithm, the work done on development of the code EFIT++ and finally information about EFIT results for COMPASS - examples of calculated equilibria and EFIT utilization in computation of global power balance. A proper computation of global power balance is important especially for small tokamaks, where many interesting phenomena (L-H transition, ELM frequency changes) happen during non-stationary discharge phases.

4.1 Equilibrium reconstruction theory

This section is an extended version of the article: Havlicek et al., *A Magnetic Equilibrium Reconstruction in Tokamak* [66]. Against the original article the text was extended to better describe the theory and discussion of some equations was added.

Equilibrium reconstruction is used to obtain information about the plasma shape, the current profile and the pressure profile parameters in tokamaks [67]. The reconstruction is performed by iterative solving of the Grad-Shafranov equation [68], [69], [70]. Various tokamak experiments have their own unique codes for equilibrium reconstruction. Some of these codes are particular versions of EFIT [67]. Tokamak geometry, currents in the poloidal field coils and magnetic measurements are fundamental input data to the EFIT code. Other diagnostics, such as Thomson scattering, Motional Stark Effect (MSE) or Faraday rotation, might be used as well.

EFIT++ is a machine-independent version of the general EFIT code and evolvement of the older EFIT2006 [71]. It adopts object-oriented code design and XML input files which are self-describing and hierarchically organized. The code is written in C++ language with computational core in Fortran 95. EFIT2006, and later EFIT++, was selected as an equilibrium reconstruction code for COMPASS.

4.1.1 Grad-Shafranov equation

Plasma can be described by different approaches. One of the models well describing plasma is the MHD one-fluid model. This model describes plasma macroscopically, as a single fluid consisting of electrons and ions. It uses set of so called MHD equations.

In this sub-section we will derive the Grad-Shafranov equation from Maxwell equations and MHD equation of motion. The Grad-Shafranov equation describes equilibrium state of the plasma and its magnetic configuration in axially symmetric devices such as tokamak.

Maxwell equations in the MHD approximation are:

$$\nabla \cdot \vec{B} = 0 \tag{4.1}$$

$$\nabla \times \vec{B} = \mu_0 \vec{j} \tag{4.2}$$

$$\nabla \times \vec{E} = -\frac{\partial \vec{B}}{\partial t}, \tag{4.3}$$

where $\vec{B}$ is magnetic induction, μ_0 is magnetic permeability, $\vec{j}$ is current density and $\vec{E}$ is electric field. It should be noted that the Maxwell equation (4.2) does not contain the term $\mu_0 \frac{\partial \vec{D}}{\partial t}$ in the MHD approximation.

MHD equation of motion is:

$$\rho \frac{\mathrm{d}\vec{v}}{\mathrm{d}t} = \vec{j} \times \vec{B} - \nabla p + \rho \vec{g}\,, \tag{4.4}$$

where ρ is plasma mass density, $\vec{v}$ is velocity, p is plasma pressure and $\vec{g}$ is gravitational acceleration. Plasma mass density, velocity and pressure are defined as:

$$\rho = n_i m_i + n_e m_e \approx n\left(m_i + m_e\right) \tag{4.5}$$

$$\vec{v} = \frac{1}{\rho}\left(n_i m_i \vec{v}_i + n_e m_e \vec{v}_e\right) \tag{4.6}$$

$$p = p_i + p_e\,, \tag{4.7}$$

where n_i, m_i, $\vec{v}_i$ and p_i is ion concentration, mass, velocity and pressure respectively. n_e, m_e, $\vec{v}_e$ and p_e is electron concentration, mass, velocity and pressure respectively.

It is possible to assume that the equilibrium configuration in tokamak is axially symmetric. This assumption neglects toroidal ripple of the toroidal magnetic field, which is negligible in the COMPASS tokamak, because the TF coils have sufficiently high distance from the vacuum vessel. It means that the magnetic induction $\vec{B}$ is independent on the toroidal angle φ in the cylindrical coordinate system (R, φ, Z). Therefore,

$$\vec{B} = \vec{B}\left(R, Z\right) \neq \vec{B}\left(\varphi\right). \tag{4.8}$$

It should be noted that the derivation of the Grad-Shafranov equation uses coordinate system (R, φ, Z) and not (R, Z, φ). That was one of the reasons to use the system (R, φ, Z) in the COMPASS Currents Convention - CCC, see Section 3.1.2.

Then it is possible to define a **poloidal flux function** $\Psi\left(R, Z\right)$:

$$\Psi\left(R, Z\right) = \frac{1}{2\pi} \int_D \vec{B} \cdot d\vec{S}\,, \tag{4.9}$$

where D denotes the area of the disc at vertical position Z with radius R perpendicular to the Z-axis. $\Psi\left(R, Z\right)$ is up to the factor 2π the flux of the total poloidal magnetic field through the area D.

Poloidal components of the magnetic induction vector $\vec{B}$ are then:

$$B_R = -\frac{1}{R}\frac{\partial \Psi}{\partial Z} \tag{4.10}$$

$$B_Z = \frac{1}{R}\frac{\partial \Psi}{\partial R}\,. \tag{4.11}$$

It should be specifically stated that the EFIT++ uses definition of the poloidal flux function from the Equation (4.9). Then the $\Psi\left(R, Z\right)$ output from the EFIT++ is in Wb/rad and Equations (4.10) and (4.11) can be used to calculate local magnetic field at the position (R, Z). This statement is necessary, because alternative definition of the poloidal flux function is occasionally used - one without factor 2π. Then the

Equations (4.10) and (4.11) are changed accordingly, as well as Grad-Shafranov equation.

The poloidal flux function $\Psi(R,Z)$, given by Equation (4.9), satisfies the Maxwell equation (4.1) for the cylindrical coordinate system:

$$\nabla \cdot \vec{B} = \frac{1}{R}\frac{\partial}{\partial R}(RB_R) + \frac{1}{R}\frac{\partial B_T}{\partial \varphi} + \frac{\partial B_Z}{\partial Z} = 0, \tag{4.12}$$

where B_T is the toroidal component of the magnetic induction vector $\vec{B}$. Note that the poloidal flux function is directly proportional to the toroidal component of the magnetic vector potential in the axisymmetric formulation: $\Psi(R,Z) = RA_T(R,Z)$.

Let us now define a function F as:

$$\vec{B}_T = \frac{F}{R}\vec{e}_T, \tag{4.13}$$

where $\vec{e}_T$ is a unit vector in the direction of toroidal angle φ.

The magnetic induction $\vec{B}$ can then be written as:

$$\vec{B} = \vec{B}_p + \vec{B}_T \tag{4.14}$$

$$\vec{B}_p = \frac{1}{R}[\nabla\Psi \times \vec{e}_T] \tag{4.15}$$

$$\vec{B}_T = \frac{F}{R}\vec{e}_T, \tag{4.16}$$

where $\vec{B}_p$ denotes the poloidal vector component of magnetic induction $\vec{B}$.

From the Maxwell equation (4.2) and the magnetic induction $\vec{B}$ defined by Equations (4.14), (4.15) and (4.16) it is possible to obtain expression for current density $\vec{j}$:

$$\vec{j} = \vec{j}_p + \vec{j}_T \tag{4.17}$$

$$\vec{j}_p = \frac{1}{R}[\nabla(F/\mu_0) \times \vec{e}_T] \tag{4.18}$$

$$\vec{j}_T = (L\Psi)\vec{e}_T, \tag{4.19}$$

where $\vec{j}_p$ and $\vec{j}_T$ are the poloidal and the toroidal components of the current density $\vec{j}$ and the operator L is defined as:

$$L = -\frac{\partial}{\partial R}\left(\frac{1}{\mu_0 R}\frac{\partial}{\partial R}\right) - \frac{\partial}{\partial Z}\left(\frac{1}{\mu_0 R}\frac{\partial}{\partial Z}\right). \tag{4.20}$$

The Equations (4.14) to (4.20) for $\vec{B}$ and $\vec{j}$ are valid in the whole space of the tokamak (plasma, vacuum, vessel, coils) because they involve only the Maxwell equations and the assumption of axial symmetry. The Equation (4.19) is practically particularly useful, because the poloidal flux function is output from the EFIT code and therefore the Equation (4.19) is used to calculate toroidal current density of the reconstructed plasma.

For tokamaks it is possible to neglect $\rho\vec{g}$ in the Equation (4.4) and for an equilibrium state $\rho\frac{\mathrm{d}\vec{v}}{\mathrm{d}t} = 0$. Equation (4.4) then becomes equilibrium equation which reflects that the force due to ∇p is compensated by the $\vec{j} \times \vec{B}$ force:

$$\nabla p = \vec{j} \times \vec{B} . \tag{4.21}$$

From the Equation (4.21) it is possible to see that:

$$\vec{B} \cdot \nabla p = \vec{B} \cdot \vec{j} \times \vec{B} = 0 \tag{4.22}$$

$$\vec{j} \cdot \nabla p = 0 , \tag{4.23}$$

which is caused by the fact that vector product is perpendicular to two vectors and scalar product of two perpendicular vectors is zero. Therefore the equilibrium magnetic field lines and current lines lie on isobaric surfaces (p = constant). These surfaces are called magnetic surfaces. The magnetic surfaces are defined by:

$$\Psi(R, Z) = \text{constant} . \tag{4.24}$$

Equations (4.15) and (4.22) indicate that ∇p is collinear with $\nabla \Psi$, therefore plasma pressure is constant on the magnetic surface:

$$p = p(\Psi) \tag{4.25}$$

and Equations (4.18) and (4.23) indicate that ∇p is collinear with ∇F, therefore F is also constant on the magnetic surface:

$$F = F(\Psi) . \tag{4.26}$$

The equilibrium equation (4.21) combined with Equations (4.14), (4.15), (4.16) and (4.17), (4.18), (4.19) for $\vec{B}$ and $\vec{j}$ becomes:

$$\nabla p = \frac{L\Psi}{R} \nabla \Psi - \frac{F}{\mu R^2} \nabla F . \tag{4.27}$$

which can be rewritten as:

$$L\Psi = R \frac{\partial p}{\partial \Psi} + \frac{1}{2\mu_0 R} \frac{\partial (F^2)}{\partial \Psi} . \tag{4.28}$$

The Equation (4.28) is the **Grad-Shafranov equation** and L is the elliptic operator defined by the Equation (4.20). Right-hand side of the Grad-Shafranov equation represents toroidal component of the plasma current density $\vec{j}_{T,pl}$.

It is important to understand underlying physics behind the Grad-Shafranov equation. The Grad-Shafranov equation is derived from two Maxwell equations (4.1), (4.2), from toroidal symmetry and from force equilibrium equation (4.21). The neglected terms are: a) $\mu_0 \frac{\partial \vec{D}}{\partial t}$ in the Equation (4.2), b) $\rho \frac{\mathrm{d}\vec{v}}{\mathrm{d}t}$ and $\rho \vec{g}$ in the Equation (4.4) to obtain Equation (4.21) and c) an assumption of toroidal symmetry. The neglecting is fully valid for tokamak plasma, without loosing any physics important for description of the equilibrium state. A rough estimation of terms in the Equation (4.4) for COMPASS experimental data during plasma disruption yields $\rho \frac{\mathrm{d}\vec{v}}{\mathrm{d}t} = 10^{20} m^{-3} \cdot 2.014 \cdot 1.66 \times 10^{-27} kg \cdot \frac{2 \cdot 0.2m}{(10^{-4} s)^2} \cong 13 \frac{Pa}{m}$,

$\rho \vec{g} = 10^{20} m^{-3} \cdot 2.014 \cdot 1.66 \times 10^{-27} kg \cdot 9.8 \frac{m}{s^2} \cong 3.3 \times 10^{-6} \frac{Pa}{m}$, which is negligible against $\nabla p = \frac{10000 Pa}{0.2m} = 5 \times 10^4 \frac{Pa}{m}$.

It should be noted that tokamaks in principle require resistive MHD model to fully describe time evolution (even though ideal MHD model is used whenever

possible), due to presence of strong skin effects in the plasma, together with appropriate time constants for magnetic field and current penetration times. The skin effect is in principle derived from Equation (4.3), which is not included in the Grad-Shafranov equation derivation. Therefore, while the Grad-Shafranov equation is still valid for time evolving tokamak plasma, it does not describe it fully. For full description, skin effects of $\vec{B}$ and $\vec{j}$ would have to be solved together with Grad-Shafranov equation.

4.1.2 EFIT algorithm

The EFIT code iteratively solves the Grad-Shafranov equation using many different constraints, e.g. [72], [73]. The Grad-Shafranov equation written with all terms representing toroidal current density is:

$$L\Psi\vec{e}_T = \vec{j}_{T,C} + \vec{j}_{T,V} + \vec{j}_{T,pl}\,, \tag{4.29}$$

where $\vec{j}_{T,C}$ is current density in the poloidal field coils, $\vec{j}_{T,V}$ is toroidal component of current density in the vacuum vessel and other passive conductive structures and $\vec{j}_{T,pl}$ is toroidal component of the plasma current density defined by right-hand side of the Equation (4.28). We can express $\vec{j}_{T,C}$ as:

$$\vec{j}_{T,C} = \sum_{i=1}^{N_C} \frac{I_i^{pf}}{|c_i|}\vec{e}_T\,, \tag{4.30}$$

where I_i^{pf} is the current in i-th poloidal field coil and $|c_i|$ is a geometric factor transforming the current in the i-th coil into current density.

In the first iterative step EFIT obtains new iteration of poloidal flux function Ψ by solving the Equation (4.29) with selected representation of the term $\vec{j}_{T,pl} = R\frac{\partial p}{\partial \Psi} + \frac{1}{2\mu_0 R}\frac{\partial\left(F^2\right)}{\partial \Psi}$. The most common is representation in the form of polynomial functions:

$$\frac{\partial p}{\partial \Psi} = \sum_{i=0}^{N_\alpha - 1} \alpha_i \Psi^i \tag{4.31}$$

$$\frac{\partial\left(F^2\right)}{\partial \Psi} = \sum_{i=0}^{N_\gamma - 1} \gamma_i \Psi^i\,, \tag{4.32}$$

where α_i and γ_i are coefficients in the polynomials and Ψ^i is i-th power of poloidal flux function.

The first iterative step is performed by Green's function method:

$$\begin{aligned}\Psi^{t+1}(\vec{r})\vec{e}_T = &\sum_{i=1}^{N_C} G_i^{pf}(\vec{r},\vec{r}_i) I_i^{pf}\vec{e}_T + \sum_{i=1}^{N_V} G_i^{V}(\vec{r},\vec{r}_i) I_i^{V}\vec{e}_T \\ &+ \int G(\vec{r},\vec{r}')\vec{j}_{T,pl}\left(\vec{r}',\Psi^t\right)dR'dZ'\end{aligned}\,, \tag{4.33}$$

where Ψ^{t+1} is new iteration of poloidal flux function, G_i^{pf} is Green's function for determination of poloidal flux function at position $\vec{r}$ from the current I_i^{pf} in the i-th poloidal field coil at the position $\vec{r}_i$, G_i^V and G are Green's functions for i-th vacuum vessel element current and plasma current density respectively.

In the second iterative step EFIT obtains new iteration of parameters α_i, γ_i, I_i^{pf} and I_i^V. In this step the physical measurements are involved. Any measured value a_M^k (k = 1,…, number of measurements) which is dependent on any of the parameters α_i, γ_i, I_i^{pf} or I_i^V (and is therefore dependent on the Ψ, $\vec{j}_T$, $\vec{B}$ or any derivative) might be used as a constraint for EFIT. In order to do so, this dependence $a^k\left(\alpha_i,\gamma_i,I_i^{pf},I_i^V\right)$ is linearized in the parameters α_i, γ_i, I_i^{pf} and I_i^V:

$$a^k\Big|_{a_0} + \sum_{i=0}^{N_\alpha-1}\frac{\partial a^k}{\partial\alpha_i}\bigg|_{a_0}\alpha_i + \sum_{i=0}^{N_\gamma-1}\frac{\partial a^k}{\partial\gamma_i}\bigg|_{a_0}\gamma_i + \sum_{i=0}^{N_C-1}\frac{\partial a^k}{\partial I_i^{pf}}\bigg|_{a_0} I_i^{pf} + \sum_{i=0}^{N_V-1}\frac{\partial a^k}{\partial I_i^V}\bigg|_{a_0} I_i^V = a_P^k, \tag{4.34}$$

where a_P^k is the predicted (= computed by EFIT) value of a_M^k.

These predicted values are compared with measured values, giving k-th constraint equation:

$$a_P^k = a_M^k. \tag{4.35}$$

Equations (4.35) constitute a system of linear algebraic equations for α_i, γ_i, I_i^{pf} and I_i^V. This set of equations is in general either over-determined or under-determined, i.e. the number of equations is different than the number of unknowns. Singular Value Decomposition method is used to find the least-square solution, while each equation is weighted by a factor σ_k, corresponding generally to the measurement accuracy:

$$\left|\sum_k\left(\frac{a_M^k - a_P^k}{\sigma_k}\right)^2\right|_{\min}. \tag{4.36}$$

This second iterative step supplies new iteration of parameters α_i, γ_i, I_i^{pf} and I_i^V from known Ψ into the first iterative step. When the EFIT starts the iteration process, the iteration of parameters α_i, γ_i, I_i^{pf} and I_i^V must be guessed based on measurement. One of the possibilities is to assume the plasma represented by thin wire in the centre of the vacuum vessel with given current.

A practical example of k-th constraint equation according (4.35) can be a measurement of plasma pressure at given position (*R*, *Z*): a_M^k is measured value of the pressure and a_P^k can be obtained by linearization of integrated from of Equation (4.31): $p(R,Z) = \int_{\Psi_b}^{\Psi}\sum_{i=0}^{N_\alpha-1}\alpha_i\Psi^i$. The linearization is not necessary in this case because the equation is already linear in α_i.

4.2 Induced Currents Module for EFIT++

Cooperation with EFIT++ principal developer, Lynton Appel (Culham Centre for Fusion Energy), was established when EFIT++ was selected as an equilibrium reconstruction code for COMPASS. The first result of the cooperation was parallelization of the EFIT++ (reported in [66]) which allows faster processing of many time slices on inter-shot basis during tokamak operation.

More importantly, a computational model to represent the induced currents in the passive structures of the tokamaks was implemented into EFIT++. The passive structures can be PF coils cases and the vacuum vessel or other structural elements, where current is not measured. The model is restricted to axisymmetric currents and provides $\vec{j}_{T,V}$ into Grad-Shafranov equation (4.29).

4.2.1 Theoretical background

The induced currents model is based on the model described in the article of G.J. McArdle and D. Taylor: *Adaptation of the MAST passive current simulation model for real-time plasma control* [74] which uses standard linear control theory and model reduction techniques described in [75].

The induced currents model is supposed to compute currents in passive structures, i.e. toroidal conductive structures, where current is not measured. Any passive structure, where toroidal current is measured, can be treated as standard PF coil in the configuration files of the EFIT++. Passive structures can be vacuum vessel or short-circuited loops or casings of PF coils. Vacuum vessel is usually described by dividing it to multiple passive structures.

The principle of the model is to solve a system of equations for unknown currents in elements describing passive structures from known currents in the PF coils and in the plasma column. The plasma is described by currents in a grid.

The model consists of solving the Kirchhoff's voltage law for induced voltage in the passive structures:

$$(U =)0 = R_{ps} \cdot I_{ps} + L_{ps2ps} \cdot \dot{I}_{ps} + L_{ps2pf} \cdot \dot{I}_{pf} + L_{ps2g} \cdot \dot{I}_{pl}, \qquad (4.37)$$

where R_{ps} is diagonal matrix of passive structure resistances, I_{ps} is vector of passive structure currents, L_{ps2ps} is matrix of self-inductances and mutual inductances of passive structures, $\dot{I}_{ps}$ is vector of time derivatives of currents in passive structures, L_{ps2pf} is matrix of mutual inductances between passive structures and PF coils, $\dot{I}_{pf}$ is time derivative of currents in the PF coils, L_{ps2g} is three dimensional matrix of mutual inductances between passive structures and computational grid and $\dot{I}_{pl}$ is two dimensional matrix of derivatives of plasma currents in the computational grid.

The physical meaning of the terms in the Equation (4.37) is: $R_{ps} \cdot I_{ps}$ describes voltage lost due to resistance of the passive structures, one row in $L_{ps2ps} \cdot \dot{I}_{ps}$ is voltage induced by self-inductance of one passive structure appropriate to the row and voltage induced from all other passive structures, the term $L_{ps2pf} \cdot \dot{I}_{pf}$ describes voltage induced by all PF coils and finally the term $L_{ps2g} \cdot \dot{I}_{pl}$ is voltage induced by plasma in the grid. Note that the movement of the passive structures or PF coils is neglected in the Equation (4.37) by equating the terms with variable matrices of inductances ($I \cdot \dot{L}$) to zero.

The Equation (4.37) differs in notation from induction equation in the article [74]. The notation used in this text is more compatible with EFIT++ internal structure.

The Equation (4.37) has derivatives of the PF coils currents and of the plasma current on the right-hand side. The derivatives can be avoided by introducing the state variable x defined by equation:

$$I_{ps} = x - L_{ps2ps}^{-1} \cdot \left(L_{ps2pf} \cdot I_{pf} + L_{ps2g} \cdot I_{pl} \right). \tag{4.38}$$

It is possible to rewrite Equation (4.37) by the means of substituting I_{ps} with state vector x:

$$\frac{dx}{dt} = A \cdot x + B \cdot u + C \cdot v \tag{4.39}$$

$$y = D \cdot x + E \cdot u + F \cdot v, \tag{4.40}$$

where individual matrices are:

$$A = -L_{ps2ps}^{-1} \cdot R_{ps}, \tag{4.41}$$

$$B = L_{ps2ps}^{-1} \cdot R_{ps} \cdot L_{ps2ps}^{-1} \cdot L_{ps2pf}, \tag{4.42}$$

$$C = L_{ps2ps}^{-1} \cdot R_{ps} \cdot L_{ps2ps}^{-1} \cdot L_{ps2g}, \tag{4.43}$$

$$D \text{ is identity matrix,} \tag{4.44}$$

$$E = -L_{ps2ps}^{-1} \cdot L_{ps2pf}, \tag{4.45}$$

$$F = -L_{ps2ps}^{-1} \cdot L_{ps2g} \tag{4.46}$$

and $u = I_{pf}$, $v = I_{pl}$.

The advantage of the Equations (4.39), (4.40) over the Equation (4.37) is in possibility to solve the Equation (4.39) numerically with fine time step while avoiding numerical differentiation of PF coils currents and currents in the grid. Equation (4.40) can be enumerated only in times when plasma equilibrium is calculated.

The eigendecomposition of the matrix A allows rewrite of the Equations (4.39), (4.40) into:

$$\frac{dx_e}{dt} = \Lambda \cdot x_e + W^{-1} \cdot B \cdot u + W^{-1} \cdot C \cdot v \tag{4.47}$$

$$y = D \cdot W \cdot x_e + E \cdot u + F \cdot v, \tag{4.48}$$

where Λ is diagonal matrix of eigenvalues of matrix $A = W \cdot \Lambda \cdot W^{-1}$, W is full matrix whose columns are eigenvectors of A and $x_e = W^{-1} \cdot x$ is state vector of eigenmodes.

The rewriting of the Equation (4.37) to the Equations (4.47) and (4.48) offers several advantages for computing of induced currents. The matrix Λ is diagonal which allows solution of the set of equations (4.47) as a set of independent equations. This feature allows truncation of the induced currents model by setting terms of the vector x_e with large negative corresponding terms of Λ to zero. Physical reasoning behind this possibility is that matrix Λ consists of $1/\tau$ time constants of eigenmodes and it is possible to neglect most rapidly decaying eigenmodes (details are explained in [74]).

The equations (4.47) and (4.48) in discrete representation are:

$$x_e(n+1) = A_d \cdot x_e(n) + B_d \cdot u(n) + C_d \cdot v(n) \tag{4.49}$$

$$y(n+1) = W \cdot x_e(n+1) + E_d \cdot u(n+1) + F_d \cdot v(n+1), \tag{4.50}$$

where matrices A_d, B_d, C_d, E_d and F_d have form depending on chosen method of solving of differential equations, i.e. the matrices differ for forward Euler method and Runge-Kutta method.

4.2.2 Implementation into EFIT++

The EFIT++ code is written in the C++ with computational core of the code in the Fortran 95. The Induced Currents Module (ICM) was implemented in the C++ part of the code.

Figure 4.1 shows dependencies of classes important for the Induced Currents Module. All of the classes are fully encapsulated and not accessible for changing inside data from outside of the class. This C++ feature forces the developer to maintain the code structure clean and systematic.

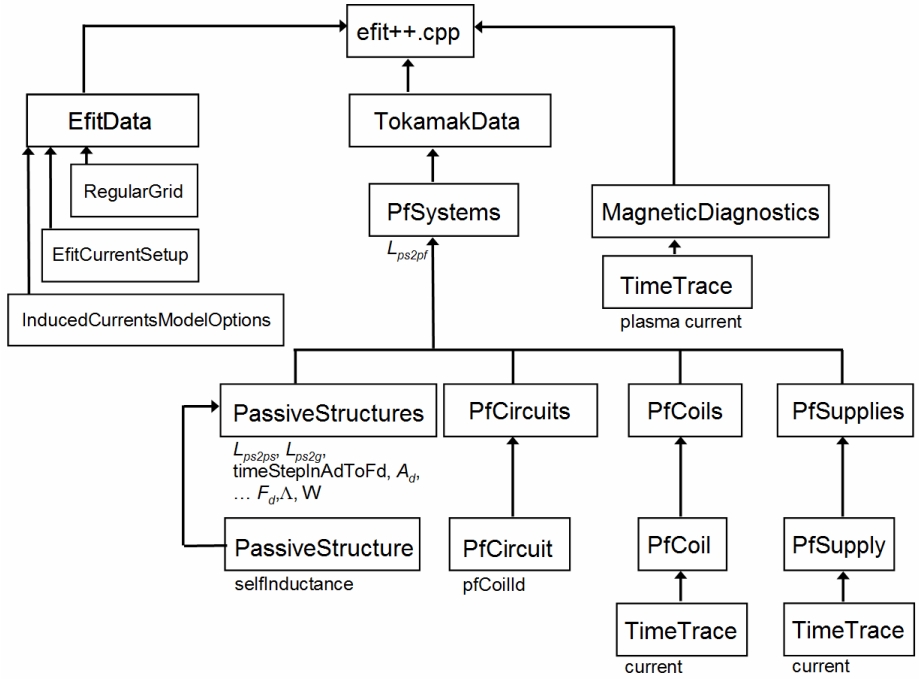

Figure 4.1: Part of the EFIT++ internal structure. Classes, which are used in the Induced Currents Module, are shown together with location of some variables used by the ICM.

The principal part of the ICM - method *computeInducedCurrents* - is located in the instance *passiveStructures* of the class *PassiveStructures*. Data about the plasma current time trace, grid geometry, required plasma current representation (ellipse with user selected parameters) and ICM options must be passed into the *passiveStructure* instance through calling appropriate methods in the *tokamakData* and *pfSystems* objects.

When the induced currents are computed, multiple variables containing the necessary data must be prepared. The most important methods and variables are summarized in the following list:

1. Class *InducedCurrentsModelOptions* holds the options for the ICM, loaded from efitOptions.xml input file. The options allow to control whether the

module is used or not (*useModel*), whether to compute (or load) response matrices for the module (*computeResponseMatrices*) with selected *integrationMethod* (implicit and explicit Euler methods are implemented currently), time when the induced currents are computed and time step desired during computation (*beginTime*, *timeStep*, *timesCount*), spatial resolution which should be used to compute mutual and self-inductances of tokamak toroidal conductive structures (*resolution*, *couplingsToGridResolution*), smoothing over 2 x *inputTimeWindow* and parameters for description of the plasma current profile used for induced currents computation (*peakingFactor* in this class and *relip*, *zelip*, *aelip*, *eelip* from *EfitCurrentSetup* class). The plasma current is represented by a user-defined elliptical profile scaled to the measured plasma current. The ICM has been implemented in a way to allow the future use of EFIT++ generated plasma current distributions.

2. Class *InductanceBaseClass*: methods *mutualInductance* and *selfInductance*, which are used to compute inductance of thin wire(-s).
3. Class *PassiveStructure*: method *computeSelfInductance* for computation of self-inductance of one passive structure. Variable *resistance* had to be changed from array to single value. This circumvents possible problems with computation of resistance for parallel or serial connection of passive structure elements.
4. Class *PassiveStructures*: method for computation of matrix of mutual and self-inductances of passive structures *computePS2PSMutualInductances* and method for computation of mutual inductances between passive structures and computational grid *computePS2GmutualInductances*. The matrix *mutualInductancePS2GArray* has three indices (dimensions): index of passive structure, *r* index of computational grid and *z* index of computational grid.
5. Class *PfSystems*: method for computation of matrix of mutual inductances between passive structures and PF coils *computePS2PFMutualInductances*.
6. Class *Profiles2D*: method *constructCurrentDistribution* intended to create artificial plasma current distribution in the ellipse shape at defined location and with defined current profile.
7. Files gsl.h and gsl.cpp store GNU Scientific Library functions wrapped into C++ interface suitable for EFIT++. The functions compute inverse matrices and eigendecomposition of matrices.
8. Class *PassiveStructures*: variables *lambdaMatrix*, *wMatrix*, *adMatrix*, *bdMatrix*, *cdMatrix*, *edMatrix* and *fdMatrix* used to store data necessary to perform computation of induced currents according equations (4.49) and (4.50). The *lambdaMatrix* will be necessary for truncation of the model, which is not implemented yet. Methods *fillAd_fdMatricesWithForwardEuler* and *fillAd_fdMatricesWithBackwardEuler* fills the variables (including wMatrix and lambdaMatrix). Variable *timeStepInAdToFd* is used when

matrices are read from response functions file to cross-check loaded and requested time step.

9. Class *PassiveStructures*: method *computeInducedCurrents* which wraps all previously prepared structures into one working model usable within the EFIT++ to compute currents in the passive structures. The EFIT++ input files can provide measured currents for either PF coils circuits or individual PF coils. In the first case, PF coils objects (see **Figure 4.1**) do not have current time traces populated. Then the method *computeInducedCurrents* creates a temporal copy of PF coil objects and populates their current time traces. The reason for this cumbersome solution is a desire to avoid any influence on the EFIT++ data flow outside of the Induced Currents Module.

The Induced Currents Module implementation imposes restrictions on the EFIT++ input files:

1. Both *pfCoils* and *passiveStructures* instances in tokamakData.xml file must be described by a set of rectangles, because ICM methods used to calculate mutual and self-inductances do not work with tilted shapes. The inductances are calculated by dividing the structures into series of infinitely thin toroidal wires with distance of the wires set by *resolution* parameter in *inducedCurrentsModelOptions* in efitOptions.xml for calculation of L_{ps2ps} and L_{ps2pf} and by *couplingsToGridResolution* parameter for calculation of L_{ps2g}.
2. It is not possible to use parallel connection of PF coils into PF circuits in the EFIT++ input files. Such connection would require the ICM to solve distribution of total current into individual parallel circuits.
3. All structures, where current is measured and provided to the EFIT++, must be listed as a *pfCoils* instance in the tokamakData.xml, regardless of whether they are active (Power Supply controlled) or passive (only induced current). Conversely, all structures listed as *passiveStructures* instance must be passive and without measured current. An active PF coil without current measurement must be listed as *pfCoil* with efitOptions.xml *weight* set to 0.
4. All *passiveStructure* instances in the tokamakData.xml must have only one resistance defined even when they are geometrically described by multiple rectangles. The current density distribution among the rectangles is assumed to be uniform.

The workflow of the Induced Currents Module consists of calculating (or loading) response matrices used in equations (4.49) and (4.49) with selected integration method. Then an artificial plasma current distribution is created in the ellipse shape at defined location. Plasma and PF coils currents provided to EFIT++ from database are interpolated to the desired time step and then smoothed. The time step should be sufficiently small to avoid numerical errors ($< 10^{-5}$ s for the MAST tokamak) and smoothing should avoid power supplies characteristic frequency (600 Hz for MAST, 720-1020 Hz for COMPASS), otherwise unphysical phase shifts in smoothed currents will occur. Finally, induced currents are calculated for the entire discharge using the artificial plasma current distribution and measured plasma

current. Eigenvalue decomposition explained in the previous text is performed, but truncation of the matrices is not implemented. The EFIT++ then uses calculated induced currents during running equilibrium reconstruction part of the code.

The induced currents module was checked for speed optimization and the achieved runtime is in the order of seconds while compiled with -O2 flag of the C++ GCC compiler. When -02 flag is not used (which is occasionally useful because debuggers can not work with optimized code) the runtime is roughly 80 seconds for 1 second discharge with $dt = 10^{-5}$ s.

4.2.3 Benchmarking and results for MAST

The Induced Currents Module implemented into the EFIT++ code was extensively tested and benchmarked against existing code INDUCTION. The MAST tokamak discharge #20790 was used for benchmarking.

The INDUCTION code was internally developed in CCFE for the MAST tokamak and was used as a standalone program for the identical purpose as the ICM. The authors of the INDUCTION code were Panos Gonos, Lynton Appel and Dave Taylor. The version of the INDUCTION code used for the benchmarking is written in the Fortran language.

The Induced Currents Module offers several advantages in comparison with the INDUCTION code. Firstly, it is incorporated into the EFIT++ code and therefore uses the identical input files with geometry and currents in the active and passive conductive structures. The INDUCTION code uses different input files than EFIT++, allowing inconsistencies between input files. Secondly, providing the calculated currents in the passive structures to the EFIT++ do not require writing results into a file on the hard drive. Thirdly, the ICM uses eigendecomposition of the problem, allowing truncation of the matrices and subsequent faster solution.

The validation of the new model against the INDUCTION showed that there were multiple differences between the results from these codes which had to be explained. The results of the validation are:

1) It was shown that the mutual and self couplings in INDUCTION code are computed incorrectly. This may result in non-negligible errors of mutual couplings for closely located coils with finite area. The self-inductances of passive structures with dimensions non-negligible with respect to radius of the passive structure are also incorrectly computed in the INDUCTION (up to 25 % self inductance error for inconel part on the central column in the MAST tokamak).

The INDUCTION module computes mutual inductance of two passive structures (or passive structure and PF coil) by dividing one of the passive structures into fine mesh and computing mutual inductance from the mesh points to the centre of second passive structure. The correct scheme used in the ICM divides both passive structures into the mesh. The self-inductance of the passive structures is computed as mutual inductance between the centre of the structure and the mesh points in the INDUCTION. This is also incorrect.

The incorrect computation of the inductances in the INDUCTION module has influence on the computed induced currents mainly during transient events like plasma current ramp-up. During the plasma flat-top phase the induced currents are computed with negligible error.

2) It was found that there is a significant difference between the ICM and INDUCTION in the level of the induced currents noise. The MAST induced currents computed by INDUCTION module showed much smaller noise than the new induced currents model (~10 % noise). The reason was a smoothing scheme applied in INDUCTION, while ICM did not use any smoothing at the time of benchmarking. The averaging scheme used by INDUCTION for MAST poloidal field coils was:

$$\frac{\mathrm{d}f}{\mathrm{d}t} = \frac{average < f(t), f(t+\tau/2) > - average < f(t-\tau/2), f(t) >}{\tau}. \qquad (4.51)$$

For the PF coils currents the τ was 5 ms and for the plasma current the τ was 12 ms. Considering the fact that some of the passive structures of the MAST have time constant L/R as small as 0.4 ms, using τ = 5 ms for smoothing has significant effect on computed induced currents.

Investigation showed that the noise observed in both codes (after temporary removal of smoothing from INDUCTION) was due to the bit noise created during the ADC sampling of the PF coils power supplies currents. The noise in the induced current elements was amplified and was much larger than one would expect - around 10 % of the (peak) induced current.

In simple terms 1 bit noise on the central solenoid current measurement was equivalent to a change of 16 A in 0.2 ms (sampling rate) which would generate a spike of 0.7 V on the loop voltage. The average loop voltage is in the range of volts therefore this bit noise creates significant noise in the induced currents, mainly in passive structures with time constant L/R comparable with sampling rate 0.2ms.

The noise is coherent between passive structures, so could be potentially problematic for equilibrium interpretation. The best option is to increase the AD converters bit resolution to remove the noise source.

The final benchmarked version of the ICM has smoothing of the input values implemented, but the averaging scheme is simple moving average with user controlled width.

3) Small (<1 %) spikes were observed in computed induced currents in the ICM, see **Figure 4.2**. Induced currents are computed with finer time step (usually dt = 1.10^{-5} s) than input PF coils currents (sampling rate 2.10^{-4} s for MAST tokamak, #20790) and the spikes were observed only during ~ 2-4.10^{-5} s after the new sample of the PF coils current was supplied. The similar spikes were found in the results from the INDUCTION code which uses completely different numerical scheme (implicit Euler method in the ICM vs. 4th order Runge-Kutta method in INDUCTION). The working hypothesis is that these spikes are mathematically meaningful response of the system of equations to the unphysical "jump" in boundary conditions (new PF coils current value supplied resulting into jump of its time derivative). The reasoning behind this hypothesis is that Λ matrix (see Section

4.2.1) has terms $1/\tau$ with time constants as low as 3.10^{-6} s, which is significantly lower time than time constant of the entire MAST vessel.

These spikes are unphysical, because PF coils self-inductance does not allow such sharp change of the current derivative. The spikes should be removed from the data provided to the EFIT++ code by sufficient smoothing of the input PF coils currents.

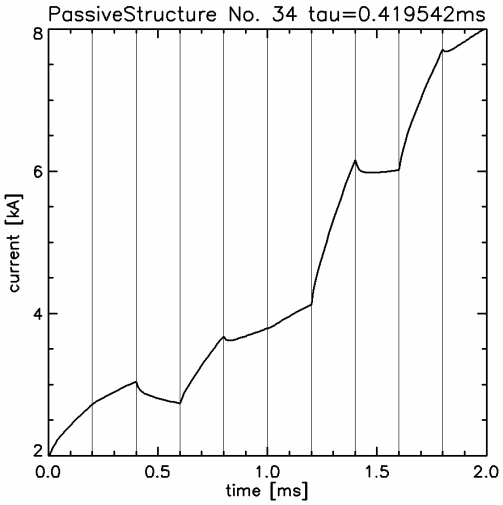

Figure 4.2: Example of spikes on the calculated current in the passive structure #34 located on the HFS of the MAST tokamak. Grey vertical lines mark new value of derivative of input PF and plasma currents. The input currents are without any smoothing for this benchmarking test.

4) There was a huge difference (~10 %) in the computed induced currents between the two codes during plasma breakdown and during plasma collapse at the end of the plasma ramp-down phase. The explanation was found in INDUCTION code: plasma current supplied to the INDUCTION code was artificially set to 0 A when measured value was lower than 50 kA. The huge voltage jump calculated from dI_{pl}/dt resulted into INDUCTION code calculating wrong passive structures currents at the time of breakdown and during plasma end with decay time constant ~ 25 ms.

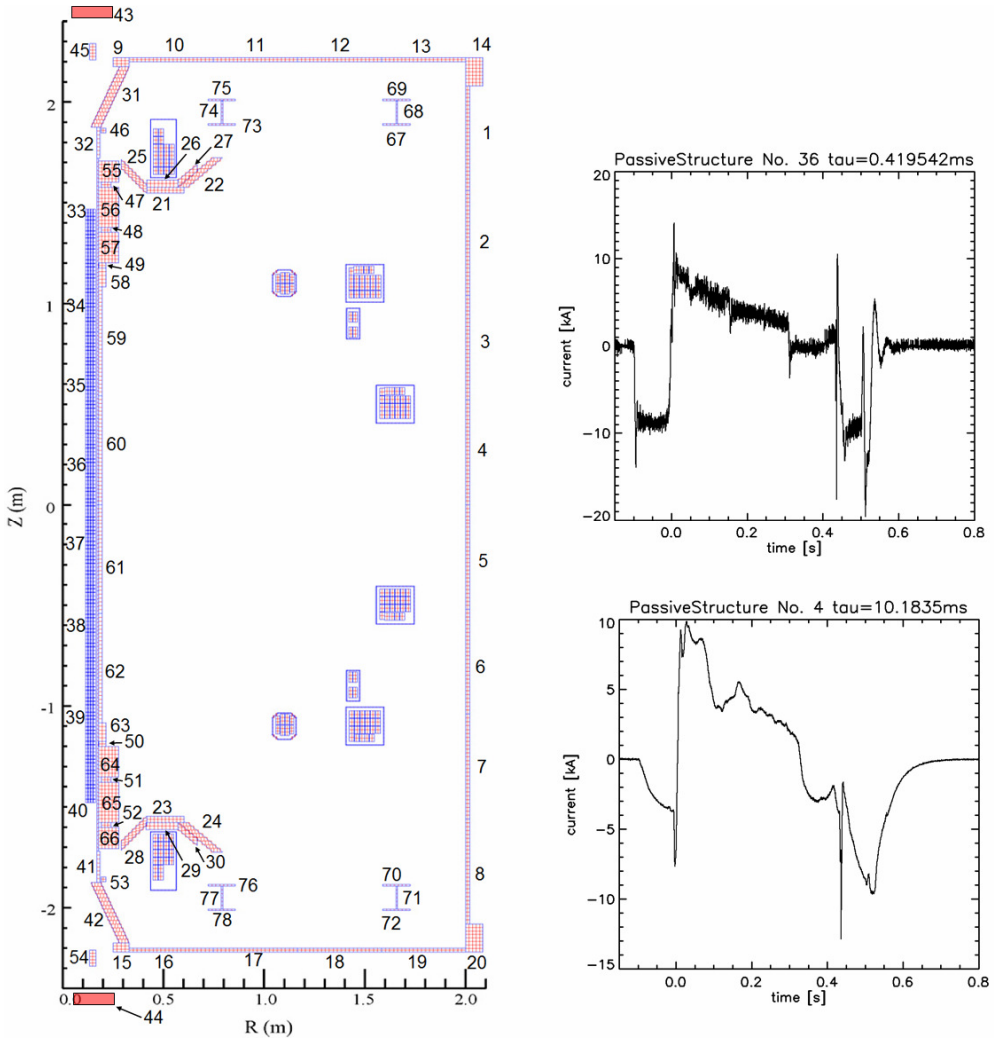

Figure 4.3: Left panel: MAST passive and active structures, reprinted from [74], added numbers of passive structures. Right panel: calculated induced currents for passive structure on the HFS (top panel) and LFS (bottom panel).

An example of computed induced currents for the MAST tokamak, discharge #20790, is in the **Figure 4.3**. The used number of passive structures was 78. It can be seen that HFS passive structures have low time constant L/R (0.4 ms for passive structure #36), while LFS passive structures have higher time constant (10.2 ms for passive structure #4). The different time constants have consequences for induced current. The induced current in the HFS passive structure has higher fluctuations than induced current in the LFS passive structure. Furthermore the negative current induced before plasma current breakdown (t = 0 s) has different shape. It should be clarified that the "effective" time constant of the induced current is not L/R of one individual passive structure, but result of induced current changes in all passive and active structures, together with plasma current changes (position and shape changes are not taken into account in the model). Therefore the negative current induced before t = 0 s has high "effective" time constant, while L/R of the passive structure #4 is only 10.2 ms.

4.3 Induced currents in the COMPASS tokamak

The Induced Currents Module implemented into the EFIT++ was used for the calculation of induced currents in the vacuum vessel of the COMPASS tokamak.

This task was complicated by the placing of the magnetic diagnostic coils in the COMPASS vacuum vessel. The vacuum vessel is welded together from eight toroidal octants made from 3 mm thick Inconel 625. There is a strengthening belt welded between each of the octants. The belt has toroidal length ~ 40 mm and its radial dimension is 7.5 mm larger than radial dimension of the octants, creating a local alcove. Some of the diagnostic coils are mounted in this alcove. The consequence is that bulk of the vessel (octants between the alcove belts) has almost identical *R* and *Z* coordinates as centres of the diagnostic coils. The geometrical information about bulk vessel, alcove and 16 Internal Partial Rogowski coils is shown in the **Figure 4.4**.

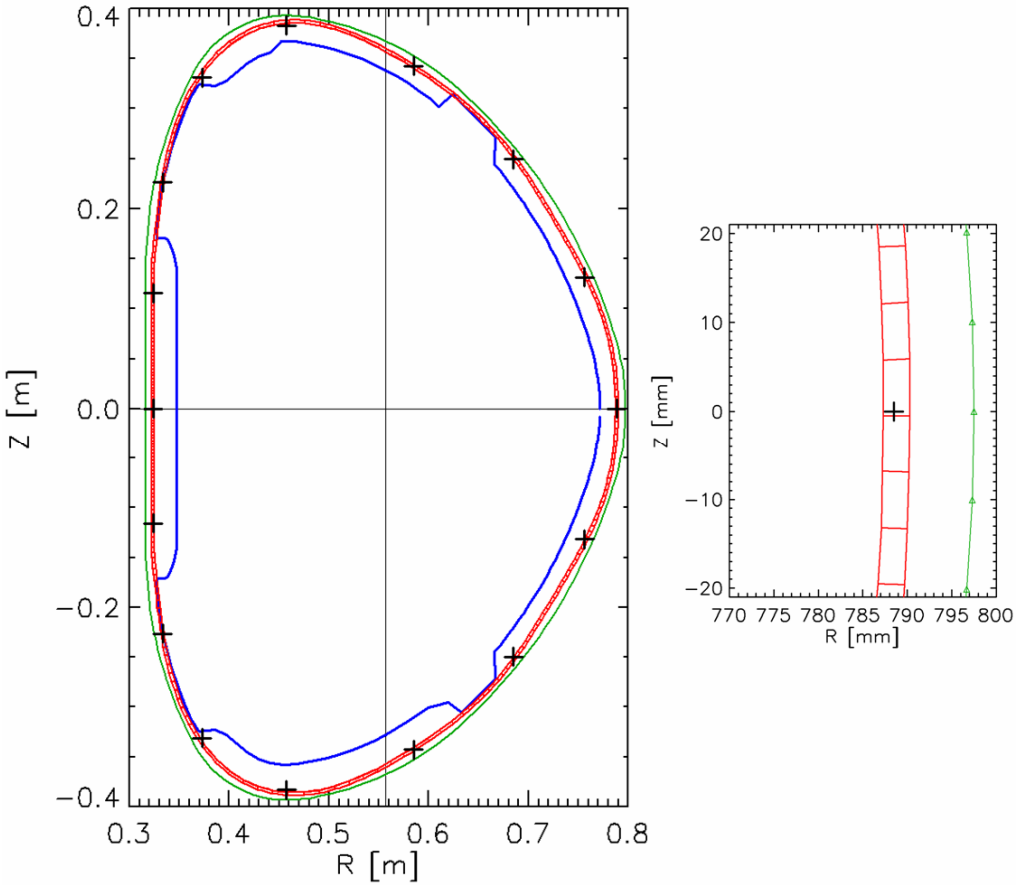

Figure 4.4: Vacuum vessel of the COMPASS tokamak. Blue: limiter, red: bulk vacuum vessel is 3 mm thick, green: belt alcove - centre of 3 mm thick alcove wall depicted, black crosses: centres of 16 IPR coils. Left panel: entire vessel, right panel: detail around IPR_01. The IPR coil and its holder have dimensions ~ 14 x 60 mm.

The influence of induced currents flowing in the vessel on the signal of the diagnostic IPR coil is not straightforward. The Induced Currents Module assumes full toroidal symmetry, which is not the case for COMPASS. The vessel current

flows in the toroidal direction in the bulk vessel and ~20 mm (half of 40 mm alcove outer dimension + thickness of the weld, alcove material is 3 mm thick) before the centre of the diagnostic coil moves 7.5 mm radially outwards, flows around the coil and returns to the position of the bulk vessel. The situation is further complicated by the fact that there is 1 mm thick metal cover mounted radially inwards from the diagnostic coils. This metal cover protects the diagnostic coils from the plasma and may carry part of the toroidal vessel current. The cover plates are spot welded in four points, providing unknown effective resistance. This radially inward current path was neglected for the purpose of the induced currents calculation in the EFIT++.

The placing of diagnostic coils in the alcove belt complicates use of the ICM. The simplest possible solution is to use positions of the bulk vessel to calculate the induced currents and then switch to positions of the alcove belt to calculate the influence of the vessel currents to the diagnostic coils. Before this solution is used, a more realistic magnetic field in the alcove should be calculated and compared with magnetic field generated by vessel on the position of the bulk vessel or the alcove belt.

		BR [mT/-kA]	BZ [mT/-kA]
IPR_01 (LFS, midplane)			
	vessel	22.74	-16.9
	alcove	-1.54	-78.55
	combined	-1.56	-70.01
IPR_09 (HFS, midplane)			
	vessel	-9.85	16.94
	alcove	1.06	67.36
	combined	1.07	85.53
IPR_05 (top)			
	vessel	71.46	-1.84
	alcove	60.95	-4.11
	combined	53.85	-4.47

Table 4-1: Magnetic field at position of representative diagnostic coils IPR_01, IPR_05 and IPR_09 from 6x1 kA current in negative direction. The current is distributed in six wires close to the diagnostic coil in three position variants: bulk vessel, alcove and combination of both. The combination means current flowing in the vessel position for entire toroidal circle with exception of 40 mm around the diagnostic coil, where it flows in the alcove position.

The code for numerical integration of the Biot-Savart law for toroidally symmetrical coil was altered to integrate the magnetic field from two positions of the toroidal coil. The second position is used for toroidal length 40 mm around the position where magnetic field is calculated. The results from this code are summarized in the **Table 3-7**. It is possible to see that a variant when current is flowing at position of the alcove is closer to the combined positions variant. The conclusion is that we can use alcove position in the Induced Currents Module to calculate influence of the vessel currents to the diagnostic coils placed inside of the

vacuum vessel. Similar analysis is necessary for the flux loops located outside of the vessel.

4.3.1 Used discharge

Discharge #7313 will be used to describe induced currents in the COMPASS vacuum vessel. This is a typical ohmic L-mode discharge in SNT divertor configuration with plasma density 5.10^{19} m^{-3} during the plasma current flat-top (1060-1250 ms), requested plasma current -200 kA and with position feedback set to request R = 0.55 m, Z = 0.03 m during the flat-top. The toroidal field is -1.15 T. The shape of the plasma during the flat-top is shown in the **Figure 4.13** and plasma shape evolution is in the **Figure 4.20** in the Section 4.5.

The currents in the PF coils circuits will be described in more detail because they are used here as well as in the Section 4.5 - Global power balance.

Figure 4.5 shows that the plasma breakdown is at 959 ms, followed by quick rise of I_{pl} to -70 kA at 964 ms. The fast rise of the plasma current corresponds to high loop voltage created by fast change of the current in the MFPS circuit. Then the plasma current rises to -185 kA at 1005 ms with slower pace. This corresponds to slower change of the current in the MFPS. As was already explained in the Section 3.1.5 - Characterization of PF coils circuits magnetic fields, the negative MFPS current is controlled by prescribed waveform and settings of the Shaper.

The plasma current is dropping between 1005 - 1020 ms. This drop is caused by the necessity to maintain MFPS current at zero for at least 5 ms when the polarity of the MFPS current is changed. During this time the anti-parallel thyristor Power Supplies are switching their duty. The process is colloquially called "MFPS passing zero". It should be noted that 15 ms duration of the MFPS passing zero is longer than minimal possible 5 ms. The actual duration is influenced by currents in the other circuits which can prevent MFPS maintaining zero current by either direct electrical connection or by mutual inductance. Furthermore the duration of the MFPS passing zero is influenced by time of switching on plasma current feedback. The feedback was activated at 1015 ms and the Power Supply spent 5 ms changing voltage before the MFPS current started to rise and provide loop voltage for the plasma. The plasma current feedback activation at 1015 or 1020 ms is generally used time for many different types of plasma current ramp-up. In this particular discharge, the available V.s of the loop voltage could have been saved and total duration of the discharge prolonged if the plasma current feedback had been activated sooner.

The plasma current rises after 1020 ms, overshoots requested -200 kA and reaches flat-top at 1066 ms. The plasma flat-top lasts until 1222 ms, when shape of the plasma starts to change again. The plasma current is maintained until 1240 ms when feedback controlled plasma current ramp-down starts.

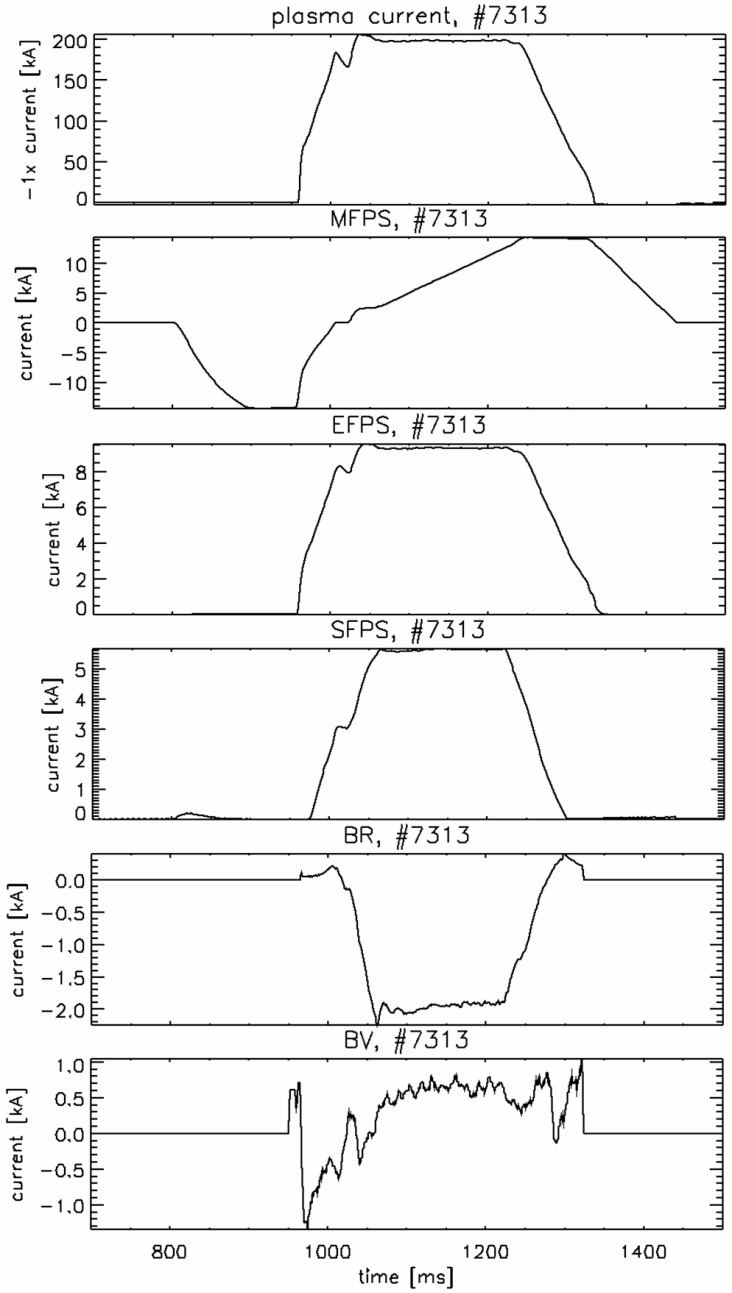

Figure 4.5: Plasma current and PF coils circuits currents of the discharge #7313. The currents are as used by EFIT++, i.e. smoothed with 2 ms moving window average.

The MFPS current request is -14 kA between 800 - 950 ms. The realized MFPS current reaches requested value at ~900 ms, providing time to settle all induced currents to zero before the plasma breakdown is initiated. The request to initiate the breakdown (by discharging capacitor into Shaper thyristors TV1 and TV2 and opening them) is at 950 ms and the actual breakdown starts at 959 ms. The MFPS current behaviour from the breakdown to the MFPS passing zero was described in the previous paragraphs. The MFPS current is controlled by plasma current feedback from time 1015 ms until the end of the discharge. It can be seen that its derivative is

changing between 1020 - 1066 ms to achieve plasma current flat-top. The plasma current flat-top is maintained by slightly changing slope of MFPS current until 1240 ms. The plasma current ramp-down is controlled by feedback, but MFPS current derivative is kept at zero or positive by the feedback. This feedback limitation was introduced to prevent quick changes of plasma current towards zero. The MFPS current decreases down to zero amps between 1325 - 1437 ms, after the end of the plasma.

The EFPS current is controlled by feedback described in the Section 3.1.5. The most significant part of the feedback requested current is directly proportional to the plasma current. It should be noted that the EFPS current dynamics shortly after the breakdown (~ 10 - 20 ms) is greatly influenced by MFPS current, preventing good feedback control. This behaviour was discussed in the Section 3.4.

The SFPS current in the **Figure 4.5** shows that the SF Power Supply cannot maintain zero current when MFPS current is changing between 800 - 900 ms, creating ~200 A in the SFPS. The SFPS requested current is either directly prescribed or proportional to the smoothed plasma current. The proportional constant (parameter) is changing during the discharge and is prescribed by the operator of the tokamak, depending on the requested shape and shape evolution. The SFPS current request had linear ramp from 0 A to 3 kA between 970 - 1005 ms, was constant 3 kA between 1005 - 1020 ms and was controlled by feedback afterwards in the discharge #7313. The plasma current used for feedback was smoothed by 13 ms wide moving average. The SFPS current request was proportional to the plasma current by constant (parameter) 0.019 - 0.028 between 1020 - 1060 ms (linear change), 0.028 between 1060 - 1220 ms and 0.028 - 0.0 between 1220 - 1300 ms. The ratio between the SFPS current and the plasma current during the flat-top controls mainly poloidal area of the plasma. The value 0.028 corresponds to larger plasma than 0.031. These two values are commonly used. The SFPS circuit configuration in the discharge #7313 was SNT.

It should be noted that the SFPS current reaches flat-top later than plasma current flat-top is achieved and leaves flat-top sooner. This setting allows easier work for the feedback system. The simultaneous control of the shape and plasma current is difficult because the changes of the SFPS current produce significant loop voltage and change the plasma current.

Both BR and BV circuits currents are controlled by the plasma position feedback. The BV circuit has additional waveform superimposed on the radial position feedback request: there is 600 A between 950 - 960 ms, followed by ramp down to 0 A at 1000 ms.

4.3.2 Description of the vessel currents

The COMPASS vacuum vessel has total toroidal resistance 0.5 mΩ and time constant ~ 0.5 ms [40]. This relatively fast time constant has several consequences:

- the vacuum vessel does not filter thyristor Power Supplies caused noise (720 - 2040 Hz, see Chapter 3, Section 3.3)

- the vertical plasma position is passively stabilized with this time constant by the vessel
- the magnetic field passing either to or from the vessel is dampened by induced vessel currents which have this effective time constant

Furthermore, the vacuum vessel toroidal resistance determines the amplitude of the induced currents.

The current waveforms showed in the **Figure 4.5** are input into the Induced Currents Module in the EFIT++. The vacuum vessel was represented by 205 individual *R*, *Z* coordinates taken from the vacuum vessel drawing for both "bulk" and "alcove" vessel position. The coordinates were grouped into 10 passive structures for the purpose of the calculation of induced currents. The EFIT response functions (signals in magnetic detectors) were calculated for alcove vessel positions. The induced currents were calculated for bulk vessel positions. The resistances of the individual passive structures were calculated from the geometry of the vessel and from the 3 mm thickness of Inconel 625. The influence of the diagnostic ports on the top, LFS and bottom of the vessel to the resistances was neglected.

The decision to divide the vacuum vessel into 10 passive structures is based on the fact that ICM calculates mutual and self-inductances from passive structures sub-elements, taking into account all 205 *R*, *Z* coordinates. Ten passive structures mean that there will be ten different currents calculated and distributed into them. Higher number of passive structures was used with negligible difference in the results.

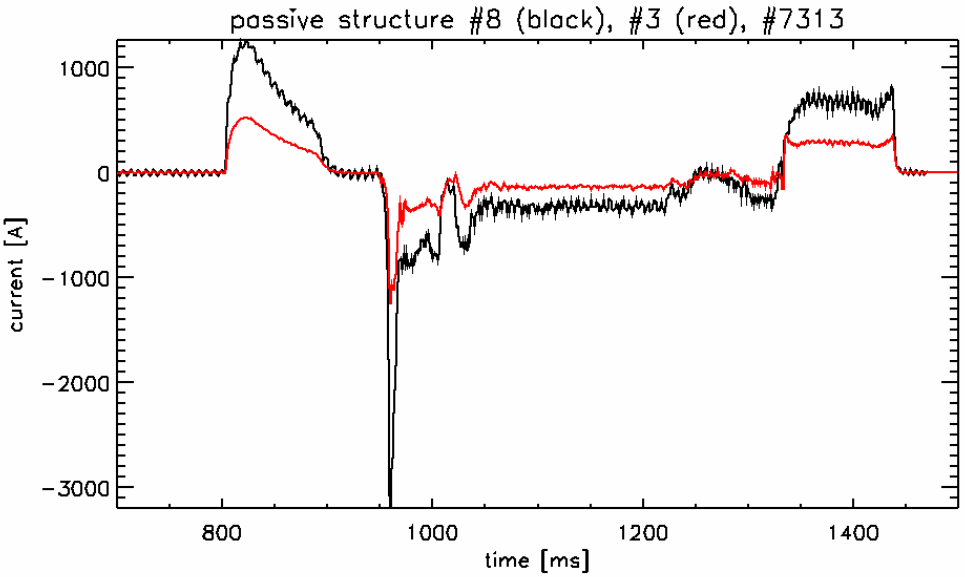

Figure 4.6: Calculated current in the passive structure on the HFS (#8, black line) and on the LFS (#3, red line). Vacuum vessel is represented by 10 passive structures. Input currents into the ICM are smoothed by 100 μs moving average window, then the induced currents are smoothed by 2 ms moving average before being saved and passed into the equilibrium calculation.

Figure 4.6 shows calculated induced currents for the discharge #7313 in two passive structures on the HFS and on the LFS of the tokamak. Passive structure #8 is

located on the HFS, on the midplane. It is represented by 21 thin wires where ten wires above the midplane are symmetrical with ten below the midplane. There is one additional wire below the midplane, therefore the passive structure #8 is not up-down symmetrical against the midplane. The vertical dimension of this passive structure is <-0.103234, 0.093402> m. The resistance of the passive structure is 4.24 mΩ.

Passive structure #3 is located on the LFS, is represented by 21 wires. It has 15 wires symmetrical with respect to the midplane, remaining 6 are above the midplane. The vertical dimension is <-0.67494, 0.122788> m. The resistance is 10.03 mΩ.

The **Figure 4.6** shows that the current induced to the HFS part of the vacuum vessel is higher than the current induced to the LFS. The reason is that the resistance on the HFS is lower than on the LFS. Furthermore it can be seen that the LFS current is smoother, which is caused by higher effective time constant L/R. It should be noted that the oscillations visible on the current of the HFS passive structure #8 in the **Figure 4.6** are caused by aliasing to the 12-pulse thyristor frequency of the Power Supplies. The flywheel was slowing down from 1500 rpm to 1350 rpm, yielding frequencies 900 - 810 Hz.

A comparison of the induced currents waveforms with respect to HFS and LFS passive structure is in the **Figure 4.7**. The figure is identical to the **Figure 4.6**, but induced current in the LFS passive structure #3 is normalized to passive structure #8. The shape of the current waveforms is almost similar, which can be expected. The effective time constant of the vacuum vessel is 0.5 ms, which is smaller than the time resolution visible in the **Figure 4.7**. Therefore the induced currents are governed by the applied voltage and by resistance of the passive structures on this time scale, with passive structures self-inductance playing minor role.

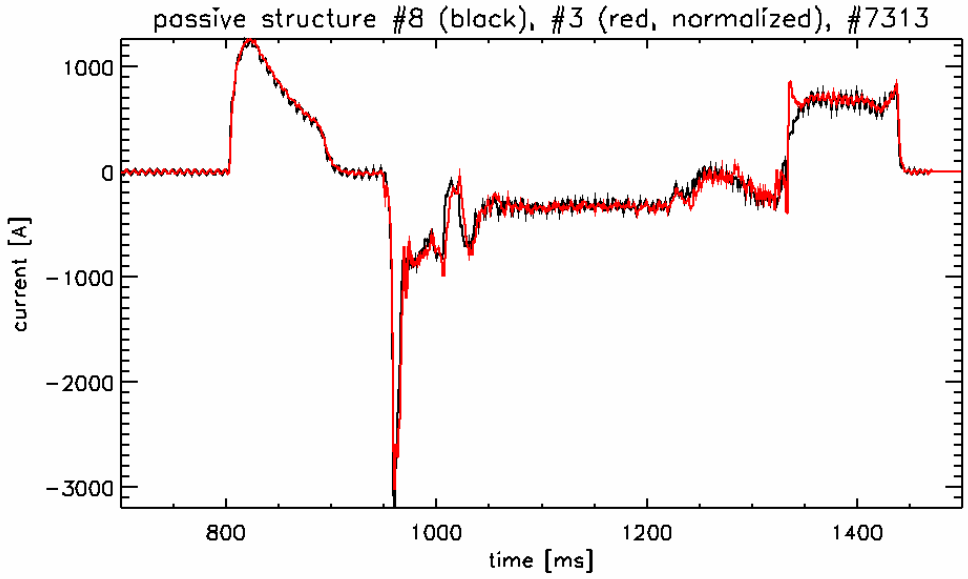

Figure 4.7: Normalized calculated current in the passive structure on the LFS (#3, red line) against passive structure on the HFS (#8, black line, not normalized).

Figure 4.8 shows comparison between measured and calculated total vacuum vessel current. The measured vacuum vessel current is obtained from difference

between Rogowski coils placed inside and outside of the vacuum vessel. The calculated induced currents agree with the measured signal.

It can be seen that the total current in the vessel is between -1.5 and -3 kA during the plasma current flat-top (see **Figure 4.5**). This value is small compared to the plasma current -200 kA and corresponds to the loop voltage -1.2 V and resistance of the vessel 0.5 mΩ. The ratio between the vessel current and the plasma current is much higher during the breakdown of the plasma. The vessel current goes up to -25 kA while plasma current is around -20 kA at that moment. The total vessel current is also significant during the MFPS current change from 0 A to -14 kA (800 - 900 ms) and from 14 kA to 0 A (1325 - 1437 ms).

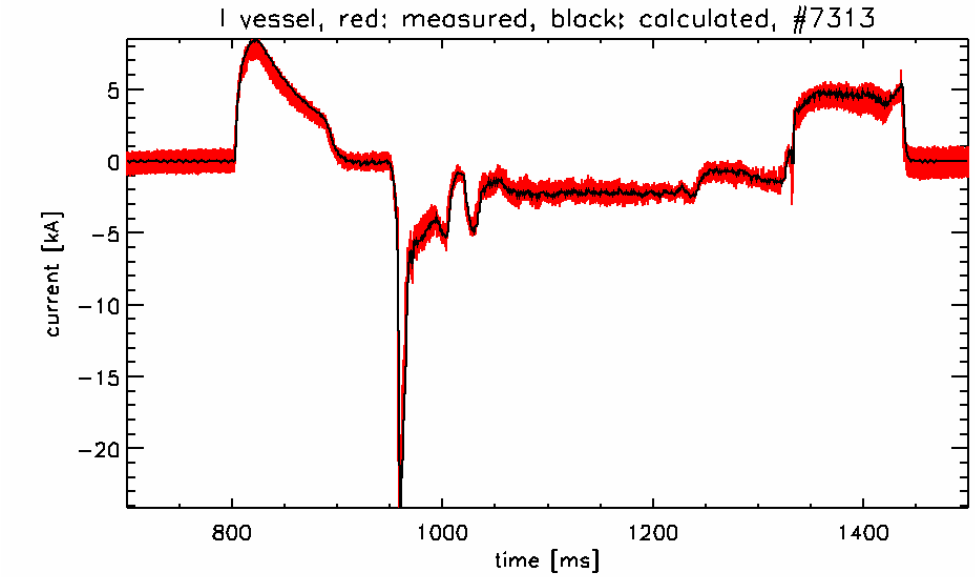

Figure 4.8: Comparison between measured and calculated total vacuum vessel current. The input currents into the ICM are smoothed by 100 μs moving average window, shown induced current is smoothed by 2 ms moving average.

Furthermore the **Figure 4.8** shows that the measured total vessel current has noise ~2 kA, while the calculated current has lower noise. This is caused by the smoothing of the calculated current.

The structure of the noise is shown in the **Figure 4.9** which compares measured and calculated total vessel current with less severe smoothing in the calculated data. The measured vessel current shows oscillations with frequency 840 Hz, which is 12-pulse thyristor Power Supply noise from flywheel with frequency 1400 rpm. The behaviour of the calculated vessel current is different. The amplitude of the fluctuations matches the measured signal, but frequency of the oscillations is halved.

Explaining the difference between the structure of measured and calculated total vessel current requires detailed analysis of the situation. The data necessary for the analysis are in the **Figure 4.10**. The first signal is the MFPS current which is responsible for the loop voltage during the plasma current flat-top (1100 - 1130 ms is in flat-top). It is possible to see that the derivative of the MFPS current is changing with frequency 420 Hz (2.38 ms). This behaviour is better demonstrated by second

signal in the **Figure 4.10**: derivative of the MFPS current multiplied by the mutual inductance to the plasma (22 μH). This signal is part of the effective loop voltage acting on the plasma column. The oscillation period 2.38 ms is better visible than in the direct MFPS current signal. Both EFPS and SFPS currents depicted in the **Figure 4.10** show oscillations with frequency 840 Hz, same as plasma current (not depicted).

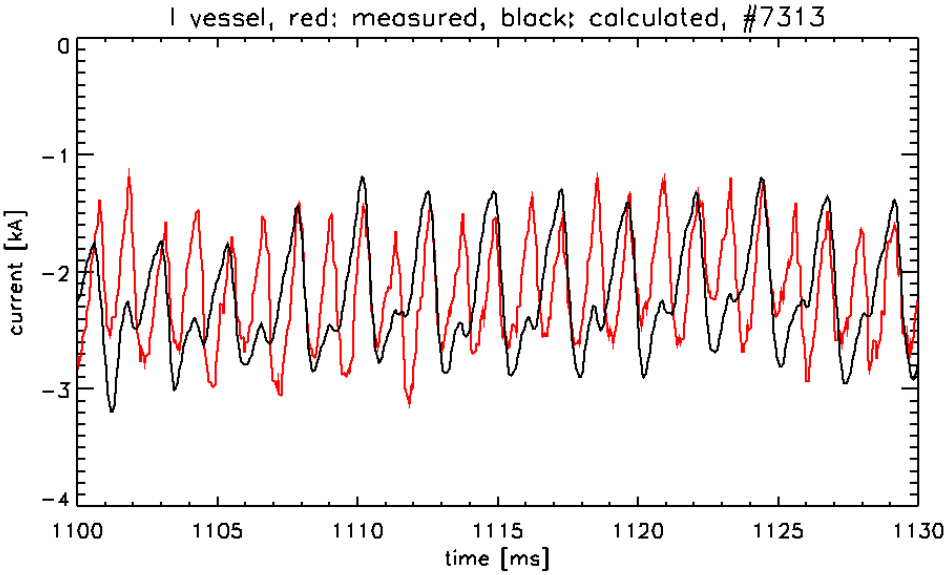

Figure 4.9: Detail of comparison between measured and calculated total vacuum vessel current during the plasma current flat-top. In this case the input currents into the ICM are smoothed by 100 μs moving average window as well as shown induced current.

The Induced Currents Module calculates the induced currents from the PF coils circuits currents and from the plasma current with assumption of user defined elliptical plasma current profile at fixed position. The last signal in the **Figure 4.10** shows the movement of the plasma column radial position. It can be seen that the radial position is changing by 1 mm with frequency 420 Hz.

This movement can possibly explain the difference between the measured and ICM calculated total vessel current in the **Figure 4.9**. The radial plasma position has oscillations locked to the half of the actual loop voltage oscillations frequency 840 Hz. When the plasma column is moving towards HFS, the magnetic field on the major axis (central solenoid) is increasing its amplitude while having direction downwards. This change of the magnetic flux induces positive voltage in the vacuum vessel, creating positive induced current. These positive induced current spikes are visible in the **Figure 4.9** on the measured signal and are missing on the ICM calculated signal.

It would be necessary to include the radial plasma movement into the ICM in order to validate the explanation. This is in principle possible because the structure of the module was prepared to take the plasma column representation from the EFIT reconstructed equilibria. This possibility would require running the ICM, calculating

the equilibria for multiple times and then running ICM again. This solution was not further pursued.

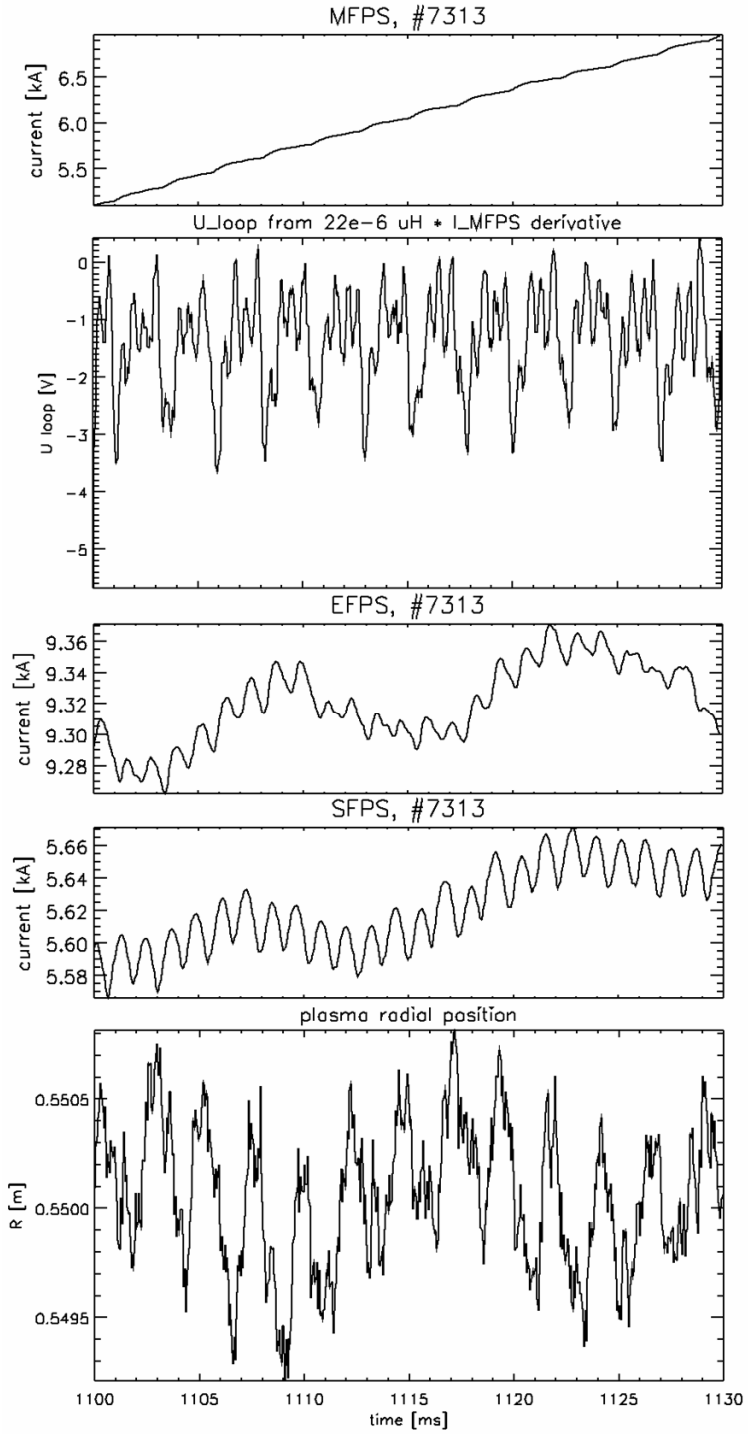

Figure 4.10: Signals for explanation of the **Figure 4.9**.

Another possible explanation of the inconsistency in the **Figure 4.9** can be in the reliability of either measured total vacuum vessel current or input currents into ICM. The measured total vacuum vessel current was validated from two sources: difference between internal and external full Rogowski coil and from numerically

integrated and summed 16 External Partial Rogowski coils. Both results show that this measurement is correct.

The measurement of the input currents into the ICM is less reliable. While the low frequencies and absolute values of the MFPS, EFPS, SFPS BR and BV are believed to, the MFPS current oscillations with 420 Hz in the **Figure 4.10** are suspicious. The oscillations are responsible for very significant loop voltage change (3 V after smoothing, **Figure 4.10**, second panel), but the voltage measured on the AD converter has oscillations with amplitude ~5 mV. This is only ~2 x more than the noise of the data acquisition system. The MFPS current signal is going through an analogue integrator before being sampled. It is possible that the signal is influenced by overhearing from the nearby channels. This possibility is supported by the fact that the shape of the ICM calculated current does not agree with measured vessel current during vacuum phase of the discharge (e.g. t = 700 ms, see **Figure 4.11**).

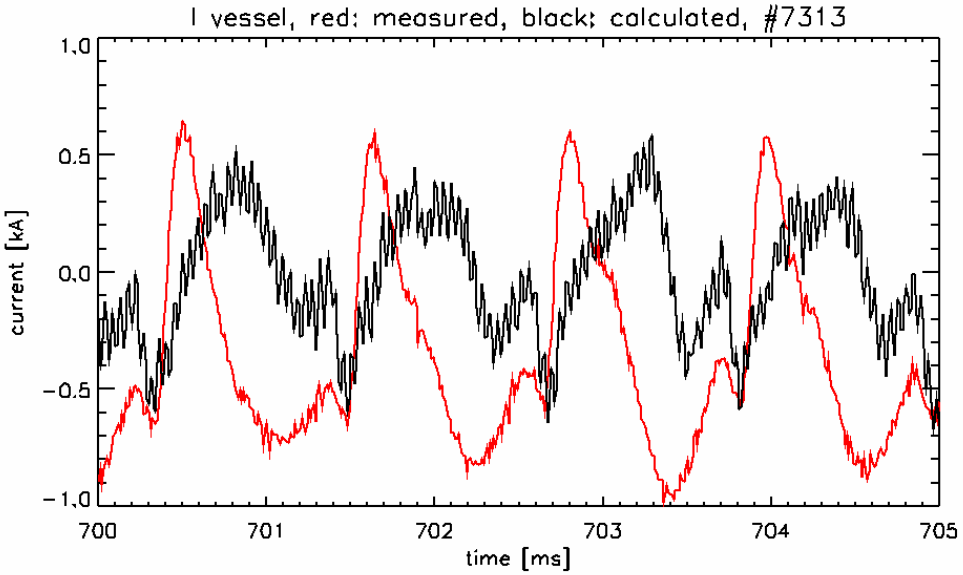

Figure 4.11: Detail of comparison between measured and calculated total vacuum vessel current during the vacuum phase of the discharge (before breakdown). The input currents into the ICM are smoothed by 100 μs moving average window as well as shown induced current.

On the other hand, the fluctuations in the **Figure 4.11** have similar frequency for both measured and calculated total vessel induced current. Therefore we can conclude that the presence of the plasma is the reason for the 420 Hz ICM currents fluctuations in the **Figure 4.9** regardless of whether the origin of the behaviour is radial movement of the plasma column or quality of the MFPS current signal.

4.3.3 Influence on the COMPASS equilibrium

The Induced Currents Module influence on the calculated equilibrium of the COMPASS tokamak was assessed.

The **Figure 4.8** shows that the total vessel current during the typical discharge (#7313) is between -1.5 kA to -3 kA during the flat-top and -25 kA during and after

the plasma breakdown. The total vessel current can be up to 40 kA when higher loop voltage is used during the plasma breakdown, depending on the MFPS and Shaper settings.

The influence of the ICM on the reconstructed equilibria is shown in the **Figure 4.12** and in the **Figure 4.13**.

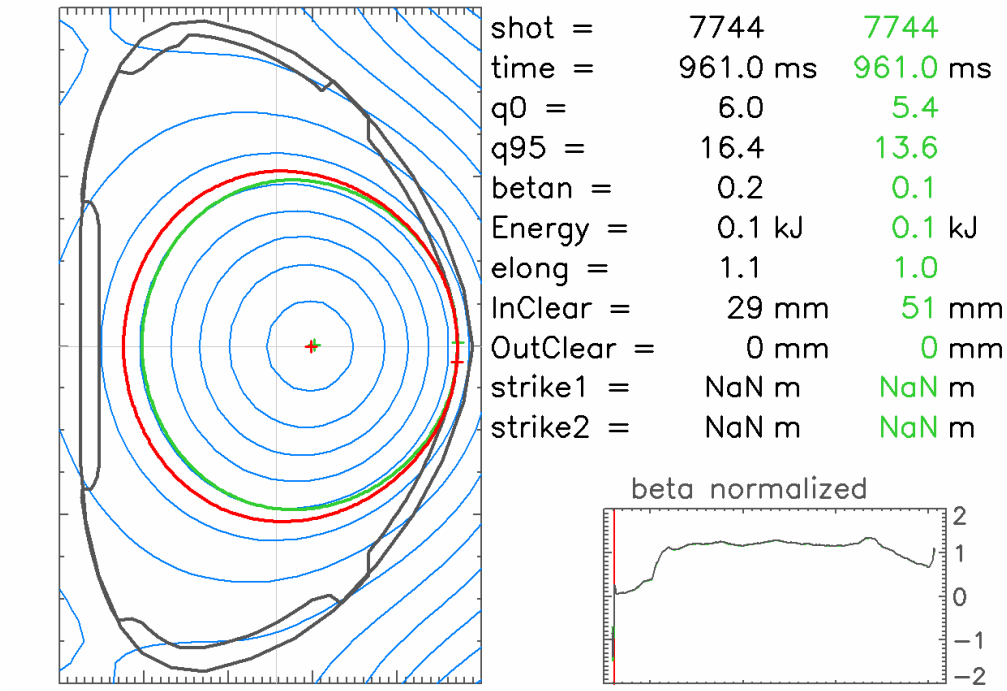

Figure 4.12: Comparison of reconstructed equilibrium just after the plasma breakdown. The plasma current is ~ -20 kA, comparable with the total vessel current (~ -20 kA). Black data (red LCFS) are without ICM, green data (green LCFS) are with ICM activated.

Figure 4.12 shows ICM influence on the reconstructed equilibrium during the start of the plasma. The plasma breakdown occurred at 956.5 ms and the plasma current rose to ~ -20 kA at 961 ms in the discharge #7744. The total vessel current was comparable with plasma current at that moment. The equilibrium with the vessel current accounted is significantly different compared to the equilibrium reconstructed without the vessel current. The Last Closed Flux Surface (LCFS) is 22 mm smaller when vessel current is accounted and profile of the safety factor is different (q0 and q95 in the **Figure 4.12**).

Figure 4.13 shows that the inclusion of the calculated induced currents has negligible influence on the reconstructed equilibria during the flat-top of the typical COMPASS discharge. The plasma current in the **Figure 4.13** is -200 kA, which is a lower value between typically used -180 kA to -350 kA plasma currents for diverted plasma. This negligible influence was observed for both circular and diverted plasmas for wide variety of plasma positions and plasma currents, both during the flat-top and during the ramp-up and ramp-down, when total vessel current is significantly smaller than plasma current.

The negligible influence of the induced currents on the reconstructed equilibria can be understood with the help of the **Table 3-7**, the **Figure 4.6** and the knowledge that the Internal Partial Rogowski coil 09 (HFS) has signal -0.34 T during the flat-top in the discharge #7313.

The **Table 3-7** shows that the IPR_09 signal from six thin wires, each with -1 kA current, is 85.53 mT. The **Figure 4.6** shows that the current in the passive structure #8 (HFS) is -300 A. The passive structure #8 has ~20 cm height, compared to ~3 cm height of six wires used in **Table 3-7**. Therefore the induced currents signal in the IPR_09 can be roughly estimated as $85.53\,\mathrm{mT}\cdot\frac{300\,\mathrm{A}}{6000\,\mathrm{A}}\cdot\frac{3\,\mathrm{cm}}{20\,\mathrm{cm}}\cong 0.64\,\mathrm{mT}$. The signal in the IPR_09 properly calculated by the ICM from -300 A in the passive structure #8 is 0.75 mT. Consequently, the magnetic signal from the current induced in the vacuum vessel is negligible against measured signal -0.34 T.

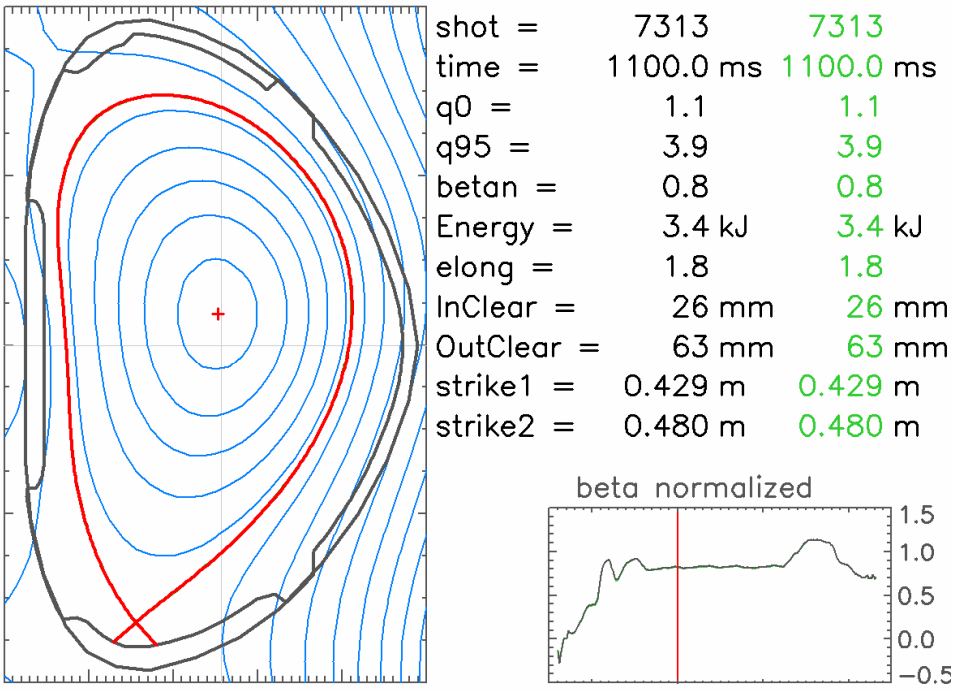

Figure 4.13: Comparison of reconstructed equilibrium during the flat-top. The plasma current is -200 kA, while the total vessel current is between -1.5 kA and -3 kA. Black data (red LCFS) are without ICM, green data (green LCFS) are with ICM activated. The plasma shapes of both reconstructions are identical.

The conclusion is that the COMPASS tokamak vacuum vessel with its toroidal resistance 0.5 mΩ and time constant ~0.5 ms has insignificant influence on the plasma MHD equilibrium with the exception of time period several ms after the plasma breakdown. The influence of the vacuum vessel on the plasma vertical position passive stabilization is out of the scope of this thesis and is not discussed here.

4.4 Utilization of EFIT

This section is focused on the utilization of the EFIT++ for COMPASS operation. The EFIT equilibrium reconstruction performed on the inter-shot basis is described. Then the various possible shapes of the plasma column are shown and described from the point of view of tokamak operation.

4.4.1 EFIT automatic run

The EFIT++ is run automatically after each discharge and a movie with reconstructed equilibria is produced and shown on the screen in the COMPASS control room. The process is described in the following text.

The script running the EFIT waits for the end of the data collection of the "ATCA1" computer, loads measured data, resamples them from 2 MS/s to 20 kS/s, numerically removes drift of the analogue integrators and saves data into a CDF (Computable Document Format) file.

The removal of the drift is performed by subtracting linear function fitted in time between 500 ms and 800 ms. This time period is specifically reserved for constant magnetic fields in the discharge sequence: Toroidal Field reaches flat-top shortly after 500 ms and first poloidal magnetic field (MFPS circuit) starts at 800 ms.

The EFIT is run after the CDF file with input data is created. This "standard" EFIT run uses limited set of the input signals and constrained degrees of freedom in the EFIT algorithm. The used inputs are: 16 Internal Partial Rogowski coils, 5 currents in the PF coils circuits, plasma current and toroidal magnetic field in the form of $B_T \cdot R$ product. All of the input data are linearized and smoothed with 2 ms moving average window defined in the EFIT configuration file "efitOptions.xml". Some of the measured input data can be disabled in particular discharges if the diagnostic coil did not work properly.

The equilibrium is reconstructed in the 33x33 grid with R = <0.3, 0.8> m and Z = <-0.4, 0.4> m. The $\partial p/\partial \psi$ and $\partial\left(F^2\right)/\partial \psi$ (see Equations (4.31) and (4.32)) are represented as 1st order polynomials. This fact limits the degrees of freedom of the EFIT reconstructed equilibria. Second order polynomials can be used, but only with manual check of the results, not in automatic run. Further constraints may be required: specification of the safety factor value in the plasma centre (q_0) or information about plasma pressure.

The EFIT is run from 970 ms with equilibrium calculated each 1 ms until the end of the discharge. The decision to not compute equilibria during the beginning of the plasma (breakdown is between 956-962 ms, depending on MFPS and Shaper settings) was caused by unreliable behaviour of the plasma in this time - particularly radial position is sometimes strongly oscillating. The equilibria reconstructed in this time period do not provide information useful to operators running the tokamak. The script running the EFIT has to deal with a known bug: EFIT++ occasionally crashes when it fails to trace the LCFS geometry in one particular time slice. In this case the script removes the problematic time slice from the run and attempts to perform the

run again. The result is that time axis of the EFIT produced data in the COMPASS DataBase (CDB) is not equidistant.

The result of the EFIT++ run is saved in a NetCDF file and then instances of EFIT signals are created in the CDB. EFIT calculates ψ function and a number of derived parameters for each requested time.

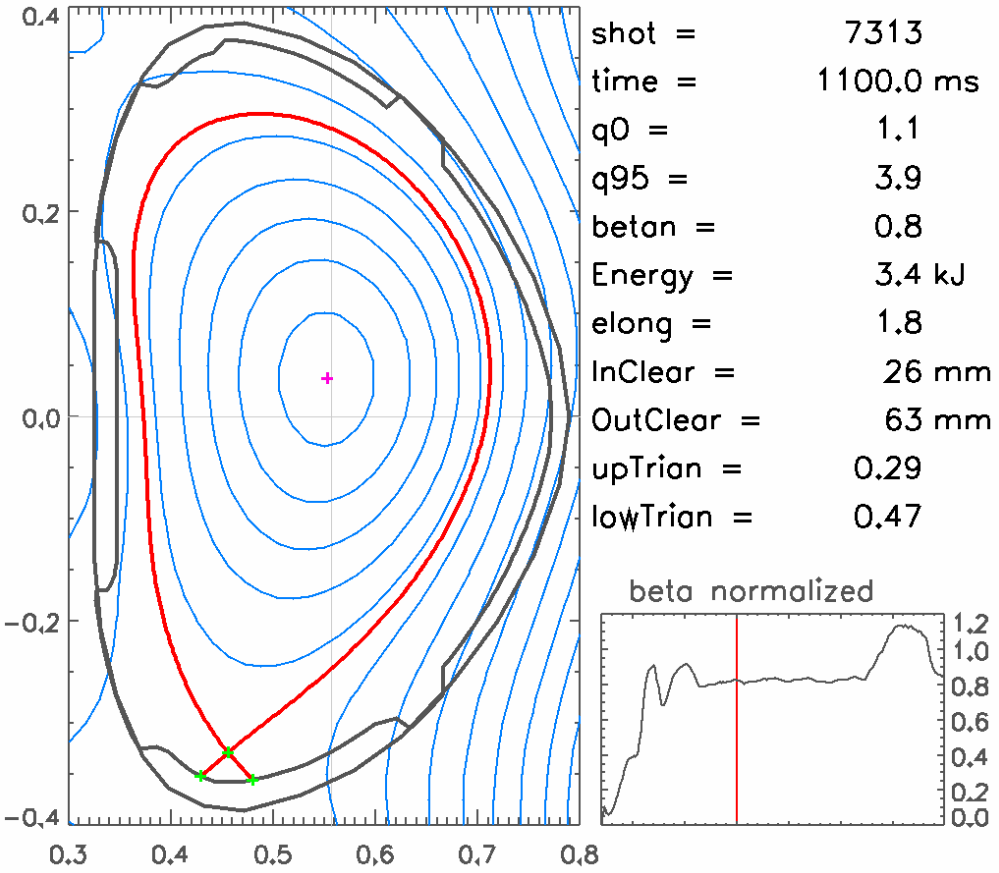

Figure 4.14: Caption from the movie prepared on inter-shot basis for discharge #7313.

Figure 4.14 shows caption from the movie produced by the EFIT script. The separatrix of the plasma is shown on the left and some important parameters calculated by EFIT++ are on the right. The parameters include safety factor in the plasma centre and on the edge (q_0, q_{95}), normalized beta β_N, EFIT reconstructed plasma energy, elongation of the plasma, clearances between separatrix and limiter on the midplane on the HFS (InClear) and on the LFS (OutClear) and upper and lower triangularity of the plasma.

The upper triangularity is defined as:

$$\delta_{upper} = \left(R_{geo} - R_{upper}\right)/a, \tag{4.52}$$

where $a = \left(R_{\max} - R_{\min}\right)/2$ is minor plasma radius, $R_{geo} = \left(R_{\max} + R_{\min}\right)/2$ is geometric major radius and R_{upper} is major radius of the highest vertical point of the LCFS. A similar definition exists for lower triangularity.

The definition of the normalized beta is:

$$\beta_N = \beta \frac{aB_T}{I_{pl}}, \tag{4.53}$$

where B_T is toroidal magnetic field in T, a is the minor radius in m and I_{pl} is plasma current in MA. The beta is defined as $\beta = \frac{\langle p \rangle}{B^2/2\mu_0}$, where B is mean total (poloidal + toroidal) magnetic field and p is plasma pressure. The normalized beta is limited by either Troyon limit 2.8 % or by empirical scaling 3.5 %.

The movie, as well as data stored in the CDB, is used by tokamak operators to determine the action necessary to achieve the physical program of the campaign. Particularly the shape of the plasma and clearances to the limiter are in the centre of interest of physicists. The clearances on the HFS, on the LFS, on the top LFS (to the LFS limiter at $Z = 0.25$ m) and height of the X-point are important parameters of the Scrape-Off Layer (SOL) and are therefore important for plasma edge diagnostics.

4.4.2 Examples of plasma shapes

The shape of the plasma is controlled by three parameters: ratio between the current in the SFPS circuit and in the plasma column, R position of the plasma centre and Z position of the plasma (see Section 3.1.5).

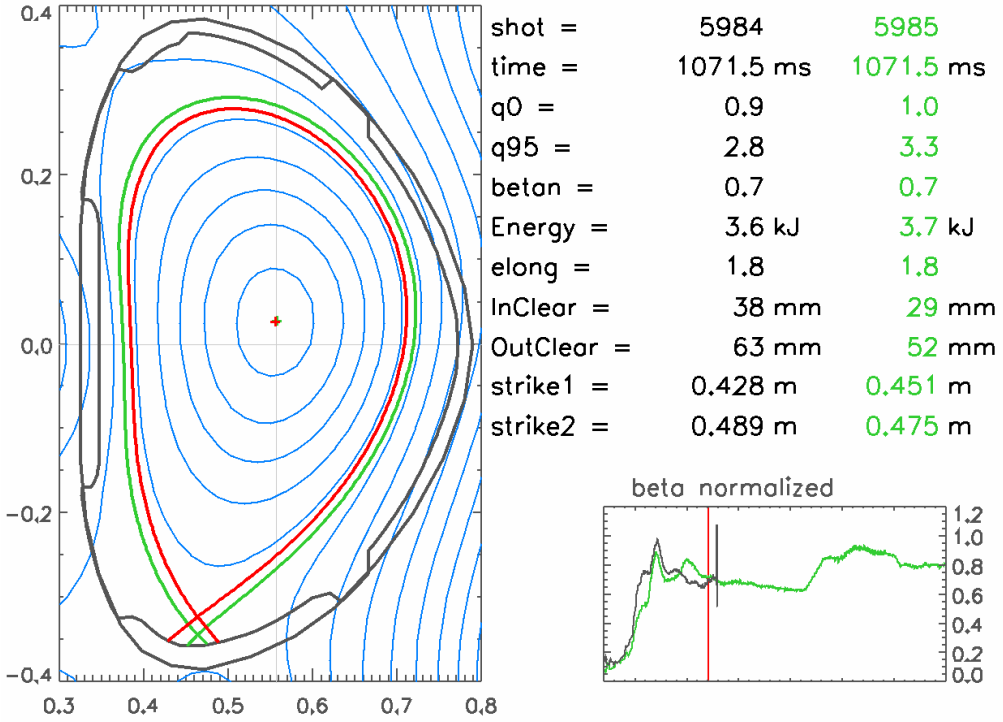

Figure 4.15: Comparison of reconstructed equilibrium for two plasmas with different ratio of I_{SFPS}/I_{pl}. Black data (red LCFS, #5984) are with $I_{SFPS}/I_{pl} = 0.032$, green data (green LCFS, #5985) are with $I_{SFPS}/I_{pl} = 0.028$.

Figure 4.15 shows equilibrium reconstruction of two COMPASS discharges with identical flat-top plasma current -240 kA, radial position $R = 0.55$ m and vertical position $Z = 0.02$ m (feedback settings, not actual position of the magnetic

axis). The difference between the discharges is ratio between the SFPS circuit current and plasma current. Larger ratio ($I_{SFPS}/I_{pl} = 0.032$) leads to the smaller plasma with identical elongation (1.8), identical upper triangularity (0.24) and slightly higher lower triangularity (0.50 vs. 0.47) and lower q_{95}. The smaller plasma is vertically less stable and the discharge ended because of insufficiently controlled vertical position. The vertical stability can be enhanced by moving plasma radially towards the LFS, thus increasing mutual inductance between the plasma and vacuum vessel.

It is not straightforward to understand why the elongation is kept and plasma poloidal area is changed when I_{SFPS}/I_{pl} is changed. The physical intuition would advise that higher I_{SFPS}/I_{pl} would lead to higher elongation and increased plasma poloidal area. It is necessary to understand the X-point area to explain the decreased poloidal area. The X-point has a zero poloidal magnetic field and it is actually a saddle point in the ψ function profile. The increase of the I_{SFPS} with constant I_{pl} moves ψ function saddle point towards the plasma column, reducing the area enclosed by the separatrix. This mechanism is accompanied by change of the separatrix shape caused by changed current in the SFPS windings around the entire plasma column.

Typically used values of the I_{SFPS}/I_{pl} ratio are 0.028 and 0.031 for "large" and "small" plasma.

Figure 4.16 shows influence of the vertical position on the plasma shape. The vertical position is set by tokamak operator in the feedback system configuration files. The used discharge is #8171, where plasma vertical position was continually changed during the plasma current flat-top. The purpose was to investigate the influence of the X-point height on the L-H transition. The plasma current was kept constant (-210 kA), as well as radial plasma position ($R = 0.555$ m) and ratio I_{SFPS}/I_{pl} (0.031). All four panels in the **Figure 4.16** show separatrix at the time $t = 1132$ ms, when feedback set plasma vertical position was $Z = 0.02$ m. The separatrix is depicted by red line and blue lines are appropriate magnetic surfaces. The green line depicts separatrix shape at different plasma vertical positions:

1. All panels (red): $t = 1132$ ms, $Z = 0.02$ m, $\delta_{upper} = 0.25$, $\delta_{lower} = 0.50$
2. Top left panel: $t = 1100$ ms, $Z = 0.03$ m, $\delta_{upper} = 0.27$, $\delta_{lower} = 0.46$
3. Top right panel: $t = 1144$ ms, $Z = 0.01$ m, $\delta_{upper} = 0.23$, $\delta_{lower} = 0.53$
4. bottom left panel: $t = 1161$ ms, $Z = 0.00$ m, $\delta_{upper} = 0.21$, $\delta_{lower} = 0.55$
5. Bottom right panel: $t = 1180$ ms, $Z = -0.01$ m, $\delta_{upper} = 0.18$, $\delta_{lower} = 0.55$

The vertical position used in this example is a position used in the feedback system, determined by the algorithm described in [Attached publication A2], [Attached publication A3]. This position is an artificial signal close to the current centre of the plasma, not to the position of the magnetic axis. The vertical position of the magnetic axis is 0.038 m when $Z = 0.03$ m and 0.0 m when $Z = -0.01$ m.

The overall triangularity of the plasma column does not change significantly (0.365-0.38), but upper and lower triangularities change significantly, as well as overall shape of the plasma.

The typically used value of plasma vertical position is from $Z = 0.01$ m to $Z = 0.03$ m.

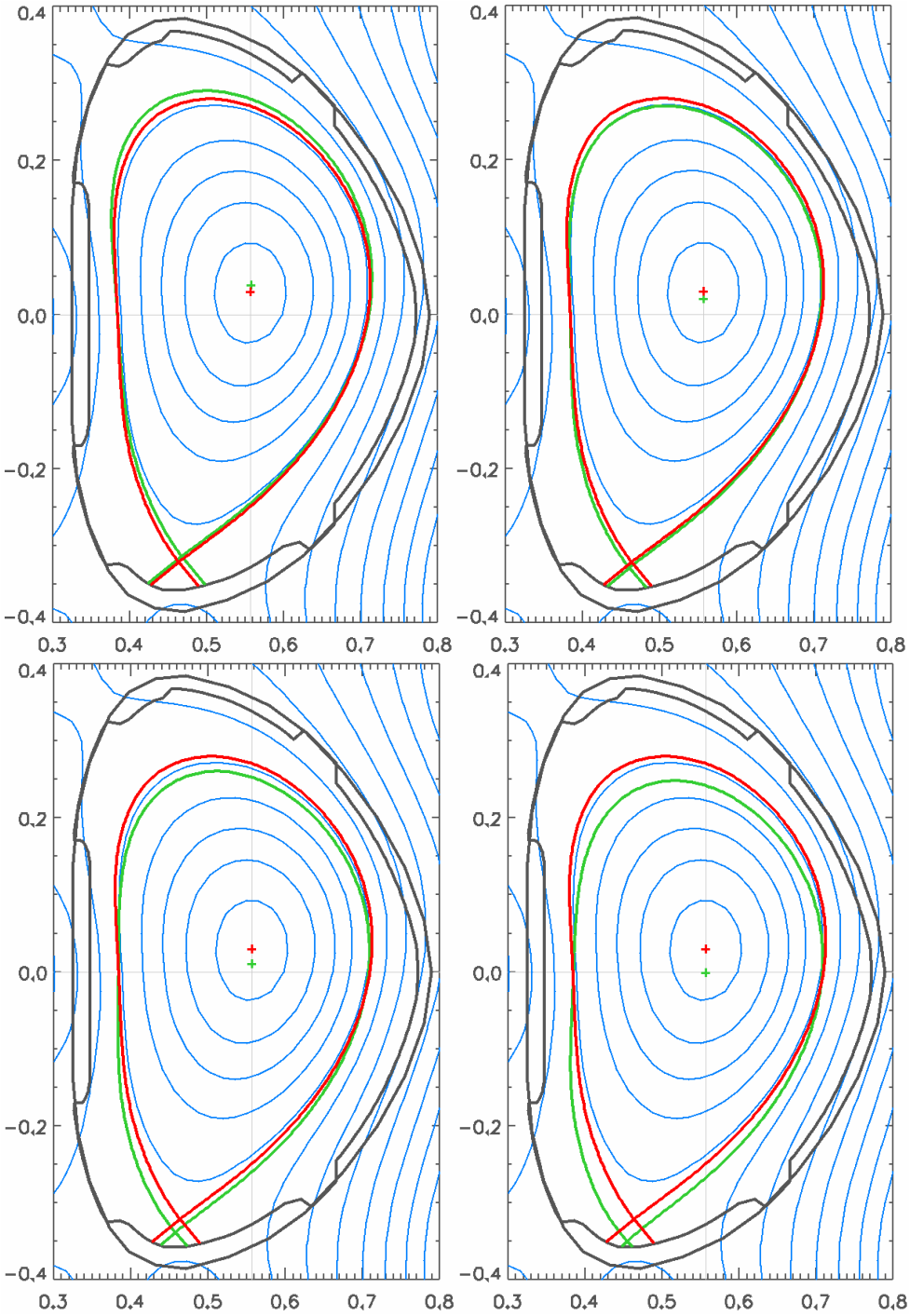

Figure 4.16: Influence of different vertical positions on otherwise similar plasma. Discharge #8171, I_{pl} = -210 kA, $I_{SFPS}/I_{pl} = 0.031$, R = 0.555 m. Red separatrix on all panels: Z = 0.02 m. Green separatrix on top left panel: Z = 0.03, top right: Z = 0.01 m, bottom left: Z = 0.0 m, bottom right: Z = -0.01 m. Note that the values are feedback settings (~current centre) and actual position of the magnetic axis is slightly different.

Figure 4.17 and **Figure 4.18** show influence of the radial position on the plasma shape. The used discharge is #9690, where plasma radial position was continually changed to sweep strike points over the divertor probes.

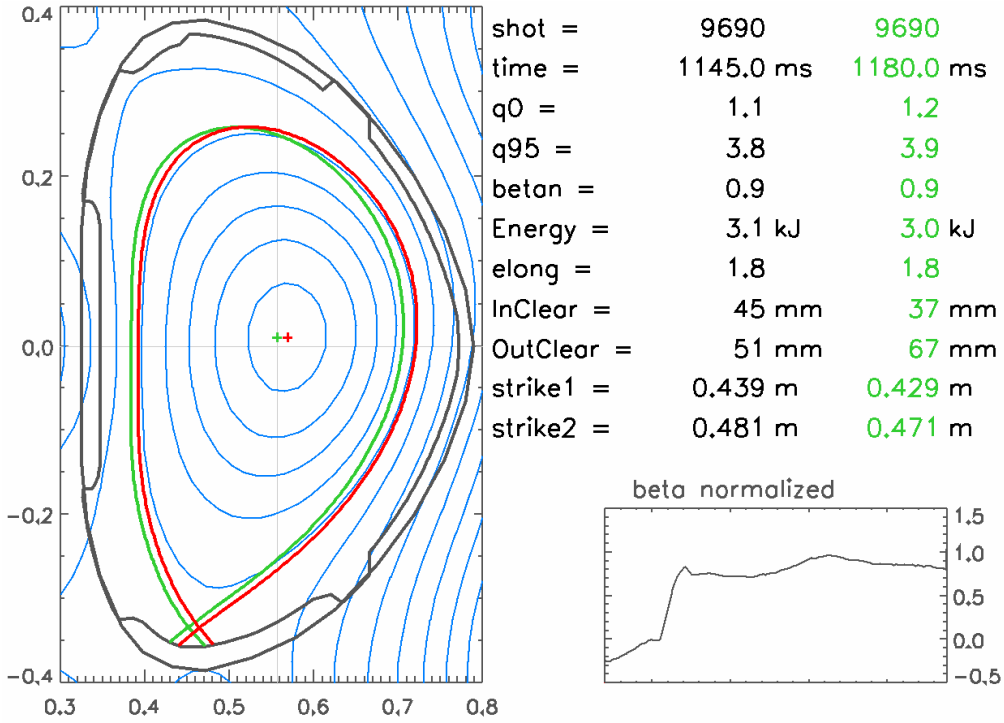

Figure 4.17: Influence of radial position on otherwise similar plasma. Discharge #9690, I_{pl} = -170 kA, I_{SFPS}/I_{pl} = 0.031, Z = 0.0 m. Red separatrix, black data: R = 0.5675 m, t = 1145 ms. Green separatrix, green data: R = 0.555 m, t = 1180 ms. Note that the values are feedback settings (~current centre) and actual position of the magnetic axis is slightly different.

The plasma current was kept constant (-170 kA), as well as the vertical plasma position (Z = 0.0 m) and ratio I_{SFPS}/I_{pl} (0.031). The plasma positions shown in the **Figure 4.17** and **Figure 4.18** are:

1. Both figures (red): t = 1145 ms, R = 0.5675 m, $\delta_{upper} = 0.21, \delta_{lower} = 0.56$
2. **Figure 4.17** (green): t = 1180 ms, R = 0.555 m, $\delta_{upper} = 0.24, \delta_{lower} = 0.58$
3. **Figure 4.18** (green): t = 1110 ms, R = 0.58 m, $\delta_{upper} = 0.19, \delta_{lower} = 0.55$

The upper triangularity changes in similar magnitude as in vertical plasma movement described previously, the lower triangularity changes less than in the vertical movement example. The poloidal area of the plasma is 0.149 m^2 for R = 0.58 m, 0.1445 m^2 for R = 0.5675 m and 0.141 m^2 for R = 0.58 m in this example discharge. The change of the poloidal area is ~6 %.

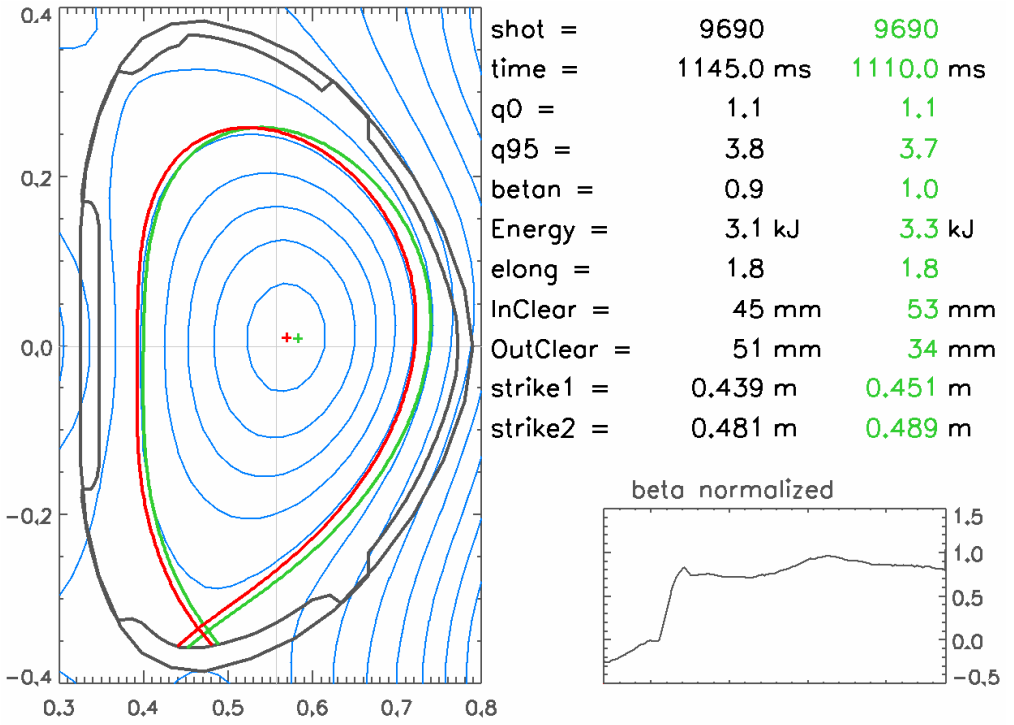

Figure 4.18: Influence of radial position on otherwise similar plasma. Discharge #9690, I_{pl} = -170 kA, I_{SFPS}/I_{pl} = 0.031, Z = 0.0 m. Red separatrix, black data: R = 0.5675 m, t = 1145 ms. Green separatrix, green data: R = 0.58 m, t = 1110 ms. Note that the values are feedback settings (~current centre) and actual position of the magnetic axis is slightly different.

The importance of the EFIT reconstruction for the tokamak operation is crucial. This section described the automatic EFIT run settings on the COMPASS tokamak and discussed some of the possible plasma shapes and which of the operator controlled parameters can achieve them in current situation of the COMPASS plasma shape control. An upgrade of number of individual Power Supplies dedicated to the plasma shape control would be necessary for increase of the flexibility. Regardless, the currently available shapes of the plasma are sufficient for the COMPASS scientific programme.

4.5 Global power balance

This section is extended form of the article Havlicek et al., *Global Power Balance in Non-Stationary Discharge Phases in the COMPASS Tokamak* [58]. More detailed discussion of results and more examples were added in comparison with the original article.

The global power balance between different input power and sink/loss channels is important for understanding of tokamak physics. It has been studied to estimate minimum auxiliary heating necessary to fulfil Lawson criterion in future self-sustained tokamak-based fusion reactors, see e.g. [76]. After the discovery of the H-mode in tokamaks, terms of the power balance entered many scaling laws describing the plasma state at the transition (L-H threshold) or directly in H-mode [77]. Later, it

was found that the edge plasma instability called Edge Localized Mode (ELM) often occurs in H-mode, and depends strongly on the power balance.

ELM frequency changes with the power through Last Closed Flux Surface (LCFS) and the basic ELM classification is based on the slope of the dependence [78]. Type III ELMs repetition frequency decreases with the power through the separatrix (separatrix is LCFS in diverted plasma), while type I ELMs have increasing ELM repetition frequency with increased power through the separatrix. Furthermore, type III ELMs occur when the power through the separatrix is just above the L-H transition threshold power, followed by ELM-free H-mode when the power through the separatrix is higher and by type I ELMs for even higher power.

It is a common practice to scale ELM frequency with the input power, e.g. [79]. This approach is based on the assumption that a change of the thermal energy stored in the plasma, radiation losses from the inside of the LCFS, plasma shape and plasma current are constant at the time of interest. These conditions are usually fulfilled in large tokamaks, where the transition to the H-mode occurs during the stationary phase of the discharge and after an auxiliary heating is switched on, see [80], [81].

This is not the case of smaller tokamaks such as COMPASS. There, the ohmic heating power is often large enough to trigger L-H transition immediately after the creation of the divertor configuration. Therefore it is not possible to use input power as a proxy for power through LCFS and the global power balance must be fully evaluated.

This section describes, quantifies and discusses the individual terms of the global power balance, including time dependent parts, and exemplifies them on several discharges of the COMPASS tokamak.

4.5.1 Global power balance - theory

The global power balance in a tokamak can be described by the equation:

$$U_{ext} \cdot I_{pl} + P_{aux} = (L \cdot \frac{\mathrm{d}I_{pl}}{\mathrm{d}t})I_{pl} + (I_{pl} \cdot \frac{\mathrm{d}L}{\mathrm{d}t})I_{pl} + \frac{\mathrm{d}W}{\mathrm{d}t} + P_{rad} + P_{sep}, \tag{4.54}$$

where U_{ext} is voltage induced to the plasma by external sources - PF coils circuits currents and passive structures currents, I_{pl} is plasma current, P_{aux} is auxiliary heating power, L is plasma column self-inductance, W is thermal energy stored in the plasma, P_{rad} are radiation losses from the inside of the LCFS (bulk plasma) and P_{sep} is power (energy flux) through separatrix (or LCFS in limiter plasma) carried by plasma particles.

The term $U_{ext} \cdot I_{pl}$ is power from external inductive sources, usually poloidal field coils circuits or vacuum vessel current. The term $(L \cdot \mathrm{d}I_{pl}/\mathrm{d}t)I_{pl}$ is power used to build up the magnetic field energy by changes of plasma current. The term $(I_{pl} \cdot dL/dt)I_{pl}$ covers a contribution of the plasma shape and current profile changes to the magnetic field energy content. The two terms for magnetic field energy changes are on the right-hand side of the Equation (4.54) because they are viewed as a sink of the energy in our notation. It is also possible to move these two terms to the left-hand side and use ohmic heating power P_{ohmic} defined as:

$$P_{ohmic} = U_{pl} \cdot I_{pl} = \left(U_{ext} - \frac{\mathrm{d}(L \cdot I_{pl})}{\mathrm{d}t} \right) \cdot I_{pl} = (U_{ext} - L \cdot \frac{\mathrm{d}I_{pl}}{\mathrm{d}t} - I_{pl} \cdot \frac{\mathrm{d}L}{\mathrm{d}t}) \cdot I_{pl}, \quad (4.55)$$

where U_{pl} is plasma voltage used for ohmic heating.

It is necessary to note that neither U_{pl} nor U_{ext} can be directly measured when plasma current or plasma shape is changing. This will be discussed in the next sub-section.

Both terms for magnetic field energy changes are derived from Faraday's law of induction and from inductance definition, see Equation (4.55) and Equation (3.25) in the Section 3.1.4 - Theory for calculation of poloidal magnetic field. The terms cannot be obtained as a time derivative of $E = 1/2\, L I_{pl}^2$, because this formula is valid only for time-constant inductances L_C:

$$E = \int_0^t P \mathrm{d}t' = \int_0^t I \cdot U \cdot \mathrm{d}t' = \int_0^t I \cdot \frac{\mathrm{d}(LI)}{\mathrm{d}t} \cdot \mathrm{d}t' = L_C \int_0^t I \cdot \frac{\mathrm{dI}}{\mathrm{d}t} \cdot \mathrm{d}t' = L_C \int_0^I i \cdot \mathrm{di} = \frac{1}{2} L_C I^2, \quad (4.56)$$

The difference between correctly (*E2*) and incorrectly (*E1*) calculated plasma column magnetic field energy is shown in the **Figure 4.19**. The difference in energy is relatively small (~5 %), but difference in required power is not negligible in the global power balance equation, see discussion in following sections and in the **Figure 4.23**. Note that the E2 does not end at zero, implying that the plasma self-inductance, calculated from EFIT reconstructed equilibria, is not fully self-consistent.

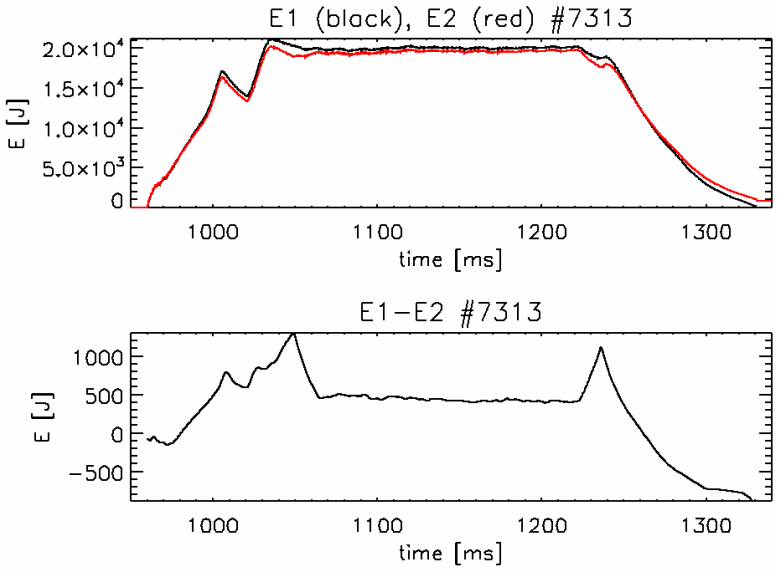

Figure 4.19: Comparison of plasma magnetic field energy calculated by two methods: $E1 = 1/2\, L_C I_{pl}^2$ and $E2 = \int_0^t I \cdot \frac{\mathrm{d}(LI)}{\mathrm{d}t'} \cdot \mathrm{d}t'$ for COMPASS discharge #7313.

The term P_{aux} in the Equation (4.54) denotes auxiliary heating power deposited inside the LCFS. In case that a non-inductive current drive is used, the term P_{aux} should include both heating and current driving power of the auxiliary heating system. Alternatively, it is possible to include non-inductive current drive into U_{ext}, but this approach is not used in this thesis. Auxiliary heating can typically be neutral

beam injection (NBI), as is the case of COMPASS [15], [16], ion cyclotron resonance heating (ICRH), electron cyclotron resonance heating (ECRH) or lower hybrid current drive (LHCD). The determination of the power deposited in the plasma can be difficult for some of these auxiliary heating systems and can require numerical models.

The term $\mathrm{d}W/\mathrm{d}t$ is the change of the thermal energy of the particles stored inside of the LCFS. The thermal energy content can be measured by diamagnetic loop, see e.g. [82].

The term P_{rad} for radiation losses from inside of the LCFS can be assessed from bolometric measurements [22] using tomographic reconstruction [23]. It is important to take into account only power radiated from the inside of the LCFS and not to include power radiated from the Scrape-Off Layer (SOL).

The term P_{sep}, power carried by particles crossing the separatrix (or LCFS in limiter plasma), cannot be measured and must be calculated. Its calculation is desired, because it is the term used in the scaling laws.

Occasionally, the terms P_{rad} and P_{sep} are combined into one common term called loss power:

$$P_{loss} = P_{rad} + P_{sep}\,. \tag{4.57}$$

The enumeration of the terms in the global power balance equation allows determination of $\tau_E = W/P_{sep}$ (energy confinement time) and $\tau_E^* = \dfrac{W}{P_{rad} + P_{sep}}$ (global energy confinement time), see [83] for reference.

4.5.2 Determination of external and plasma voltage

As was already mentioned in the previous section, both external inductive voltage U_{ext} and plasma voltage U_{pl} cannot be directly measured during non-stationary phases of the tokamak discharge. The external voltage U_{ext} is voltage induced to the plasma from external inductive sources:

$$U_{ext} = -\sum_{PFC}\left(L_{PFC-pl}\frac{\mathrm{d}I_{PFC}}{\mathrm{d}t} + I_{PFC}\frac{\mathrm{d}L_{PFC-pl}}{\mathrm{d}t}\right) - \sum_{ps}\frac{\mathrm{d}\left(L_{ps-pl}\cdot I_{ps}\right)}{\mathrm{d}t}, \tag{4.58}$$

where $L_{PFC\text{-}pl}$ are mutual inductances between the poloidal field coils circuits and plasma column, I_{PFC} are currents in the poloidal field coils circuits, $L_{ps\text{-}pl}$ are mutual inductances between passive structures (e.g. elements describing vacuum vessel) and plasma column and I_{ps} are currents in the passive structures. The terms with time derivative of the mutual inductance are important during plasma shape and current profile changes.

By combining the Equations (4.55) and (4.58) we obtain an expression for the plasma voltage:

$$U_{pl} = -\sum_{PFC} L_{PFC-pl} \frac{\mathrm{d}I_{PFC}}{\mathrm{d}t} - \sum_{PFC} I_{PFC} \frac{\mathrm{d}L_{PFC-pl}}{\mathrm{d}t} - \sum_{ps} L_{ps-pl} \frac{\mathrm{d}I_{ps}}{\mathrm{d}t} - \sum_{ps} I_{ps} \frac{\mathrm{d}L_{ps-pl}}{\mathrm{d}t} - (L \cdot \frac{\mathrm{d}I_{pl}}{\mathrm{d}t}) - (I_{pl} \cdot \frac{\mathrm{d}L}{\mathrm{d}t}) \quad (4.59)$$

Tokamaks are equipped with so called flux loops: toroidally wound coils located at different positions outside of the plasma, usually nearby the vacuum vessel. These diagnostic coils directly measure loop voltage U_{FL}:

$$U_{FL} = -\sum_{PFC} L_{PFC-FL} \frac{\mathrm{d}I_{PFC}}{\mathrm{d}t} - \sum_{PFC} I_{PFC} \frac{\mathrm{d}L_{PFC-FL}}{\mathrm{d}t} - \sum_{ps} L_{ps-FL} \frac{\mathrm{d}I_{ps}}{\mathrm{d}t} - \sum_{ps} I_{ps} \frac{\mathrm{d}L_{ps-FL}}{\mathrm{d}t} - (L_{pl-FL} \cdot \frac{\mathrm{d}I_{pl}}{\mathrm{d}t}) - (I_{pl} \cdot \frac{\mathrm{d}L_{pl-FL}}{\mathrm{d}t}) \quad , \quad (4.60)$$

where $L_{PFC\text{-}FL}$ are mutual inductances between the poloidal field coils circuits and the flux loop, $L_{pl\text{-}FL}$ is mutual inductance between the plasma column and the flux loop, $L_{ps\text{-}FL}$ are mutual inductances between passive structures and the flux loop and I_{ps} are currents in the passive structures.

In the Equation (4.60) the second and fourth terms on the right-hand side can be neglected if constant positions of the PF coils and passive structures are assumed. This is not necessarily correct approach because the forces acting on the PF coils can be large enough to change their geometry during the discharge significantly (up to ~ 1 % change of the length of the central solenoid).

It is clearly visible that $U_{pl} \neq U_{FL}$ in general case because the inductances between the PF coils circuits or passive structures and plasma column or flux loop are not equal. Similarly, the self-inductance of the plasma column L is not equal to the mutual inductance between plasma column and the flux loop $L_{pl\text{-}FL}$. Only in the flat-top phase of the discharge it is possible to equate U_{pl} and U_{FL} because the plasma current, plasma shape and current profile are constant, same as currents in some of the poloidal field coils circuits. The only changing current would be the plasma current drive circuit and it is possible to find a location for the diagnostic flux loop fulfilling $L_{PFC(current\ drive)\text{-}pl} = L_{PFC(current\ drive)\text{-}FL}$.

Time-varying inductances in the tokamak

The evaluation of the tokamak global power balance from Equations (4.54) and (4.58) requires knowledge of plasma self-inductance and mutual inductances between the poloidal field coils circuits (or passive structures) and plasma column. These inductances can be calculated if a time development of the plasma current density profile is known. The current density profile can be obtained from the equilibrium reconstruction performed by EFIT on the selected space grid for multiple time slices.

The equation used to calculate the mutual inductance between the plasma column (described by the current density j_{grid} in the predefined grid points with area ΔS) and a PF coils circuit (described by a set of elements created by infinitely thin wires with a given number of toroidal turns N_{PFe} and orientation represented by a sign of N_{PFe}) is:

$$L_{PFC-pl} = 1/I_{pl} \sum_{\mathrm{PFe}} \sum_{\mathrm{grid}} j_{grid} \cdot \Delta S \cdot L_{\mathrm{grid-PFe}} N_{\mathrm{PFe}} \,, \tag{4.61}$$

where $L_{grid\text{-}PFe}$ is mutual inductance of two one-turn thin wires. The theory was described in greater detail in the Section 3.1.4 - Theory for calculation of poloidal magnetic field.

Similar equation can be used to calculate the plasma self-inductance. The plasma column is represented by grid points and their mutual inductance $L_{m\text{-}n}$ (m and n are indices of grid points) can be used similarly as mutual inductance between grid points and PF circuits elements:

$$L = \Delta S^2 / I_{pl}^2 \left(\sum_{\mathrm{m} \neq \mathrm{m}} \sum_{\mathrm{n}} j_{\mathrm{m}} \cdot j_{\mathrm{n}} \cdot L_{\mathrm{m\text{-}n}} + \sum_{\mathrm{m}} j_{\mathrm{m}}^2 \cdot L_{m-m} \right), \tag{4.62}$$

where $L_{\mathrm{m}-m} = \mu_0 r \left(\ln(8r/a) - 1.75 \right)$ is the self-inductance of the grid point at the major radius r with characteristic minor radius of the grid point a (0.575x distance between two grid was used). The contribution of the second term on the right-hand side of the Equation (4.62) is decreasing with the number of grid points. The Equation (4.62) is application of the Equation (3.33) from Section 3.1.4.

4.5.3 Detailed analysis for L-mode discharge #7313

The COMPASS discharge #7313 is used as an example of the global power balance calculation from Equations (4.54) and (4.58). It is an ohmic L-mode discharge with flat-top plasma current -200 kA, line-averaged density $5.10^{19}\,\mathrm{m}^{-3}$, performed in deuterium with the shaping field configuration SNT and toroidal field -1.15 T. The PF coils circuits currents were already discussed in the detail in the Section 4.3.1. The beginning of the discharge is ignored and the calculation is performed for $t > 970$ ms, therefore the passive structures currents in the Equation (4.58) are negligible as discussed in the Section 4.3.2 and 4.3.3.

The time evolution of the plasma column shape during the discharge is in the **Figure 4.20**. The discharge begins in the circular limiter configuration (see **Figure 4.20a**), then the shaping starts (**Figure 4.20b**), reaches maximal area of the plasma cross-section just before the divertor configuration is created (**Figure 4.20c**) and then the flat-top plasma shape (stationary phase) is achieved (**Figure 4.20d**).

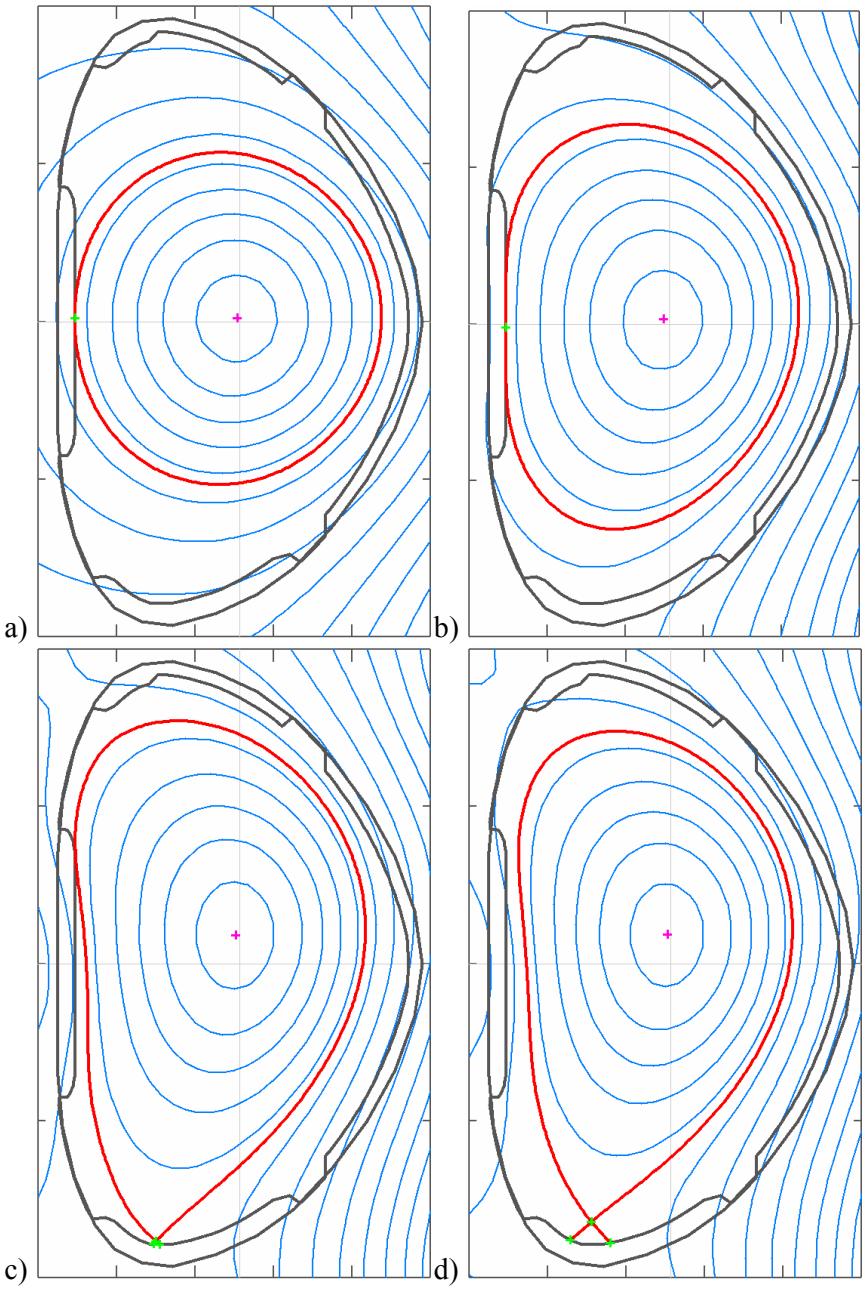

Figure 4.20: Plasma shape changes during current ramp-up and divertor creation for #7313. a) t = 980 ms, b) t = 1010 ms, c) t = 1050 ms, d) t = 1100 ms.

Figure 4.21 shows the time evolution of the plasma current, plasma self-inductance and mutual inductances between plasma and COMPASS PF coils circuits. These are used to calculate the individual terms in the global power balance equation (4.54). Furthermore, the mutual inductance between the plasma and Flux Loop #4 located at $R = 0.325$ m, $Z = 0$ m is shown in the **Figure 4.21c**, which is used to estimate the error of the method by calculating $U_{FL4,calc}$ according the Equation (4.60) and comparing it with $U_{FL4,meas}$.

The vertical lines in the **Figure 4.21** show important times: t = 1005-1021 ms is a time when current in the MFPS circuit has zero derivative during switching between positive and negative current. At this time U_{ext} is around zero and plasma current reacts by a decrease. The vertical lines at t = 1066 ms and t = 1222 ms enclose the time when both plasma shape and current are constant (see **Figure 4.21b**). The shape of the plasma column and its self-inductance is changing significantly in time between 1021 ms and 1066 ms. The transition between limiter and divertor configuration occurs during this time.

Figure 4.21 also shows that:

1. Plasma self-inductance is around 1 μH.
2. The mutual inductance between the plasma column and the MFPS circuit is constant regardless of the plasma shape and is 22 μH. This feature of the MFPS circuit was already shown in the **Table 3-3** in the Section 3.1.6 - Mutual inductances of poloidal field coils circuits.
3. The mutual inductances between the plasma column of the discharge #7313 and EFPS, SFPS-SNT, BR and BV are changing within values specified in the **Table 3-3**.
4. The mutual inductance between the plasma column and Flux Loop #4 is ~40 % of the plasma self-inductance, which is important when comparing U_{pl} and U_{FL} according the Equations (4.59) and (4.60).

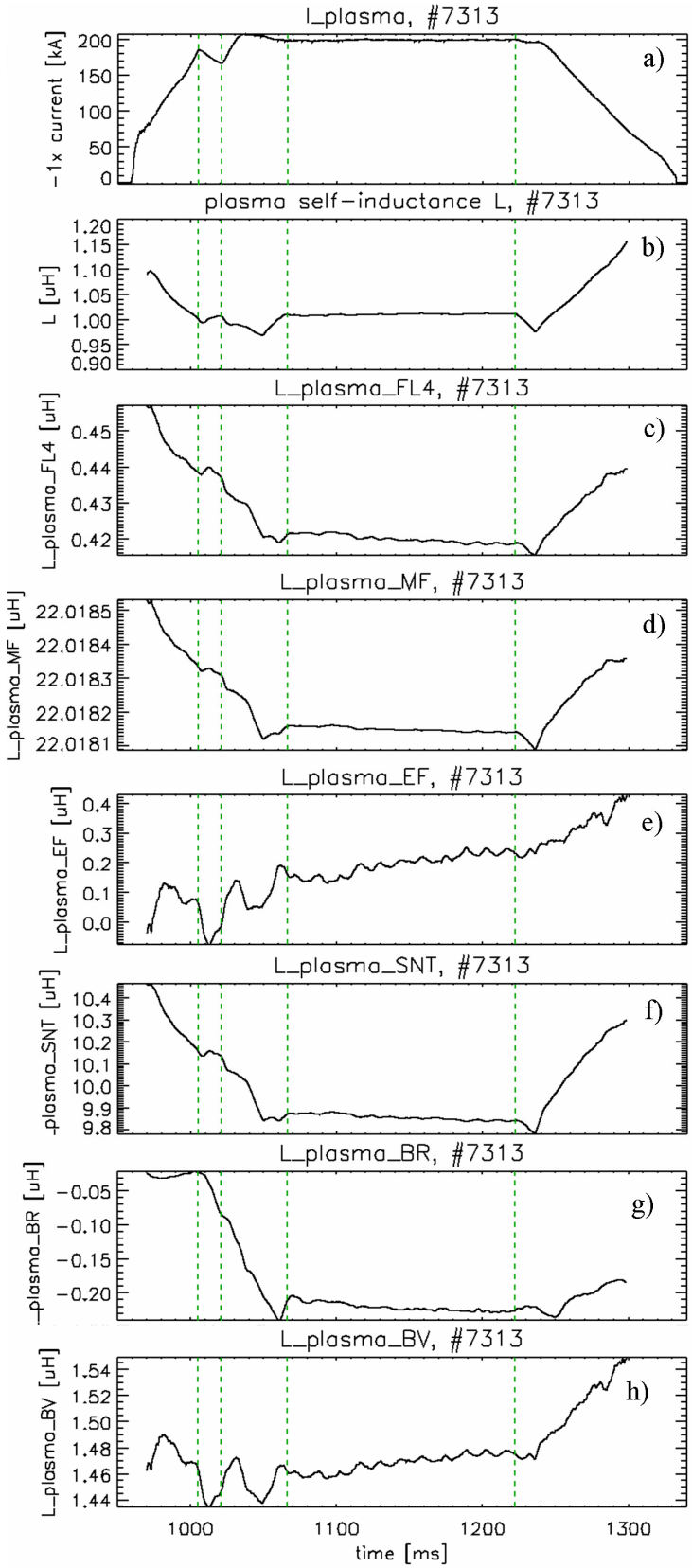

Figure 4.21: Plasma current and inductances calculated from EFIT.

Error estimation

U_{pl} should be calculated according the Equation (4.55) in order to enumerate the global power balance. It is difficult to determine the precision of such calculation. In order to estimate the error of the U_{pl} calculation a comparison of measured and calculated loop voltage U_{FL4} ($R = 0.325$ m, $Z = 0$ m) was performed. U_{FL4} is calculated according the Equation (4.60), compared to measured value and obtained relative difference is assumed to be similar to the error of U_{pl}.

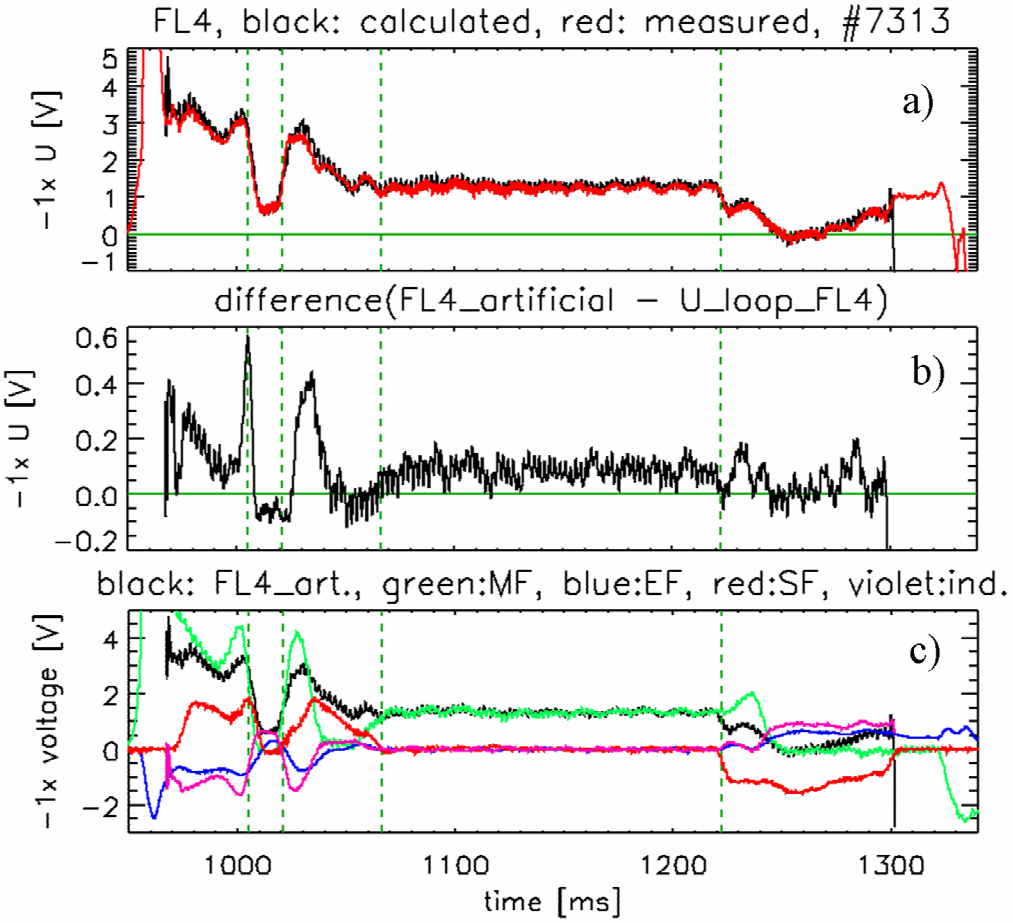

Figure 4.22: Comparison of measured and calculated loop voltage on flux loop FL4. FL4_art is calculated (artificial) loop voltage, ind. means contribution from plasma current and mutual inductance changes - last two terms in the Eq. (4.60).

The results are shown in the **Figure 4.22a**, **b**. The agreement between measured and calculated loop voltage U_{FL4} is good, even though during the transitions of the MF current passing zero ($t = 1005$-1021 ms) the error is largest. The reason for this behaviour is probably in the quality of the equilibrium reconstruction from EFIT. The inputs into the EFIT, as used on COMPASS (see Section 4.4.1), are not sufficient to reliably reconstruct plasma current density profile and therefore its changes associated with short-term zero external loop voltage U_{ext} applied.

The individual contributing terms according the Equation (4.60) are shown in the **Figure 4.22c**. The $L_{pl\text{-}FL4}$ was used as in the **Figure 4.21c**, the terms $\mathrm{d}L_{PFC-FL}/\mathrm{d}t$

were neglected, as well as passive structures contribution. The used mutual inductances between PF coils circuits and Flux Loop #4 were taken from the **Table 3-4**: $L_{MF\text{-}FL4}$ = 22 μH, $L_{EF\text{-}FL4}$ = -6.62 μH, $L_{SNT\text{-}FL4}$ = 17.01 μH, $L_{BR\text{-}FL4}$ = 0 μH and $L_{BV\text{-}FL4}$ = 0.4 μH.

The **Figure 4.22c** shows that:

1. The MFPS circuit induced voltage (green) is the only contributing term to the loop voltage on the Flux Loop #4 during the flat-top phase of the discharge (1066 - 1222 ms). See **Figure 4.5** for time-traces of the PF coils circuits currents.
2. The loop voltage U_{FL4} is ~0.5 V during MFPS passing zero. The MFPS and EFPS contributions are zero, but plasma current and self-inductance change and SFPS current change generate small loop voltage at the position of the HFS Flux Loop.
3. The MFPS circuit induced loop voltage (green) is the largest but not dominant during the plasma current ramp-up. The MFPS current is constant during the ramp-down and its contribution to the loop voltage is small.
4. The EFPS circuit (blue) contributes opposite voltage than MFPS (green) and SFPS-SNT (red). That is caused by opposite sign in the mutual inductance between the EFPS and plasma. It should be highlighted that this is a contribution to the loop voltage measured by Flux Loop #4. The plasma column voltage U_{pl} does not have the same behaviour ($L_{EF\text{-}FL4}$ = -6.62 μH while $L_{EF\text{-}pl}$ = <-0.1, -0.4> μH, see **Figure 4.21e**).
5. The SFPS-SNT circuit induced loop voltage (red) has significant contribution during both ramp-up and ramp-down phase of the discharge.
6. The changes of plasma current and mutual inductance to Flux Loop #4 have significant influence on the loop voltage U_{FL4}.

The conclusion from the analysis of the structure of the loop voltage measured by the HFS Flux Loop #4 is that there are many different significant contributors to the U_{FL4} when the plasma is not in the flat-top phase.

Global power balance during discharge

The results from the calculation of all terms of the global power balance equation for the discharge #7313 are shown in the **Figure 4.23**.

The externally induced power (**Figure 4.23a**) is ~ 200-300 kW during the flat-top, up to 1 MW during ramp-up and negative during plasma current ramp-down phase. The plasma current change power (**Figure 4.23b**) consumes a majority of the available power during the ramp-up, provides power during the MFPS current zero-derivative phase and during the I_{pl} ramp-down (negative sign vs. P_{ext}). The term for the change of plasma shape (**Figure 4.23c**) is non-negligible and contributes up to +/- 150 kW. This term is the least reliable due to reliability of the EFIT reconstruction. The term for the plasma thermal energy (**Figure 4.23d**) change has also surprisingly significant contribution to the global power balance. During H-mode and particularly at L-H transition it can be even more important. The radiation losses (**Figure 4.23e**) are relatively stable in L-modes, on the other hand, they rise

strongly during ELM-free H-modes in COMPASS due to rise of the plasma density. There is also a significant uncertainty in their absolute calibration: correction factor 1.4-2 against off-situ calibration is generally used (factor 2 is used in this thesis). **Figure 4.23f** shows the desired P_{sep} graph. Obtained values are reasonable during the flat-top, believable during the slow current changes and questionable during the fast shape changes. The results calculated for these discharge phases are possible but probably strongly influenced by the reliability of the EFIT equilibrium reconstruction.

Particularly interesting is the P_{sep} rise during the time period 1222-1235 ms. The reason of the rise is the term for the change of plasma shape (**Figure 4.23c)**. The plasma column is expanding its poloidal area during return to the limiter configuration by decrease of the I_{SFPS}/I_{pl}. The increase of the diverted plasma poloidal area and subsequent increase of the P_{sep} can be potentially interesting for easier L-H transitions.

The smoothing used to create the **Figure 4.23** should be discussed in detail. The majority of the terms used in the global power balance equation is calculated by means of numerical differentiation of measured signals. The numerical differentiation creates large noise. The noise is removed by application of simple 6 ms moving average window on the individual terms shown in the **Figure 4.23**. The noise of the plasma thermal energy content measured by diamagnetic loop (used CDB signal: "diamagnet_PP_EnergyBT") is so high that the moving average window is applied twice, effectively creating 2nd order filter. Furthermore, the EFIT reconstruction is used to calculate the inductances. The EFIT automatic run inputs are smoothed by 2 ms moving average window.

The filtering complicates interpretation of P_{sep} for transient phenomena like L-H transition. It should be kept in the mind that the P_{sep} at the moment of the L-H transition is influenced by P_{sep} $+/-6$ ms around.

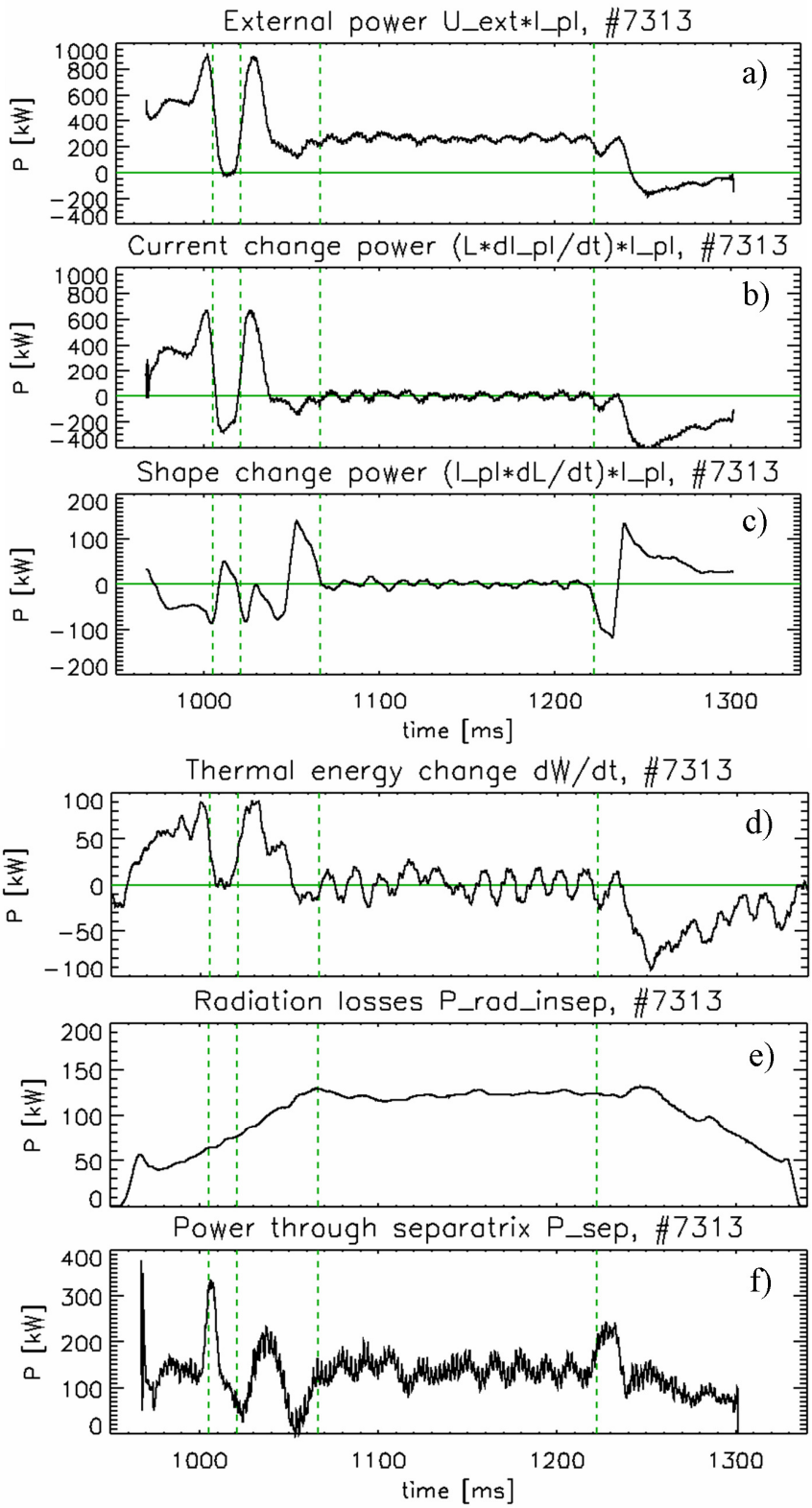

Figure 4.23: Individual terms of the global power balance equation (#7313). The signals are smoothed with moving average over 6 ms, with exception of d) thermal energy change which is smoothed with a 2nd order moving average filter. Signs conform to the COMPASS Currents Convention.

4.5.4 Examples for various discharges

This section contains examples of the global power balance analysis for several interesting discharges, all of them with B_T = -1.15 T. These are:

- #6317: -300 kA ohmic discharge with H-mode, frequency of the ELMs is changing and the ELMs are possibly type I ELMs; the density is changing between 6-9.10^{19} m^{-3} during the flat-top
- #9757: -300 kA ohmic discharge with large ELMs and RMP experiment; the density is 5-7.10^{19} m-3
- #9253: -240 kA ohmic discharge with long ELM free H-mode followed by three large ELMs; the density is rising from 5.10^{19} m^{-3} to 12.10^{19} m^{-3}

The discharge #6317 (**Figure 4.24**, **Figure 4.25**) has X-point formed at t = 1080 ms, the L-H transition occurs together with the X-point formation. The flat-top with stable plasma current and stable plasma shape is reached at t = 1100 ms. The delay between the X-point formation and flat-top is visible from the fact that Shape change power in the **Figure 4.24** reaches ~ 0 kW at t = 1100 ms. The SFPS circuit contribution to the U_{FL4} (**Figure 4.25**) also reaches 0 V at t = 1100 ms. The power through separatrix rises slowly between t = 1100 ms and t = 1160 ms, together with ELM frequency. The density, radiation losses and thermal energy start to decrease at t = 1160 ms, while the power through separatrix increases, together with frequency of ELMs. It should be noted, that radiation losses are higher in this discharge (#6317) compared to the two others (#9757, #9253) - 300 kW at the density 8.10^{19} m^{-3}. The higher impurity content is probable the reason. The behaviour of the ELM frequency with P_{sep} suggests that there are type I ELMs in this discharge.

Figure 4.26 and **Figure 4.27** describe discharge #9757. The H-mode starts at t = 1053 ms, while the plasma is in limiter configuration with contact point on the lower limiter. The clear X-point is formed at t = 1063 ms, 10 ms after L-H transition. The flat-top is achieved at t = 1075 ms. The P_{sep} is around 350 kW between t = 1075 ms and t = 1090 ms, when large ELMs with stable frequency are present. The P_{sep} is higher than in #6317, while ELM frequency is lower. This would indicate type III ELMs, but it is necessary to understand that the density, shape and impurity content of the plasma is different, which means that the plasmas are not directly comparable. The frequency of ELMs decreases together with P_{sep} after t = 1090 ms in the discharge #9757, again indicating type I ELMs.

Figure 4.28 and **Figure 4.29** describe discharge #9253 with ELM-free H-mode. This discharge has lower plasma current and therefore lower external power against the other two discharges. The H-mode starts only after the X-point is formed and flat-top achieved. The ELM-free H-mode increases density and therefore stored thermal energy and radiation losses until t = 1040 ms when radiation losses rise sharply, the thermal energy starts to decrease and a disruption follows. The P_{sep} is low for the duration of the ELM-free H-mode.

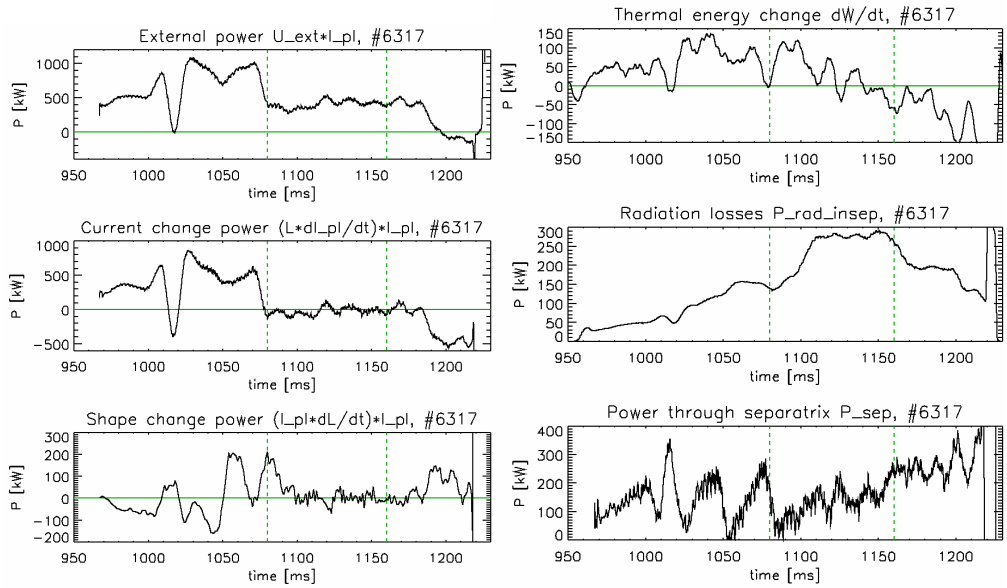

Figure 4.24: Discharge #6317. Individual terms of the global power balance equation for discharge with changing frequency of the ELMs. Vertical lines denote: a) t = 1080 ms - formation of the X-point and L-H transition, b) t = 1160 - density decrease and change of the ELM frequency.

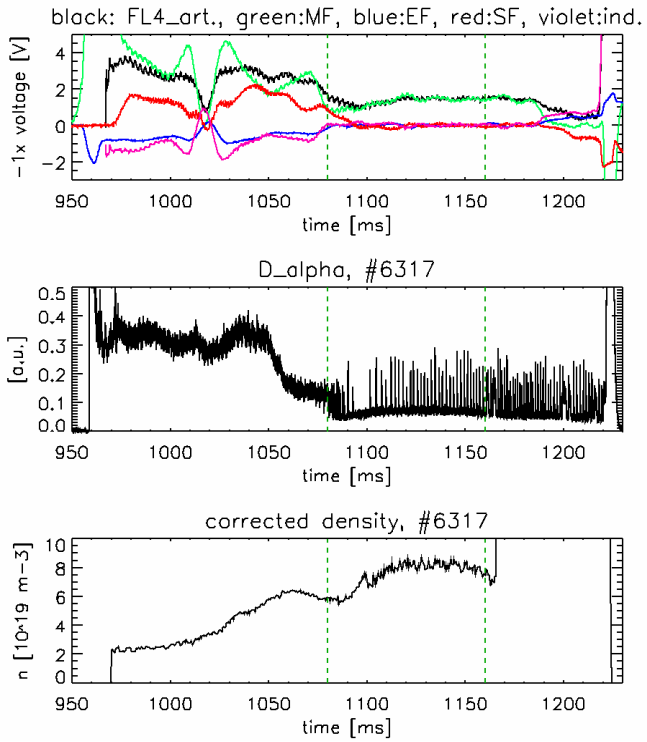

Figure 4.25: Discharge #6317 - U_{FL4} contributing terms, D-alpha signal and plasma density. FL4_art is calculated (artificial) loop voltage, ind. means contribution from plasma current and mutual inductance changes. The density signal had fringe jump at t = 1155 ms, the real density was decreasing from 8.10^{19} m^{-3} to $4{,}5.10^{19}$ m^{-3} until the end of the discharge.

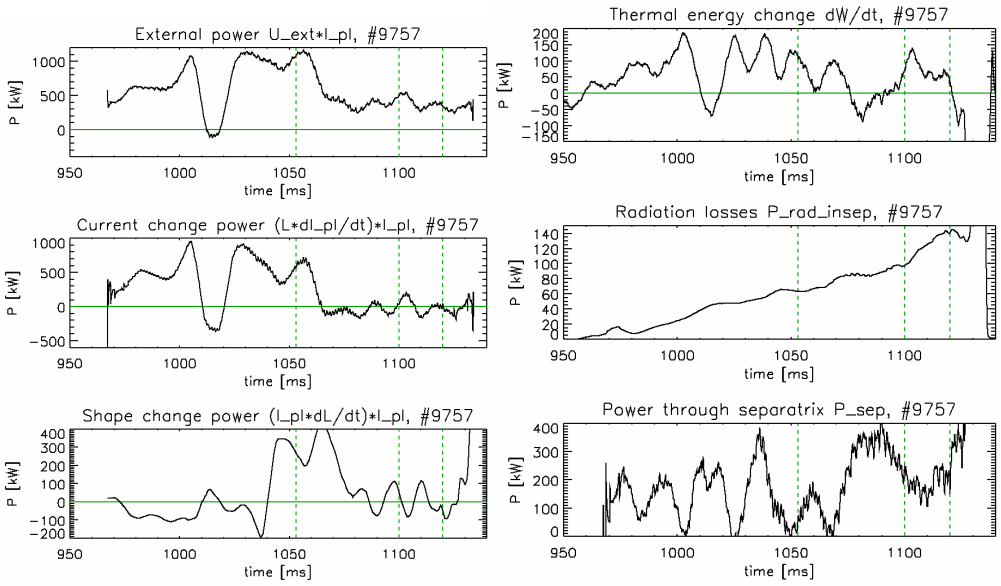

Figure 4.26: Discharge #9757. Individual terms of the global power balance equation for discharge with large ELMs. Vertical lines denote: a) t = 1053 ms - transition to the H-mode, b) t = 1100 ms - start of density rise, c) t = 1120 ms - start of 4 ms long RMP current. The X-point is formed at t = 1063 ms and flat-top is achieved at t = 1080 ms.

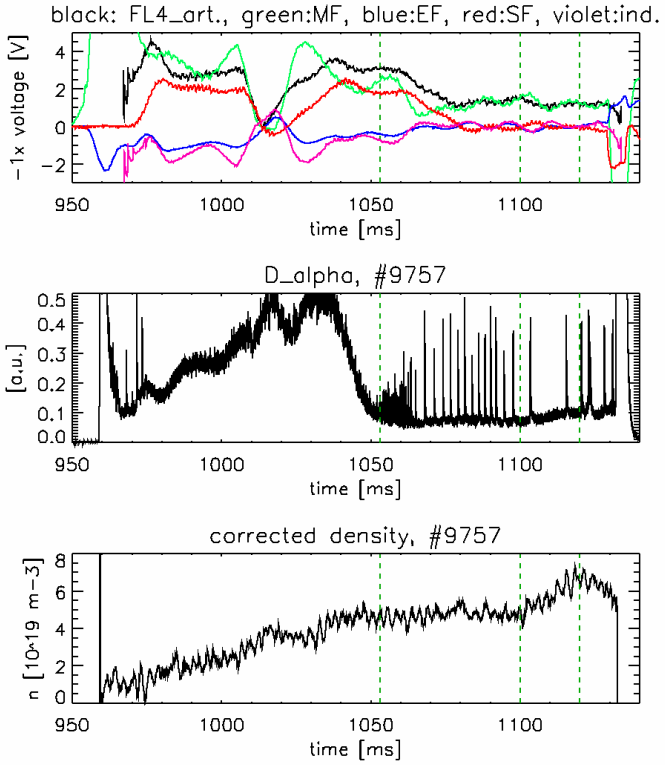

Figure 4.27: Discharge #9757 - U_{FL4} contributing terms, D-alpha signal and plasma density. FL4_art is calculated (artificial) loop voltage, ind. means contribution from plasma current and mutual inductance changes.

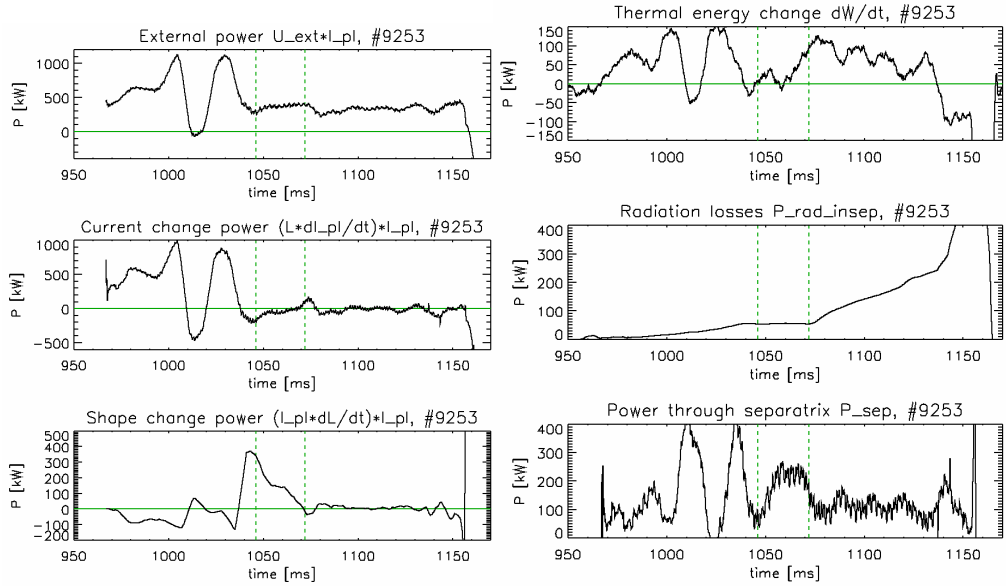

Figure 4.28: Discharge #9253. Individual terms of the global power balance equation for discharge with long ELM-free H-mode followed by three ELMs. Vertical lines denote: a) t = 1046 ms - the X-point formation, b) t = 1072 ms - transition to the H-mode.

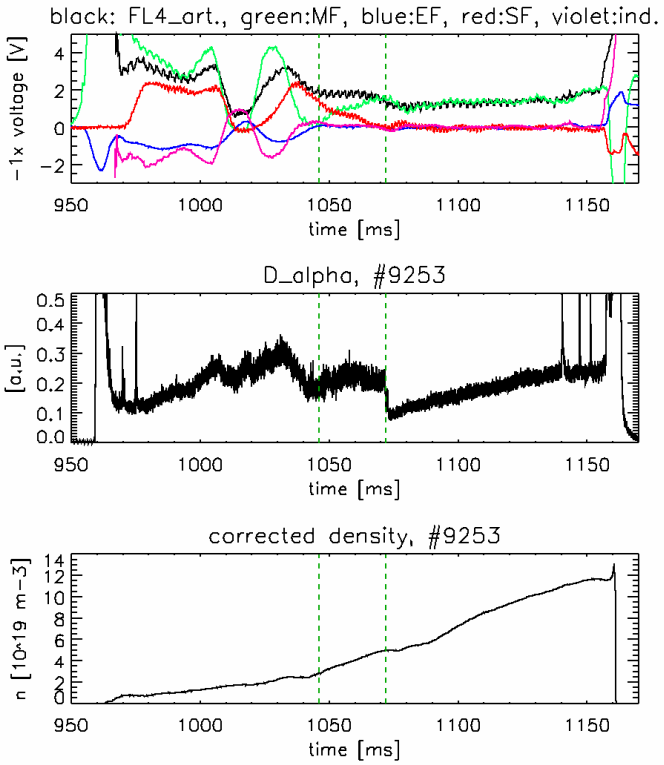

Figure 4.29: Discharge #9253 - U_{FL4} contributing terms, D-alpha signal and plasma density. FL4_art is calculated (artificial) loop voltage, ind. means contribution from plasma current and mutual inductance changes.

All three discharges demonstrate the importance of detailed analysis of the global power balance and its individual terms. The L-H transition occurs during plasma shape changes which must be taken into account in calculation of the proper power through separatrix P_{sep}. Evaluation of the individual terms in the global power balance equation using calculated rather than measured voltage allows more precise determination of both ohmic power and power through separatrix in non-stationary tokamak discharge phases.

The question of the ELM type in the discharges is still open. While the dependence of ELM frequency on the power through separatrix is consistent with type I ELMs, the plasma density is changing during ELMs. The pedestal stability diagram will be necessary to decide the type of ELMs.

5 General conclusions

This thesis summarizes some of the technical and physical work of the author performed during his doctoral studies and during the reinstallation of the COMPASS tokamak in Prague. The two main topics are: 1) physical engineering description of the COMPASS magnetic field systems, and 2) utilization of the MHD equilibrium reconstruction for COMPASS physical programme.

Chapter 2 of the thesis provides brief description of the COMPASS tokamak, the physical programme and overall diagnostics. A special section is dedicated to the introduction of the magnetic diagnostics, particularly diagnostic coils used further in the thesis.

Chapter 3 provides physical engineering description of the COMPASS magnetic field systems. The geometry of the poloidal field (PF) coils and connection into circuits is described. The COMPASS Currents Convention, which codifies orientations and signs of currents and magnetic fields, is introduced. A theory for numerical calculation of the magnetic field of the toroidal coil is explained.

The information about PF coils geometry and connections was used to characterize the vacuum magnetic fields of the COMPASS poloidal field coils circuits. Both in-vessel magnetic fields and outside (stray) magnetic fields were described and discussed. The self-inductances and mutual inductances of the PF coils circuits, important in-vessel points and diagnostic flux loops were calculated.

Chapter 3 also provides description of the design of the PF coils circuit LC filter units. The filter is simple in principle, but the challenge is in power requirements (~ kA current in the filter with frequencies around ~1 kHz, < 1 MW energy dissipation) and in necessity to prevent oscillation with tokamak coil.

The final section in the Chapter 3 provides description of the thyristor Power Supply controller and improvements implemented in the controller algorithm.

The primary purpose of the Chapter 3 is to provide a comprehensive summary of technical and physical characteristics of the COMPASS PF coils circuits. The information contained in the Chapter 3 was used during COMPASS reinstallation and commissioning in Prague, particularly during the commissioning of the plasma control system. The information contained in the Chapter 3 is also important for the tokamak operators and Session Leaders, because it allows to understand the capabilities, possibilities and limitations of the COMPASS control system.

The work described in the Chapter 3 is closely connected to the publications [A1], [A2] and [A3] attached to the thesis.

The publication Havlicek et al.: *Power supplies for plasma column control in COMPASS tokamak* [A1] broadens the information contained in the Chapter 3 by describing two fast Power Supplies for plasma position control. The Power Supplies

were designed by external contractor and then manufactured, tested and commissioned by IPP Prague.

The attached publications Janky et al.: *Determination of the plasma position for its real-time control in the COMPASS tokamak* [A2] and Janky et al., *Upgrade of the COMPASS tokamak real-time control system* [A3] describe the work done on the creation of the COMPASS plasma feedback system. A simple algorithm for the real-time plasma position determination is described, together with feedback for the plasma radial and vertical position and for plasma shaping. The author of this thesis is second author of these publications.

It should be noted that the information contained in the Chapter 3 and in the attached articles is a part of "know-how" to commission the tokamak and its feedback control system. This information is difficult to obtain, because the published articles often describe either improvements in the existing feedback systems or advanced and complicated feedback systems, which are unsuitable for a small tokamak with limited manpower. The articles do not include the practical issues faced during commissioning of plasma control system.

Chapter 4 focuses on the numerical reconstruction of the MHD equilibrium, induced currents in the tokamak vacuum vessel and utilization of the reconstructed equilibria to determine plasma properties useful both for tokamak operators and for physicists studying the tokamak plasma.

The theory of the MHD equilibrium in the toroidally symmetrical devices - the Grad-Shafranov equation - is described, together with algorithm used in the EFIT (Equilibrium FITting) code. The EFIT++ version of the EFIT code was adapted for the COMPASS tokamak geometry, diagnostics and database. The work done in the improvement of the code is described. The induced currents model was implemented into the EFIT++ and benchmarked against older standalone code. The induced currents flow in the passive structures of the tokamak - vacuum vessel, PF coils casings or in the support structure. The induced currents model was used for the COMPASS tokamak and the calculated vacuum vessel currents were successfully compared with the measurements.

The influence of the calculated induced currents on the EFIT reconstructed equilibrium was assessed for COMPASS with surprising results: the influence of the induced currents is negligible during the plasma flat-top (which was expected), but it is also minimal during the plasma current ramp-up, even when the vessel current is comparable with plasma current. This is an unexpected result.

Chapter 4 also describes the utilization of the EFIT during routine operation of the COMPASS tokamak. The EFIT is calculated automatically on inter-shot basis and the movie with plasma shape and basic parameters is created and projected on the screen in the control room. The movie is used by tokamak operators to adjust the feedback setting for the plasma shape and parameters according to the physical requirements. The examples of the plasma shapes and practical control system settings are provided.

The last section of the Chapter 4 focuses on the calculation of the global power balance during the non-stationary discharge phases in the tokamak plasma. The distribution of the input power (ohmic and additional heating) to the different sink channels is discussed. The sink channels are: a) the build-up of the plasma column magnetic field energy, b) the plasma thermal energy build-up, c) radiation losses and d) power carried by particles crossing Last Closed Flux Surface. The calculation of the global power balance requires calculation of the time-varying mutual inductances between the PF coils circuits and the plasma column. The EFIT reconstructed equilibria computed for different times are used for this purpose.

The proper calculation of the global power balance is important for the COMPASS tokamak, because the important events, like L-H transition or ELMs frequency changes, often occur during the non-stationary discharge phases. The L-H transition can occur immediately after the X-point creation, during plasma shape change. The ELM frequency often changes together with the plasma thermal energy.

The analysis of the global power balance is provided for several representative discharges. The results show that all of the terms in the global power balance equation play important role and none can be neglected.

The results presented in this thesis provide the reader with comprehensive description of the COMPASS poloidal field coils circuits and with utilization of the equilibrium reconstruction code EFIT. The principal physical results are: 1) creation of the algorithm for the real-time plasma position determination, 2) implementation of the induced currents model into EFIT++ and 3) calculation of the global power balance for the COMPASS tokamak.

The work performed during the author's doctoral studies was used in several publications in impacted journals: the engineering articles focused on plasma control and feedback [A1], [A2], [A3], [55], [56], [84] and physical articles [17], [20], [23], [29], [30], [33], [85].

References

[1] Panek, R., J. Stockel, J. Havlicek, F. Janky, M. Hron, V. Weinzettl, P. Bilkova, M. Dimitrova, P. Hacek, R. Dejarnac, M. Aftanas, P. Bohm, P. Cahyna, M. Imrisek, E. Stefanikova, J. Varju and the COMPASS team, Characterization of Ohmic and NBI heated H-mode in the COMPASS tokamak, *Europhysics Conference Abstracts*, 2013, 37D, P4.103-P4.103.

[2] *COMPASS Project, COMPASS PHASE II, Application for preferential support*, Culham Laboratory: UKAEA, 1983, SP 82/108/2.

[3] *The COMPASS Project, THE COMPASS PROJECT SAFETY ASSESSMENT*, Culham Laboratory: UKAEA, 1989, CPS/SAC/022/S2.

[4] *TOKAMAK OPERATIONS COMPASS-D, Tokamak Operations Training Course Sep. 1997*, ed. Brian Lloyd, Culham Laboratory: UKAEA, 1997.

[5] Bond, A., et al., The COMPASS tokamak/pinch load assembly design, *Proceedings of the 13th Symposium on Fusion Technology*, Varese (I), 1984, pp. 753-758.

[6] Bayes, D.V., et al., COMPASS electrical power and control systems design, *Proceedings of the 13th Symposium on Fusion Technology*, Varese (I), 1984, pp. 889-894.

[7] Noyes, R.J., et al., Future AC and DC Power Systems at Culham, *Proceedings of the 13th Symposium on Fusion Technology*, Varese (I), 1984, pp. 895-898.

[8] Bold, D., D.C. Edwards, J.W. Gray, J.H. Hay, S.E.V. Warder, Compass Poloidal Field Power Supply System, *Proceedings of the 14th Symposium on Fusion Technology*, Avignon (F), 1986, pp. 847-852.

[9] Fielding, S.J., R.J. Buttery, A.R. Field, P.B. Jones, H. Meyer, M. Valovic, H.R. Wilson and the COMPASS-D Physics and ECRH Teams, ELM control in COMPASS-D, *Europhysics Conference Abstracts*, 2001, 25A, 1825-1828.

[10] Pánek, R., O. Bilyková, V. Fuchs, M. Hron, P. Chráska, P. Pavlo, J. Stöckel, J. Urban, V. Weinzettl, J. Zajac and F. Žáček, Reinstallation of the COMPASS-D Tokamak in IPP ASCR, *Czechoslovak Journal of Physics*, 2006, 56(2), B125-B137.

[11] Carvalho, I.S., *Real-time control for long ohmic alternate current discharges*, Ph.D. thesis, Universidade Técnica de Lisboa, Instituto Superior Técnico, 2013

[12] Szappanos, A., M. Berta, M. Hron, R. Pánek, J. Stöckel, S. Tulipán, G. Veres, V. Weinzettl, S. Zoletnik, EDICAM fast video diagnostic installation on the COMPASS tokamak, *Fusion Engineering and Design*, 2010, 85(3-4), pp. 370-373.

[13] Crossland, R.T., R.J. Hayward, T.N. Todd, P.S. Haynes, J.W. Hill, A.W. Morris, P. Nicholson, R.A. Crook, COMPASS TF coil dynamic vertical preload device and PF coil alignment using a fixed coil array, *Proceedings of the 16th Symposium on Fusion Technology*, London, 1990, pp. 632-635.

[14] Havlicek, J., O. Kudláček, F. Janky, J. Horáček, R. Beňo, D.F. Valcárcel, J. Fixa, J. Brotánková, J. Zajac, M. Hron, R. Pánek, P. Cahyna, Status of Magnetic Diagnostics on COMPASS, in *WDS'10 Proceedings of Contributed Papers: Part II - Physics of Plasmas and Ionized Media* (eds. J. Safrankova and J. Pavlu), Prague, Matfyzpress, 2010, pp. 12-17.

[15] Urban, J., V. Fuchs, R. Pánek, J. Preinhalter, J. Stöckel, F. Žáček, V. Davydenko and V. Mishagin, NBI system for reinstalled COMPASS-D tokamak, *Czechoslovak Journal of Physics*, 2006, 56(2), B176-B181.

[16] Mitošínková, K., *Additional plasma heating of tokamak plasma by injected of powerful beam of H/D atoms,* Master thesis, Masaryk University, 2014.

[17] Weinzettl, V., R. Panek, M. Hron, J. Stockel, F. Zacek, J. Havlicek, P. Bilkova, D.I. Naydenkova, P. Hacek, J. Zajac, R. Dejarnac, J. Horacek, J. Adamek, J. Mlynar, F. Janky, M. Aftanas, P. Bohm, J. Brotankova, D. Sestak, I. Duran, R. Melich, D. Jares, J. Ghosh, G. Anda, G. Veres, A. Szappanos, S. Zoletnik, M. Berta, V.F. Shevchenko, R. Scannell, M. Walsh, H.W. Müller, V. Igochine, A. Silva, M. Manso, R. Gomes, Tsv. Popov, D. Sarychev, V.K. Kiselov, S. Nanobashvili, Overview of the COMPASS diagnostics, *Fusion Engineering and Design,* 2011, 86(6-8), pp. 1227-1231.

[18] Havlicek, J., J. Horacek, V. Weinzettl, O. Hronova, D. Naydenkova, J. Zajac, Magnetic Diagnostics for Start-up Phase of COMPASS, in *WDS'09 Proceedings of Contributed Papers: Part II - Physics of Plasmas and Ionized Media* (eds. J. Safrankova and J. Pavlu), Prague, Matfyzpress, 2009, pp. 148-152.

[19] Bílková, P., M. Aftanas, P. Böhm, V. Weinzettl, D. Šesták, R. Melich, J. Stöckel, R. Scannell, M. Walsh, Design of new Thomson scattering diagnostic system on COMPASS tokamak, *Nuclear Instruments and Methods in Physics Research Section A*, 2010, 623[2], pp. 656-659.

[20] Bohm, P., M. Aftanas, P. Bilkova, E. Stefanikova, O. Mikulin, R. Melich, F. Janky, J. Havlicek, D. Sestak, V. Weinzettl, J. Stockel, M. Hron, R. Panek, R. Scannell, L. Frassinetti, A. Fassina, G. Naylor and M. J. Walsh, Edge Thomson scattering diagnostic on COMPASS tokamak: Installation, calibration, operation, improvements, *Review of Scientific Instruments*, 2014, 85[11], 11E431-11E431.

[21] Šesták, D., V.Weinzettl, P. Bílková, P. Böhm, M. Aftanas, D.I. Naydenkova, J. Stöckel, I. Ďuran, M.J.Walsh, Design and engineering of optical diagnostics for COMPASS, *Fusion Engineering and Design*, 2009, 84[7-11], pp. 1755–1758.

[22] Weinzettl, V., D.I. Naydenkova, D. Sestak, J. Vlcek, J. Mlynar, R. Melich, D. Jares, J. Malot, D. Sarychev, V. Igochine, Design of multi-range tomographic system for transport studies in tokamak plasmas, *Nuclear Instruments and Methods in Physics Research Section A*, 2010, 623[2], pp. 806-808.

[23] Mlynar, J., M. Imrisek, V. Weinzettl, M. Odstrcil, J. Havlicek, F. Janky, B. Alper, A. Murari, JET-EFDA Contributors, Introducing minimum Fisher regularisation tomography to AXUV and soft x-ray diagnostic systems of the COMPASS tokamak, *Review of Scientific Instruments*, 2012, 83, 10E531.

[24] Weinzettl, V, G. Shukla, J. Ghosh, R. Melich, R. Panek, M. Tomes, M. Imrisek, D. Naydenkova, J. Varju, T. Pereira, R. Gomes, I. Abramovic, R. Jaspers, M. Pisarik, T. Odstrcil, G. Van Oost, High-resolution spectroscopy diagnostics for measuring impurity ion temperature and velocity on the COMPASS tokamak, *Fusion Engineering and Design*, in press, http://dx.doi.org/10.1016/j.fusengdes.2015.04.006.

[25] Janky, F., M. Hron, J. Havlicek, M. Varavin, F. Zacek, J. Seidl, R. Panek and COMPASS Team, Plasma density control in real-time on the COMPASS tokamak, *Fusion Engineering and Design*, in press, http://dx.doi.org/10.1016/j.fusengdes.2015.04.065.

[26] J. Zajac, J. Preinhaelter, J. Urban, D. Sestak, A. Krivska, S. Nanobashvili, EBW/ECE Radiometry on COMPASS tokamak – design and first measurements, *Radio Frequency Power in Plasmas: Proceedings of the 18th Topical Conference*, 2009, 1187, AIP Conference Proceedings, pp. 473–476.

[27] J. Zajac, J. Preinhaelter, J. Urban, F. Zacek, D. Sestak, S. Nanobashvili, EC-EBW emission diagnostics for the COMPASS tokamak, *Proceedings of the 18th Topical Conference on High-Temperature Plasma Diagnostics, Wildwood (USA), Review of Scientific Instruments,* 2010, 81[10], pp. 10D911-10D911.

[28] Adamek, J., J. Horacek, J. Seidl, H.W. Müller, R. Schrittwieser, F. Mehlmann, P. Vondracek, S. Ptak, COMPASS Team andASDEX Upgrade Team, Direct Plasma Potential Measurements by Ball-Pen Probe and Self-Emitting Langmuir Probe on COMPASS and ASDEX Upgrade, *Contributions to Plasma Physics*, 2014, 54[3], pp. 279-284.

[29] Dimitrova,M., Tsv.K. Popov, P. Ivanova, E. Vasileva, E. Hasan, J. Horáček, P. Vondráček, R. Dejarnac, J. Stöckel, V. Weinzettl, J. Havlicek, F. Janky and R. Panek, Evaluation of the scrape-off-layer plasma parameters by a horizontal reciprocating Langmuir probe in the COMPASS tokamak, *Journal of Physics: Conference Series*, 2014, 514[1], pp. 012049-012049.

[30] Dimitrova, M., R. Dejarnac, Tsv.K. Popov, P. Ivanova, E. Vasileva, J. Kovačič, J. Stöckel, J. Havlicek, F. Janky and R. Panek, Plasma Parameters in the COMPASS Divertor During Ohmic Plasmas, *Contributions to Plasma Physics*, 2014, 54[3], pp. 255-260.

[31] Zoletnik, S., G. Petravich, A. Bencze, M. Berta, S. Fiedler, K. McCormick, J. Schweinzer, Two-dimensional density and density fluctuation diagnostic for the edge plasma in fusion devices, *Review of Scientific Instruments*, 2005, 76[7], 073504-073504.

[32] Hacek, P., V. Weinzettl, J. Stöckel, G. Anda, G. Veres, S. Zoletnik, M. Berta, Diagnostic Lithium Beam System for COMPASS Tokamak, in *WDS'11 Proceedings of Contributed Papers: Part II - Physics of Plasmas and Ionized Media* (eds. J. Safrankova and J. Pavlu), Prague, Matfyzpress, 2011, pp. 215-220.

[33] Berta, M., G. Anda, M. Aradi, A. Bencze, Cs. Buday, I.G. Kiss, Sz. Tulipán, G. Veres, S. Zoletnik, J. Havlicek, P. Háček, Development of atomic beam probe for tokamaks, *Fusion Engineering and Design*, 2013, 88(11), pp. 2875-2880.

[34] Mitosinkova, K., J. Stockel, M. Tomes, J. Varju., Energy Spectra Measured by NPA on the COMPASS Tokamak During NBI Heating, in *WDS'15 - Proceedings of Contributed Papers - Physics*, to be published.

[35] Havlicek, J., O. Hronová, Characterization of Magnetic Fields in the COMPASS Tokamak, in *WDS'08 Proceedings of Contributed Papers: Part II - Physics of Plasmas and Ionized Media* (eds. J. Safrankova and J. Pavlu), Prague, Matfyzpress, 2008, pp. 110-114.

[36] Havlicek J., Horacek J., Modelling of COMPASS tokamak PF coils magnetic fields, *Europhysics Conference Abstracts*, 2008, 32D, P4.080-P4.080.

[37] Zajac, J., F. Zacek, V. Lejsek, Z. Brettschneider, Short-term power sources for tokamaks and other physical experiments, *Fusion Engineering and Design*, 2007, 82(4), pp. 369-379.

[38] Zajac, J., R. Pánek, F. Žáček, J. Vlček, M. Hron, A. Křivská, R. Hauptmann, M. Daněk, J. Šimek, J. Prošek, Power supply system for COMPASS tokamak re-installed at the IPP, Prague, *Fusion Engineering and Design*, 2009, 84(7–11), pp. 2020–2024.

[39] Pavelka, J., R. Hauptmann, J. Šimek, P. Pavelka, Tokamak, in *ELEKTRO, odborný časopis pro elektrotechniku*, 2015, 2, pp. 6-13.

[40] Vyas, P., D. Mustafa, A. W. Morris, Vertical Position Control on COMPASS-D, *Fusion Science and Technology*, 1998, 33(2), 97-105.

[41] Kudláček, O., *Elektromagnetická pole v zařízeních s magnetickým udržením horkého plazmatu*, Bc. thesis, Czech Technical University in Prague, 2009.

[42] Urban, J., J. Pipek, M. Hron, F. Janky, R. Papřok, M. Peterka, A.S. Duarte, Integrated Data Acquisition, Storage, Retrieval and Processing Using the COMPASS DataBase (CDB), *Fusion Engineering and Design*, 2014, 89(5), pp. 712-716.

[43] Horacek, J., P. Vondracek, R. Panek, R. Dejarnac, M. Komm, R.A. Pitts, M. Kocan, R.J. Goldston, P.C. Stangeby, E. Gauthier, P. Hacek, J. Havlicek, M. Hron, M. Imrisek, F. Janky, J. Seidl, Narrow heat flux channels in the COMPASS limiter scrape-off layer, *Journal of Nuclear Materials*, in press, http://dx.doi.org/10.1016/j.jnucmat.2014.11.132.

[44] Dejarnac, R., P.C. Stangeby, R.J. Goldston, E. Gauthier, J. Horacek, M. Hron, M. Kocan, M. Komm, R. Panek, R.A. Pitts, P. Vondracek, Understanding narrow SOL power flux component in COMPASS limiter plasmas by use of Langmuir probes, *Journal of Nuclear Materials*, in press, http://dx.doi.org/10.1016/j.jnucmat.2014.12.100.

[45] Kocan, M., R.A. Pitts, G. Arnoux, I. Balboa, P.C. de Vries, R. Dejarnac, I. Furno, R.J. Goldston, Y. Gribov, J. Horacek, M. Komm, B. Labit, B. LaBombard, C.J. Lasnier, R. Mitteau, F. Nespoli, D. Pace, R. Panek, P.C. Stangeby, J.L. Terry, C. Tsui, P. Vondracek, Impact of a narrow limiter SOL heat flux channel on the ITER first wall panel shaping, *Nuclear Fusion*, 2015, 55(3), 033019 (16pp).

[46] Markovič, T., *Measurement of Magnetic Fields on GOLEM Tokamak*, Master thesis, Czech Technical University in Prague, 2012.

[47] Gryaznevich, M., T.G. Kilovataya, V.N. Pyatov, Effect of ferromagnet on the equilibrium of a tokamak plasma, *Sov. J. Plasma Phys.*, 1983, vol. 9.

[48] Carlson, B.C., Numerical computation of real or complex elliptic integrals, *Numerical Algorithms*, 1995, 10(1), pp. 13-26. Available from: http://arXiv.org/abs/math/9409227

[49] Milne-Thomson, L.M., Elliptic Integrals. In: M. Abramowitz and I.A. Stegun, *Handbook of Mathematical Functions with Formulas, Graphs, and Mathematical Tables*, New York: Dover Publications, 1970, pp. 591-592.

[50] Wikipedia contributors, Inductance, *Wikipedia, The Free Encyclopedia*, [viewed 19 April 2015]. Available from: http://en.wikipedia.org/wiki/Inductance.

[51] Sartori, F., G. De Tomassi, F. Picollo, The Joint European Torus - Plasma position and shape control in the world's largest tokamak, *IEEE Control Systems Magazine*, 2006, 26(2), pp. 64-78.

[52] Ariola, M., A. Pironti, Plasmashape control for the JET tokamak, *IEEE Control Systems Magazine*, 2005, 25(5), pp. 1101-1111.

[53] Neto, A., G. De Tommasi, R. Albanese, G. Ambrosino, M. Ariola, G. Artaserse, A.J.N. Batista, B. Carvalho, F. Crisanti, H. Fernandes, P.J. Lomas, F. Maviglia, A. Pironti, F. Rimini, F. Sartori, L. Zabeo and JET-EFDA Contributors, Exploitation of modularity in the JET tokamak vertical stabilization system, *Control Engineering Practice*, 2012, 20(9), pp. 846-856.

[54] Stockel, J., J. Brotankova, R. Dejarnac, J. Havlicek, M. Hron, D. Naydenkova, R. Panek, V. Weinzettl, J. Zajac, F. Zacek, M. Berta, A. Szappanos, Sz. Tulipán, G. Veres, S. Zoletnik, D. Valcarcel, T. Pereira, I. Cavalho, A. Duarte, A. Neto, H. Fernandes and the COMPASS Team, Plasma Breakdown Studies on COMPASS, *Europhysics Conference Abstracts*, 2009, 33E, P5.141-P5.141.

[55] Valcárcel, D.F., A. Neto, I.S. Carvalho, B.B. Carvalho, H. Fernandes, J. Sousa, F. Janky, J. Havlicek, R. Beňo, J. Horáček, M. Hron, R. Pánek: The COMPASS Tokamak Plasma Control Software Performance, *IEEE Transactions on Nuclear Science*, 2011, 58(4), pp. 1490-1496.

[56] Hron, M., F. Janky, J. Pipek, J. Sousa, B.B. Carvalho, H. Fernandes, P. Vondráček, P. Cahyna, J. Urban, R. Papřok, O. Mikulín, M. Aftanas, R. Pánek, J. Havlíček, J. Fortunato, A.J.N. Batista, B.A. Santos, A. Duarte, T. Pereira, D. Valcárcel, Overview of the COMPASS CODAC system, *Fusion Engineering and Design*, 2014, 89(3), pp. 177-185.

[57] Beňo, R., *Modelování systému řízení polohy plazmatu v tokamaku COMPASS*, Bc. thesis, Czech Technical University in Prague, 2008.

[58] Havlicek, J., M. Imríšek, K. Kovařík, V. Weinzettl, Global Power Balance in Non-Stationary Discharge Phases in the COMPASS Tokamak, in *WDS'14 Proceedings of Contributed Papers - Physics* (eds. J. Safrankova and J. Pavlu), Prague, Matfyzpress, 2014, pp. 204-210.

[59] Havlicek, J., J. Zajac, Design and Preliminary Results of the COMPASS Power Supplies Filters, in *WDS'13 Proceedings of Contributed Papers: Part II - Physics of Plasmas and Ionized Media* (eds. J. Safrankova and J. Pavlu), Prague, Matfyzpress, 2013, pp. 91-96.

[60] Junek, P., *Zprovoznění cívek pro řízení rezonančních magnetických odchylek*, Bc. thesis, Czech Technical University in Prague, 2010.

[61] Andresen, R.P., 5Spice Analysis Software, http://www.5spice.com

[62] Hauptmann, R., *Vliv filtrů na chování zdrojů pro vinutí tokamaku Compass*. Praha: ČKD Elektrotechnika, 2012. No PE 50665.

[63] Havlicek, J., R. Beňo, J. Stöckel, A Simulation of the COMPASS Equilibrium Field Power Supply PID Controller, in *WDS'11 Proceedings of Contributed Papers: Part II - Physics of Plasmas and Ionized Media* (eds. J. Safrankova and J. Pavlu), Prague, Matfyzpress, 2011, pp. 221-226.

[64] Astrom, K.J., T. Hagglund, *PID Controllers: Theory, Design, and Tuning*, 2nd edition, North Carolina: Instrument Society of America, 1995.

[65] *AVR221: Discrete PID controller*, Application Note, Atmel Corporation, 2006.

[66] Havlicek, J., J. Urban, A Magnetic Equilibrium Reconstruction in Tokamak, in *WDS'07 Proceedings of Contributed Papers: Part II - Physics of Plasmas and Ionized Media* (eds. J. Safrankova and J. Pavlu), Prague, Matfyzpress, 2007, pp. 234-239.

[67] Lao, L.L., H. St. John, R. D. Stambaugh, A.G. Kellman and W. Pfeiffer, Reconstruction of current profile parameters and plasma shapes in Tokamaks, *Nuclear Fusion*, 1985, 25(11), pp. 1611.

[68] Grad, H. and H. Rubin, Hydromagnetic equilibria and force-free fields, in *Proceedings of the 2nd UN Conference on the Peaceful Uses of Atomic Energy*, Geneva, IAEA, 1958, 31, pp. 190-197.

[69] Shafranov, V.D., Plasma equilibrium in a magnetic field, *Reviews of Plasma Physics*, 1966, 2, pp. 103.

[70] Shafranov, V. D., Determination of the parameters β_l and l_l in a Tokamak for arbitrary shape of plasma pinch cross-section, *Plasma Physics*, 1971, 13(9), pp. 757-762.

[71] Appel, L.C., G.T.A. Huysmans, L.L. Lao, P.J. McCarthy, D.G. Muir, E.R. Solano, J. Storrs, D. Taylor and W. Zwingmann, A Unified Approach to Equilibrium Reconstruction, *Europhysics Conference Abstract*, 2006, 30I, P-2.184.

[72] Lao, L.L., J.R. Ferron, R.J. Groebner, W. Howl, H. St. John, E.J. Strait and T.S. Taylor, Equilibrium analysis of current profiles in tokamaks, *Nuclear Fusion*, 1990, 30(6), pp. 1035.

[73] Appel, L.C., M.K. Bevir and M.J. Walsh, Equilibrium reconstruction in the START tokamak, *Nuclear Fusion*, 2001, 41(2), pp. 169-180.

[74] McArdle, G.J. and D. Taylor, Adaptation of the MAST passive current simulation model for real-time plasma control, *Fusion Engineering and Design*, 2008, 83, pp. 188-192.

[75] Tinios, G., S.F. Horne, I.H. Hutchinson and S.M. Wolfe, Model reduction for axisymmetric tokamak control, *Fusion Technology*, 1993, 24(4), pp. 355-365.

[76] Bertolini, E., F. Engelmann, M.A. Hoffman, A. Taroni, Plasma power balance models for self-sustained tokamak reactors, *Nuclear Fusion*, 1977, 17(5), pp. 955.

[77] Wagner, F., A quarter-century of H-mode studies, *Plasma Physics and Controlled Fusion*, 2007, 49, pp. B1–B33.

[78] Zohm, H., Edge localized modes (ELMs), *Plasma Physics and Controlled Fusion*, 1996, 38, pp. 105–128.

[79] Sartori, R., G. Saibene, L.D. Horton, M. Becoulet, R. Budny, D. Borba, A. Chankin, G.D. Conway, G. Cordey, D. McDonald, K. Guenther, M.G. von Hellermann, Yu Igithkanov, A. Loarte, P.J. Lomas, O. Pogutse, J. Rapp, Study of Type III ELMs in JET, *Plasma Physics and Controlled Fusion*, 2004, 46, pp. 723–750.

[80] Bell, M.G., R.J. Fonck, B. Grek, K.P. Jaehnig, R. Kaita, S.M. Kaye, T. McBride, D. Mueller, D.K. Owens, G.L. Schmidt, The energy balance of divertor discharges in the PDX tokamak, *Journal of Nuclear Materials*, 1984, 121, pp. 132–137.

[81] Müller, E.R., M. Keilhacker, K. Steinmetz, ASDEX Team, NI Team, Power balance of neutral-beam heated divertor discharges in the ASDEX tokamak, *Journal of Nuclear Materials*, 1984, 121, pp. 138–143.

[82] Shen, B., B.N. Wan, X.Q. Zhang, Diamagnetic measurement on HT-7 superconducting tokamak, *Fusion Engineering and Design*, 2004, 70(4), pp. 311-318.

[83] Van Oost, G., E. Rebhan, Thermonuclear burn criteria, *Fusion Science and Technology*, 2008, 53(2T), pp. 16-26.

[84] Hron, M., J. Sova, J. Šíba, J. Kovář, J. Adámek, R. Pánek, J. Havlicek, J. Písačka, J. Mlynář, J. Stőckel, Interlock system for the COMPASS tokamak, *Fusion Engineering and Design*, 2010, 85(3-4), pp. 505-508.

[85] Ďuran, I., O. Hronová, J. Stöckel, J. Sentkerestiová, J. Havlicek, Magnetic measurements using array of integrated Hall sensors on the CASTOR tokamak, *Review of Scientific Instruments*, 2008, 79[10], 10F123-10F123.

List of Abbreviations

ATCA1 - name of the data acquisition and control system based on the **Advanced Telecommunications Computing Architecture**

CCC - **COMPASS Currents Convention** - convention of the orientations and signs of the currents and mag. fields in COMPASS

CCFE - **Culham Centre for Fusion Energy** - research centre in United Kingdom

CDB - **COMPASS DataBase** - name of the database

CDF - **Computable Document Format** - file format for storing scientific data

CODAC - **Control, Data Access and Communication** - a term for system dedicated to control tokamak, acquire and store measured data

COMPASS - **Compact Assembly** - name of the tokamak

CS - **Central Solenoid** - coil closest to the major axis; responsible for induced current in the plasma

ECRH - **Electron Cyclotron Resonance Heating** - type of auxiliary heating system

EF - **Equilibrium Field** - main vertical magnetic field, used for maintaining plasma radial position

EFIT - **Equilibrium FITting** code - code for numerical reconstruction of the MHD equilibrium

EFPS - **Equilibrium Field Power Supply** - name of the power supply

ELMs - **Edge Localized Modes** - type of plasma instability during H-mode

EPR - **External Partial Rogowski** coil - name of the group of diagnostic coils; located outside of the vacuum vessel

FA - **Fast Amplifier** - name of the power supply with fast switching frequency (~40 kHz)

FABR - **Fast Amplifier, B_{radial}** - name of the power supply in the BR circuit, used for plasma vertical position stabilization

FABV - **Fast Amplifier, $B_{vertical}$** - name of the power supply in the BV circuit, used for plasma radial position stabilization

FPGA - **Field-Programmable Gate Array** - configurable integrated circuit

HFBR - family of fiber optic link components

HFS - **High Field Side** - inner side of tokamak, with higher toroidal field

H-mode - plasma mode with higher energy confinement

ICM - **Induced Currents Module** - a module in EFIT++ code; used for calculation of induced currents

ICRH - **Ion Cyclotron Resonance Heating** - type of auxiliary heating system

IDL - **Interactive Data Language** - programming language

IPP Prague - **Institute of Plasma Physics** of the Czech Academy of Sciences

IPR - **Internal Partial Rogowski** coil - name of the group of diagnostic coils located in the vacuum vessel

IST Lisbon - **Instituto Superior Técnico** - a school of engineering

INDUCTION - name of the code for calculation of induced currents in tokamak

ITER - **International Thermonuclear Experimental Reactor** - tokamak under construction

LCFS - **Last Closed Flux Surface** - the boundary between closed and open field lines in tokamak plasma in limiter configuration; in divertor configuration the boundary is called separatrix

LFS - **Low Field Side** - outer side of tokamak, with lower toroidal magnetic field

L-mode - plasma mode with lower energy confinement

L-H transition - transition between L-mode and H-mode

MARTe - **Multithreaded Application Real-Time executor** - software used for the COMPASS tokamak control system

MAST - **Mega Amp Spherical Tokamak** - name of the tokamak in UK

MF - **Magnetizing Field** - magnetic field used to generate voltage for the plasma in COMPASS

MFPS - **Magnetizing Field Power Supply** - name of the power supply

MHD - **Magnetohydrodynamics**

NBI - **Neutral Beam Injection** - type of auxiliary heating system

Nimbus - name of the data acquisition system based on NI PXIe-6368 cards

PF - **Poloidal Field**

PID - **Proportional-Integral-Derivative** controller

PS - **Power Supply**

RFPS - **Radial Field Power Supply** - obsolete name for FABR

RMP PS - **Resonant Magnetic Perturbation Power Supply** - name of the PS for RMP coils

SF - **Shaping Field** -magnetic field used for plasma shaping in COMPASS

SFPS - **Shaping Field Power Supply** - name of the power supply

Shaper - a part of the MFPS circuit; used for fast current change which produces voltage necessary for plasma breakdown

SND - **Single Null Divertor** - configuration of the SFPS circuit

SNT - **Single Null divertor, higher Triangularity** - configuration of the SFPS circuit

SOL - **Scrape-Off Layer** - plasma region characterized by open field lines

TF - **Toroidal Field** - magnetic field used to confine the plasma

TFPS - **Toroidal Field Power Supply**

UKAEA - **UK Atomic Energy Authority** - UK government research organization

VFPS - **Vertical Field Power Supply** - obsolete name for FABV

VKPS - **Vertical Kicks Power Supply** - PS for fast changes of vertical plasma position

X-point - saddle point on the ψ function; creates boundary between closed and opened field lines

Attached publication

I

Power supplies for plasma column control in COMPASS tokamak

Havlicek, J., R. Hauptmann, O. Peroutka, M. Tadros, M. Hron, F. Janky, P. Vondráček, P. Cahyna, O. Mikulín, D. Šesták, P. Junek, R. Pánek,
Fusion Engineering and Design, 2013, 88(9-10), pp. 1640-1640.

Attached publication

II

Determination of the plasma position for its real-time control in the COMPASS tokamak

Janky, F., J. Havlicek, D. Valcárcel, M. Hron, J. Horacek, O. Kudlacek, R. Panek and B.B. Carvalho,
Fusion Engineering and Design, 2011, 86(6-8), pp. 1120-1124.

Attached publication

III

Upgrade of the COMPASS tokamak real-time control system

Janky, F., J. Havlicek, A.J.N. Batista, O. Kudlacek, J. Seidl, A.C. Neto, J. Pipek, M. Hron, O. Mikulin, A.S. Duarte, B.B. Carvalho, J. Stockel, R. Panek,
Fusion Engineering and Design, 2014, 89(3), pp. 186-194.